University of Alberta

Elastic Properties of Sedimentary Rocks

by

Jaime Meléndez Martínez

A thesis submitted to the Faculty of Graduate Studies and Research
in partial fulfillment of the requirements for the degree of

Doctor of Philosophy

in

Geophysics

Department of Physics

Abstract

Sedimentary rocks are an important research topic since such rocks are associated to sources of ground water as well as oil, gas, and mineral reservoirs. In this work, elastic and physical properties of a variety of sedimentary samples that include glacial sediments, carbonates, shales, one evaporite, and one argillite from a variety of locations are investigated. Assuming vertical transverse isotropy, ultrasonic compressional- and shear-waves (at 1 MHz central frequency) were measured as a function of confining pressure on all samples with the exception of glacial samples which were tested assuming isotropy. Tensile strength tests (Brazilian test) were also carried out on selected glacial samples and, in addition, static-train measurements were conducted on shales and argillite samples. Lithological and textural features of samples were obtained through thin section techniques, scanning electron microscopy images and micro-tomography images. X-ray diffraction and X-Ray fluorescence provided the mineralogical oxides content information. Porosity, density, and pore structure were studied by using a mercury intrusion porosimeter and a helium pycnometer. The wide range of porosities of the studied samples (ranging from a minimum of 1% for shales to a maximum 45% for some glacial sediments) influence the measured velocities since high porosity sample shows an noticeable velocity increment as confining pressure increases as a consequence of closure of microcracks and pores, unlike low porosity samples where increment is quasi-lineal.

Implementation of Gassmann´s relation to ultrasonic velocities obtained from glacial samples has negligible impact on them when assuming water saturated

samples, which suggests that state of saturation it is no so important in defining such velocities and instead they are mainly frame-controlled. On the other hand, velocities measured on carbonate and evaporite samples show that samples are at best weak anisotropic, thus the intrinsic anisotropy of such rocks has a minor contribution on anisotropy observed at seismic scales. In contrast, shales and argillite samples are highly anisotropic, with the dynamic modulus obtained from velocities up to 3.31 times higher than static modulus obtained from static-strain measurements at pressures <3 MPa.

Acknowledgements

Table of Contents

List of Tables

List of Figures

List of Symbols

σ_{ij} Stress tensor

C_{ij} Elastic stiffness

ε_{ij} Strain tensor

ε_k Strain scalar

u Displacement

S_{ij} Elastic compliance

λ Lamé parameter

μ, G Shear modulus

E Young modulus

K Bulk modulus

ρ Density

A Wave amplitude

k Wave number

V_p Phase velocity magnitude (scalar)

ω Angular frequency

$\hat{v}$ Unit vector parallel to displacement

n Unit vector normal to displacement

$\vec{V}$ Phase velocity vector

δ Kronecker delta

Γ Christtoffel´s symbol

V_P Compressional wave velocity

V_S	Shear wave velocity
V_{SH}	Horizontally polarized shear wave velocity
V_{SV}	Vertically polarized shear wave velocity
θ	Polar angle
$\emptyset$	Porosity
T	Temperature
α	Thermal expansion coefficient
C_p	Specific heat
T_{st}	Tensile strength
F	Compressive loading
L	Length
D	Diameter
ε	Thomsen parameter (compressional wave anisotropy)
γ	Thomsen parameter (shear wave anisotropy)
δ	Thomsen parameter (anellipticity)
p	Pressure
βl	Linear compressibility
Kl	Linear deformation
β	Volumetric compressibility
R	Electrical resistance
G_f	Gauge factor
V	Voltage
$\vec{g}$	Group velocity

Δt_P Compressional wave transducer excitation delay

Δt_S Shear wave transducer excitation delay

Θ Volumetric strain

H Height

D_x Lateral energy displacement

Δ Angle between phase and group angles

ϵ Electrical strain

r Coefficient lineal of correlation

V_{void} Void volume

m Mass

$V_{envelope}$ Volume envelope

Z Atomic number

A_w Molecular weight

T_{perm} TinyPerm value

K_{perm} Air permeability

CHAPTER 1

Introduction

1.1 Objectives

Elastic properties of rocks are important to know because they are related to the intrinsic properties such as porosity, permeability, mineralogy, texture, and pore structure. Establishing relationships between elastic and physical properties provides the tools needed to optimize reservoir characterization, seismic imaging and determination of geomechanical properties. Obtaining the required information to characterize a given rock mass through *in situ* measurements is complicated; and one must often resort to direct studies on core materials retrieved from depth. This is particularly true if we desire information on the mechanical anisotropy of the rock. The overall rock mass character may differ from what we observe at the decimeter core scale, but these core-scale properties provide constraints to what the rock mass scale properties might be.

There are essentially two experimental methodologies used to measure rock elasticity: dynamic or pseudo-static. Dynamic measurements measure wave speeds at a variety of frequencies (ultrasonic, sonic, and seismic) or track strains induced during forced oscillations. Pseudo-static techniques observe directly stress-strain relationships and hence provide measures of the static elastic moduli directly. In non-porous, conservative (i.e. perfectly elastic) materials such as steel, we expect both methods to give in identical results. However a rock is a much more complex material with elastic properties depending on strain amplitudes and

the frequency of deformation; as such dynamic and static measurements on rock seldom agree (Tutuncu et al 1998).

Poorly consolidated geologic materials such as glacial sediments are considered to be seismically isotropic; however seismic anisotropy, defined as the variation of compressional and shear velocities as a function of direction propagation and particle polarization, has been observed in sedimentary rocks whose cause are attributed to fine layering (Lo, Coyner and Toksoz 1986; Johnston and Christensen 1994; Hornby 1998; Mah 2005) and preferred orientation of cracks and minerals (Kaarsberg 1959; Rai and Hanson 1988; Vernik and Nur 1992; Maltman 1994;Johnston and Christensen 1995; Sayers 2005, Cholach and Schmitt, 2006). Thus, it is important to investigate seismic anisotropy on such materials since their intrinsic anisotropy may contribute to the observed anisotropy at basin scale (Dey-Barsukov *et al*. 2000; Schijns *et al* 2012). In this sense, it is important to understand the effects of elastic anisotropy on wave propagation (dynamic effects) to avoid errors during time-to-depth conversion when processing seismic images, particularly in areas with presence of thick shale layers (Banik 1984). From the geomechanical point of view, knowledge of the static elastic properties of sedimentary rocks is required for development of borehole stability and mechanical modeling in order to avoid drilling related failures (Carvajal-Jiménez *et al* 2007).

The purpose of this research is to investigate the physical properties and the elastic properties as a function of confining pressure of variety of sedimentary rocks. Among studied geological materials are glacial sediment samples from the

2

ANtartic geological DRILLing program (ANDRILL) of Southern McMurdo Sound Project (SMS) (Paulsen et al 2012). For this set of samples in particular, ultrasonic compressional- and shear-wave velocities were obtained. Applying Gassman´s equation to the compressional wave data and then comparing the results with those obtained from core and wireline logging allows understanding the impact of rock´s frame on velocities.

On the other hand, elastic dynamic anisotropy of four carbonates and one evaporite from the reservoir rocks of the International Energy Agency Weyburn project (Moberg, Stewart and Stachniak 2003) is investigated. The objective of this experiment is to study the influence of the intrinsic anisotropy such rocks may have on the observed anisotropy at seismic scales.

Simultaneous dynamic and static anisotropic elastic properties on four shale samples and one argillaceous sample from Southern Alberta, Canada is also investigated. Measurements are carried out on prism-like shaped samples which, in the case of shales, are challenging to obtain due to their fissible nature; however the objective/advantage of this method is that allows overcoming heterogeneity problems (Melendez and Schmitt, 2013), which are inherent to conventional methods that use independent measurements that characterize a single core sample.

Thus, this research contributes with experimental data that, to our knowledge are the first ultrasonic compressional- and shear- wave and deformation measurements in the different formations studied here, wherewith we hopes to contribute to the understanding to the aspects that influence dynamic and static

properties (isotropic or anisotropic) in sedimentary rocks through validation of predictive rock physics models.

1.2 Organization of the thesis

In **Chapter 2**, a brief description about theory of elasticity is given for both the isotropic and anisotropic cases.

In **Chapter 3**, the physical and geomechanical properties of glacial sediment samples obtained from the AND-2A Drillcore, Southern McMurdo Sound are studied. The samples' characterization includes laboratory estimation of bulk and grain density, and imaging of pore structure. Assuming isotropy, the ultrasonic compressional- and shear-wave velocities as a function of confining pressure are measured. A description of the methodology used to take the measurements, as well as sample description is provided. Tensile strength by performing Brazilian test is carried out on selected samples. This chapter is primarily one of characterization of poorly understood materials and many of the techniques applied throughout the thesis are introduced. A version of this chapter is in preparation for publication.

In **Chapter 4**, assuming a medium with Vertical Transverse Isotropy symmetry (VTI), the elastic anisotropy as a function of confining pressure of carbonate and evaporite samples from the Williston sedimentary basin in Saskatchewan, Canada is investigated by using ultrasonic velocity measurements on cylindrical plugs. This chapter also introduces the use of Thomsen parameters (Thomsen 1986) to

scientifically characterize anisotropy. This chapter is a version of our manuscript recently published in the journal Geophysical Prospecting (Melendez and Schmitt, 2013).

Chapter 5 is a preparatory chapter of **Chapter 6** and presents a description of the origin and the mineral composition of shales as well as the physical and chemical processes that occur during burial which are important to know since such processes play an important role in the production of oil and gas through kerogen maturation. Implications of textural features of shales on seismic anisotropy are also discussed.

In **Chapter 6**, assuming a VTI symmetry, the static and dynamic moduli of one argillaceous sample and four shale samples under confining pressure from Southern Alberta, Canada are simultaneously investigated by taking ultrasonic velocity and deformation measurements on prism-like shaped samples. Dynamic moduli were estimated under two different approximations: assuming an anisotropic single crystal and assuming an isotropic composite (polycrystalline) material. Thus this chapter introduces the dynamic Voigt-Reuss-Hill elastic moduli theory. A description of the methodology used to simultaneously take the dynamic and static measurements is provided, as well as sample description. A version of this chapter is also in preparation for publication and the work presented here has been already disseminated through a number of presentations and expanded abstracts at, for example, the 2012 AGU Fall Meeting (San

Francisco), the 2nd International Workshop on Rock Physics (Southampton, 2013), and the 2nd EAGE Workshop on Rock Physics (Muscat, 2013).

Finally **Chapter 7** summarizes the general discussion and conclusions of the results obtained in this research.

Bibliography

Banik, N.C. 1984. Velocity anisotropy of shales and depth estimation in the North-Sea basin, *Geophysics,* 49, 1411-1419.

Carvajal-Jiménez, J.M., Valera-Lara, L.C., Rueda, A. and Saavedra.Trujillo, N. 2007. Geomechanical wellbore stability modeling of exploratory wells - study case at middle Magdalena basin, *CT&F Ciencia, Tecnología y Futuro,* 3, 85-102.

Cholach, P.Y. and Schmitt, D.R. 2006. Intrinsic elasticity of a textured transversely isotropic muscovite aggregate: Comparisons to the seismic anisotropy of schists and shales, Journal of Geophysical Research-Solid Earth, 111.

Dey-Barsukov, S., Durrast, H., Rabbel, W., Siegesmund, S. and Wende, S. 2000. Aligned fractures in carbonate rocks: laboratory and in situ measurements of seismic anisotropy, *International Journal of Earth Sciences,* 88, 829-839.

Hornby, B.E. 1998. Experimental laboratory determination of the dynamic elastic properties of wet, drained shales, *Journal of Geophysical Research-Solid Earth,* 103, 29945-29964.

Johnston, J.E. and Christensen, N.I. 1994. Elastic constants and velocity surfaces of indurated anisotropic shales, *Surveys in Geophysics,* 15, 481-494.

Johnston, J.E. and Christensen, N.I. 1995. Seismic anisotropy of shales, *Journal of Geophysical Research-Solid Earth,* 100, 5991-6003.

Kaarsberg, E.A. 1959. Introductory studies of natural and artificial argillaceous aggregates by sound-propagation and x-ray diffraction methods, *Journal of Geology,* 67, 447-472.

Lo, T.W., Coyner, K.B. and Toksoz, M.N. 1986. Experimental determination of elastic-anisotropy of Berea sandstone, Chicopee shale, and Chelmsford granite, *Geophysics,* 51, 164-171.

Mah, M. 2005. Determination of the elastic constants of orthorhombic and transversely isotropic materials: experimental application to a kerogen rich rock*, PhD Thesis*, University of Alberta, Edmonton, Alberta, Canada.

Maltman, A. 1994. *The geological deformation of sediments.* Chapman & Hall.

Meléndez, J. and Schmitt, D.R. 2013. Anisotropic elastic moduli of carbonates and evaporites from the Weyburn-Midale reservoir and seal rocks, *Geophysical Prospecting,* 61, 363-379.

Moberg, R., Stewert, D.B. and Stachniak, D. 2003. The IEA Weyburn CO_2 monitoring and storage project, *6th International Conference on Greenhouse Gas Control Technologies*, Kyoto, Japan, 219-224.

Rai, C.S. and Hanson, K.E. 1988. Shear-wave velocity anisotropy in sedimentary rocks: A laboratory study, *Geophysics,* 53, 800-806.

Sayers, C.M. 2005. Seismic anisotropy of shales, *Geophysical Prospecting,* 53, 667-676.

Schijns, H., Schmitt, D.R., Heikkinen, P.J. and Kukkonen, I.T. 2012. Seismic anisotropy in the crystalline upper crust: observations and modelling from the Outokumpu scientific borehole, Finland, *Geophysical Journal International,* 189, 541-553.

Thomsen, L. 1986. Weak elastic anisotropy, *Geophysics,* 51, 1954-1966.

Tutuncu, A.N., Podio, A.L., Gregory, A.R. and Sharma, M.M. 1998. Nonlinear viscoelastic behavior of sedimentary rocks, Part I: Effect of frequency and strain amplitude, *Geophysics,* 63, 184-194.

Vernik, L. and Nur, A. 1992. Ultrasonic velocity and anisotropy of hydrocarbon source rocks, *Geophysics,* 57, 727-735.

Chapter 2

Theoretical background

2.1 Theory of elasticity

Hooke´s Law states that, for small elastic deformations, the strain that a deformed body experiences is linearly proportional to the applied stress, which mathematically can be expressed as

$$\sigma_{ij} = C_{ijkl}\varepsilon_{kl} \qquad\qquad 2.1$$

where σ is the second-rank stress tensor, C represents a fourth-rank tensor of elastic stiffnesses ($ijkl = 1,2,3$ indicate one of the three orthogonal axes) with 3^4=81 components, and ε is a second rank strain tensor

$$\varepsilon_{kl} = \frac{1}{2}\left(\frac{\partial u_k}{\partial x_l} + \frac{\partial u_l}{\partial x_k}\right) \qquad\qquad 2.2$$

where u is the displacement. Figure 2.1 shows the nine component stress tensor acting on a cube volume.

Alternatively, equation 2.1 can be expressed as

$$\varepsilon_{ij} = S_{ijkl}\sigma_{kl} \qquad\qquad 2.3$$

Where S is the fourth rank tensor of elastic compliances and is the inverse of C the with 3^4=81 components as well.

The 81 components of the elastic stiffness tensor are not all independent. Since C presents the following intrinsic symmetry

$$C_{ijkl} = C_{jikl} = C_{ijlk} = C_{jilk},$$

the elastic stiffness tensor can be reduced from 81 to 36 independent components

or elastic constants. After conservation of energy considerations (Hudson and

Harrison 2000), it can be shown that

$$C_{ijkl} = C_{klij},$$

so that the stiffness tensor reduces to 21 independents components. In this sense,

after introducing Voigt notation [i.e., $ijkl$ indices are replaced by i and j indices:

ij(kl) $\rightarrow$ i(j)], equation 2.1 can be written

$$\begin{pmatrix} \sigma_1 \\ \sigma_2 \\ \sigma_3 \\ \sigma_4 \\ \sigma_5 \\ \sigma_6 \end{pmatrix} = \begin{pmatrix} C_{11} & C_{12} & C_{13} & C_{14} & C_{15} & C_{16} \\ C_{12} & C_{22} & C_{23} & C_{24} & C_{25} & C_{26} \\ C_{13} & C_{23} & C_{33} & C_{34} & C_{35} & C_{36} \\ C_{14} & C_{24} & C_{34} & C_{44} & C_{45} & C_{46} \\ C_{15} & C_{25} & C_{35} & C_{45} & C_{55} & C_{56} \\ C_{16} & C_{26} & C_{36} & C_{46} & C_{56} & C_{66} \end{pmatrix} = \begin{pmatrix} \varepsilon_1 \\ \varepsilon_2 \\ \varepsilon_3 \\ \varepsilon_4 \\ \varepsilon_5 \\ \varepsilon_6 \end{pmatrix}, \qquad 2.4$$

which describes the stress-strain relations for a general anisotropic material such

as that observed in a triclinic symmetry. Figure 2.2 shows a schematic of both the

elastic stiffnesses tensor C_{ijkl} and the elastic compliances tensor S_{ijkl} for different

geometries represented in Voigt notation.

Thus, in the isotropic case, the stiffness tensor comprises only 2 independent

elastic constants, C_{33} and C_{44}:

$$C_{ij} = \begin{pmatrix} C_{33} & C_{33} - 2C_{44} & C_{33} - 2C_{44} & 0 & 0 & 0 \\ C_{33} - 2C_{44} & C_{33} & C_{33} - 2C_{44} & 0 & 0 & 0 \\ C_{33} - 2C_{44} & C_{33} - 2C_{44} & C_{33} & 0 & 0 & 0 \\ 0 & 0 & 0 & C_{44} & 0 & 0 \\ 0 & 0 & 0 & 0 & C_{44} & 0 \\ 0 & 0 & 0 & 0 & 0 & C_{44} \end{pmatrix}, \qquad 2.5$$

where

$$C_{33} = \lambda + 2\mu \qquad 2.6$$

and

$$C_{44} = \mu \qquad 2.7$$

λ and μ are the Lamé parameters. μ is also known as the shear modulus. Such parameters can be used estimate the Young (E) and bulk modulus (K):

$$E = \frac{\mu(3\lambda + 2\mu)}{\lambda + \mu} \qquad 2.8$$

$$K = \lambda + \frac{2\mu}{3}. \qquad 2.9$$

In a body with hexagonal symmetry or transverse isotropic symmetry (TI) the elastic stiffness tensor can be reduced to 5 elastic constants:

$$C_{ij} = \begin{pmatrix} C_{11} & C_{11} - 2C_{66} & C_{13} & 0 & 0 & 0 \\ C_{11} - 2C_{66} & C_{11} & C_{13} & 0 & 0 & 0 \\ C_{13} & C_{13} & C_{33} & 0 & 0 & 0 \\ 0 & 0 & 0 & C_{44} & 0 & 0 \\ 0 & 0 & 0 & 0 & C_{44} & 0 \\ 0 & 0 & 0 & 0 & 0 & C_{66} \end{pmatrix}. \qquad 2.10$$

Where $C_{11}, C_{33}, C_{44}, C_{66}$, and C_{13} are the five elastic stiffnesses needed to describe

a VTI medium. The corresponding compliance matrix in TI medium is given by

$$S_{ij} = \begin{pmatrix} S_{11} & S_{12} & S_{13} & 0 & 0 & 0 \\ S_{12} & S_{11} & S_{13} & 0 & 0 & 0 \\ S_{13} & S_{13} & S_{33} & 0 & 0 & 0 \\ 0 & 0 & 0 & S_{44} & 0 & 0 \\ 0 & 0 & 0 & 0 & S_{44} & 0 \\ 0 & 0 & 0 & 0 & 0 & 2(S_{11} + S_{12}) \end{pmatrix}. \qquad 2.11$$

An alternative 'engineering' expression for equation 2.11 is given in terms of the

Young´s moduli (E), shear modulus (G) and the Poisson ratios (ν) that define a

VTI medium with plane of isotropy is parallel to Cartesian axes X_1 and X_2 and

perpendicular to the Cartesian axis X_3:

$$S = \begin{pmatrix} \dfrac{1}{E_1} & -\dfrac{\nu_{12}}{E_1} & -\dfrac{\nu_{31}}{E_3} & 0 & 0 & 0 \\[2ex] -\dfrac{\nu_{12}}{E_1} & \dfrac{1}{E_1} & -\dfrac{\nu_{31}}{E_3} & 0 & 0 & 0 \\[2ex] -\dfrac{\nu_{13}}{E_1} & -\dfrac{\nu_{13}}{E_1} & \dfrac{1}{E_3} & 0 & 0 & 0 \\[2ex] 0 & 0 & 0 & \dfrac{1}{G_{23}} & 0 & 0 \\[2ex] 0 & 0 & 0 & 0 & \dfrac{1}{G_{23}} & 0 \\[2ex] 0 & 0 & 0 & 0 & 0 & \dfrac{2(1 + \nu_{12})}{E_1} \end{pmatrix}. \qquad 2.12$$

By symmetry constrains it holds that $E_3 v_{13} = E_1 v_{31}$, which leads to four independent elastic parameters: E_1 , E_3, v_{12} and v_{31} that are known as the horizontal and vertical Young moduli and the horizontal and vertical Poisson´s ratio respectively. More precisely, E_1 (=E_2) is the ratio of the uniaxial stress magnitude applied in the isotropic X_1-X_2 plane to its parallel strain. Similarly, E_3 is the ratio of the uniaxial stress to the linear strain in the X_3 direction perpendicular to the isotropic plane. The Poisson's ratio v_{12} measured completely in the plane of isotropy while v_{13} would be found in a uniaxial compression in the X_1 direction measuring the linear strains in both the X_1 and X_3 directions. Young moduli, Poisson ratio´s and shear modulus can be defined in terms the five elastic constants as follows (King 1969; Mavko, Mukerji and Dvorkin 2009)

$$E_1 = \frac{(C_{11} - C_{12})[C_{33}(C_{11} + C_{12}) - 2C_{13}^2]}{C_{11}C_{33} - C_{13}^2} \qquad 2.13$$

$$E_3 = \frac{C_{33}(C_{11} + C_{12}) - 2C_{13}^2}{C_{11} + C_{12}} \qquad 2.14$$

$$v_{12} = \frac{C_{33}C_{12} - C_{13}^2}{C_{11}C_{33} - C_{13}^2} \qquad 2.15$$

$$v_{31} = \frac{C_{13}}{C_{11} + C_{12}} \qquad 2.16$$

$$G_{23} = C_{44}. \qquad 2.17$$

2.2 Phase velocities in VTI medium

Newton´s second law can be expressed as

$$\sigma_{ij,j} = \rho \ddot{u}_{i.} \qquad 2.18$$

where ρ is the density of the medium, σ and u as described as before. By using equations 2.1 and 2.2 we obtain the equation of motion for any medium:

$$C_{ijkl}u_{k,lj} - \rho \ddot{u}_i = 0. \qquad 2.19$$

Consider a monochromatic plane wave as a general solution of 2.19:

$$u_i = A\hat{v}_i exp\left[ik\left(n_j x_j - V_{p(n_j)}t\right)\right]. \qquad 2.20$$

A represents the wave amplitude, k the wave number, $V_p = \frac{\omega}{k}$ is the phase velocity and ω is the angular frequency. $\hat{v}_i$ and n_j are unit vectors in the direction of displacement and normal to the wavefront respectively. Hence, combining equations 2.19 and 2.20 we obtain

$$\left(C_{ijkl}n_j n_l - \rho V_{p(n_j)}^2 \delta_{ij}\right)\hat{v}_i = 0. \qquad 2.21$$

The latter is known as the Christoffel´s equation, where solution of equation of motion 2.19 has been expressed as a problem of eigenvalues V_p and eigenvectors $\hat{v}_i$. Using Voigt notation, equation 2.21 can be re-written as

$$\left(\Gamma_{ij} - \rho V_{p(n_j)}^2 \delta_{ij}\right)\hat{v}_i = 0, \qquad 2.22$$

where

$$\Gamma_{ij} = C_{ijkl}n_j n_{l.} \qquad 2.23$$

is the Christtoffel´s matrix. The eigenvalues of equation 2.22 provide three phase velocities for each orthogonal mode of propagation, and because we do not want a trivial solution to 2.22 we use determinant $| \, | = 0$ (Auld 1973), i.e.,

$$det \left| \Gamma_{ij} - \rho V_{p(n_j)}^2 \delta_{ij} \right| = 0, \qquad 2.24$$

where *det* means determinant. Equation 2.24 can be expressed in matrix form as follows:

$$det \begin{vmatrix} \Gamma_{11} - \rho V^2 & \Gamma_{12} & \Gamma_{13} \\ \Gamma_{21} & \Gamma_{22} - \rho V^2 & \Gamma_{23} \\ \Gamma_{31} & \Gamma_{32} & \Gamma_{33} - \rho V^2 \end{vmatrix} = 0. \qquad 2.25$$

In a TI medium, Christoffel´s matrix can be expressed as

$$\Gamma_{11} = C_{11} n_1^2 + C_{66} n_2^2 + C_{44} n_3^2 \qquad 2.26$$

$$\Gamma_{22} = C_{66} n_1^2 + C_{11} n_2^2 + C_{44} n_3^2 \qquad 2.27$$

$$\Gamma_{33} = C_{44} (n_1^2 + n_2^2) + C_{33} n_3^2 \qquad 2.28$$

$$\Gamma_{12} = (C_{11} + C_{66}) n_1 n_2 \qquad 2.29$$

$$\Gamma_{13} = (C_{13} + C_{44}) n_1 n_3 \qquad 2.30$$

$$\Gamma_{23} = (C_{13} + C_{44}) n_2 n_3. \qquad 2.31$$

Due to symmetry in a TI medium, analysis of velocities can be reduced within the plane that is contained by the Cartesian axis X_1 and X_3 (see Figure 2.3), hence *n2=0* and equation 2.25 becomes

$$\det \begin{vmatrix} C_{11}n_1^2 + C_{44}n_3^2 - \rho V^2 & 0 & (C_{13} + C_{44})n_1 n_3 \\ 0 & C_{66}n_1^2 + C_{44}n_3^2 - \rho V^2 & 0 \\ (C_{13} + C_{44})n_1 n_3 & 0 & C_{44}n_1^2 + C_{33}n_3^2 - \rho V^2 \end{vmatrix} \quad 2.32$$

$$= 0$$

where

$$n_1 = sin(\theta) \qquad\qquad 2.33$$

and

$$n_3 = cos(\theta) \qquad\qquad 2.34$$

represent the direction of the unit vector n_i with in terms of the angle θ with respect to the symmetry axis that lies parallel to the Cartesian axis X_3. From equation 2.32, Daley and Hron (1977) and subsequently Thomsen (1986), derive the phase velocities in a medium with vertical transverse isotropic symmetry (VTI) in terms of the direction of propagation:

$$V_P(\theta) = \left\{ \frac{C_{11}sin^2(\theta) + C_{33}cos^2(\theta) + C_{44} + \sqrt{M}}{2\rho} \right\}^{\frac{1}{2}} \qquad\qquad 2.35$$

$$V_{SV}(\theta) = \left\{ \frac{C_{11}sin^2(\theta) + C_{33}cos^2(\theta) + C_{44} - \sqrt{M}}{2\rho} \right\}^{\frac{1}{2}} \qquad\qquad 2.36$$

$$V_{SH}(\theta) = \left\{ \frac{C_{66}sin^2(\theta) + C_{44}cos^2(\theta)}{\rho} \right\}^{\frac{1}{2}} \qquad\qquad 2.37$$

where

$$M = \{(C_{11} - C_{44})sin^2(\theta) - (C_{33} - C_{44})cos^2(\theta)\}^2 + \qquad\qquad 2.38$$

$$(C_{13} + C_{44})^2 sin^2(2\theta),$$

ρ is the bulk density of the sample and the subscripts P, SV, and SH indicate the compressional, the vertically polarized shear, and the horizontally polarized shear waves, respectively.

Therefore, from equations 2.35, 2.36 and 2.37 we have that:

$$C_{11} = \rho V_{P_{90^o}}^2 \qquad\qquad 2.39$$

$$C_{33} = \rho V_{P_{0^o}}^2 \qquad\qquad 2.40$$

$$C_{44} = \rho V_{S_{0^o}}^2 \qquad\qquad 2.41$$

$$C_{66} = \rho V_{SH_{90^o}}^2 \qquad\qquad 2.42$$

$$C_{13} = -C_{44} + \left[\frac{\left(4\rho V_{P_{45^o}}^2 - C_{11} - C_{33} - 2C_{44}\right)^2 - (C_{11} - C_{33})^2}{4} \right]^{\frac{1}{2}} \qquad\qquad 2.43$$

Equations 2.39 through 2.43 allow estimating elastic constants from recorded waveforms via the wave speeds so determined.

In the latter part of this thesis we will generally assume that the materials have TI symmetry and that their elastic properties may be determined by the appropriate measurement of the wave speeds. Further, we will use linear compressibilities, defined in more detail in the relevant chapters, to make comparisons of the elastic moduli determined from strain gauges (pseudo-statically) versus dynamically (from the ultrastonic measurements).

Figures
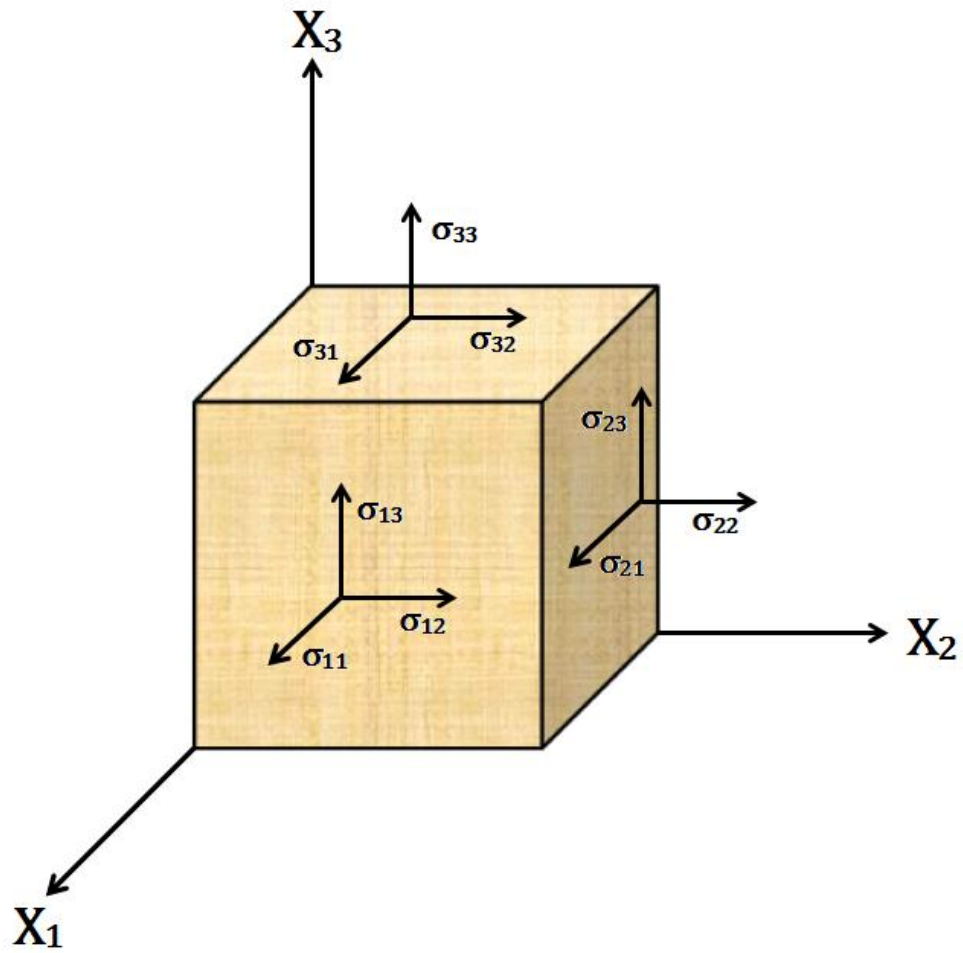
Figure 2.1 Nine stress components acting on an element of volume.

Form of the (S_{ij}) and (C_{ij}) matrices

KEY TO NOTATION

Symbol	Meaning
·	zero component
●	non-zero component
●—●	equal components
●—○	components numerically equal, but opposite in sign
For S ◉	twice the numerical equal of the heavy dot component to which it is joined
For C ◉	the numerical equal of the heavy dot component to which it is joined
For S ✘	$2(S_{11} + S_{12})$
For C ✘	$1/2(C_{11} - C_{12})$

All the matrices are symmetrical about the leading diagonal

TRICLINIC

Both classes
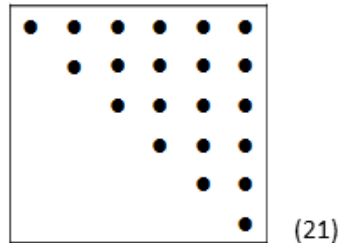
(21)

MONOCLINIC

All classes
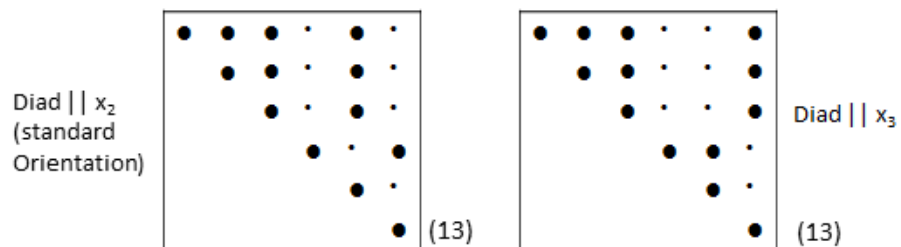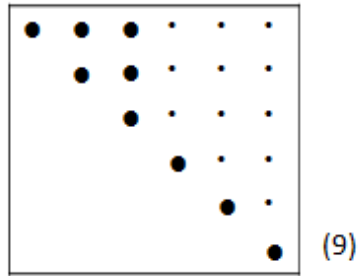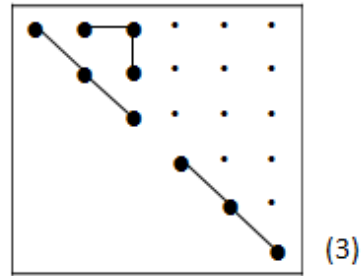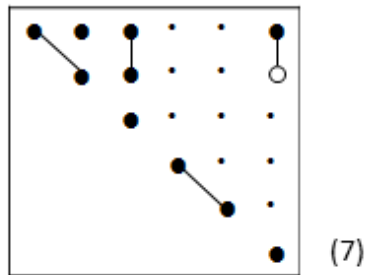
Diad || x_2 (standard Orientation)

(13)

Diad || x_3

(13)
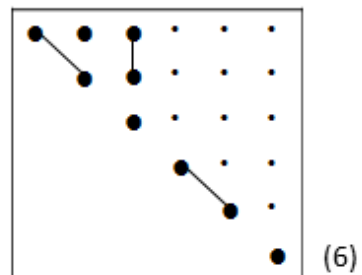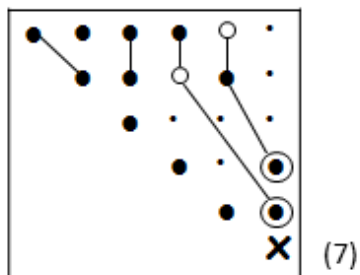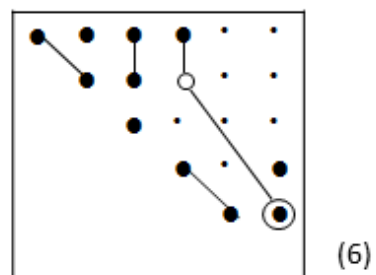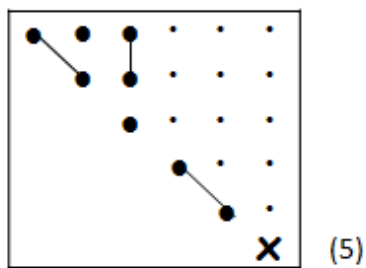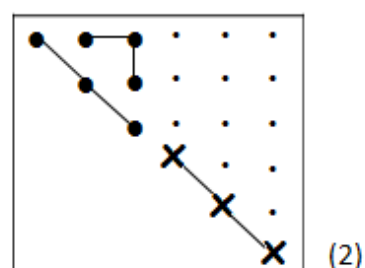
Figure 2.2 Elastic stiffnesses tensor C_{ijkl} and the elastic compliances tensor S_{ijkl} for different geometries represented in Voigt notation. Modified from Nye (1985).
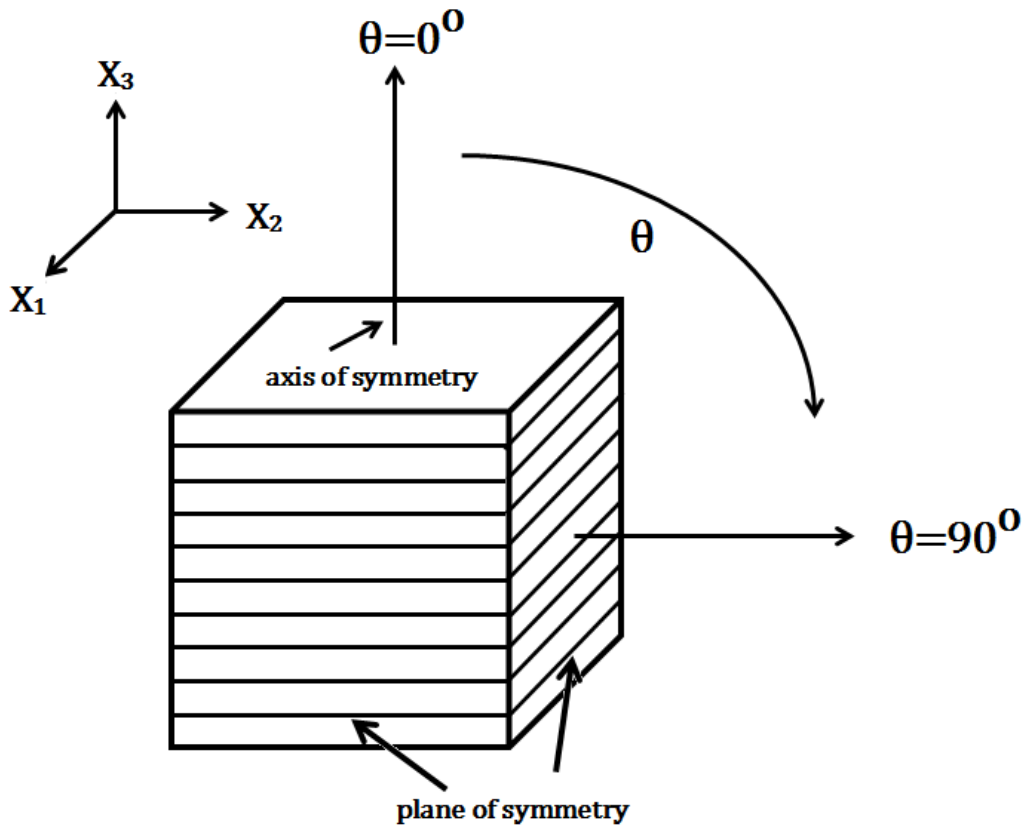
Figure 2.3 Schematic of a Vertical Transverse Isotropy (VTI) symmetry.

Bibliography

Auld, B.A. 1973. *Acoustic fields and waves in solids.* 1.Wiley-Interscience
    Publication.

King, M.S.,1969. Static and dynamic elastic moduli of rocks under pressure. 11th
    U.S., *Symposium on Rock Mechanics*, Berkeley, CA, 329–351.

Daley, P.F. and Hron, F. 1977. Reflection and transmission coefficients for
    transversely isotropic media, *Bulletin of the Seismological Society of
    America,* 67, 661-675.

Hudson, J.A. and Harrison, J.P. 2000. *Engineering Rock Mechanics: An
    Introduction to the Principles.* Pergamon.

Mavko, G., Mukerji, T. and Dvorkin, J. 2009. *The Rock Physics Handbook: Tools
    for Seismic Analysis of Porous Media.* Cambridge University Press.

Nye, J.F. 1985. Physical properties of crystals.Oxfrod University Press.

Thomsen, L. 1986. Weak elastic anisotropy, *Geophysics,* 51, 1954-1966.

CHAPTER 3

Physical and geomechanical properties of samples from the AND-2A Drillcore, ANDRILL Southern McMurdo Sound Project, Antarctica

3.1 Introduction

Glacially deposited sediments provide the clearest evidence for cycles of glaciation on the earth leading back to at least the Proterozoic. Antarctica has experienced continuous ice sheets since the Cenozoic and the Northern Hemisphere endured repeated glaciations since the beginning of the Pliocene. Consequently, large areas of the earth's continents, including regions now submerged, are blanketed with various glacial sediments. Large populations, particularly in the Northern Hemisphere, live and build upon and within, retrieve water from, and deposit waste into these sediments. Knowledge of the physical properties of such materials consequently becomes of increasing importance both for engineering design and for geophysical evaluations. Despite this importance, there is little information about their physical properties available.

There are a number of reasons for this. Such sediments are often heterogeneous and may not appear viable candidates for measurement. Most appear at the surface where, while they may retain substantial strength, obtaining proper samples may be problematic.

In this contribution, we take advantage of the existence of well-preserved glacial sediment cores from the 2007 ANDRILL South McMurdo Sound scientific drill hole. The samples studied are primarily diamictites but also include glacially derived sands and shales. Correlative physical property logging of the core and of geophysical logging of the borehole is compared to a suite of laboratory petrophysical measurements that include the pressure dependence of the compressional V_P and shear V_S wave speeds at ultrasonic frequencies to in situ pressures.

3.2 Background

The AND-2A Drillhole ($77^o45.488$ S; 165° 16.613E) was accomplished by the ANtartic geological DRILLing program (ANDRILL) through Southern McMurdo Sound Project (SMS) (Paulsen *et al* 2012). Drilling was carried out from an 8.5 m thick sea ice platform which was floating over 380 m of water and was completed to a depth of 1138.54 m below the sea floor [mbsf] (Florindo, Harwood and Levy 2008; Harwood *et al* 2009). One of the purposes of the drilling was to recover evidence about variation of Antartica ice sheets during past periods of global warming, particularly the middle Miocene (14-15 million years ago), which had a vital role in the evolution of the Cenozoic cryosphere (Harwood *et al* 2009). The AND-2A Drillcore obtained glacial sediments covering three different stratigraphic intervals (Acton *et al* 2008-2009) that corresponds to lower Miocene (340 meter-thick, 1138.54 to 800 mbsf), middle Miocene (623 meter-thick, 800 to 223 mbsf), and upper Miocene to more recent intervals (223 meter thick, 223 to 0.0 mbsf).

On site characterization of the AND-2A Drillcore presented in this work include measurements of core diameter, P-wave travel time and gamma ray density by using a GEOTEK Multi-Sensor-Core-Logger (MSCL) (Dunbar *et al* 2009). Measurements were taken by pushing the core passing a 0.02 mm resolution laser caliper (core diameter), a pair of ^{137}Cs source and detector (gamma ray), and a pair of pulser-receiver 230 kHz central frequency compressional piezo-electric ceramic transducer (P-wave travel time) [see http://www.geotek.co.uk/ for further details about the MSCL operation process]. Wet Bulk Density (WBD), and P-wave velocity were obtained from such measurements (Dunbar *et al* 2009). WBD obtained from MSCL is labelled WBD(MSCL).

In addition, downhole density, sonic velocity and porosity were obtained from wireline logging in the AND-2A borehole (Wonik *et al* 2008-2009). The logging tools that were lowered into the AND-2A borehole to take the required measurements consisted of a ^{137}Cs source and NaI, detectors (density), a 14 MeV minitron neutron accelerator and He-3 counters (porosity), and piezo sparker acoustic transmitter and two acoustic receiver to measure compressional travel times (sonic logs) [for further details about the description of the logging tools see Cape Roberts Science Team 1999].

Glacial sediments are also important to study since they represent geological records that allow understanding of climate transitions through Earth´s history (Hall and Horn 1993; Jensen 1993; Hall 1999; Colhoun *et al* 2010; Bahlburg and Dobrzinski 2011; Talarico and Sandroni 2011; Fujimoto *et al* 2012; Talarico *et al* 2012; Wilson *et al* 2012). Moreover, glacial deposits are associated to sources of

ground water (Stephenson, Fleming and Mickelson 1988; Harte and Winter 1995; Boyce and Eyles 2000; Juhlin *et al* 2000; Meriano and Eyles 2003; Saad 2008; Root *et al* 2010; Ismail, Schwarz and Pedersen 2011), gold and titanium resource (Eyles and Kocsis 1989; Saarnisto, Tamminen and Vaasjoki 1991; Dabkowska-Naskret and Jaworska 2001), formation of oil reservoirs (Braakman, Levell and Rutten 1983; Franca and Potter 1991; Clark-Lowes 2005), and are used as waste disposal (Stephenson *et al.* 1988).

Hydraulic conductivity of glacial sediments, for example, is required for ground-water studies (Stephenson *et al.* 1988). This hydraulic property depends on the intrinsic permeability of the rock and is related to its pore and grain size, and hence its bulk density, grain density and porosity which can be determined through laboratory and on situ/in situ studies. Hydraulic conductivity also depends on the lithological features of the sediments since stratified deposits of sand or sand and gravel have higher capacity to transmit ground water than till deposits (Stephenson *et al.* 1988). Compressional- and shear-wave velocities as well as density and porosity of such sediments are also important to know since they provide information on their compaction and lithology (Niessen, Jarrard and Bücker 1998).

Despite the importance of glacial sediments there have been few studies, both laboratory and on situ/in situ, regarding their physical properties. Brink and Jarrard (1998), for example, measured compressional and shear wave velocities versus confining pressure, as well as bulk density and porosity of 18 core plugs from the Cape Roberts Project (CRP-1) Drillcore, Victoria Land Basin, Antartica.

In such work, both bulk density and porosity results follow the general trend as that of the ones obtained from continuous whole-core records (Niessen *et al.* 1998), while compressional wave velocities are up 10% higher than those of the obtained from whole-core measurements (Niessen *et al.* 1998), being both core-plugs and whole-core velocities markedly dependent on porosity (Niessen and Jarrard 1998).

In this work, laboratory characterization includes grain density (helium pycnometer based), bulk density, compressional- and shear-wave ultrasonic velocities (*Vp* and *Vs* respectively) using the pulse transmission method assuming isotropy. Gassmann´s substitution of fluids was used to investigate the influence that water saturated samples might have on seismic velocities. Influence of isothermal bulk modulus on compressional velocities is also investigated.

Pore size diameter and permeability as well as grain and bulk density are investigated by using a mercury porosimeter.

Additionally, Scanning Electron Microscopy images (SEM) and thin sections of representative samples are provided in order to study textural features. X-ray Microtomography (μ-CT) is used to scan the pore structure of such samples. X-Ray Diffraction (XRD) provides the mineralogical composition of six selected samples.

Because the fraction of clay minerals in the diamicton mud rich matrix of glacial sediments is usually associated with weak rocks that can affect engineering works (Hart 1993; Jiang, Yoneda and Tanabashi 2001; Cai, Esaki and Jiang 2004; Dai *et al* 2004), when using such sediments/deposits, it is important to know their

geomechanical properties. In this sense, the tensile strength on samples corresponding to the lower Miocene was estimated through indirect tensile strength test (Brazilian test).

In this contribution, a lithological and textural description of the samples analyzed is first given followed by methodologies used.

3.3 Lithology and texture

Recovered AND-2A Drillcore was subdivided into fourteen lithostratigraphic units (LSU´s) by the SMS core logging teams (Fielding *et al* 2011) which include muds, silts sands and gravels as well as diatomites, diamictites and volcanic material. Lithological descriptions as provided by http://www.sms.andrill.org of the samples as a function of the depth interval (mbsf) in which samples were taken is given in Table 3.1.

Figures 3.1 and 3.2 show photographs of thin sections, 15.6 μm resolution μ-CT images and SEM images for three selected samples corresponding each one to following stratigraphic intervals: upper Miocene (sample 94.16 [mbsf], middle Miocene (749.58 [mbsf]) and lower Miocene (sample 879.75 [mbsf]). These three samples are provided as representative of the coarse to fine grained textures encountered throughout the core.

Mineralogical composition of six selected samples, included the above mentioned, is obtained from XRD and is shown in Table 3.2.

Thin section photographs and μ-CT images show the heterogeneous nature in texture of AND-2A Drillcore at different depths. Sample 94.16 [mbsf] for

27

example (Figure 3.1a), is a poorly sorted diamictite composed by coarse sand-sized fragments of quartz and volcanic clasts as well as feldspars such as anorthite and albite. Presence of diamictite is representative of an ice-proximal environment (Fielding *et al.* 2011; Passchier *et al* 2011). The µ-CT image for this sample (Figure 3.1b) reveals its very coarse sand-sized clast rich structure as shown in its thin section image. Additionally, pore space (black spots on image) up to 1 mm large can be observed. Details of this space can also be observed in Figure 3.1c where feldspar crystals are seen to grow in a cavity.

Texture of sample 749.58 [mbsf] corresponds to a coarse sandstone with dispersed to common angular to well-rounded clasts as seen in Figure 3.1d. This sample contains antigorite and quartz and also feldspars minerals such as anorthite, orthoclase and albite. The µ-CT for this image (Figure 3.1e) shows a better sorted sample than the previous one where a decrease in the pore size can also be observed. Honeycomb structure shown by smectite minerals observed in SEM image obtained for this sample (Figure 3.1f) suggests that such minerals are authigenic (Chamley 1989; Ehrmann 1998; Vitali *et al* 1999; de la Fuente *et al* 2000; Buatier, Karpoff and Charpentier 2002; Fesharaki *et al* 2007), which agrees with Iacoviello *et al* (2012) who through XRD analysis and SEM techniques carried out on sediments from the AND- 2A Drillcore conclude that nature of smectite found between 440 and 1123.20 mbsf is predominantly authigenic which is formed from submarine weathering of volcanic material such as glass, pyroxenes and feldspars (Biscaye 1965; Chamley 1989; Iacoviello *et al.* 2012) and by precipitation of fluids as a consequence of hydrothermal processes (Cole

and Shaw 1983; Moorby and Cronan 1983; Huertas *et al* 2000; Iacoviello *et al.* 2012).

Sample 879.41 [mbsf] is a well sorted siltstone with dispersed clasts (Figure 3.2a). The fine grain nature of this sample can also be observed in its µ-CT image (Figure 3.2b). Mineralogical composition of this sample comprises quartz, feldspars (sanidine, albite), zeolites (clinoptitolite), iron carbonates (siderite) and clays (illite). Illite minerals (from XRD analysis) such as the observed in the SEM image (Figure 3.2c) are, along with smectite minerals, the dominant clay minerals in the AND-2A Drillcore (Iacoviello *et al.* 2012). Iacoviello *et al.* (2012) also suggest that illite at this depth could have been generated from the authigenic smectite related to hydrothermal processes that reached enough temperature to transform to illite.

As it can be noted from Table 3.1, the presence volcanic material is prominent in the AND-2A Drillcore, representing more than 50% of the clast type in nine of the fourteen LSU´s (Panter *et al*. 2008; 2009). The Erebus Volcanic Province (Kyle 1990) has been proposed as a potential source of volcanic material since recent Ar-40-Ar30 dating of samples from the AND-2A Drillcore correlates to that of the Erubus Volcanic Province´s volcanic deposits (Di Vincenzo *et al* 2010).

3.4 Methodologies

3.4.1 Grain density, bulk density and pore size diameter

To avoid the presence of water in the samples, these were dried under a vacuum at 70° C for 48 hours before carrying out the measurements.

Grain density was estimated on thirty two samples obtained from the AND-2A Drillcore (covering the three stratigraphic intervals: lower Miocene, middle Miocene and upper Miocene). A helium pycnometer (Micrometrics MVP-6DC) provided measures of solid grain volume that divided by the dry mass of the sample gave the grain density. A Micrometrics Geopyc (1360) was used to estimate envelope volume. The bulk density (dry) was then simply the ratio of the envelope volume to the mass.

A mercury porosimeter (Micromeritics Autopore IV) was used to study pore structure and estimate grain and bulk density of ten selected samples (Giesche 2006).

Downhole density and WBD(MSCL) were estimated from their respective gamma ray logs. Gamma rays are electromagnetic radiation and hence consisting of photons. When such photons pass through the formation, they are scattered (Compton scattering) by the electrons present in the composite with energy loss, i.e., the radiation is attenuated. This attenuation is related to the electron density of the formation, ρ_e, and this in turn is related the bulk density, ρ_{bulk}:

$$\rho_e = 2\rho_{bulk} \frac{Z}{A_w} \qquad\qquad 3.1$$

Where Z and A are respectively the atomic number and molecular weight of the composite. For most of the minerals composing rock we can take with $\dfrac{Z}{A_W} = \dfrac{1}{2}$ with little error.

On the other hand, downhole porosity was estimated from neutron logs. Neutrons emitted by the minitron accelerator collide with the hydrogen atoms present in the formation, so that the number of scattered off neutrons is detected by the He-3 counters. Since hydrogen (i.e. water present in pore space or within phyllite crystal structures) has the biggest effect in decelerating and capturing neutrons; a large number of returned detected neutrons will indicate a low porosity. Conversely, a small number of detected neutrons will indicate high porosity. However, if the pore space is filled with gas which is less dense and consequently has fewer H atoms, the estimate of porosity will be in error.

3.4.1 Permeability

The permeability of these samples is low and is only poorly constrained by the current measurements. Attempts were made to obtain direct values of the air permeability on seventeen selected samples using an air permeameter (New England Research, TinyPerm). The TinyPerm consist in a rubber nozzle attached to a syringe unit, a microcontroller unit and an interface cable. In order to take the measurements, the rubber nozzle is pressed against the sample and then vacuum is generated inside the syringe so that air is withdrawn from sample to the instrument. When vacuum inside the syringe dissipates, the microcontroller

estimates a specific value, T_{perm}, that is related to the air permeability of the rock, K_{perm}, as follows:

$$T_{perm} = -0.8206 \, log_{10} K_{perm} + 12.8737 \qquad\qquad 3.2$$

where K_{perm} is given in milidarcies (mD).

However, due to the low permeability of the studied samples, attempts to completely dissipate vacuum inside the syringe were unsuccessful after a wait of two hours, thus a limit of 10 minutes was taken and the obtained T_{perm} was provided as a final number to perform the calculations so that only an upper bound could be provided.

Permeability was also estimated from the Hg injection porosimetry under the assumption that the pores and pore throats are all cylindrical. However, given that the air permeameter suggests that the permeability must be in all cases less than 2 mD, we do not believe the permeabilities calculated from the Hg injection porosimetry to be valid.

3.4.3 Ultrasonic measurements

The ultrasonic pulse transmission method is used to measure compressional and shear wave speeds as a function of confining pressure on twenty samples of cylindrically shaped core-plugs of 2.5 cm in diameter and of about 2.27 cm to 3.91 cm in length obtained from the AND-2A Drillcore.

The pulse transmission method is the most common method of ultrasonic measurements used to determine the velocities of geologic materials at centimeter scale (Birch 1960; Birch 1961; Podio, Gregory and Gray 1968; Timur 1977;

Christensen and Wang 1985; Rai and Hanson 1988; Sondergeld and Rai 1992; Marion, Mukerji and Mavko 1994; Vernik and Liu 1997; Dey-Barsukov *et al* 2000; Wang 2002; Melendez and Schmitt 2011; Meléndez and Schmitt 2013) and. in particular, this method has been extensively used assuming isotropy (Rafavich, Kendall and Todd 1984; Best 1997; Baechle *et al* 2005; Adam, Batzle and Brevik 2006; Scotellaro, Vanorio and Mavko 2007; Verwer, Braaksma and Kenter 2008; Bakhorji 2010); however to our knowledge, this is the first time that this method has been performed on samples obtained from the AND-2A Drillcore. Indeed, the only other similar tests on indurated glacial sediments were described by Brink and Jarrard (1998).

This method involves generating and recording P and S ultrasonic waves traveling through the sample. Transducers constructed each from identical single pieces of transversely poled ceramic made from lead zirconate titanate (PZT) mounted on aluminum buffers that allow a simultaneous measurement of the P- and S-wave velocities (See Bakhorji (2010) for further details about construction of the source/receiver transducers) are placed on each side of the sample so one of them plays the role of transmitter and the other one is the receiver. In this step proper alignment of the horizontally polarized S-wave transmitter and receiver ceramics is essential. Each assembly of the piezo-electric ceramics with the buffer is called an endcap.

A fast-rise voltage (5 ns) 200 V square wave is applied to the transmitter that sends a broad-band pulse (usually centered near 1 MHz) that propagates through the sample and endcaps. When this pulse arrives at the receiver, a voltage is

generated as a response. The generated elastic wave is then recorded by the digital oscilloscope. The transit time through a sample is then picked from the first extremum of the recorded waveform. Knowing the length of the sample and accounting for the calibrated time delays through the endcaps, the velocity of the wave can be easily calculated.

In order to minimize errors in the velocity measurements and improve pulse transmission, the top and bottom of the samples were ground to be parallel to one another (within +/- 0.01 mm).

In obtaining the measurements, the samples were pushed inside a Tygon ^{TM} tubing in order to exclude the confining pressure oil contained in the pressure vessel from entering the rock's pore space. Then two ultrasonic transducers are set at the ends of the sample as shown in Figure 3.3a.

Once the transducers are properly aligned, we proceed to seal the sample by tightening the Tygon ^{TM} just above the aluminum part of the endcaps by using two steel hose clams as is shown in Figure 3.3b. The sample assembly is then located inside the pressure vessel. Figure 3.4 shows the experimental setup used in the experiment.

Since P- and S-wave velocities are measured as a function of confining pressure by using a pressure vessel in two different cycles: compressing (Up Cycle) and decompressing (Down Cycle). The peak pressure reached in the measurements ranges from 40 to 51 MPa.

3.4.4 Gassmann´s equation and adiabatic/isothermal bulk moduli

Gassmann´s fluid substitution relation is used to investigate the effect of water saturated samples on the obtained velocities as well as the applicability of Gasssmann´s theory (Gassmann 1951) on such sediments for ultrasonic measurements. Gassmann´s relation, derived under the assumption of an elastic, isotropic medium, allows predict the bulk modulus for fluid saturated rocks from known parameters:

$$K_{sat} = K_{dry} + \frac{\left(1 - \frac{K_{dry}}{K_{mineral}}\right)^2}{\frac{\emptyset}{K_{fluid}} + \frac{1 - \emptyset}{K_{mineral}} - \frac{K_{dry}}{K_{mineral}^2}} \qquad 3.3$$

where the predicted saturated bulk modulus, K_{sat}, is estimated from the bulk modulus of the dry rock, K_{dry}, the bulk modulus of the mineral that conforms the rock, $K_{mineral}$, the bulk modulus of the fluid, K_{fluid}, and the porosity of the rock, $\emptyset$. In this work, $K_{mineral}$ is assumed to be 50 GPa for glacial sediments (Brink and Jarrard 1998). K_{fluid} for water is 2.2 GPa (Granger 1985). K_{dry} is estimated by using the compressional and shear ultrasonic wave velocities:

$$K_{dry} = \rho \left(V_p^2 - \frac{4}{3}V_s^2\right) \qquad 3.4$$

being ρ is the dry bulk density of the sample. Hence, combining equations 3.3 and 3.4, and knowing that rock´s shear modulus remains unchanged from dry to fluid-saturated (Berryman 1999), the expected compressional wave velocities can be easily calculated.

Should be noted that the bulk modulus obtained from ultrasonic measurements is affected for changes in temperature, therefore known as the adiabatic bulk

modulus, K_{ad}. However, isothermal bulk modulus, K_{iso}, can be estimated from K_{ad} according to the following relation for the isotropic case (Landau *et al* 1986):

$$\frac{1}{K_{iso}} = \frac{1}{K_{ad}} + \frac{T\alpha^2}{C_p}$$ 3.5

where T is the temperature (^{o}K), α is the thermal expansion coefficient and C_p is the specific heat at constant pressure. In this case, as in Gassmann theory, the shear modulus remains unchanged as well (Landau *et al.* 1986). Expected compressional wave velocities assuming an isothermal bulk modulus can be then estimated. In our calculations, C_p is assumed to be as that as silty clay, i.e., 1087.84 J/Kg ^{o}K (Bowers and Hanks 1962), $\alpha = 0.33 \times 10^{-6}$ ^{o}K^{-1} for quartz, and $K_{ad} = K_{dry}$.

3.4.5 Indirect Tensile Strength measurements

Indirect tensile strength tests (Brazilian test) were carried out on twelve cylindrically-shaped core-plugs of 2.1 cm in diameter and of about 1.0 cm to 1.1 cm in length obtained from the AND-2A Drillcore to estimate strength of such samples under uniaxial tensile load without fracturing. These measurements were conducted in commercial facilities by TerraTek (A Schlumberger Company), Salt Lake City by Dr. D. Handwerger.

Although the Brazilian test was originally designed as an indirect measure of tensile strength on concrete specimens (Fairbairn and Ulm 2002), this test has also been performed on geologic materials (Jaeger and Hoskins 1966; Jaeger 1967; Mellor and Hawkes 1971; Schroede 1972; Henry and Paquet 1977; Pandey and Singh 1986; Andreev 1991a; Andreev 1991b; Lee, Juang and Lei 1996; Chen, Pan

and Amadei 1998; Claesson and Bohloli 2002; Aydin and Basu 2006; Efimov 2009; Tavallali and Vervoort 2010b; Tavallali and Vervoort 2010a). The Brazilian test involves loading cylindrically-shaped core plugs across their diameter. Such loading produces a tensile stress in the direction perpendicular to the loaded direction, which leads to fracture of the core plug by splitting when the applied load reaches a critical point. Thereby, tensile strength can be indirectly estimated from 2-D elastic theory (Frocht 1941; Timoshenko and Goodier 1969)

$$T_{st} = \frac{2F}{\pi LD} \qquad 3.6$$

where T_{st} is the tensile strength, F is the compressive loading at critical point (fracture), L is the length of the core plug and D is the its diameter. Figure 3.5 shows a schematic of the Brazilian test.

3.5 Results

3.5.1 Density and porosity

Table 3.3 shows the grain and bulk densities obtained for each sample as well as their estimated porosity. Samples were labelled by their upper depth limit in mbsf Density and porosity values obtained from wireline logging as well as density values obtained from core logging at the given samples´s depth [mbsf] are also shown. In addition, WBD was also estimated for each sample using the estimated porosity and assuming water-saturated samples:

$$WBD(estimated) = \frac{(V_{void} \cdot \rho_w) + m_{dry}}{V_{envelope}} \qquad 3.7$$

Where V_{void} is the void volume estimated from porosity, $\rho_w = 0.998$ g/cm^3 is the water density at 20°C, m_{dry} is the sample´s dry mass and $V_{envelope}$ is the volume envelope.

Figure 3.6 shows a comparison between the borehole logging, the core based MSCL data, and the laboratory core measurements where it can be observed that the latter follows the general trend of the curves generated by wireline logging and MSCL values; however, differences with the actual values are present.

As is expected, grain density is greater than bulk density. It can be noted that bulk density values are lower than those obtained from both logging and MSCL. Density obtained from wireline logging is up to 1.41 times higher than that of the bulk density which corresponds to sample 997.32 [mbsf], and it is up to 1.14 times higher than that of the WBD (MSCL), corresponding to sample 758.12 [mbsf]. Pearson´s coefficient of correlation (LeBlanc 2004) between bulk density and wireline logging density and WBD (MSCL) are 0.47 and 0.55 respectively.

Such lower laboratory bulk density values than MSCL and wireline logging may be caused by a rebound and dehydration effects of the sediments affecting core plugs (Brink and Jarrard 1998). Rebound increases volume and hence decreases density so that the values obtained at laboratory can be significantly different from those of the MSCL values since laboratory measurements can take place several months after MSCL measurements.

When comparing wireline logging density and WBD (MSCL) values to WBD (Estimated) values, differences are a maximum of 1.27 and 1.16 times respectively and both corresponding to sample 997.32 [mbsf], having WBD

(MSCL) and WBD (Estimated) the closest values which appear to indicate that the samples are water filled. Pearson´s coefficient of correlation, *r*, between WBD (estimated) and wireline logging density and WBD (MSCL) are 0.36 and 0.57 respectively. Figure 3.7 shows the cross-plots of the various density measures.

3.5.2 Pore size structure and permeability

Pore size diameter and permeability for samples 231.27 [mbsf], 237.23 [mbsf], 302.51 [mbsf], 307.06 [mbsf] and 333.09 [mbsf] corresponding to the middle Miocene, and lower Miocene samples 810.31 [mbsf], 1048.54 [mbsf], 1060.99 [mbsf], 1123.85 [mbsf] and 1138.81 [mbsf] are analyzed using the above mentioned mercury injection porosimeter. Figure 3.8 shows some examples of the incremental mercury intrusion against pore size diameter curves. The mono modal distribution of the curves with sharp peaks at specific values of pore size diameter for samples 231.27 [mbsf], 1060.99 [mbsf], and 1138.81 [mbsf] indicates that their porosity is contained in a unique range of pore size unlike sample 333.09 [mbsf] where its curve shows a bi-modal distribution with sharp peaks at 0.68 and 0.08 μm. On the other hand, air permeability was estimated on samples 359.08 [mbsf], 385.18 [mbsf], 459.64 [mbsf], 466.72 [mbsf], 536.16 [mbsf], 560.91 [mbsf], 623.07 [mbsf], 630.36 [mbsf], 646.02 [mbsf], 683.94 [mbsf], 713.64 [mbsf], 720.76 [mbsf], and 749.59 [mbsf] (middle Miocene) as well as 874.75 [mbsf], 960.18 [mbsf], 974.84 [mbsf], 997.33 [mbsf] (lower Miocene). A summary of the results obtained from both mercury porosimeter and air permeameter is given in Table 3.4. However, given the experience with the air

permeameter, we believe that the Hg injection permeability estimates are too high likely because of the assumptions inherent to this calculation.

A plot of pore size diameter versus depth [mbsf] is shown in Figure 3.9, where about one order of magnitude in pore size reduction can be observed for samples from the lower Miocene as a consequence of compaction due of pressure exerted by the weight overlying sediments. The authigenic clay minerals present on such samples (see Table 3.1) have a contribution on the low permeability values of the order of mDarcies.

3.5.2 Velocity results

Some examples of P- and S-waveforms obtained in the experiment are shown in Figure 3.10.

Table 3.5 summarizes the ultrasonic P- and S-wave velocities measured at peak pressure along with the sonic and MSCL velocities averaged over a 1 m long interval centred at the depth that corresponds to each sample, as well as the estimated compressional wave velocities obtained from Gassmann´s relation and the calculated adiabatic, K_{ad}, and isothermal, K_{iso}, bulk modulus. Figure 3.11 shows a comparison between ultrasonic P- and S-wave velocities from Table 3.5 and whole data from sonic and MSCL P-wave velocities. Note that there is a lack of sonic P-wave velocity data for the first 640 mbsf.

Ultrasonic P- and S-wave velocities have maximum values of 3655 m/s and 2220 m/s respectively for interbedded sandy conglomerate and medium fine sandstone (sample 215.49 [mbsf]). The maximum value of MSCL P-wave velocity shown in Table 3.5 (4343 m/s) also corresponds to a depth of 215.49 mbsf which is part of

the upper Miocene interval that covers from 195 to 225 mbsf where a significant increment of velocity and density can be observed (see Figures 3.6 and 3.11). Minimum ultrasonic P- and S-wave velocity values correspond to 1638 m/s and 1058 m/s respectively and are associated to clast-rich sandy diamictite (sample 94.16 [mbsf]). On the other hand, minimum MSCL P-wave velocity value is 2378 m/s at 101.91 mbsf (fine grained sandstone). Even though those minimum values do not correspond to the same depth, they are associated to a range of depth (0 to 135 mbsf) of low velocities and densities in the upper Miocene (see Figures 3.6 and 3.11). Pearson´s coefficient of correlation between ultrasonic P-wave velocities and MSCL P-wave velocities is 0.73, being MSCL P-wave velocities of 8% higher in average than ultrasonic velocities.

Taking into account measurements from 640 mbsf, ultrasonic P-wave velocities and sonic P-wave velocities have a Pearson´s coefficient of correlation of -0.07 with ultrasonic P-wave velocities 13% higher than sonic P-wave velocities. Minimum values of each data series corresponds to 2509 m/s at 646.01 mbsf (sandy mudstone) and 2304 m/s at 879.41 (siltstone). Correspondingly, maximum values are 3264 m/s at 749.58 mbsf (Volcanic bearing fine sandstone) and 2987 m/s at 974.83 mbsf (lower Miocene).

In general, ultrasonic P wave velocities follow the same trend as MSCL and sonic P-wave velocities than sonic velocities but MSCL P-wave velocities are better fit to the ultrasonic P-wave velocities than sonic velocities.

Ultrasonic P-wave velocities follow the same trend as ultrasonic S-wave velocities, with the ultrasonic P-wave velocities between 1.5 and 1.7 times those

for the ultrasonic S-wave velocities. Such Vp/Vs ratios correspond to shale and sandstone lithologies (Miller 1989), which agrees with the lithological description given in Tables 3.1. Pearson´s coefficient of correlation between these velocities is 0.99.

With the exception of sample 214.19 [mbsf], Gassmann´s relation has a scaling effect on ultrasonic velocities, being average MSCL compressional velocities only 0.71% higher than Gassmann compressional velocities, however, its coefficient of correlation decreases to 0.72. Such scaling effect extends the difference between Gassmann compressional velocities and sonic compressional velocities from 13 to 19% in average and increases its coefficient of correlation by 0.03.

Figure 3.11 shows a comparison between the MSCL and the sonic log, the laboratory ultrasonic, and the calculated Gassmann compressional velocities. The error bars in Figure 3.12 corresponds to the standard deviation associated to each velocity. Despite the scaling effect of Gassmann´s relation on ultrasonic velocities, the resulting values still lie within standard deviation error bars associated to MSCL P-wave velocities, which suggests that the velocities are mostly controlled by the frame, and that the state of saturation is not so important in these samples. In contrast, both P-wave ultrasonic and Gassmann velocities do not lie within error bars of compressional sonic velocities. Higher compressional ultrasonic velocities at peak pressure than compressional wireline logging velocities would suggest that peak pressures are higher than those which would be found at Earth´s interior at the drillcore site.

Differences between the adiabatic and the isothermal bulk modulus are negligible for these samples as it can be observed in Table 3.5, where results for such bulk moduli are shown with five significant figures. In this sense, impact of isothermal bulk modulus on compressional wave velocities is also negligible.

3.5.3 Tensile strength results

Tensile strength for the twelve samples studied here is shown in Table 3.6 and are plotted as a function of depth in Figure 3.13. Lithology of those samples covers from interbedded fine siltstone/sandstone to interbedded clast rich sandy diamictite/sandstone. Results ranges from a minimum of 1.691 MPa for sample 1075.52 [mbsf] to a maximum of 6.368 MPa for sample 1070.39 [mbsf]. Such values appear not to be correlated to depth or lithology, instead, they may be related to cementation.

The values obtained here are in the range of those for other Brazilian tests carried out on several geological materials such as Gosford sandstone, 3.72 MPa (Jaeger 1967), Indiana limestone, 6.21 MPa (Mellor and Hawkes 1971), sandstone, 7.80 MPa (Pandey and Singh 1986), Grey and White Gypsum, 1.99 MPa and 1.29 MPa respectively (Andreev 1991a; Andreev 1991b) and Ufalei Marble, 6.90 MPa (Efimov 2009).

3.6 Conclusions

Heterogeneous textural features of the AND-2A Drillcore can be observed from thin sections and SEM and μ-CT images of three selected samples obtained from the three stratigraphic intervals that include lower Miocene, middle Miocene and

upper Miocene. Forming particles of the AND-2A Drillcore include silt-sized particles to granule gravel particles. Lithological description of studied samples points out the constant presence of volcanic material in the AND-2A Drillcore (Panter *et al* 2008-2009), which is suggested as a potential source of the authigenic smectite minerals observed in the SEM images (Iacoviello *et al.* 2012). Results also show that analyzed samples are porous but yet of low permeability which suggest that pore space is poorly connected.

Ultrasonic compressional velocities follow the same trend as those of MSCL and wireline logging velocities, where MSCL velocities are better fit to ultrasonic velocities than sonic velocities; however exact values are not expected since different volume are measured and materials can be affected by rebound effects (Brink and Jarrard 1998).

Gassmann´s fluid substitution relation assuming water saturated samples has little impact on ultrasonic velocities when compared with MSCL compressional wave velocities within error. This suggests that velocities on those samples are mainly controlled by the frame and that the state of saturation appears to be not so important. Meanwhile, isothermal bulk modulus has no impact on velocities.

Tensile strength results obtained from lower Miocene samples are comparable to those that have been obtained for different geological materials such as gypsum, limestone, sandstone and marble.

Tables

Sample Interval [mbsf]	Lithologies	Grain Size [φ]	Grain Size [name]	Description
(94.16-96.41)	100% till, diamicton.	-0.75	Very Coarse Sand	CLAST-RICH SANDY DIAMICTITE, greenish gray to olive gray.
(101.8-102.65)	100% bedded, sand,sandstone.	2.4	Fine Sand	FINE SANDSTONE, greenish gray to olive gray.
(167.02-168.33)	100% till,diamicton.	0.3	Coarse Sand	CLAST-POOR SANDY DIAMICTITE, greenish gray.
(215.48-215.57)	100% massive,sand, Sandstone.	1.9	Medium Sand	MEDIUM SANDSTONE, greenish gray.
(226.21-237.5)	100% till,diamicton	-0.3	Very Coarse Sand	CLAST-RICH SANDY DIAMICTITE, greenish gray.
(301.24-305.80)	100% till,diamicton	0.25	Coarse Sand	CLAST-POOR SANDY DIAMICTITE, dark gray to dark greenish gray.
(306.99-310.02)	100% till,diamicton	0.8	Coarse Sand	CLAST-POOR MUDDY DIAMICTITE, dark gray.
(332.88-333.19)	100% massive,sand,sandstone	2.35	Fine Sand	MEDIUM-COARSE SANDSTONE WITH ABUNDANT CLASTS, dark greenish gray.
(379.12-386.45)	90% till,diamicton; 10% till,diamicton, volcanic.	0.25	Coarse Sand	VOLCANIC-BEARING CLAST-POOR SANDY DIAMICTITE, very dark gray to dark greenish gray.
(452.00-459.8)	100% argillaceous, shaly,sandstone.	0.75	Coarse Sand	MUDDY VERY FINE SANDSTONE WITH DISPERSED CLASTS, very dark gray.
(558.45-562.96)	50% massive, sand,sandstone; 50% conglomerate.	-1.6	Granule Gravel	MEDIUM-COARSE SANDSTONE WITH DISPERSED CLASTS AND SANDY CONGLOMERATE, both black.
(622.8-628.81)	90% massive,sand, sandstone; 10% massive,sand, sandstone,volcanic.	-0.2, 1.3	Very Coarse Sand, Medium Sand	VOLCANIC-BEARING FINE TO MEDIUM SANDSTONE WITH DISPERSED CLASTS, very dark gray.
(628.81-630.89)	90% sandy,silty, shale; 10% sandy,silty, shale,volcanic.	1.3, 0.8	Medium Sand, Coarse Sand	VOLCANIC-BEARING SANDY MUDSTONE (SILTSTONE) WITH DISPERSED CLASTS, very dark gray.

(645.2-646.91)	100% sandy,silty, shale.	1.3	Medium Sand	SANDY MUDSTONE (SILTSTONE) WITH DISPERSED CLASTS, very dark gray.
(713.43-716.28)	100% till,diamicton.	-0.25, 0.25	Very Coarse Sand, Coarse Sand	CLAST-POOR SANDY DIAMICTITE, very dark greenish gray.
(718.95-721.87)	90% till,diamicton; 10% till,diamicton, volcanic.	0.35	Coarse Sand	VOLCANIC-BEARING CLAST-POOR SANDY DIAMICTITE, black.
(747.45-749.9)	90% massive,sand, sandstone; 10% massive,sand, sandstone,volcanic.	0.15, -0.7	Coarse sand, Very coarse sand	VOLCANIC-BEARING MEDIUM TO COARSE SANDSTONE WITH DISPERSED TO COMMON CLASTS, very dark greenish gray.
(756.19-774.94)*	90% till,diamicton; 10% till,diamicton, volcanic.	0.8	Coarse Sand	VOLCANIC-BEARING CLAST-POOR SANDY DIAMICTITE TO CLAST-POOR SANDY DIAMICTITE, very dark greenish gray.
(785.08-785.88)	100% argillaceous, shaly,sandstone.	2.5	Fine Sand	SILTY FINE SANDSTONE, black.
(808.69-812.65)	100% sandy,silty,shale	1.35	Medium Sand	SANDY MUDSTONE (SILTSTONE) WITH DISPERSED CLASTS, black.
(879.41-879.58)	100% silt,siltstone,silty, shale.	6.03	Silt	SILTSTONE AND MUDDY (SILTY) SANDSTONE WITH DISPERSED CLASTS TO VOLCANIC SANDSTONE WITH DISPERSED CLASTS, very dark gray.
(957.61-964.38)	100% argillaceous, shaly,sandstone.	0.75	Coarse Sand	MUDDY (SILTY) FINE SANDSTONE WITH DISPERSED CLASTS, black.
(974.1-979.42)	100% till,diamicton	0.3	Coarse Sand	CLAST-POOR SANDY DIAMICTITE, black.
(996.69-997.5)	100% sandy,silty, Shale.	1.35	Medium Sand	SANDY MUDSTONE WITH DISPERSED CLASTS AND MUDDY SANDSTONE WITH DISPERSED CLASTS, black.
(1027.88-1033.87)	50% silt,siltstone,silty, shale; 50% massive sandstone	0.75	Coarse Sand	SILTSTONE WITH DISPERSED CLASTS, gray to dark gray, AND VERY FINE SANDSTONE WITH DISPERSED CLASTS, light gray to gray.

(1037.98-1039.27)	100% interbedded, sandsone,siltstone	4	Silt	FINE SILTSTONE, gray to dark gray,
(1040.28-1042.55)	100% massive,sand,sandstone	-0.75	Very Coarse Sand	CLAST-RICH SANDY DIAMICTITE AND SANDSTONE WITH COMMON TO ABUNDANT CLASTS, very dark gray to black.
(1042.55-1044.06)	100% argillaceous,shaly, sandstone	0.75	Coarse Sand	MUDDY FINE SANDSTONE WITH DISPERSED CLASTS TO SILTY FINE SANDSTONE, black.
(1044.06-1064.47)	100% till,diamicton	0.15	Coarse Sand	CLAST-POOR SANDY DIAMICTITE, black
(1065.91-1076.15)	100% till,diamicton	-0.25	Very Coarse Sand	CLAST-RICH SANDY DIAMICTITE, black.
(1078.90-1092.86)	100% till,diamicton	0.3	Coarse Sand	CLAST-POOR TO CLAST-RICH MUDDY DIAMICTITE, black.
(1093.52-1094.25)	100% massive,sand,sandstone	0.1	Coarse Sand	FINE SANDSTONE WITH DISPERSED CLASTS, black.
(1126.06-1124.67)	100% interbedded,sandstone,siltstone	1.8	Medium Sand	FINE-MEDIUM SANDSTONE WITH DISPERSED CLASTS, black.
(1127.9-1138.54)	100% till,diamicton	0.3	Coarse Sand	CLAST-POOR SANDY DIAMICTITE TO CLAST-POOR MUDDY DIAMICTITE, black.

Table 3.1 Lithological description of the samples obtained from the AND-2A Drillcore: upper Miocene (yellow), middle Miocene (green), and lower Miocene (blue).

Sample [mbsf]	Minerals
94.16	Siderite, Ferrotschermakite, Phlogopite, Anorthite, Quartz, Albite, Phillipsite.
215.49	Phillipsite, Quartz, Anorthite, Orthoclase.
630.35	Albite, Microline, Muscovite, Quartz.
749.58	Quartz, Anorthite, Orthoclase, Talc-2M, Antigorite-T, Albite.
879.41	Quartz, Siderite, Sanidine, Albite, Illite, Clinoptinolite.
974.84	Quartz, Sanidine, Albite, Muscovite, Phillipsite.

Table 3.2 Mineralogical composition of selected samples.

Sample [mbsf]	Grain Density (Dry) [g/cm³]	Bulk Density (Dry) [g/cm³]	Porosity [Estimated] %	Density (*) [g/cm³]	Porosity (*) %	WBD (MSCL) [g/cm³]	WBD (Estimated) [g/cm³]
94.16	2.92	1.94	33.56	2.38	21.14	2.16	2.28
101.91	2.78	1.60	42.45	2.17	21.59	1.98	2.02
168.13	2.88	1.64	43.06	2.22	18.49	2.06	2.07
215.49	2.96	2.02	31.76	2.49	12.97	2.32	2.34
231.27	2.71	2.06	23.99	2.28	16.32	2.24	2.30
237.23	2.61	1.83	29.89	2.28	---	2.15	2.13
302.51	2.59	1.93	25.48	2.32	---	2.31	2.18
307.51	2.63	1.95	25.86	2.18	---	2.17	2.21
333.09	2.63	2.16	17.87	2.50	---	2.43	2.34
385.18	2.82	2.01	28.72	2.27	---	2.46	2.30
459.63	2.82	1.97	30.14	2.17	12.28	2.25	2.27
560.9	2.95	2.02	31.53	2.51	14.78	2.50	2.34
623.06	2.83	1.86	34.28	2.21	18.38	2.21	2.20
630.35	2.67	1.73	35.21	2.29	23.30	2.15	2.08
646.01	3.08	1.70	44.81	2.34	16.04	2.15	2.14
713.64	2.86	1.91	33.22	2.54	19.53	2.33	2.24
720.75	2.64	1.87	29.17	2.49	21.57	2.25	2.16
749.58	2.57	2.10	18.29	2.51	19.07	2.46	2.28
758.12	2.70	1.91	29.26	2.65	12.88	2.32	2.21
768.92	2.57	1.92	25.29	2.47	17.58	2.28	2.18
785.37	2.73	2.09	23.44	2.55	21.22	2.36	2.32
810.31	2.63	2.03	22.81	2.31	20.32	2.30	2.26
879.41	2.92	2.15	26.37	2.5	19.13	2.31	2.42
960.17	2.55	1.91	25.10	2.47	20.66	2.33	2.16
974.83	2.73	2.20	19.41	2.60	14.14	2.45	2.40
997.32	2.27	1.82	19.82	2.57	20.58	2.26	2.02
1028.11	2.30	2.17	5.65	---	---	2.22	1.91
1031.80	2.28	2.05	10.09	---	---	2.19	1.99
1033.64	2.48	2.09	15.73	---	---	2.26	2.33
1038.60	2.21	2.15	2.71	---	---	2.24	1.97
1042.25	2.33	2.16	7.30	---	---	2.33	2.28
1043.67	2.26	2.13	5.75	---	---	2.36	2.35
1051.96	2.31	2.26	2.16	---	---	2.25	2.16
1060.99	2.67	2.23	16.48	---	---	2.33	2.39
1070.39	2.30	2.23	3.04	---	---	2.27	2.13
1075.52	2.48	2.45	1.21	---	---	2.34	2.24
1087.87	2.39	2.30	3.77	---	---	2.41	2.22
1093.57	2.42	2.37	2.07	---	---	2.28	2.18

1123.85	2.78	2.01	27.70	---	---	2.09	2.29
1133.81	2.67	2.19	17.98	---	---	2.21	2.17
1138.81	2.30	2.22	3.48	---	---	---	2.37

Table 3.3 Physical properties of the samples obtained from the AND-2A Drillcore: upper Miocene (yellow), middle Miocene (green), and lower Miocene (blue). Red values are mercury porosimeter based. (*) values obtained from logging.

Sample [mbsf]	Pore Size Diameter * [µm]	Permeability* [mDarcies]	Permeability** [mDarcies]
231.27	0.06	5.692	- - -
237.23	0.1	0.004	- - -
302.51	0.1	5.708	- - -
307.06	0.1	0.004	- - -
333.09	0.68, 0.08	7.837	- - -
359.08	- - -	- - -	1.069
385.18	- - -	- - -	1.001
459.64	- - -	- - -	1.363
466.72	- - -	- - -	2.411
536.16	- - -	- - -	0.695
560.91	- - -	- - -	0.742
623.07	- - -	- - -	0.823
630.36	- - -	- - -	4.773
646.02	- - -	- - -	0.676
683.94	- - -	- - -	0.763
713.64	- - -	- - -	0.749
720.76	- - -	- - -	1.110
749.59	- - -	- - -	0.807
810.31	0.02	7.891	- - -
874.75	- - -	- - -	0.435
960.18	- - -	- - -	0.982
974.84	- - -	- - -	0.722
997.33	- - -	- - -	0.435
1048.54	0.01	0.117	- - -
1060.99	0.02	2.837	- - -
1123.85	0.01	0.501	- - -
1138.81	0.03	11.24	- - -

Table 3.4 Summary of results obtained from Mercury Porosimeter* and Air Permeameter**.

Sample [mbsf]	Peak Pressure [MPa]	Vp (Ultrasonic) [m/s]	Vs (Ultrasonic) [m/s]	Average Vp (Sonic) [m/s]	Standard deviation [m/s]	Average Vp (MSCL) [m/s]	Standard deviation [m/s]	Vp (Gassmann) [m/s]	K_{ad} [GPa]	K_{iso} [GPa]
94.16	50.5	1638	1058	---	---	2890	189	2169	2.30968	2.30968
101.91	50.5	2353	1454	---	---	2378	130	2534	4.34846	4.34846
168.13	50.0	2388	1528	---	---	2713	283	2547	4.24678	4.24678
215.49	51.0	3655	2220	---	---	4343	389	3607	13.71141	13.71141
385.18	50.5	2921	1851	---	---	3150	170	3103	7.96759	7.96759
459.63	50.5	2769	1724	---	---	2660	150	2971	7.29779	7.29779
560.90	50.0	3141	1979	---	---	3873	304	3218	9.38080	9.38080
623.06	50.0	2882	1822	---	---	2723	173	3004	7.21620	7.21620
630.35	50.0	2561	1647	---	---	2680	99	2779	5.08950	5.08950
646.01	50.0	2509	1577	2625	267	2706	58	2603	5.06460	5.06460
713.64	50.0	2706	1716	2610	29	3069	203	2887	6.48680	6.48680
720.75	50.0	3145	1966	2386	95	3179	187	3279	8.85909	8.85909
749.58	40.5	3264	2073	2690	128	3713	219	3565	10.34024	10.34024
758.12	49.5	2750	1720	2611	29	2986	231	2977	6.91032	6.91032
768.92	40.0	2719	1796	2377	10	2931	67	3066	6.46257	6.46257
785.37	50.5	3146	1953	2576	108	3263	258	3373	9.76776	9.76776
879.41	49.5	3257	2010	2304	102	3202	437	3367	11.22569	11.22569
960.17	50.0	2863	1716	2477	59	3030	167	3135	8.15677	8.15677
974.83	50.5	3077	2014	2987	135	3289	155	3387	8.93127	8.93127
997.32	50.5	3211	1966	2494	37	3173	262	3533	9.38570	9.38570

Table 3.5 Ultrasonic P- and S-wave velocities at peak pressure for each studied sample along with their associated averaged sonic and MSCL P-wave velocities, Gassmannn velocities and adiabatic/ isothermal moduli.

Sample [mbsf]	Average Length [m]	Average Diameter [m]	Maximum load [N]	Tensile Strength [MPa]
1028.11	0.011	0.021	1138.745	3.162
1031.80	0.011	0.021	814.025	2.191
1033.64	0.011	0.021	1426.780	3.707
1038.60	0.010	0.021	2022.707	5.990
1042.25	0.010	0.021	1223.630	3.626
1043.67	0.010	0.021	2093.017	6.337
1051.96	0.011	0.021	815.616	2.298
1070.39	0.011	0.021	2254.933	6.368
1075.52	0.011	0.021	606.152	1.691
1087.87	0.010	0.021	1502.411	4.422
1093.57	0.011	0.021	1066.791	2.864
1133.81	0.010	0.021	1128.146	3.405

Table 3.6 Estimation of tensile strength by using equation 4. Samples studied correspond to lower Miocene.

Figures
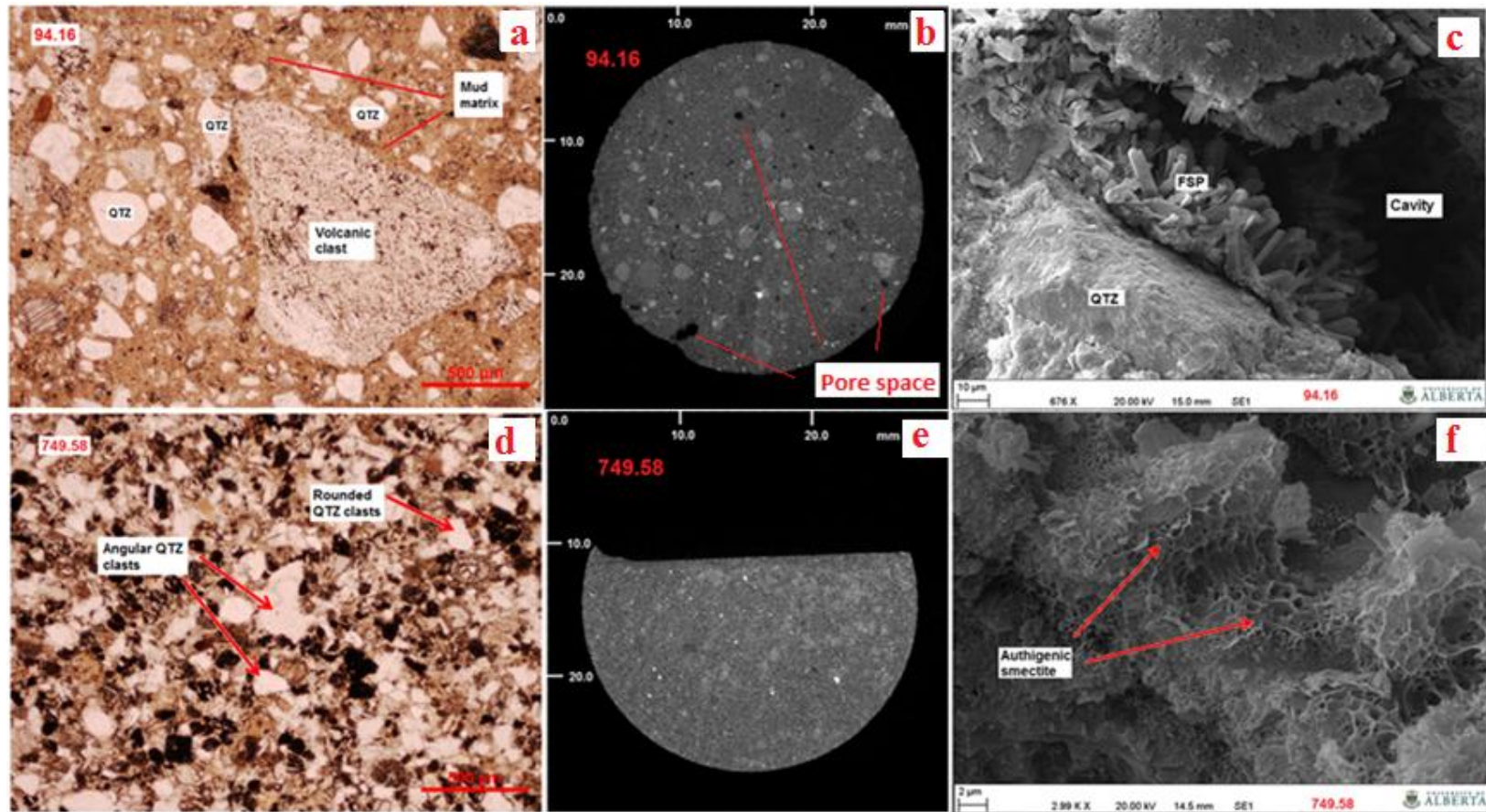
Figure 3.1 a) Thin section for sample 94.16 [mbsf]. Poorly sorted dispersed volcanic and quartz clasts in a rich mud matrix. Quartz (QTZ) and volcanic clasts are identified. b) μ- CT image of sample 94.16 [mbsf] dispersed clast and pore space can be observed in this image. c) SEM image for sample 94.16 [mbsf] showing feldspar (FSP) minerals growing in a cavity. d) Thin section for sample 749.58 [mbsf] which is composed by medium to coarse sandstone. e) μ- CT image of sample 749.58 [mbsf]. A significant decrease in the pore space with respect to sample 94.16 [mbsf] can be observed. f) SEM image for sample 749.58 [mbsf]. Honeycomb structure characteristic of authigenic smectite is shown in this image.
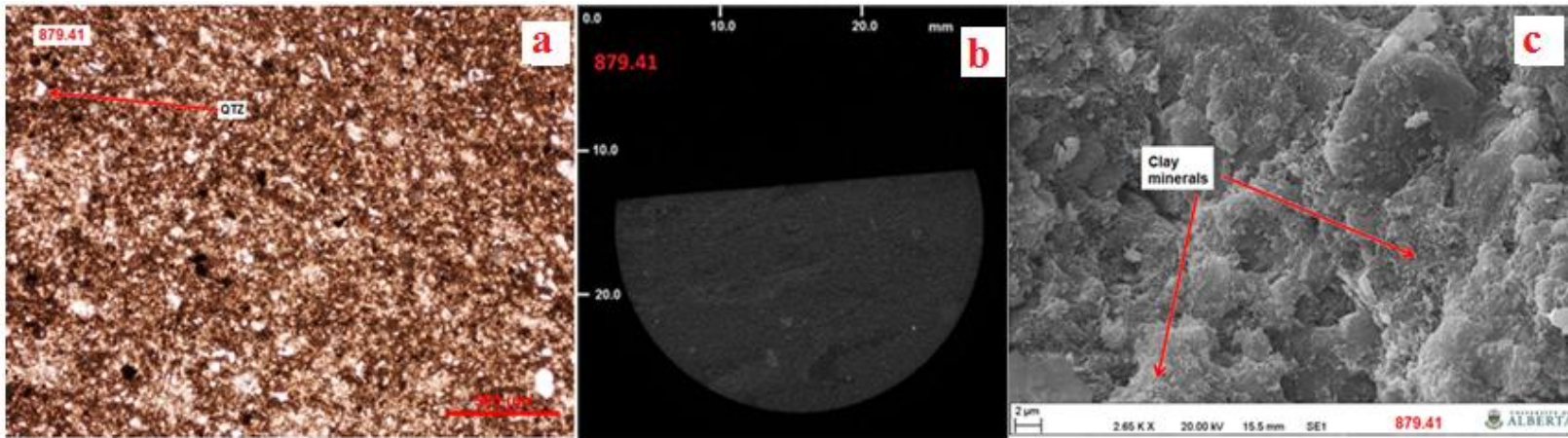
Figure 3.2 a) Thin section for sample 879.41[mbsf]. Siltstone with dispersed clasts. b) µ- CT image of sample 879.41[mbsf]. Well sorted and fine grained siltstone is observed in this image. c) SEM image for sample 879.41[mbsf]. Clay minerals can be observed in this simple.
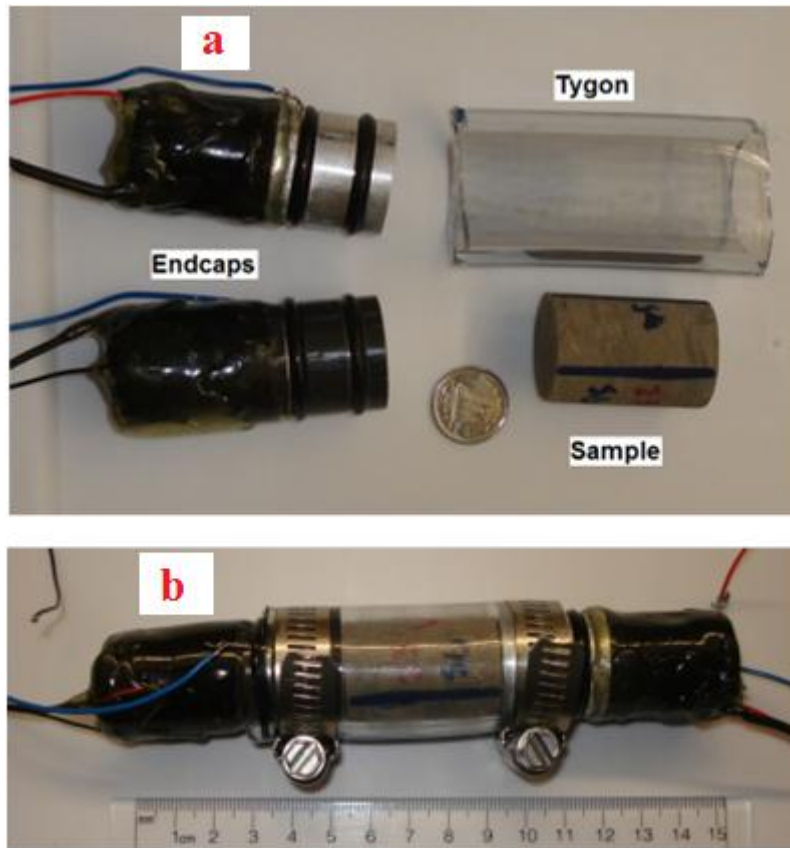
Figure 3.3 Photographs showing the individual components (a) and the assembled components (b) prior to measurements. The coin used as a reference has diameter of 18.03 mm.
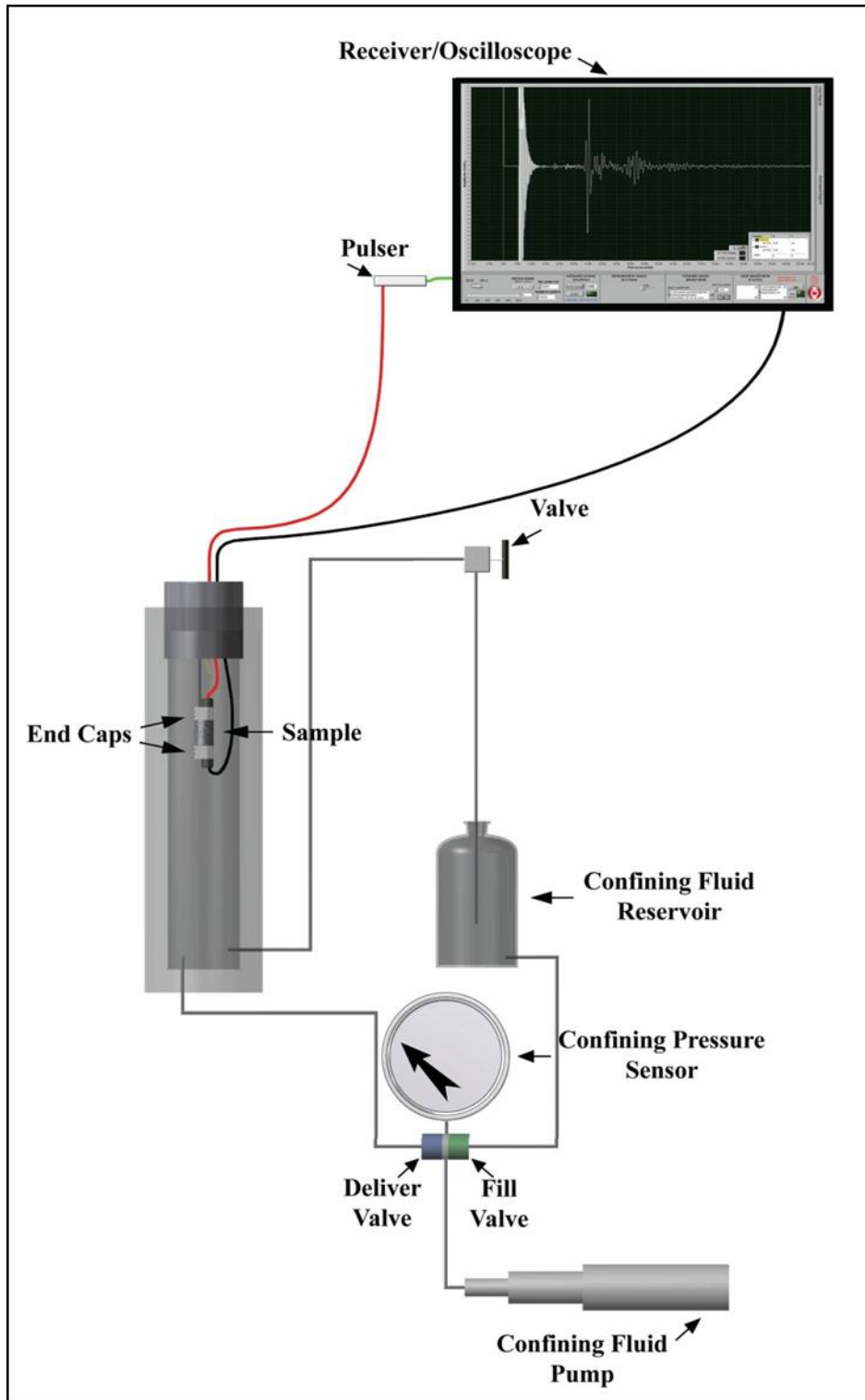
Figure 3.4 Experimental setup.
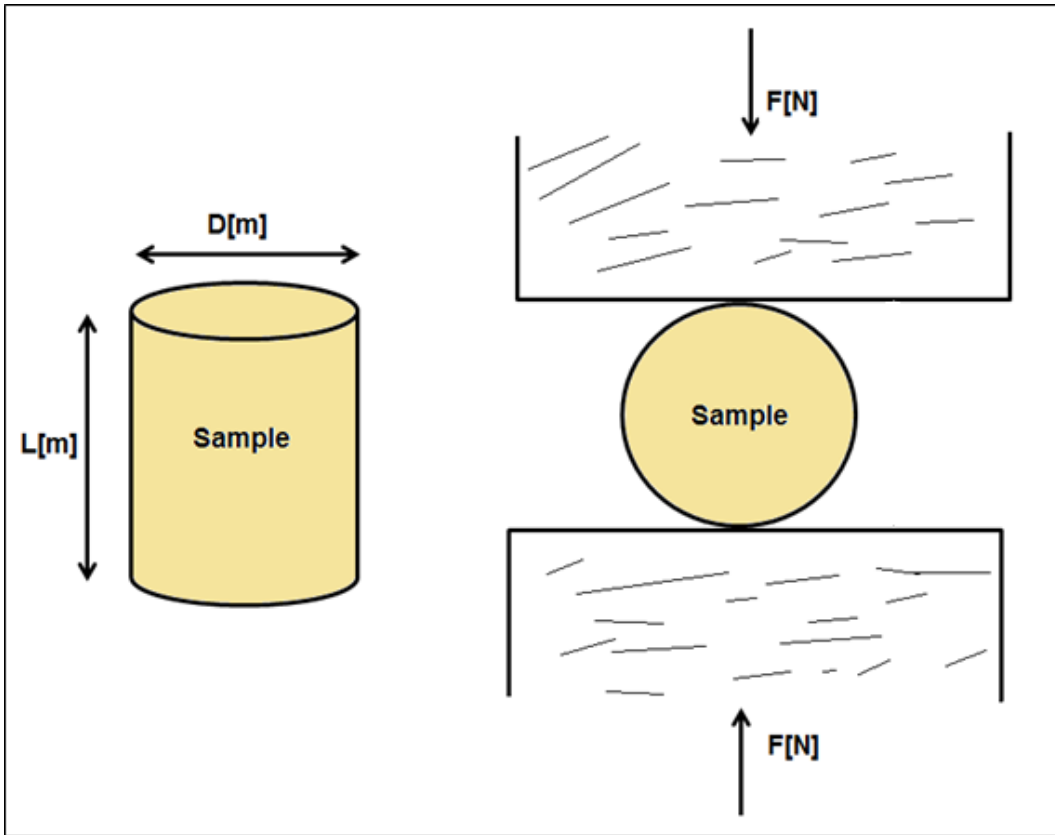
Figure 3.5 Schematic of the indirect tensile strength test (Brazilian test).
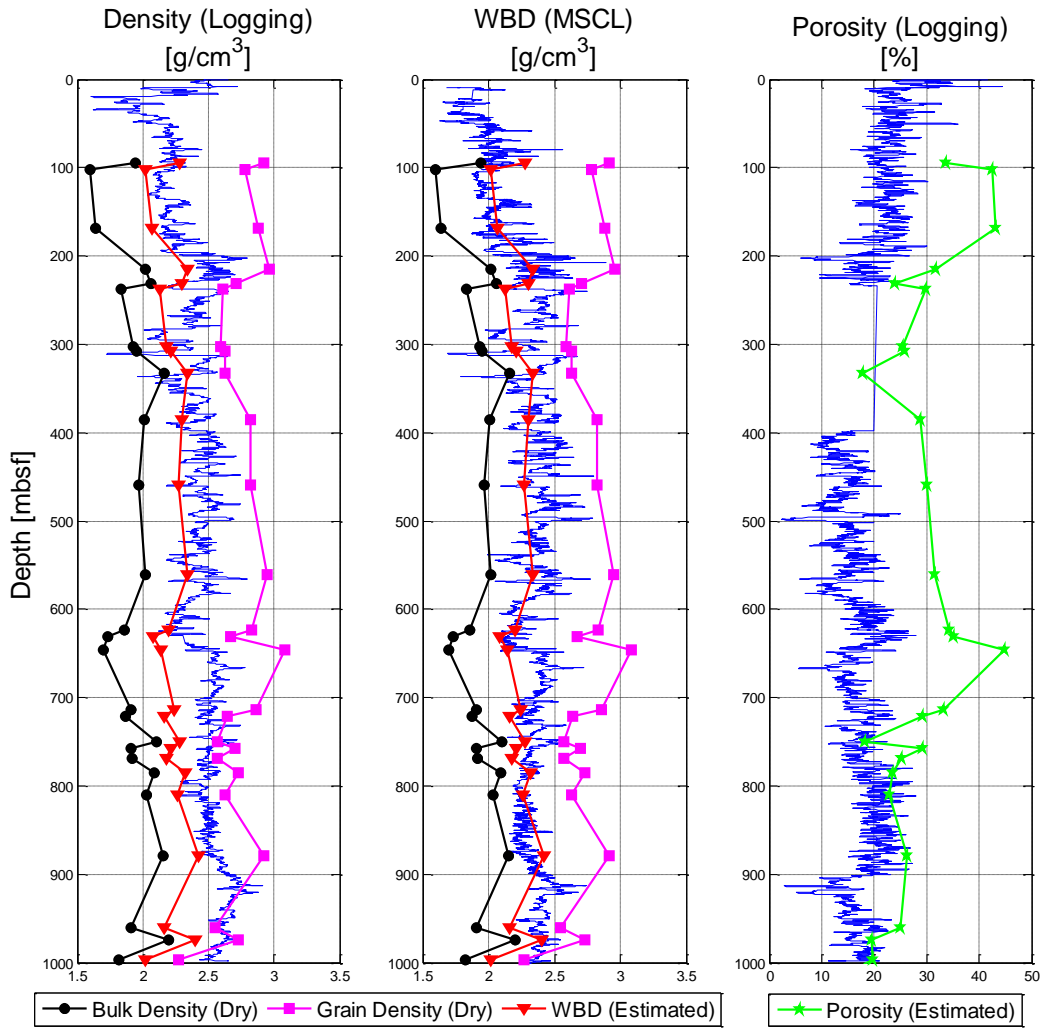
Figure 3.6 Comparison among laboratory measurements, wireline logging, and Multi-sensor core logging (MSCL) data. There is a gap in the wireline logging porosity data between 234.2 [mbsf] and 397.4 [mbsf].
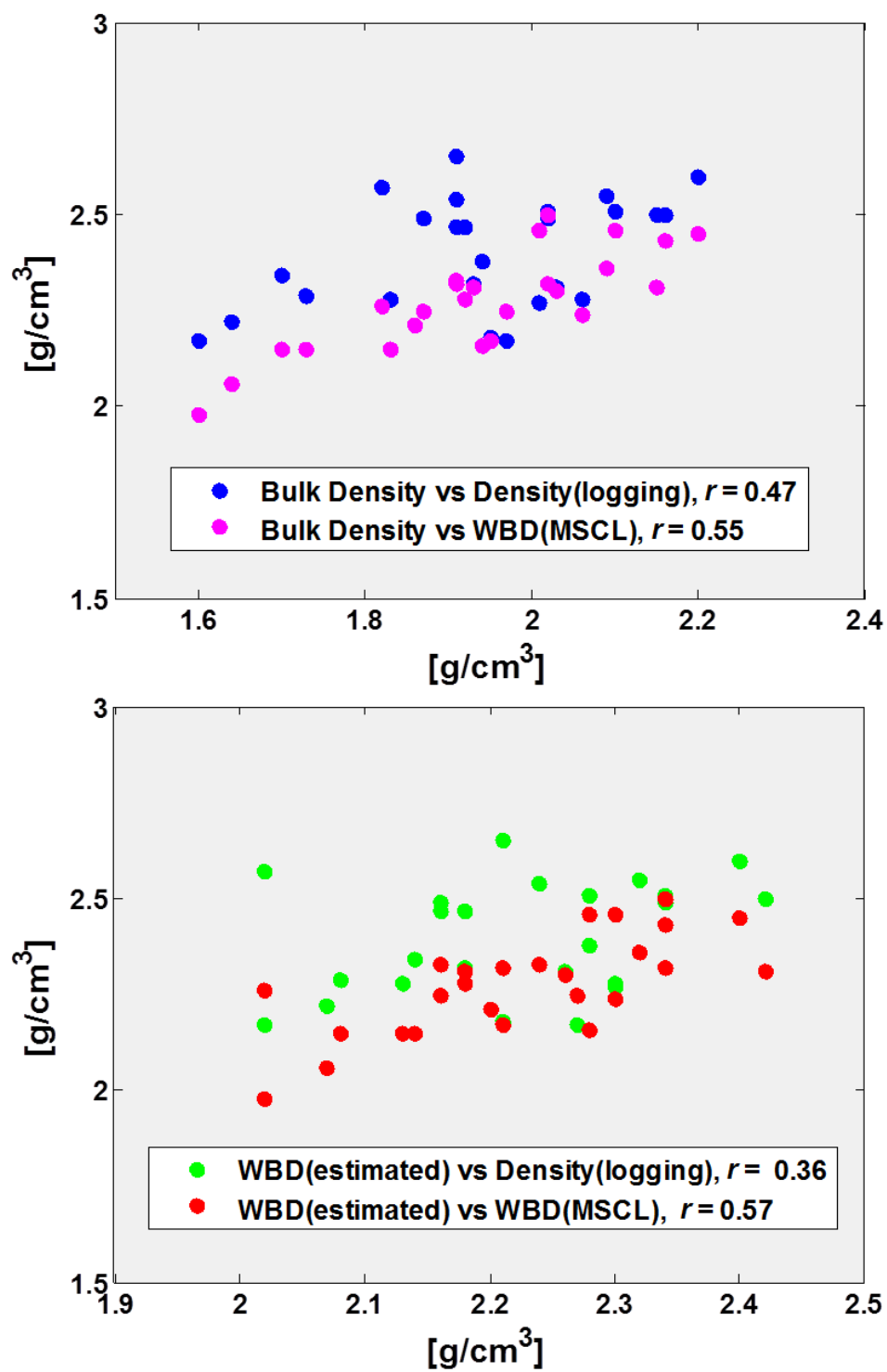
Figure 3.7 Cross plots among different density measures.
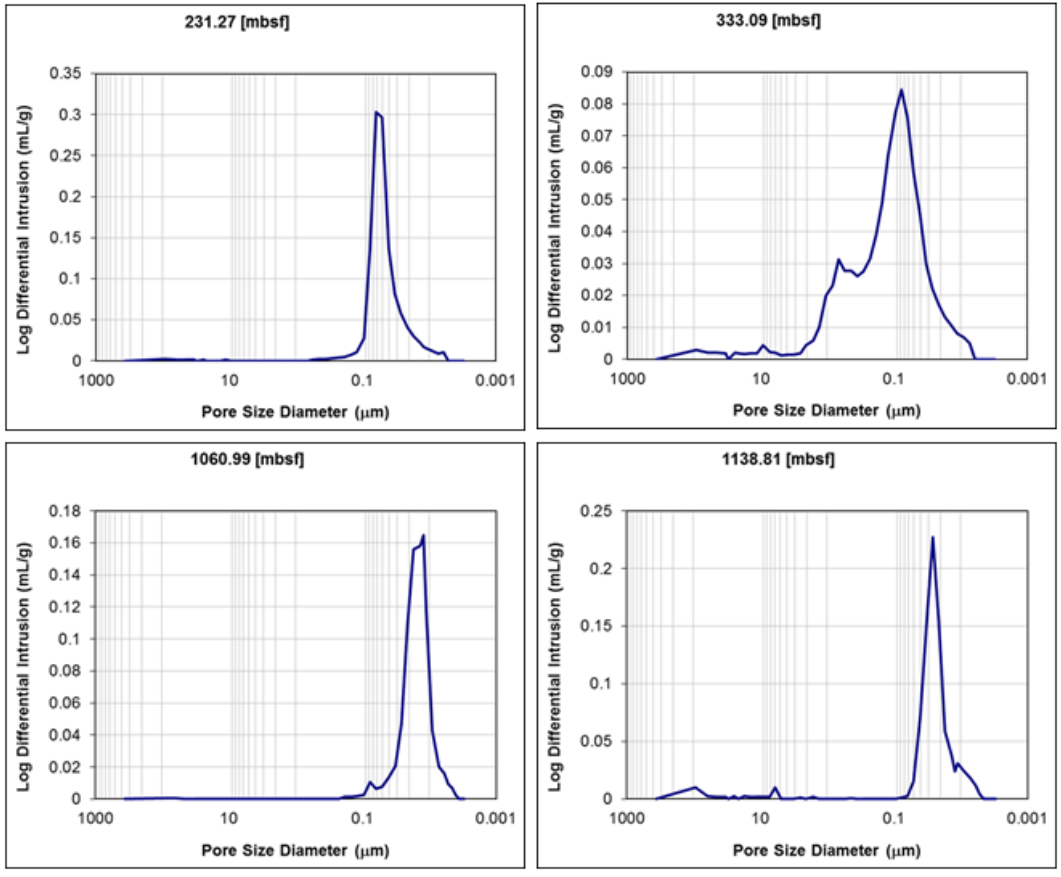
Figure 3.8 Some examples of differential mercury intrusion (log) versus pore size diameter curves.
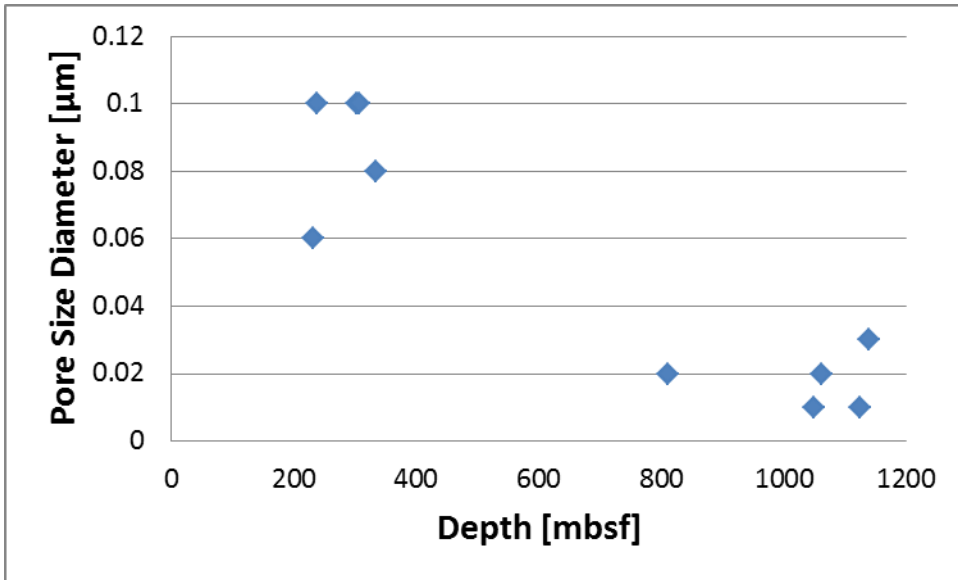
Figure 3.9 Pore size diameter versus depth. A reduction in pore size diameter with depth can be observed. Point 0.68 from sample 333.09 [msbf] was removed in order to show the decrease in pore size as a function of depth.
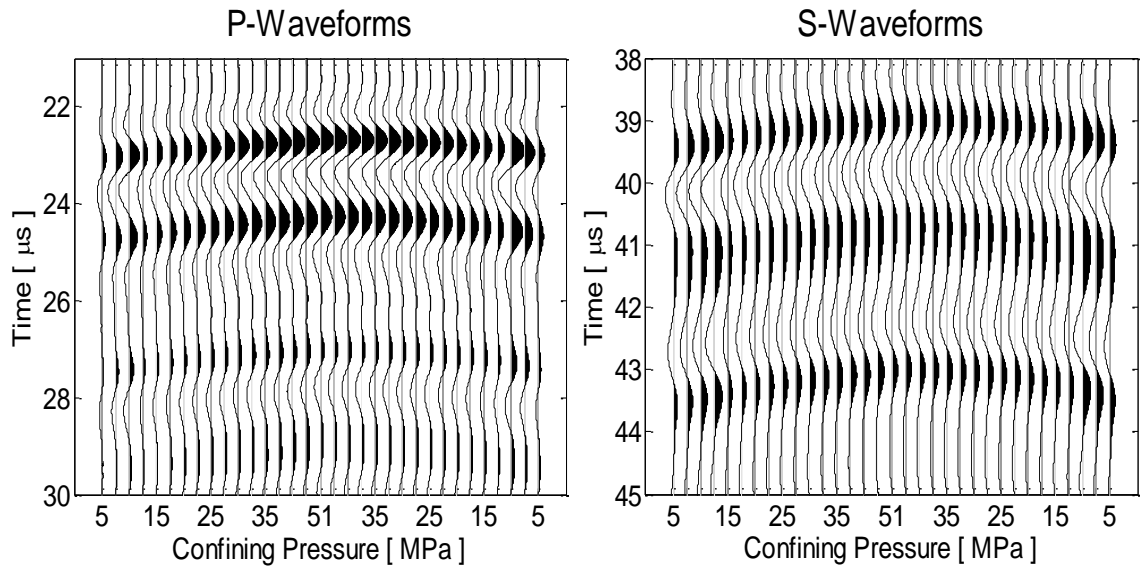
Figure 3.10 Set of measurements for sample 94.16 [mbsf] . Waveforms show an increase of velocity as pressure increases.
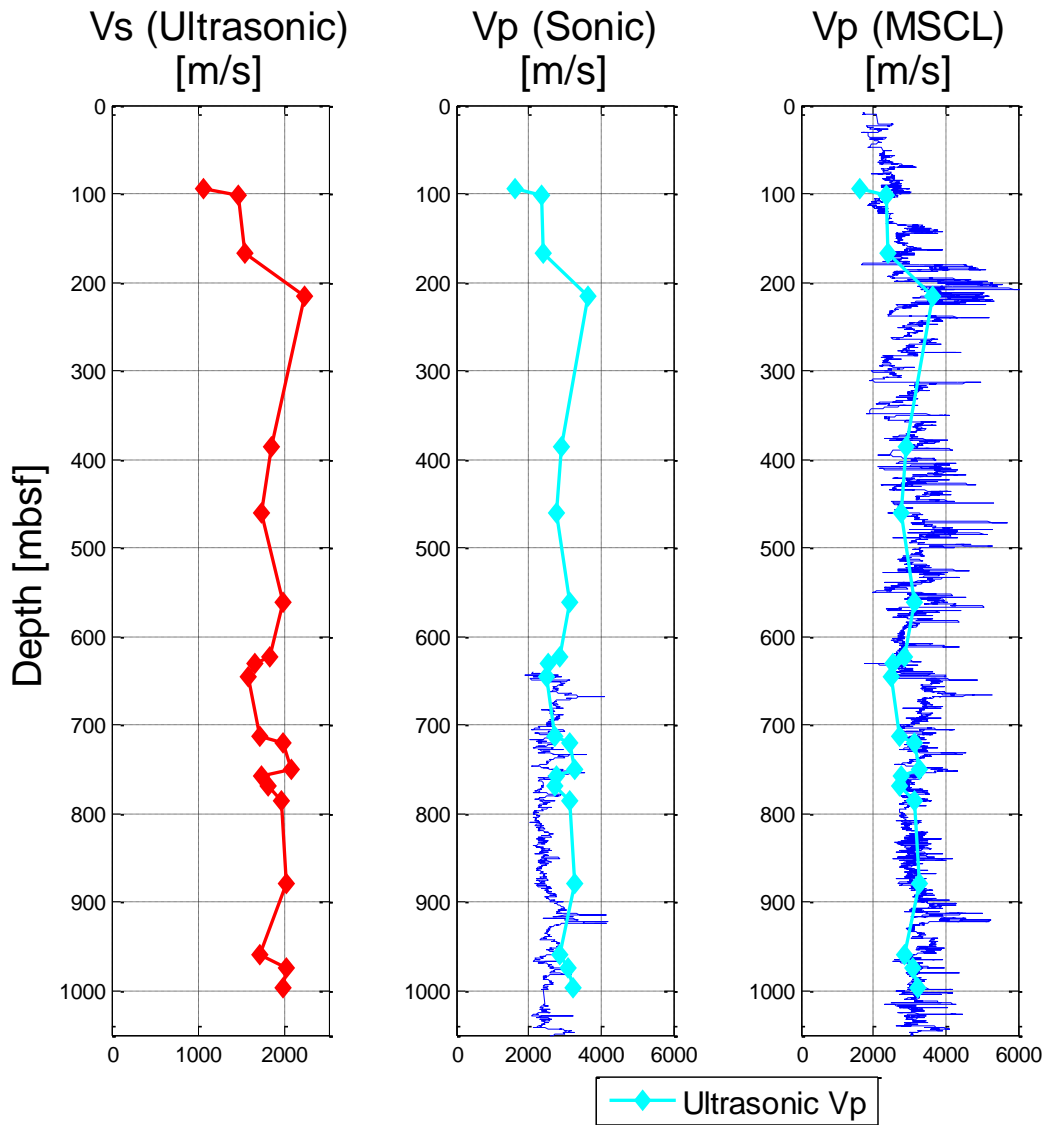
Figure 3.11 Comparison between ultrasonic P- and S-wave velocities and sonic and MSCL P-wave velocities.
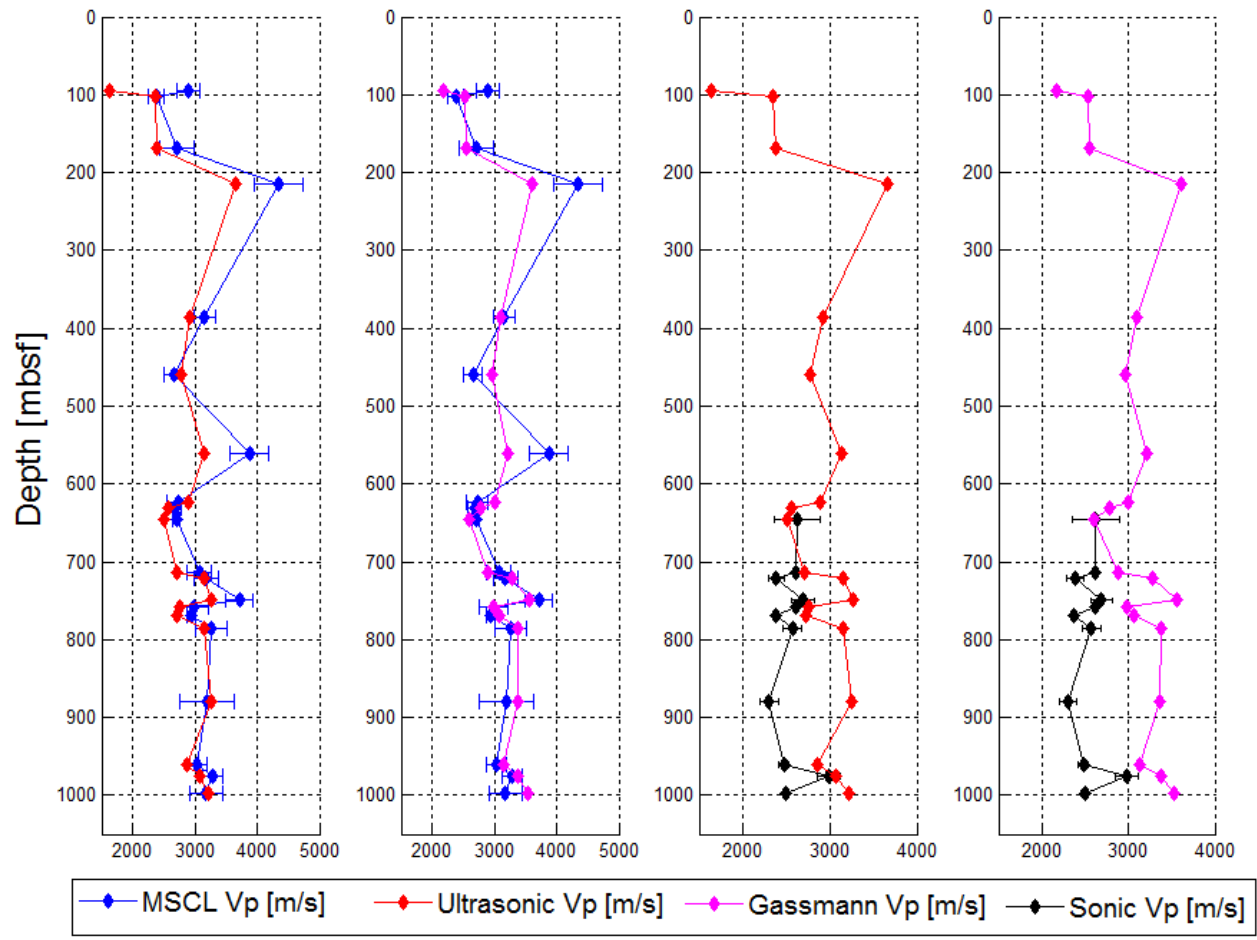
Figure 3.12 Comparison among ultrasonic and Gassmann compressional velocities with MSCL and Sonic compressional velocities.
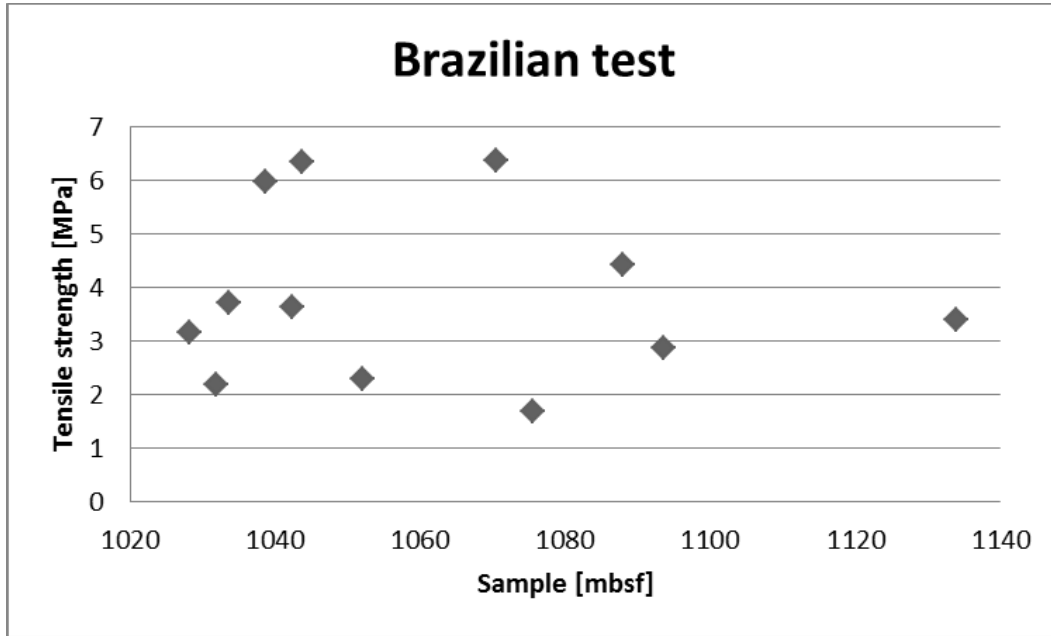
Figure 3.13 Tensile strength for samples obtained from lower Miocene.

Bibliography

Acton, G., Crampton, J., Di Vincenzo, G., Fielding, C.R., Florindo, F., Hannah, M., Harwood, D.M., Ishman, S., Johnson, K., Jovane, L., Levy, R., Lum, B., Marcano, M.C., Mukasa, S., Ohneiser, C., Olney, M., Riesselman, C., Sagnotti, L., Stefano, C., Strada, E., Taviani, M., Tuzzi, E., Verosub, K.L., Wilson, G.S., Zattin, M. and The ANDRILL-SMS Science Team. 2008-2009. Preliminary Integrated Chronostratigraphy of the AND-2A Core, ANDRILL Southern McMurdo Sound Project, Antarctica, *Terra Antartica,* 15 (1), 211-220.

Adam, L., Batzle, M. and Brevik, L. 2006. Gassmann's fluid substitution and shear modulus variability in carbonates at laboratory seismic and ultrasonic frequencies, *Geophysics,* 71, F173-F183.

Andreev, G.E. 1991a. A review of the Brazilian test for rock tensile strength determination. Part I: calculation formula, *Mining Science and Technology,* 13, 445-456.

Andreev, G.E. 1991b. A review of the Brazilian test for rock tensile strength determination. Part II: contact conditions, *Mining Science and Technology,* 13, 457-465.

Auld, B.A. 1973. *Acoustic fields and waves in solids.* 1 Wiley-Interscience Publication.

Aydin, A. and Basu, A. 2006. The use of Brazilian test as a quantitative measure of rock weathering, *Rock Mechanics and Rock Engineering,* 39, 77-85.

Baechle, G.T., Weger, R.J., Eberli, G.P., Massaferro, J.L. and Sun, Y.-F. 2005. Changes of shear moduli in carbonate rocks: Implications for Gassmann applicability, *Leading Edge,* 24, 507-510.

Bahlburg, H. and Dobrzinski, N. 2011. A review of the Chemical Index of Alteration (CIA) and its application to the study of Neoproterozoic glacial deposits and climate transitions. In: *Geological Record of Neoproterozoic Glaciations,*Vol. 36 (eds. E. Arnaud, G.P. Halverson and G. ShieldsZhou), pp. 81-92. Geological Society Memoirs.

Bakhorji, A.M. 2010. Laboratory measurements of static and dynamic elastic properties in carbonate, *PhD Thesis*, University fo Alberta, Edmonton, Alberta, Canada.

Berryman, J.G. 1999. Origin of gassmann's equations, *Geophysics,* 64, 1627-1629.

Best, A.I. 1997. The effect of pressure on ultrasonic velocity and attenuation in near-surface sedimentary rocks, *Geophysical Prospecting,* 45, 345-364.

Birch, F. 1960. The velocity of compressional waves in rocks to 10-kilobars, Part 1, *Journal of Geophysical Research,* 65, 1083-1102.

Birch, F. 1961. The velocity of compressional waves in rocks to 10 kilobars, Part 2, *Journal of Geophysical Research,* 66, 2199-2224.

Biscaye, P.E. 1965. Mineralogy and sedimentation of recent deep-sea clay in Atlantic ocean and adjacent seas and oceans, *Geological Society of America Bulletin,* 76, 803-832.

Bowers, S.A. and Hanks, R.J. 1962. Specific heat capacity of soils and minerals as determined with a radiation calorimeter, *Soil Science,* 94, 392-396.

Boyce, J.I. and Eyles, N. 2000. Architectural element analysis applied to glacial deposits: Internal geometry of a late Pleistocene till sheet, Ontario, Canada, *Geological Society of America Bulletin,* 112, 98-118.

Braakman, J.H., Levell, B.K. and Rutten, K.W. 1983. Oil-bearing glacial deposits from Permo-Carboniferous Haushi group, Oman, *American Association of Petroleum Geologists Bulletin,* 67, 429-429.

Brink, J. and Jarrard, R.D. 1998. Petrophysics of core plugs from CRP-1 drillhole, Victoria Land Basin, Antarctica, *Terra Antartica,* 5 (3), 291-297

Buatier, M.D., Karpoff, A.M. and Charpentier, D. 2002. Clays and zeolite authigenesis in sediments from the flank of the Juan de Fuca Ridge, *Clay Minerals,* 37, 143-155.

Cai, Y., Esaki, T. and Jiang, Y.J. 2004. An analytical model to predict axial load in grouted rock bolt for soft rock tunnelling, *Tunnelling and Underground Space Technology,* 19, 607-618.

Cape Roberts Science Team. 1999. Initial Report on CRP-2/2A, Cape Roberts Project, Antarctica, *Terra Antartica*, 6(1/2), 27-48.

Carvajal-Jiménez, J.M., Valera-Lara, L.C., Rueda, A. and Saavedra.Trujillo, N. 2007. Geomechanical wellbore stability modeling of exploratory wells - study case at middle Magdalena basin, *CT&F Ciencia, Tecnología y Futuro,* 3, 85-102.

Claesson, J. and Bohloli, B. 2002. Brazilian test: stress field and tensile strength of anisotropic rocks using an analytical solution, *International Journal of Rock Mechanics and Mining Sciences,* 39, 991-1004.

Clark-Lowes, D.D. 2005. Arabian glacial deposits: recognition of palaeovalleys within the upper Ordovician Sarah Formation, Al Qasim district, Saudi Arabia, *Proceedings of the Geologists Association,* 116, 331-347.

Cole, T.G. and Shaw, H.F. 1983. The nature and origin of authigenic smectites in some recent marine-sediments, *Clay Minerals,* 18, 239-252.

Colhoun, E.A., Kiernan, K.W., McConnell, A., Quilty, P.G., Fink, D., Murray-Wallace, C.V. and Whitehead, J. 2010. Late Pliocene age of glacial deposits at Heidemann Valley, East Antarctica: evidence for the last major glaciation in the Vestfold Hills, *Antarctic Science,* 22, 53-64.

Chamley, H. 1989. *Clay sedimentology.* Springer-Verlag.

Chen, C.S., Pan, E. and Amadei, B. 1998. Determination of deformability and tensile strength of anisotropic rock using Brazilian tests, *International Journal of Rock Mechanics and Mining Sciences,* 35, 43-61.

Christensen, N.I. and Wang, H.F. 1985. The influence of pore pressure and confining pressure on dynamic elastic properties of Berea sandstone, *Geophysics,* 50, 207-213.

Dabkowska-Naskret, H. and Jaworska, H. 2001. Titanium in Alfisols formed from glacial deposits of different ages in Poland, *Quaternary International,* 78, 61-67.

Dai, H.L., Wang, X., Xie, G. and Wang, X.Y. 2004. Theoretical model and solution for the rheological problem of anchor-grouting a soft rock tunnel, *International Journal of Pressure Vessels and Piping,* 81, 739-748.

Daley, P.F. and Hron, F. 1977. Reflection and transmission coefficients for transversely isotropic media, *Bulletin of the Seismological Society of America,* 67, 661-675.

de la Fuente, S., Cuadros, J., Fiore, S. and Linares, J. 2000. Electron microscopy study of volcanic tuff alteration to illite-smectite under hydrothermal conditions, *Clays and Clay Minerals,* 48, 339-350.

Dey-Barsukov, S., Durrast, H., Rabbel, W., Siegesmund, S. and Wende, S. 2000. Aligned fractures in carbonate rocks: laboratory and in situ measurements of seismic anisotropy, *International Journal of Earth Sciences,* 88, 829-839.

Di Vincenzo, G., Bracciali, L., Del Carlo, P., Panter, K. and Rocchi, S. 2010. Ar-40-Ar-39 dating of volcanogenic products from the AND-2A core (ANDRILL Southern McMurdo Sound Project, Antarctica): correlations with the Erebus Volcanic Province and implications for the age model of the core, *Bulletin of Volcanology,* 72, 487-505.

Dunbar, G.B., Atkins, C., Magens, D. and Niessen, F. 2009. Physical Properties of the AND-2A Core, ANDRILL Southern McMurdo Sound Project, *Terra Antartica,* 15(1), 49-56.

Efimov, V.P. 2009. The rock strength in different tension conditions, *Journal of Mining Science,* 45, 569-575.

Ehrmann, W. 1998. Implications of late Eocene to early Miocene clay mineral assemblages in McMurdo Sound (Ross Sea, Antarctica) on paleoclimate and ice dynamics, *Palaeogeography Palaeoclimatology Palaeoecology,* 139, 213-231.

Eyles, N. and Kocsis, S.P. 1989. Sedimentological controls on gold in a late Pleistocene glacial placer deposit, Cariboo Mining District, British Columbia, Canada, *Sedimentary Geology,* 65, 45-68.

Fairbairn, E.M.R. and Ulm, F.J. 2002. A tribute to Fernando L. L. B. Carneiro (1913-2001) - Engineer and scientist who invented the Brazilian test, *Materials and Structures,* 35, 195-196.

Fesharaki, O., Garcia-Romero, E., Cuevas-Gonzalez, J. and Lopez-Martinez, N. 2007. Clay mineral genesis and chemical evolution in the Miocene sediments of Somosaguas, Madrid Basin, Spain, *Clay Minerals,* 42, 187-201.

Fielding, C.R., Browne, G.H., Field, B., Florindo, F., Harwood, D.M., Krissek, L.A., Levy, R.H., Panter, K.S., Passchier, S. and Pekar, S.F. 2011. Sequence stratigraphy of the ANDRILL AND-2A drillcore, Antarctica: A long-term, ice-proximal record of Early to Mid-Miocene climate, sea-level and glacial dynamism, *Palaeogeography Palaeoclimatology Palaeoecology,* 305, 337-351.

Florindo, F., Harwood, D. and Levy, R. 2008. ANDRILL's Success During the 4th International Polar Year, *Scientific Drilling*, 29-31.

Franca, A.B. and Potter, P.E. 1991. Stratigraphy and reservoir potential of glacial deposits of the Itarare Group (Carboniferous Permian), Parana Basin, Brazil, *American Association of Petroleum Geologists Bulletin,* 75, 62-85.

Frocht, M.M. 1941. *Photoelasticity.* J. Wiley.

Fujimoto, T., Otoh, S., Orihashi, Y., Hirata, T., Yokoyama, T.D., Shimojo, M., Kouchi, Y., Obara, H., Ishizaki, Y., Tsukada, K., Kurihara, T., Nuramkhan, M. and Gonchigdorj, S. 2012. Permian Peri-glacial Deposits from Central Mongolia in Central Asian Orogenic Belt: A Possible Indicator of the Capitanian Cooling Event, *Resource Geology,* 62, 408-422.

Gassmann, F. 1951. *Über die Elastizität poröser Medien.* Kümmerly & Frey.

Giesche, H. 2006. Mercury porosimetry: A general (practical) overview, *Particle & Particle Systems Characterization*, 23, 9-19.

Granger, R.A. 1985. *Fluid Mechanics.* Dover Publications.

Hall, R.D. 1999. Effects of climate change on soils in glacial deposits, Wind River Basin, Wyoming, *Quaternary Research,* 51, 248-261.

Hall, R.D. and Horn, L.L. 1993. Rates of hornblende etching in soils in glacial deposits of the northern Rocky-mountains (Wyoming-Montana, USA) - influence of climate and characteristics of the parent material, *Chemical Geology,* 105, 17-29.

Hart, P.A. 1993. Foundation behavior in reusable tunnels in weak rocks, *International Journal of Rock Mechanics and Mining Sciences & Geomechanics Abstracts,* 30, 239-246.

Harte, P.T. and Winter, T.C. 1995. Simulations of flow in crystalline rock and recharge from overlying glacial deposits in a hypothetical New-England setting, *Ground Water,* 33, 953-964.

Harwood, D., Florindo, F., Talarico, F., Levy, R., Kuhn, G., Naish, T., Niessen, F., Powell, R., Pyne, A. and Wilson, G. 2009. Antarctic Drilling Recovers Stratigraphic Records From the Continental Margin, *Eos, Transactions American Geophysical Union,* 90, 90-91.

Henry, J.P. and Paquet, J. 1977. Fracture mechanics applied to Brazilian tests on disks and rings of rocks, *Comptes Rendus Hebdomadaires Des Seances De L Academie Des Sciences Serie B,* 284, 511-514.

Hornby, B.E. 1998. Experimental laboratory determination of the dynamic elastic properties of wet, drained shales, *Journal of Geophysical Research-Solid Earth,* 103, 29945-29964.

Hudson, J.A. and Harrison, J.P. 2000. *Engineering Rock Mechanics: An Introduction to the Principles.* Pergamon.

Huertas, F.J., Cuadros, J., Huertas, F. and Linares, J. 2000. Experimental study of the hydrothermal formation of smectite in the beidellite-saponite series, *American Journal of Science,* 300, 504-527.

Iacoviello, F., Giorgetti, G., Nieto, F. and Memmi, I.T. 2012. Evolution with depth from detrital to authigenic smectites in sediments from AND-2A drill core (McMurdo Sound, Antarctica), *Clay Minerals,* 47, 481-498.

Ismail, N., Schwarz, G. and Pedersen, L.B. 2011. Investigation of groundwater resources using controlled-source radio magnetotellurics (CSRMT) in glacial deposits in Heby, Sweden, *Journal of Applied Geophysics,* 73, 74-83.

Jaeger, J.C. 1967. Failure of rocks under tensile conditions, *International Journal of Rock Mechanics and Mining Sciences & Geomechanics Abstracts,* 4, 219-227.

Jaeger, J.C. and Hoskins, E.R. 1966. Rock failure under the confined Brazilian test, *Journal of Geophysical Research,* 71, 2651–2659.

Jensen, J.B. 1993. Late Weichselian deglaciation pattern in the southwestern Baltic: Evidence from glacial deposits off the island of Mon, Denmark, *Bulletin of the Geological Society of Denmark,* 40, 314-331.

Jiang, Y., Yoneda, H. and Tanabashi, Y. 2001. Theoretical estimation of loosening pressure on tunnels in soft rocks, *Tunnelling and Underground Space Technology,* 16, 99-105.

Johnston, J.E. and Christensen, N.I. 1994. Elastic constants and velocity surfaces of indurated anisotropic shales, *Surveys in Geophysics,* 15, 481-494.

Juhlin, C., Palm, H., Mullern, C.F. and Wallberg, B. 2000. High-resolution reflection seismics applied to detection of groundwater resources in glacial deposits, Sweden, *Geophysical Research Letters,* 27, 1575-1578.

Kyle, P.R. 1990. A. McMurdo Volcanic Group Western Ross embayment. In: *Volcanoes of the Antarctic Plate and Southern Oceans,*Vol. 48 (eds. W.E. LeMasurier and J.W. Thomson), pp. 18-145. American Geophysical Union.

Landau, L.L.D., Lifshits, E.M., Kosevič, A.M. and Pitaevskiĭ, L.P. 1986. *Theory of Elasticity 7.* Elsevier.

LeBlanc, D.C. 2004. *Statistics: Concepts and Applications for Science.* Jones & Bartlett Publishers.

Lee, D.H., Juang, C.H. and Lei, I.M. 1996. High-temperature Brazilian test for tensile strength of metamorphic limestone, *Geotechnical Testing Journal,* 19, 223-226.

Lo, T.W., Coyner, K.B. and Toksoz, M.N. 1986. Experimental determination of elastic-anisotropy of Berea sandstone, Chicopee shale, and Chelmsford granite, *Geophysics,* 51, 164-171.

Mah, M. 2005. Determination of the elastic constants of orthorhombic and transversely isotropic materials: experimental application to a kerogen rich rock*, PhD Thesis*, University of Alberta, Edmonton, Alberta, Canada.

Marion, D., Mukerji, T. and Mavko, G. 1994. Scale effects on velocity dispersion - from ray to effective-medium theories in stratified media, *Geophysics,* 59, 1613-1619.

Mavko, G., Mukerji, T. and Dvorkin, J. 2009. *The Rock Physics Handbook: Tools for Seismic Analysis of Porous Media.* Cambridge University Press.

Melendez, J. and Schmitt, D.R. 2011. Investigating anisotropy in rocks by using pulse transmission method, *Canadian Society of Exploration Geophysicists Recorder,* 36, 38-42.

Meléndez, J. and Schmitt, D.R. 2013. Anisotropic elastic moduli of carbonates and evaporites from the Weyburn-Midale reservoir and seal rocks, *Geophysical Prospecting,* 61, 363-379.

Mellor, M. and Hawkes, I. 1971. Measurement of tensile strength by diametral compression of discs and annuli, *Engineering Geology,* 5, 173–225.

Meriano, M. and Eyles, N. 2003. Groundwater flow through Pleistocene glacial deposits in the rapidly urbanizing Rouge River-Highland Creek watershed, City of Scarborough, southern Ontario, Canada, *Hydrogeology Journal,* 11, 288-303.

Miller, S.L.M. 1989. Analysis of array sonic logs from the Medicine River field, Alberta. In: *CREWES Research Report*, 159-171.

Moorby, S.A. and Cronan, D.S. 1983. The geochemistry of hydrothermal and pelagic sediments from the Galapagos Hydrothermal Mounds Field, D.S.D.P. Leg 70, *Mineralogical Magazine,* 47, 291-300.

Niessen, F. and Jarrard, R.D. 1998. Velocity and porosity of sediments from CRP-1 drillhole, Ross Sea, Antarctica *Terra Antartica,* 5 (3), 311-318

Niessen, F., Jarrard, R.D. and Bücker, C. 1998. Log-based physical properties of the CRP-1 Core, Ross Sea, Antarctica, *Terra Antartica,* 5 (3), 299-310

Pandey, P. and Singh, D.P. 1986. Deformation of a rock in different tensile tests, *Engineering Geology,* 22, 281-292.

Panter, K.S., Talarico, F., Bassett, K., Del Carlo, P., Field, B., Frank, T., Hoffmann, S., Kuhn, G., Reichelt, L., Sandroni, S., Taviani, M., Bracciali, L., Cornamusini, G., von Eynatten, H., Rocchi, S. and Team, T.A.-S.S. 2008-2009. Petrologic and Geochemical Composition of the AND-2A Core, ANDRILL Southern McMurdo Sound Project, Antarctica, *Terra Antartica,* 15(1), 147-192.

Passchier, S., Browne, G., Field, B., Fielding, C.R., Krissek, L.A., Panter, K., Pekar, S.F. and Team, A.-S.S. 2011. Early and middle Miocene Antarctic glacial history from the sedimentary facies distribution in the AND-2A drill hole, Ross Sea, Antarctica, *Geological Society of America Bulletin,* 123, 2352-2365.

Paulsen, T.S., Pompilio, M., Niessen, F., Panter, K. and Jarrard, R.D. 2012. Introduction: The ANDRILL McMurdo Ice Shelf (MIS) and Southern McMurdo Sound (SMS) Drilling Projects, *Geosphere,* 8, 546-547.

Podio, A.L., Gregory, A.R. and Gray, K.E. 1968. Dynamic properties of dry and water-saturated Green River shale under stress, *Society of Petroleum Engineers Journal,* 8, 389-&.

Rafavich, F., Kendall, C.H.S. and Todd, T.P. 1984. The relationship between acoustic properties and the petrographic character of carbonate rocks, *Geophysics,* 49, 1622-1636.

Rai, C.S. and Hanson, K.E. 1988. Shear-wave velocity anisotropy in sedimentary rocks: A laboratory study, *Geophysics,* 53, 800-806.

Root, T.L., Gotkowitz, M.B., Bahr, J.M. and Attig, J.W. 2010. Arsenic geochemistry and hydrostratigraphy in Midwestern U.S. glacial deposits, *Ground Water,* 48, 903-912.

Saad, D.A. 2008. Agriculture-related trends in groundwater quality of the glacial deposits aquifer, central Wisconsin, *Journal of Environmental Quality,* 37, S209-S225.

Saarnisto, M., Tamminen, E. and Vaasjoki, M. 1991. Gold in bedrock and glacial deposits in the Ivalojoki area, Finnish Lapland, *Journal of Geochemical Exploration,* 39, 303-322.

Scotellaro, C., Vanorio, T. and Mavko, G. 2007. The effect of mineral composition and pressure on carbonate rocks, *SEG Technical Program Expanded Abstracts,* 26, 1684-1689.

Schroede, C. 1972. Influence of lithology on mechanical behavior of rocks in uniaxial compression and Brazilian tests, *Engineering Geology,* 6, 31-42.

Sondergeld, C.H. and Rai, C.S. 1992. Laboratory observations of shear-wave propagation in anisotropic media, *The Leading Edge,* 11, 38-43.

Stephenson, D.A., Fleming, A.H. and Mickelson, D.M. 1988. Glacial deposits. In: *Hydrogeology: The Geology of North America,*Vol. 2 (eds. W. Back, J.S. Rosenshein and P.R. Seaber), pp. 301-314. Geological Society of America.

Talarico, F.M., McKay, R.M., Powell, R.D., Sandroni, S. and Naish, T. 2012. Late Cenozoic oscillations of Antarctic ice sheets revealed by provenance of basement clasts and grain detrital modes in ANDRILL core AND-1B, *Global and Planetary Change,* 96-97, 23-40.

Talarico, F.M. and Sandroni, S. 2011. Early Miocene basement clasts in ANDRILL AND-2A core and their implications for paleoenvironmental changes in the McMurdo Sound region (western Ross Sea, Antarctica), *Global and Planetary Change,* 78, 23-35.

Tavallali, A. and Vervoort, A. 2010a. Effect of layer orientation on the failure of layered sandstone under Brazilian test conditions, *International Journal of Rock Mechanics and Mining Sciences,* 47, 313-322.

Tavallali, A. and Vervoort, A. 2010b. Failure of Layered Sandstone under Brazilian Test Conditions: Effect of Micro-Scale Parameters on Macro-Scale Behaviour, *Rock Mechanics and Rock Engineering,* 43, 641-653.

Thomsen, L. 1986. Weak elastic anisotropy, *Geophysics,* 51, 1954-1966.

Timoshenko, S. and Goodier, J.N. 1969. *Theory of elasticity.* McGraw-Hill.

Timur, A. 1977. Temperature-dependence of compressional and shear wave velocities in rocks, *Geophysics,* 42, 950-956.

Vernik, L. and Liu, X.Z. 1997. Velocity anisotropy in shales: A petrophysical study, *Geophysics,* 62, 521-532.

Verwer, K., Braaksma, H. and Kenter, J.A.M. 2008. Acoustic properties of carbonates: Effects of rock texture and implications for fluid substitution, *Geophysics,* 73, B51-B65.

Vitali, F., Blanc, G., Larque, P., Duplay, J. and Morvan, G. 1999. Thermal diagenesis of clay minerals within volcanogenic material from the Tonga convergent margin, *Marine Geology,* 157, 105-125.

Wang, Z.J. 2002. Seismic anisotropy in sedimentary rocks, part 2: Laboratory data, *Geophysics,* 67, 1423-1440.

Wilson, G.S., Naish, T.R., Powell, R.D., Levy, R.H. and Crampton, J.S. 2012. 'Late Neogene chronostratigraphy and depositional environments on the Antarctic Margin: New results from the ANDRILL McMurdo Ice Shelf Project', *Global and Planetary Change,* 96-97, 1-8.

Wonik, T., Grelle, T., Handwerger, D., Jarrard, R.D., McKee, A., Patterson, T., Paulsen, T., Pierdominici, S., Schmitt, D.R., Schroeder, H., Speece, M. and Wilson, T. 2008-2009. Downhole Measurements in the AND-2A Borehole, ANDRILL Southern McMurdo Sound Project, Antarctica, *Terra Antartica,* 15(1), 57-68.

CHAPTER 4

Anisotropic Elastic Moduli of Carbonates and Evaporites from the Weyburn Midale Reservoir and Seal Rocks[1]

4.1 Introduction

Recent interest in unconventional reservoirs broadly motivates our work in laboratory measurements of seismic anisotropy. Seismic anisotropy is the variation in speed of a wave as a function of its direction of propagation and its particle polarization. Knowledge of the seismic anisotropy of a geological formation obviously assists imaging and depth estimation. Analyzing anisotropy in unconventional reservoirs is further useful because the anisotropy leads, for example, to differential stresses upon loading that could affect hydraulic stimulations (Reinicke *et al*. 2010; Zimmermann and Reinicke 2010). In this sense, laboratory measurements are an important tool to study seismic anisotropy because they provide information on the anisotropy intrinsic to the rock material itself. This is important to know as the material's intrinsic anisotropy contributes to the observed seismic anisotropy that is also influenced by stress states and fractures.

Here, the elastic anisotropy of a series of four carbonates and one evaporite from the Williston sedimentary basin in Saskatchewan are investigated. The carbonates

---

[1] A version of this chapter has been published: Meléndez, J. and Schmitt, D.R. 2013. Anisotropic elastic moduli of carbonates and evaporites from the Weyburn-Midale reservoir and seal rocks, *Geophysical Prospecting*, 61, 363-379.

studied are representative of the reservoir rocks of the International Energy Agency Weyburn project (Moberg, Stewert and Stachniak 2003) where injected CO_2 is used to enhance oil recovery. The evaporite is representative of the caprock sequences. At the reservoir scale, anisotropy observed at Weyburn is caused by presence of fracture sets (Bunge 2000; Brown 2002; Bellefleur *et al* 2003; Verdon and Kendall 2011).

The purpose of this work is to investigate the degree to which intrinsic properties of these rocks might contribute to any anisotropy observed at seismic scales (Dey-Barsukov *et al*. 2000; Schijns *et al* 2012). However, to our knowledge these measurements are also the first laboratory measurements of the full set of elastic constants assuming a VTI medium for the formations studied here.

In sedimentary basins seismic anisotropy is influenced by depositional and diagenetic processes as well as local and regional stress fields. Those effects result from layering, preferred mineralogical alignment or preferred orientation of cracks and pores. Horizontal orientation of the above mentioned causes of anisotropy leads to a VTI medium. As such, anisotropy arises naturally in siliclastic mudstones as they display this layering down to microscopic levels, the anisotropy in such rocks is even further enhanced by preferential layering of anisotropic phyllitic clay minerals. In contrast, chemical or biological precipitation often controls the deposition of many carbonate and evaporite rocks. Later diagenetic processes in such rocks additionally modify or replace any original texture. Together, these processes do not result in clearly layered structures or preferentially aligned minerals, and the anisotropy of such rocks is

not expected to be significant. Correspondingly, most studies on carbonates or evaporites have never tested these materials for anisotropy and, in this sense, there are extensive ultrasonic laboratory studies on such rocks that assume isotropy and measure only in one direction (e.g. Rafavich, Kendall and Todd 1984; Baechle *et al*. 2005; Adam, Batzle and Brevik 2006; Best, Sothcott and McCann 2007; Scotellaro, Vanorio and Mavko 2007; Verwer, Braaksma and Kenter 2008; Bakhorji 2010).

In order to fully determine the elastic moduli of an ideal transverse isotropic medium, velocity measurements must be made in a minimum of three different directions. These are often taken for the sake of convenience to be perpendicular, parallel, and oblique to the material´s layering with the assumption that the perpendicular and parallel directions align with the principal anisotropic axes. However, there are a number of experimental geometries that have been used to obtain the appropriate information. These include multiple measurements on specially machined samples (e.g. Cheadle, Brown and Lawton 1991; Schmitt and Li 1995; Wang 2002a; Wong *et al*. 2008), on multiple core plugs taken at different angles from a single sample (e.g. Johnston and Christensen, 1994; Vernik and Liu 1997; Hornby 1998; Hemsing 2007) under the assumption that phase speeds are obtained. Another class of methods use strategically located arrays of receiving transducers (e.g., Mah and Schmitt 2001; Kebaili and Schmitt 1997) where anisotropy is analyzed by using slant stacking to provide more continuous measures of the variations of wave speed with angle of incidence. This method provides directly measures of the phase (i.e. component plane wave)

velocity that may then be directly inverted to provide the full set of elastic constants defining an orthorhombic material.

In this work we first use the multicore method (Johnston and Christensen 1994; Vernik and Liu 1997; Hornby 1998; Hemsing 2007; Meléndez and Schmitt 2011) with ultrasonic pulse transmission to measure compressional and shear wave speeds on a suite of carbonate and evaporite rock samples. These observed velocities are then used to obtain the full suite elastic constants for these materials under the assumption of VTI symmetry.

When using the multicore plug method, the assumption of VTI symmetry requires core plugs be cut from the sample in a minimum of three independent directions as shown in Figure 4.1: perpendicular to bedding (along X_3, $\theta=0^o$), parallel to bedding (along X_1 or X_2, $\theta=90^o$) and at 45° between the axis of symmetry X_3 and the plane of symmetry X_1-X_2. Velocities of one P-waveform and two S-waveforms are measured independently in each core-plug.

A brief theoretical overview of anisotropic parameters is first given, followed by descriptions of the rocks and the experimental procedures employed. The results show that, generally, these rocks are at best weakly anisotropic suggesting that the 'intrinsic' rock properties contribute little to field observations of anisotropy at the formation scale.

4.2 Theoretical background

Unlike an isotropic medium, P- and S- wave velocities vary with wave direction propagation and particle motion polarization in an anisotropic medium. In each

direction there are one P- wave and two orthogonal S waves with polarizations controlled by the symmetry of the material. Figure 4.2 shows the direction of propagation and particle polarization for each mode.

Since the polarization of the S-wave transducers is controlled by their orientation, a horizontally polarized shear wave $SH(90^o)$ is obtained when the direction of particle motion is parallel to bedding. Similarly, a vertically polarized shear wave $SV(90^o)$ is obtained when the direction of the particle motion is perpendicular to bedding. Mutually orthogonal shear waves $SH(45^o)$ and $SV(45^o)$ are obtained when the direction of propagation is 45° with respect bedding. Polarization of S-waveforms in the vertical direction of propagation can take any azimuth as long as the material is truly transversely isotropic; in this sense, $Sa(0^o) = Sb(0^o)$, in fact, any S-wave travelling in such direction regardless of its particle polarization can be referred simply as $S(0^o)$.

As seen earlier in chapter 2, only five velocities are needed to estimate the elastic constants that define a VTI medium; however the redundancy in velocity measurements it is useful to test the VTI assumption. In particular, for a VTI symmetry $V_{Sa}(0^o) = V_{Sb}(0^o) = V_{SV}(90^o) < V_{SH}(90^o),$ and $V_P(0^o) < V_P(45^o) < V_P(90^o)$, which leads to $C_{33} < C_{11}$ and $C_{66} > C_{44}$.

To more easily quantify anisotropy in a VTI medium, Thomsen (1986) developed an approximation valid for 'weak' anisotropy that reduced the five independent elastic stiffnesses to only three "Thomsen parameters":

$$\varepsilon = \frac{C_{11} - C_{33}}{2C_{33}} \qquad\qquad 4.1$$

$$\gamma = \frac{C_{66} - C_{44}}{2C_{44}} \qquad\qquad 4.2$$

$$\delta = \frac{(C_{13} + C_{44})^2 - (C_{33} - C_{44})^2}{2C_{33}(C_{33} - C_{44})} \qquad\qquad 4.3$$

where ε measures P-wave anisotropy, γ measures SH-wave anisotropy, and δ can be viewed as a measure of the anellipticity of the P wave curve.

4.3 Sample description

The samples were taken from a variety of formations associated with the Weyburn-Midale reservoir and seal. Three cylindrically shaped core-plugs of 2.45 cm in diameter and of about 2.01 cm to 3.70 cm length at the orientations needed to characterize a VTI medium were obtained from each formation (Figure 4.3). Physical properties for each core-plug are given in Table 4.1.

Sample (a) is representative of the Top Midale Evaporite Formation. Figure 4.4 shows a Scanning Electron Microscopy image, SEM, for sample (a). This specimen consist of very tight and fine grained dolomite-rich matrix, microcracks that cut across the rock are filled with anhydrite crystals and calcite. The porosity is intercrystalline.

Samples (b), (c), (d) and (e) were obtained from the Marly formation (carbonates). Dolomite and calcite are the main minerals present in these samples. Other

minerals such as ankerite, quartz, feldspars, and anhydrite are also present in x-ray diffraction. Porosity is also intercrystalline.

Samples can be subdivided in two groups based on their porosity: tight low porosity < 8% sample (b) and porous (15-29 %) samples (c), (d), and (e). Figure 4.5 show a SEM image of the tight low porosity sample (b). Crystallized carbonate minerals (cement) fill pore spaces present in the rich tight calcite matrix. Figure 4.6 shows a SEM image of porous sample (e) which dolomite matrix shows alternating tight and loose domains.

The pore size for samples (a), (b) and (e) are analyzed using a mercury injection porosimeter (Micromeritics Autopore IV). Figures 4.7, 4.8 and 4.9 show the incremental mercury intrusion against pore size diameter. These curves indicate a mono-modal distribution with sharp peaks at pore throat sizes of 0.43 μm, 0.23 μm and 2.52 μm respectively, which suggests that the porosity of the sample is mainly contained in a unique range of pore size. Permeability and porosity based on mercury porosimeter measurements are 0.82 mD and 2 % for sample (a), 0.03 mD and 5 % for sample (b), and 2.57 mD and 28 % for sample (e). Such low values of permeability agree with the values found for air permeability (see Table 4.1) and are expected in an unconventional reservoir where permeability is of the order of mDarcies.

4.4 Methodologies

Seismic anisotropy and its dependence on pressure are studied by using the pulse transmission method. Experimental procedure and sample preparation follows the same methodology as that of section 3.4.3; however, in this case, two mutually

orthogonal S-waves were measured on each plug. Pressure was increased from 0 to 45 MPa in the compressing cycle and from 45 to 0 MPa in the decompressing cycle. The waveforms were recorded at approximately every 5 MPa increment for sample (a) and every 3 MPa from the rest of the samples.

4.5 Results

One P-wave and two mutually perpendicular S-wave velocities were measured in all three cores from each sample (i.e. Perpendicular to bedding, parallel to bedding and 45 degrees with respect to bedding). Some examples of P- and S-waveforms obtained in the test are shown in Figure 4.10.

Since travel time also involves the signal traveling through the endcaps, it is necessary to take into account this effect when estimating velocities. In this sense, velocities were calculated using the travel time of the waveforms by picking first extremum of the recorded signal and then subtracting the travel time through the aluminum endcaps in the absence of any sample at a given pressure by picking the first extremum of the signal as well (Figure 4.11). The estimated error in measurements is a maximum of 1.5% at low pressures (< 20 MPa) and a maximum of 1.3% at high pressures (> 20 MPa) for P-waves and a maximum of 1.1% at low pressures (< 20 MPa) and a maximum of 0.9% at high pressures (> 20 MPa) for S-waves.

Figure 4.12 and 4.13 show the measured velocities as a function of confining pressure in different directions for all samples. An incremental change in velocity can be observed as pressure increased. Pressurization velocities are slightly lower than depressurization velocities; this effect is called hysteresis (Gardner, Wyllie

and Droschak 1965). When a sample is pressurized, microcracks and pores begin closing at a certain rate; however, when depressurizing, due frictional forces, the opening rate of microcracks and pores is lower than the closing rate for a given pressure.

Since microcracks are more compliant than equant pores, microcracks close at relatively low pressures and affect the overall velocities more than rounded pores (Kuster and Toksöz 1974). In particular, a high gradient velocity increase at low pressures followed by a slow velocity increase at higher pressures characterizes a velocity increase due to microcracks (He 2006). The latter is observed in samples (a), (c) and (d), suggesting that microcracks play an important role in defining velocities at low pressures (<35 MPa) unlike measured velocities in samples (b) and (e) which show a quasi-linear behaviour.

Estimated elastic constants for all samples are shown in Figure 4.14. Elastic constants show that hysteresis effects as a consequence of hysteresis present in the velocities. Table 4.2 shows the calculated elastic constants for all samples at low and at the highest pressure in the compressive cycle. C_{13} presents the highest error due the more complex form in equation 2.43. From Figure 4.14 and Table 4.2, an increase in the stiffness of the samples as a function of confining pressure can be observed as a consequence of closure of microcracks and pores.

In order quantify the degree of anisotropy (or lack of it), Thomsen parameters are also calculated for all the samples (Figure 4.15). Error bars are included as well in order to comparatively show the influence of the estimated error in C_{13}. Table

86

4.3 indicates the Thomsen parameters at low and at the highest pressure in the compressive cycle as well.

Thomsen parameter ε for sample (a) show weak P –wave anisotropy at low pressures with a value of $\varepsilon= 0.068$ +/- 0.022 at 5 MPa, but as pressure increases the material becomes less anisotropic ($\varepsilon = 0.026$ +/-0.022 at 45 MPa) as a consequence of the closure of microcracks which can also be observed in the higher hysteresis of δ at low pressures than a high pressures.

On the other hand, this sample shows a lack of anisotropy in S-wave velocities in all range of pressures, i.e.,$\gamma = 0.004$ +/- 0.015 at 5 MPa and $\gamma = -0.003$ +/- 0.016 at 45 MPa).This is also observed in elastic constants C_{11} and C_{33} where both have practically the same value in all the range of pressures as well (see Table 4.2).

In sample (b) the P-wave velocity parallel to bedding is significantly lower than those in the perpendicular and oblique directions. P-wave velocity parallel to bedding at 12 MPa is 344 m/s lower than that in the oblique and 289 m/s lower than that in vertical direction. At the peak pressure of 45 MPa these differences decrease to 229 m/s and 200 m/s respectively. When analyzing P wave anisotropy it can be observed that absolute value of ε decreases as pressure increases, in particular $\varepsilon = -0.065$ +/- 0.015 at 9 MPa and $\varepsilon = -0.043$ +/- 0.016 at 45 MPa, however the decay of the anisotropy is quasi- linear suggesting that rounded pores (which have lower compliance than microcracks) aligned in an off-axis angle with respect to the assumed plane of symmetry is causing the behaviour observed in the P-wave velocities.

In contrast, the S-wave velocities show an isotropic behaviour where the Thomsen parameter γ is practically zero in all measured pressure ranges (see Table 4.3 and Figure 4.15(b)). The negative values of ε and δ are in concordance with higher P-wave velocities in the vertical directions than in the horizontal direction (this is also reflected in elastic constants where $C_{11} > C_{33}$).

The high gradient in P- and S-wave velocities in sample (c) as pressure increases suggests that velocities are largely controlled by microcracks. For P-wave velocities parallel to bedding, for example, the increment percent from low pressures (10 MPa) to high pressures (45 MPa) is 15.27 % while for sample (b), which velocities are controlled by rounded pores, this increment is 4.96 % from 9 MPa to 45 MPa. Intrinsic heterogeneity of sample (c) has also an impact in defining P and S-wave velocities since lower values along the horizontal direction agree with higher porosity of the horizontal plug (ϕ=19%, see Table 4.1) than porosity of vertical and oblique plugs (ϕ=15%, see Table 4.1) . ε and γ experience a decrement as a function of confining pressure and tend to zero at pressures >30 MPa as a consequence of closure of microcracks, on the other hand, δ increases at low pressures and stabilizes for pressure > 15 MPa (see Figure 3.15(c)).

P- and S-wave velocities for sample (d) are also controlled by microcracks. In this case for P-wave velocities perpendicular to bedding, for example, the increment percent from low pressures (6 MPa) to high pressures (45 MPa) is 15.19 % while for sample (b) this increment is 2.48 % from 6 MPa to 45 MPa. Thomsen parameters ε, γ and δ experience a high gradient decrease as function of confining

pressure and converge to zero as shown in Figure 4.15(d) again due to closure of microcracks.

In sample (e), P- and S-waves in the direction oblique to bedding are significantly lower than those traveling in the directions vertical and perpendicular to bedding (see Figure 4.13). These differences, as in sample (c), can be explained due the intrinsic heterogeneity of the sample since the core-plug cut in the oblique direction is so different in terms of porosity and density from those in the vertical and perpendicular directions as is shown in Table 4.1. Additionally, the quasi-linear increment of velocities as a function of confining pressure suggests that equant pores also influence velocities which also have an impact in the Thomsen parameters as shown in Figure 4.15(e) which tend to stabilize at pressures > 15 MPa.

4.6 Conclusions

We found that microcracks played a major role in the anisotropy observed at low pressures in samples (a) and (d). Equant pores controls the anisotropy observed in sample (b), while microcracks and natural heterogeneity control anisotropy in (c). On the other hand, equant pores and natural heterogeneity as well define anisotropy in (e).

Thomsen parameters ε and γ suggest weak anisotropy for all samples. However, large values of Thomsen parameter δ up to 0.40 for sample (a) for example, can be consequence of intrinsic heterogeneity of samples and the error introduced by

the estimation of δ resulting from the determination of C_{13} and the δ parameter itself from equation 4.3 (see Figure 4.15).

Analysis of velocities shows a dependence on pressure of travel times for both P- and S-waves, where this behaviour is more evident in carbonates than in the evaporite. Hysteresis effects are observed in all samples during pressurization and depressurization.

For a truly VTI medium it holds that $V_P(0^o) < V_P(45^o) < V_P(90^o)$, $V_{Sa}(0^o) = V_{Sb}(0^o) = V_{SV}(90^o) < V_{SH}(90^o)$, however, the variability in velocities for samples (a), (b) and (d) suggests that microcracks and pores may be aligned along angles that deviate of the horizontal direction. In the case of samples (c) and (e), differences in velocities can be explained by the fact that there is a possibility that coring samples dissimilar heterogeneities of the main material, in this sense, heterogeneity issues are a disadvantage of the three-core method when estimating elastic constants and hence anisotropy parameters. In order to overcome this disadvantage, methods that use a single sample to estimate elastic constants can be used (Wang 2002b; Wong et al. 2008).

Since these rocks are at the best weakly anisotropic, inherent rock properties contribute little to field observations of anisotropy at the seismic scale. The latter agrees with Verdon and Kendall (2011) where they determine from microseismic data that observed anisotropy at Weyburn is the consequence of the presence of multifracture sets rather than inherent anisotropy.

Tables

Sample	Formation	Sample Location: Depth (m)	Plug Length (cm)	Dry Mass (g)	Bulk Density (g/cm^3)	Grain Density (g/cm^3)	Porosity (%)	Air Permeability (mD)
(a)	Top Midale Evaporite	1433.47	*(V)*: 2.01	27.0	2.71	2.80	3	< 2
			(H): 2.42	32.1	2.80	2.88	3	< 2
			(O): 2.54	33.4	2.79	2.89	3	< 2
(b)	Marly	1443.15	*(V)*: 3.20	38.0	2.51	2.66	6	< 2
			(H): 2.38	28.8	2.56	2.68	5	< 2
			(O): 2.89	34.8	2.55	2.67	5	< 2
(c)	Marly	1440.33	*(V)*: 2.25	24.3	2.28	2.67	15	< 2
			(H): 3.13	33.6	2.27	2.79	19	< 2
			(O): 2.47	26.7	2.29	2.68	15	< 2
(d)	Marly	1440.94	*(V)*: 3.70	39.9	2.28	2.75	17	< 2
			(H): 3.65	39.5	2.29	2.76	17	< 2
			(O): 3.54	38.4	2.29	2.73	16	< 2
(e)	Marly	1443.84	*(V)*: 3.10	32.1	2.19	2.74	20	< 2
			(H): 3.39	36.4	2.27	2.74	17	< 2
			(O): 2.13	19.1	1.90	2.67	29	< 2

Table 4.1 Physical properties of samples. Three plugs were cut in the directions vertical (V), horizontal (H) and oblique (O) with respect to bedding.

Sample	Pressure (MPa)	C_{11} (GPa)	C_{33} (GPa)	C_{44} (GPa)	C_{66} (GPa)	C_{13} (GPa)
(a)	5	56.18 +/-1.52	49.48 +/-1.53	26.50 +/-0.62	26.71 +/-0.52	12.46 +/-13.02*
	45	60.14 +/-1.68	57.19+/- 1.88	28.61 +/-0.69	28.41 +/- 0.57	11.21 +/-14.43
(b)	12	44.55 +/- 1.16	50.90 +/-1.04	20.45 +/-0.28	20.22 +/- 0.37	2.44 +/-12.88
	45	48.77 +/-1.32	53.32 +/- 1.12	21.29 +/- 0.30	21.09 +/- 0.39	3.50 +/-13.45
(c)	10	21.48 +/-0.32	22.68 +/-0.52	11.65 +/-0.19	10.02 +/-0.11	2.01 +/-6.01
	45	28.54 +/-0.48	28.51 +/-0.67	13.50 +/-0.23	13.06 +/-0.16	4.56 +/- 7.16
(d)	12	31.51 +/- 0.47	28.34 +/- 0.40	12.81 +/- 0.13	12.85 +/- 0.13	5.24 +/-7.17
	45	32.91 +/-0.50	33.54 +/-0.50	14.47 +/-0.15	14.43 +/-0.15	4.87 +/-8.40
(e)	12	30.24 +/-0.50	29.43 +/- 0.53	10.54 +/- 0.12	11.66 +/- 0.13	10.19 +/-9.59
	45	32.21 +/- 0.55	30.83 +/-0.56	11.58 +/-0.14	12.80 +/-0.15	10.86 +/- 9.30

Table 4.2 Elastic constants for all samples at low and peak pressure. *Elastic constant estimated at 9 MPa.*

Sample	ε	γ	δ
(a)	0.068 +/-0.022 **(5 MPa)**	0.004 +/- 0.015 **(5 MPa)**	0.401 +/- 0.102 **(5 MPa)**
	0.026 +/-0.022 **(45 MPa)**	-0.003 +/- 0.016 **(45 MPa)**	0.232 +/- 0.059 **(45 MPa)**
(b)	-0.065 +/-0.015 **(9 MPa)**	0.000 +/- 0.012 **(3 MPa)**	-0.195 +/ -0.049 **(12 MPa)**
	-0.043 +/-0.016 **(45 MPa)**	-0.005 +/- 0.012 **(45 MPa)**	-0.208 +/ -0.052 **(45 MPa)**
(c)	-0.072 +/- 0.013 **(5 MPa)**	-0.085 +/- 0.009 **(5 MPa)**	0.066 +/- 0.017 **(10 MPa)**
	0.001+/- 0.015 **(45 MPa)**	-0.016 +/- 0.011 **(45 MPa)**	0.119 +/- 0.030 **(45 MPa)**
(d)	0.056 +/- 0.011 **(12 MPa)**	0.018 +/- 0.007 **(12 MPa)**	0.097 +/- 0.025 **(12 MPa)**
	-0.009 +/- 0.011 **(45 MPa)**	-0.002 +/- 0.008 **(45 MPa)**	0.008 +/- 0.002 **(45 MPa)**
(e)	0.014 +/- 0.012 **(12 MPa)**	0.053 +/- 0.009 **(12 MPa)**	0.066 +/-0.021 **(12 MPa)**
	0.022 +/- 0.013 **(45 MPa)**	0.053 +/- 0.009 **(45 MPa)**	0.112 +/-0.021 **(45 MPa)**

Table 4.3 Thomsen parameters for all samples at low and peak pressure.

Figures
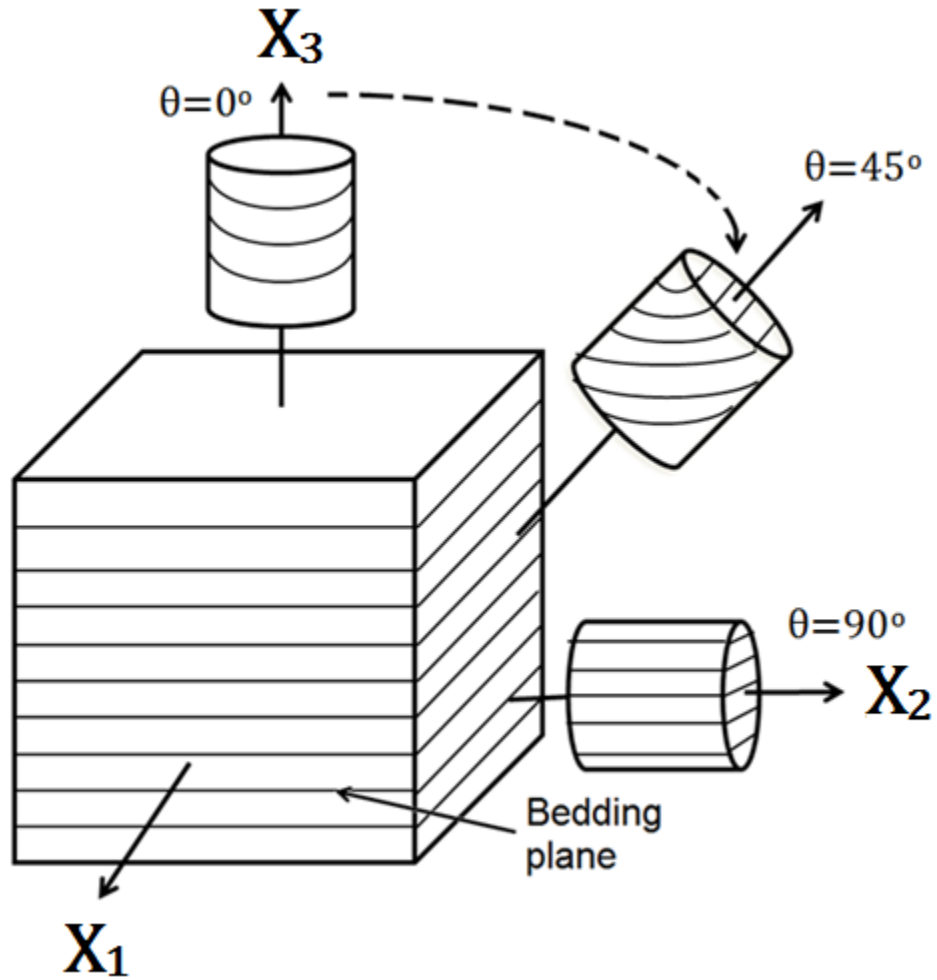
Figure 4.1 Schematic of the three plug cores needed to estimate the elastic constants that define a VTI symmetry.
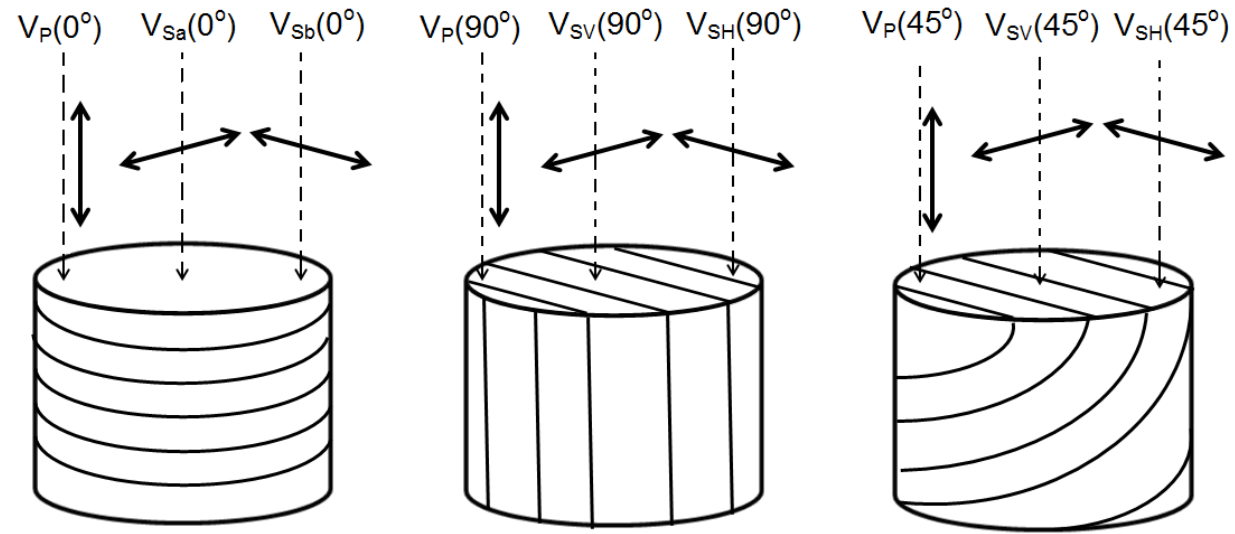
Figure 4.2 In the multi-core method three core-plugs are cut in three directions as indicated in Figure 1 and the velocities of the P- and S-waveforms measured independently in each core-plug: vertical, $V_P(0^o)$, $V_{Sa}(0^o)$ and $V_{Sb}(0^o)$; horizontal, $V_P(90^o)$, $V_{SV}(90^o)$ and $V_{SH}(90^o)$; and at 45° with respect to the sample's axis of symmetry, $V_P(45^o)$, $V_{SV}(45^o)$, and, $V_{SH}(45^o)$. Dashed lines represent the direction of propagation and solid lines represent particle polarization.
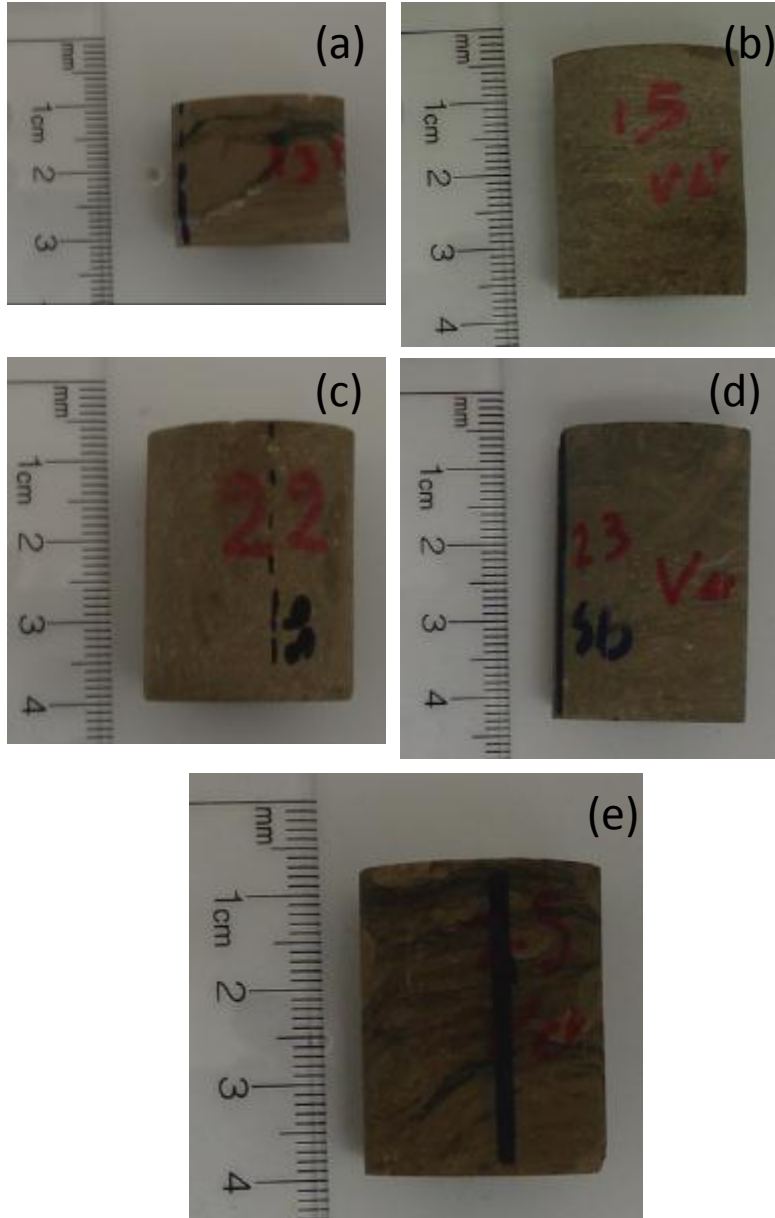
Figure 4.3 Pictures of the evaporite, (a) and carbonates (b), (c) and (d) (vertical cuts are shown) used in the measurements. Sample (a) is mainly composed of dolomite and anhydrite crystals and calcite. Dolomite and calcite is the main mineral present in sample (b), and dolomite in samples (c) and (d). Calcite, quartz and feldspar are present in (e).

96
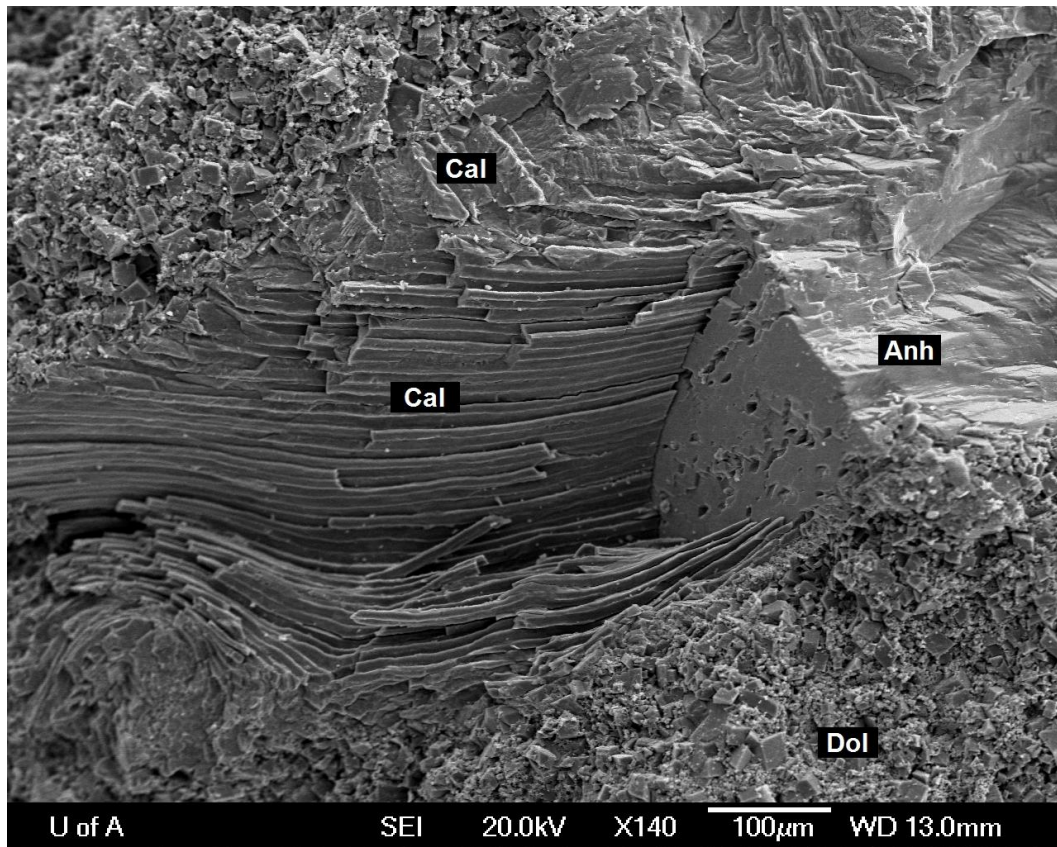
Figure 4.4 SEM image for sample (a). Microcracks that cut across the rich dolomite (Dol) matrix rock are filled with anhydrite (Anh) crystals and calcite (Cal).
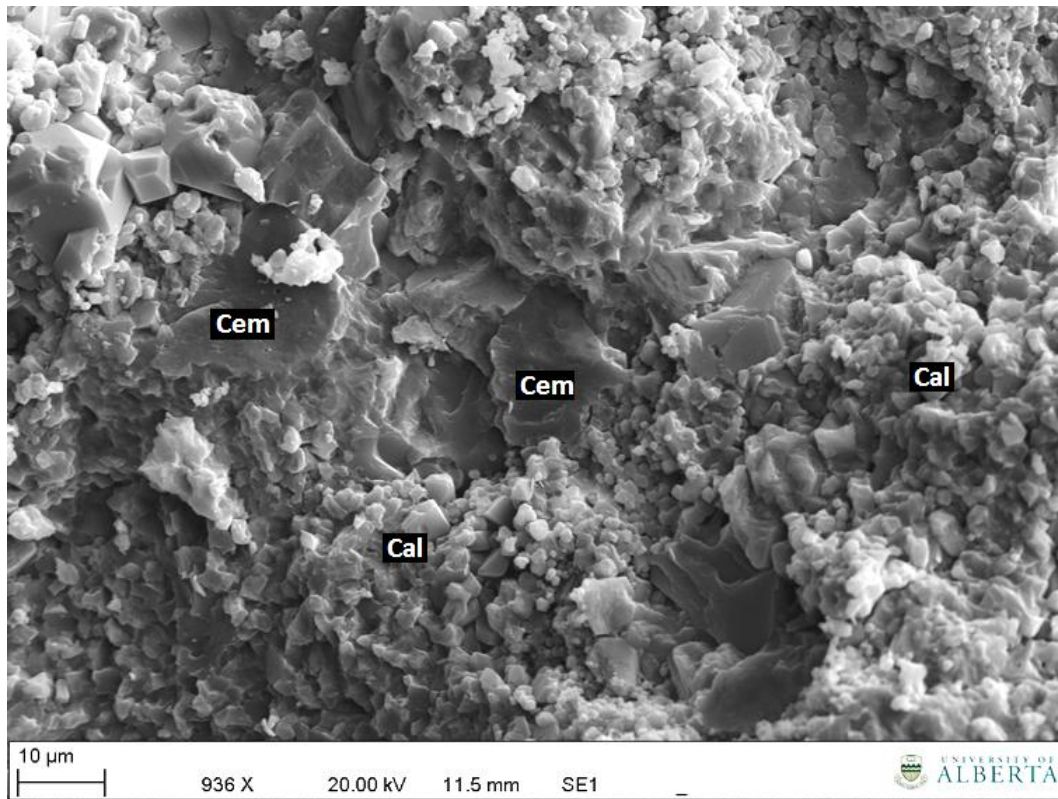
Figure 4.5 SEM, for sample (b). Note the presence of cement (Cem) that fill the pore space in the rich calcite (Cal) matrix which likely contributes to decrease the porosity.
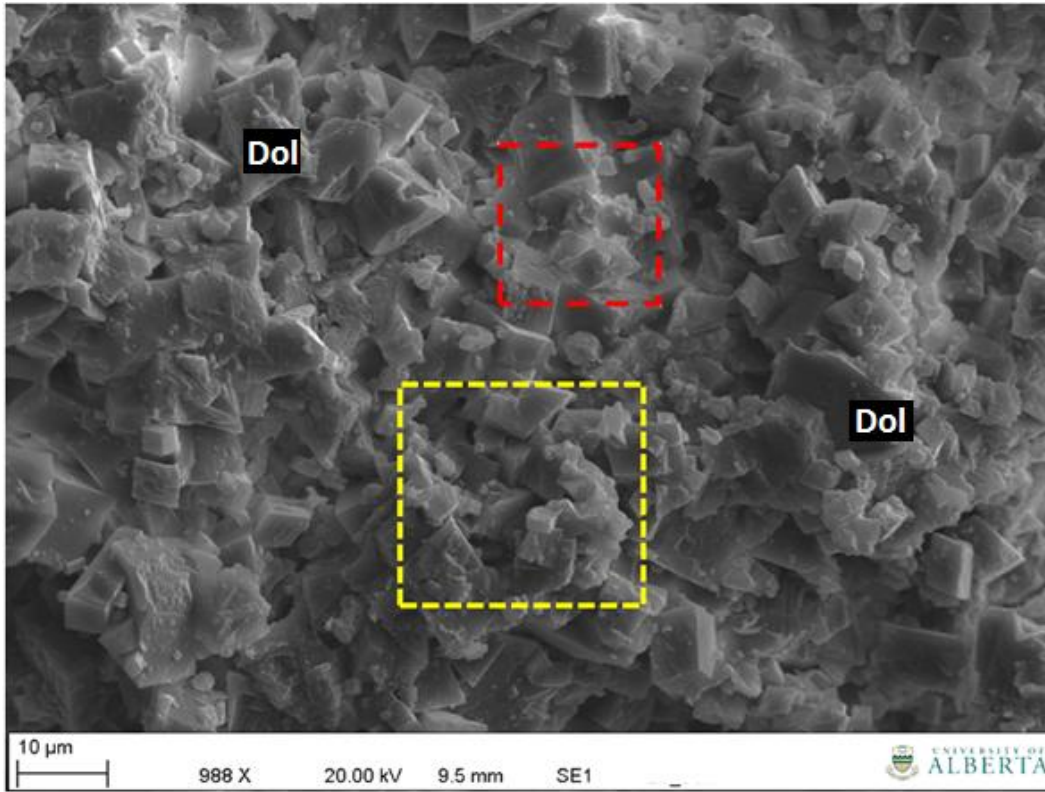
Figure 4.6 SEM image for sample (e).Note that dolomite matrix shows alternating tight (red box) and loose domains (yellow box).
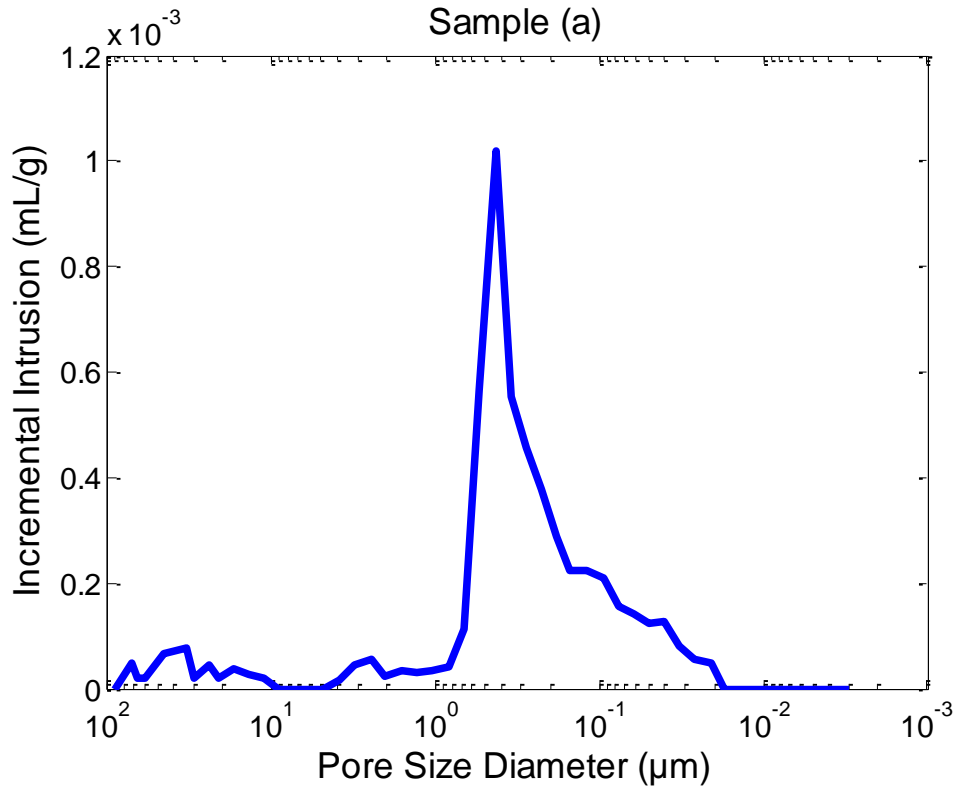
Figure 4.7 Incremental mercury intrusion against pore size diameter for sample (a).
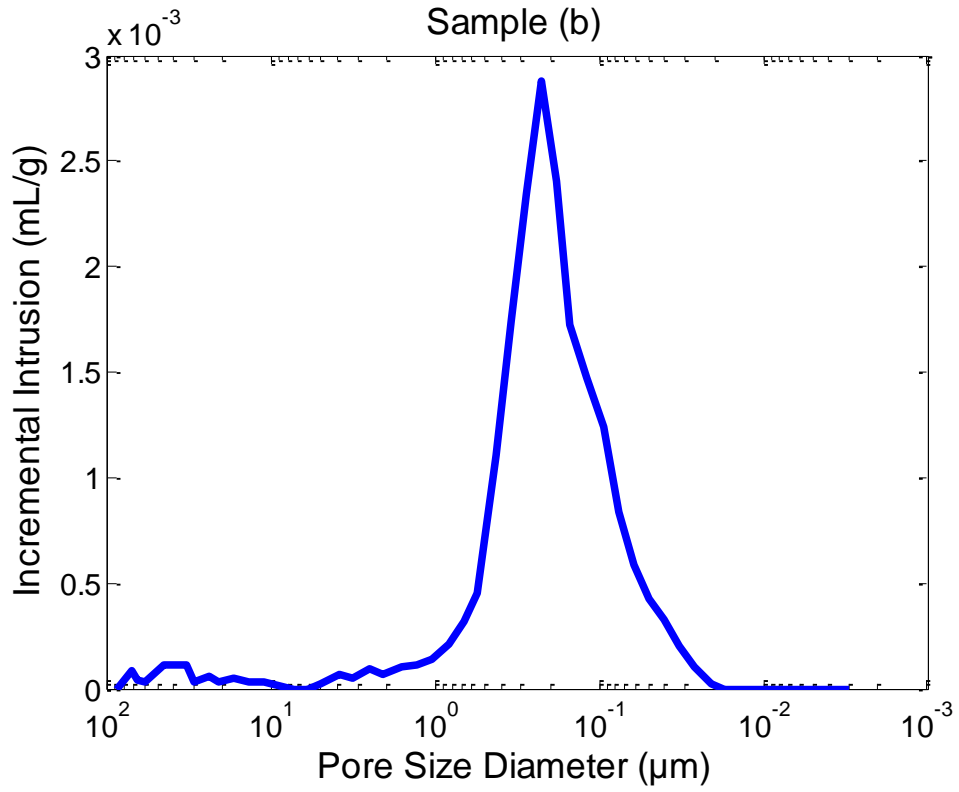
Figure 4.8 Incremental mercury intrusion against pore size diameter for sample (b).
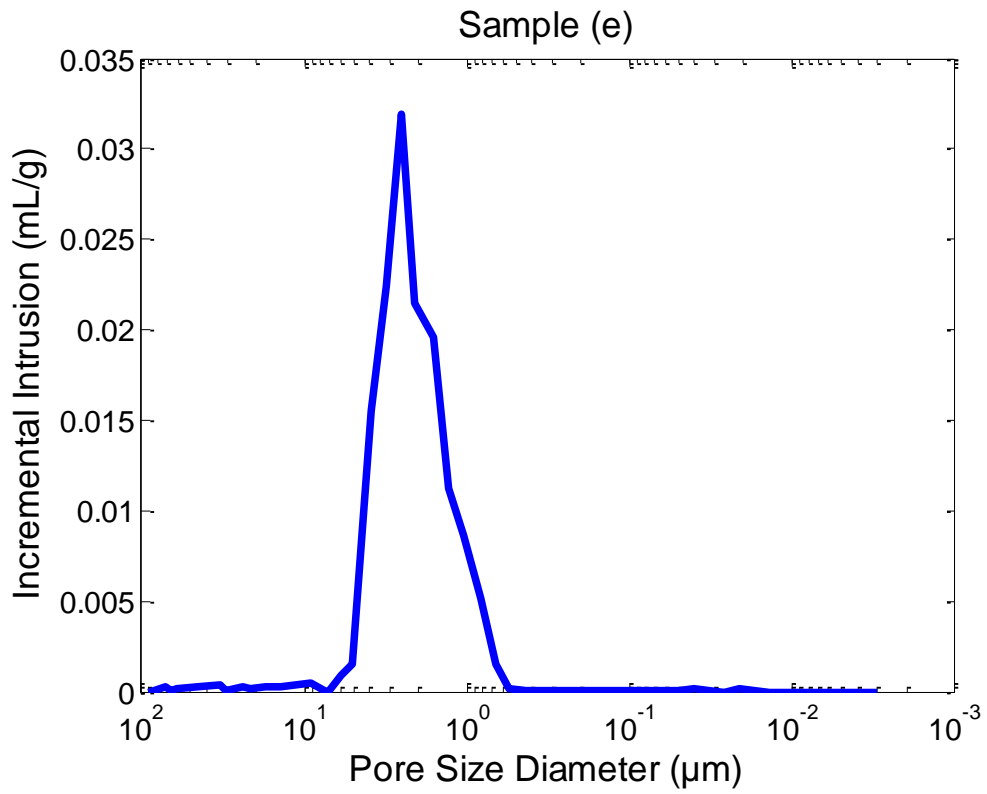
Figure 4.9 Incremental mercury intrusion against pore size diameter for sample (e).
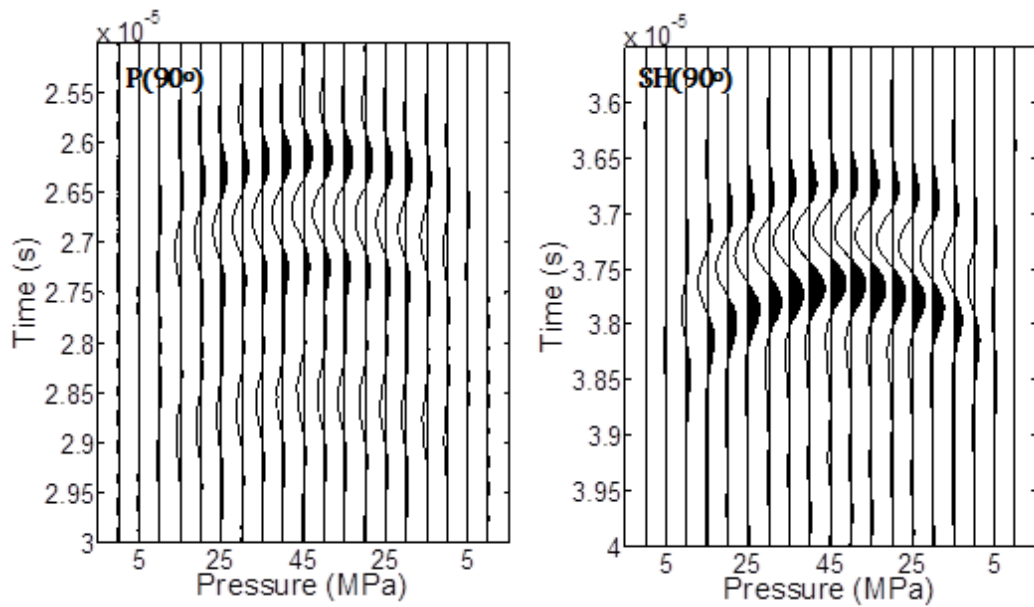
Figure 4.10 Set of measurements for sample (c) along bedding. Waveforms show a dependence of velocity as pressure increases.
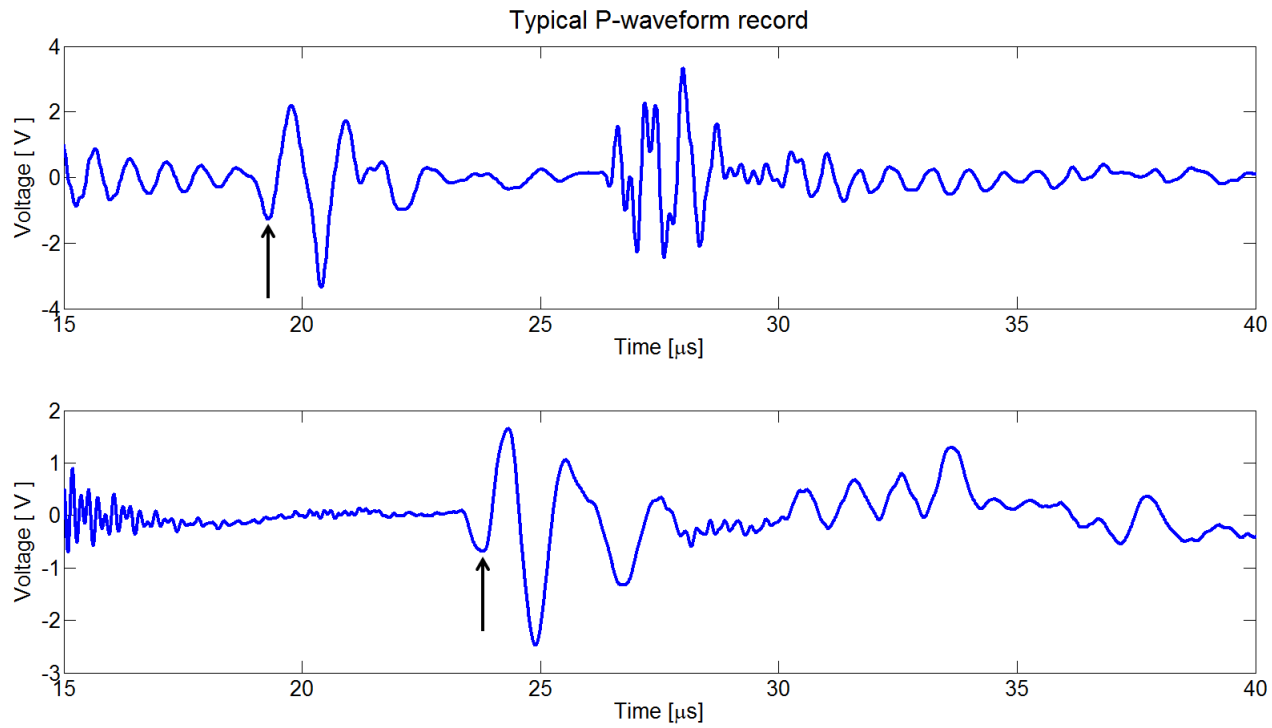
Figure 4.11 Top: signal travelling through the endcaps, Bottom: signal travelling through endcaps and sample. Travel time for both signals is picked from the first extremum pointed out with an arrow.

Estimated P velocities for sample (a)

Estimated S velocities for sample (a)

Estimated P velocities for sample (b)

Estimated S velocities for sample (b)

Estimated P velocities for sample (c)

Estimated S velocities for sample (c)
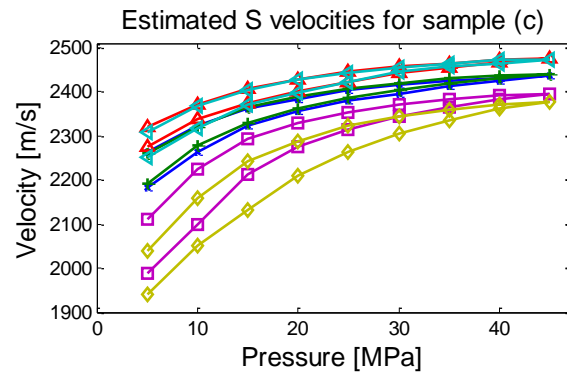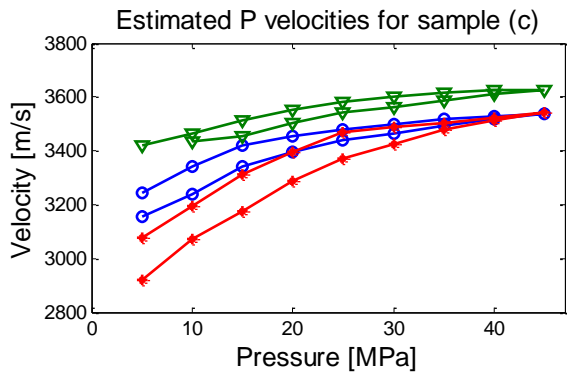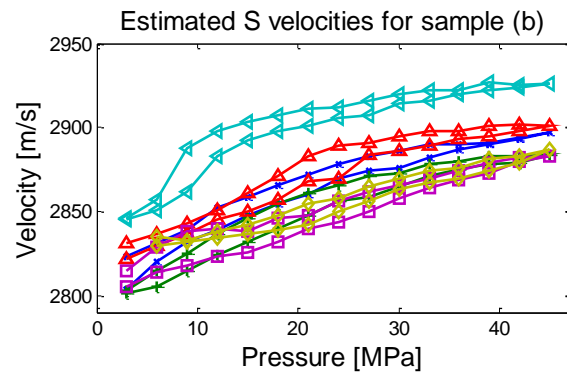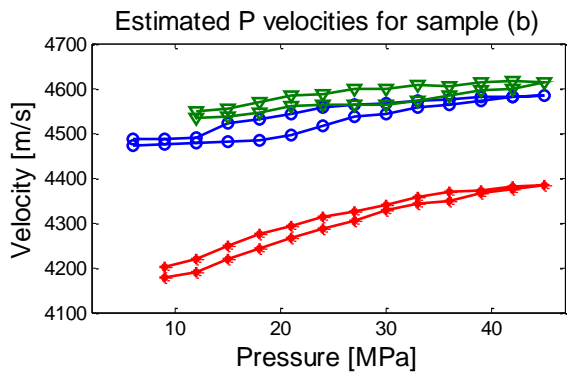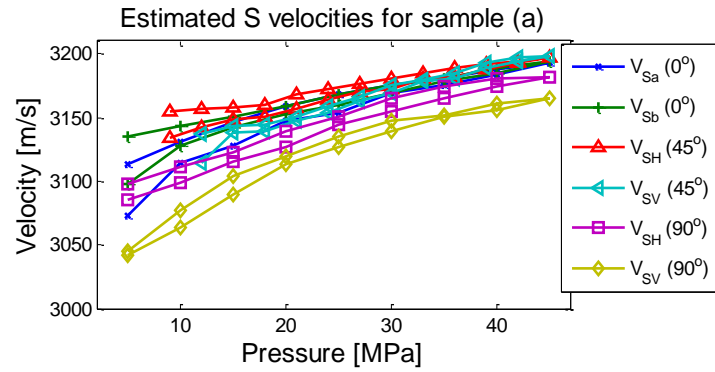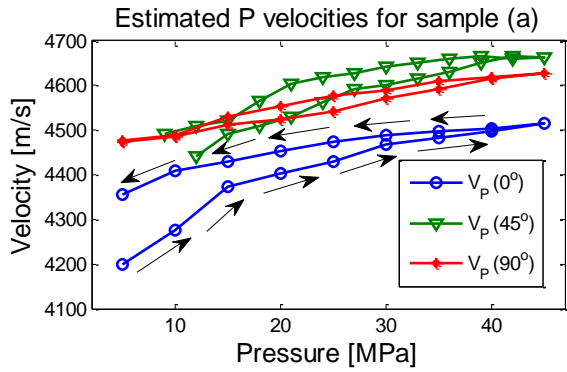
Figure 4.12 Estimated P- and S-wave velocities for samples (a), (b) and (c). Arrows show the evolution of measurements and follow the sample trend for all samples. Effect of hysteresis can be observed in the pressurization (up) and depressurization (down) cycles.
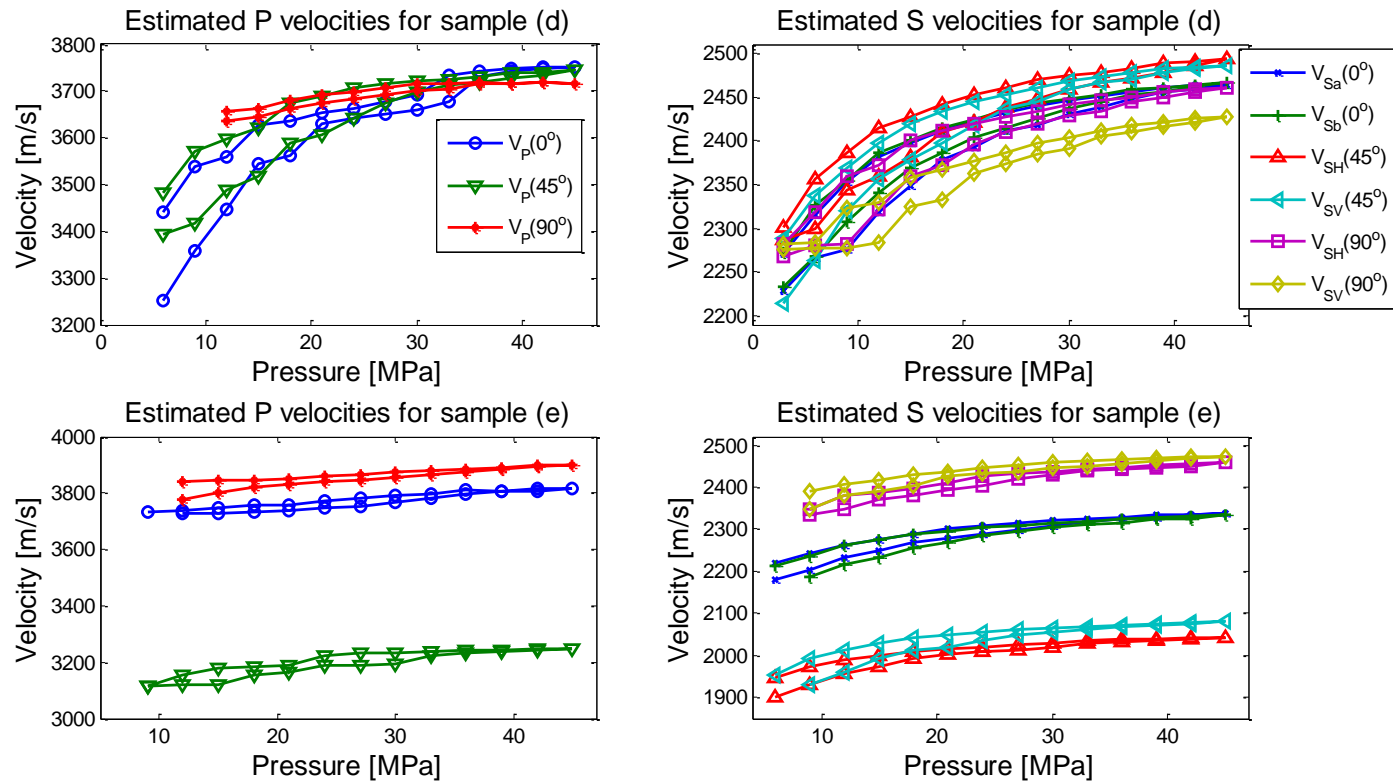
Figure 4.13 Estimated P- and S-wave velocities for samples (d) and (e). Effect of hysteresis for these samples also can be observed in the pressurization (up) and depressurization (down) cycles as well.
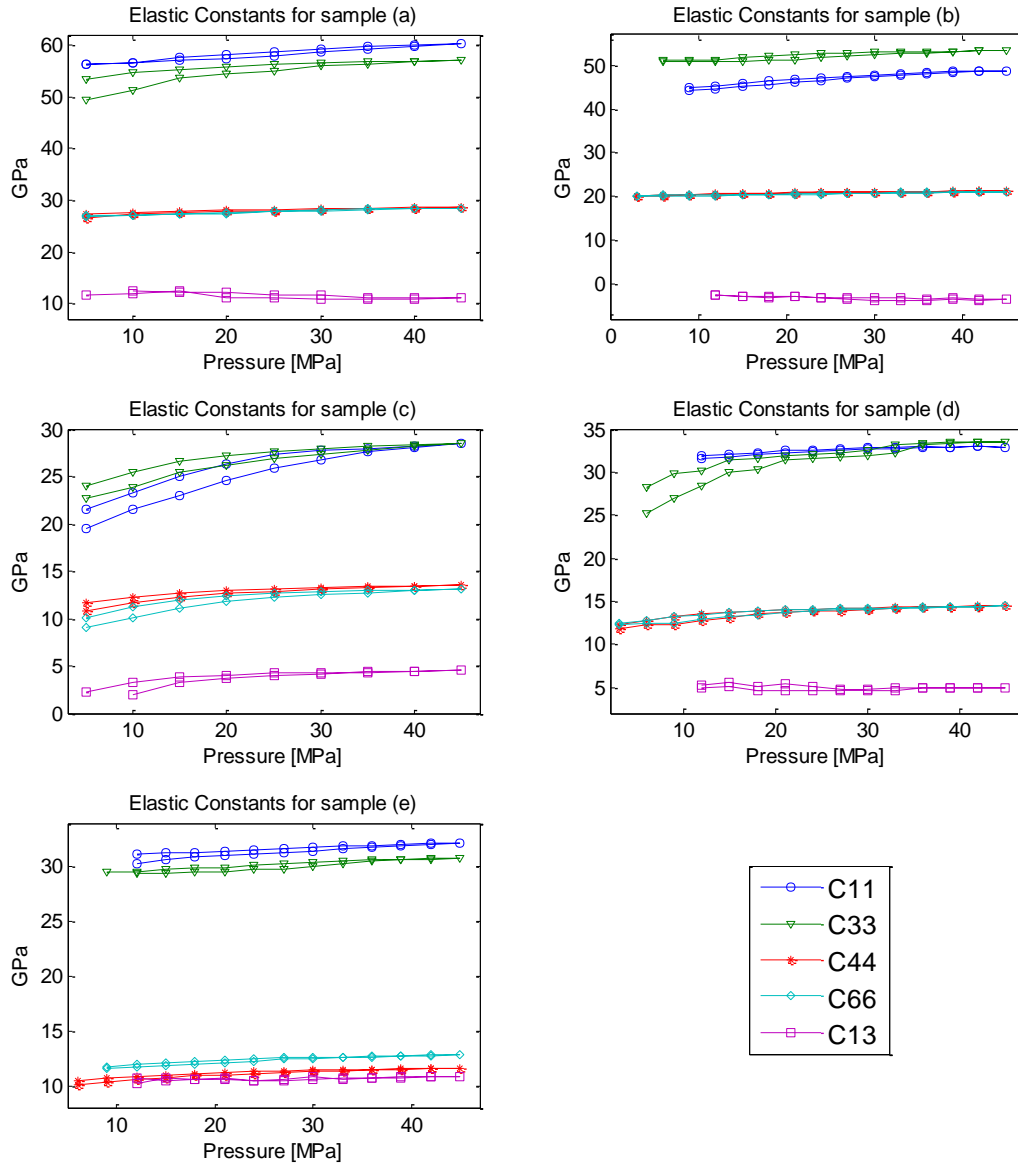
Figure 4.14 Estimated elastic constants as a function of confining pressure for all the samples. Elastic constants show hysteresis as a consequence of hysteresis in the velocities. Samples also become stiffer as confining pressure increases.
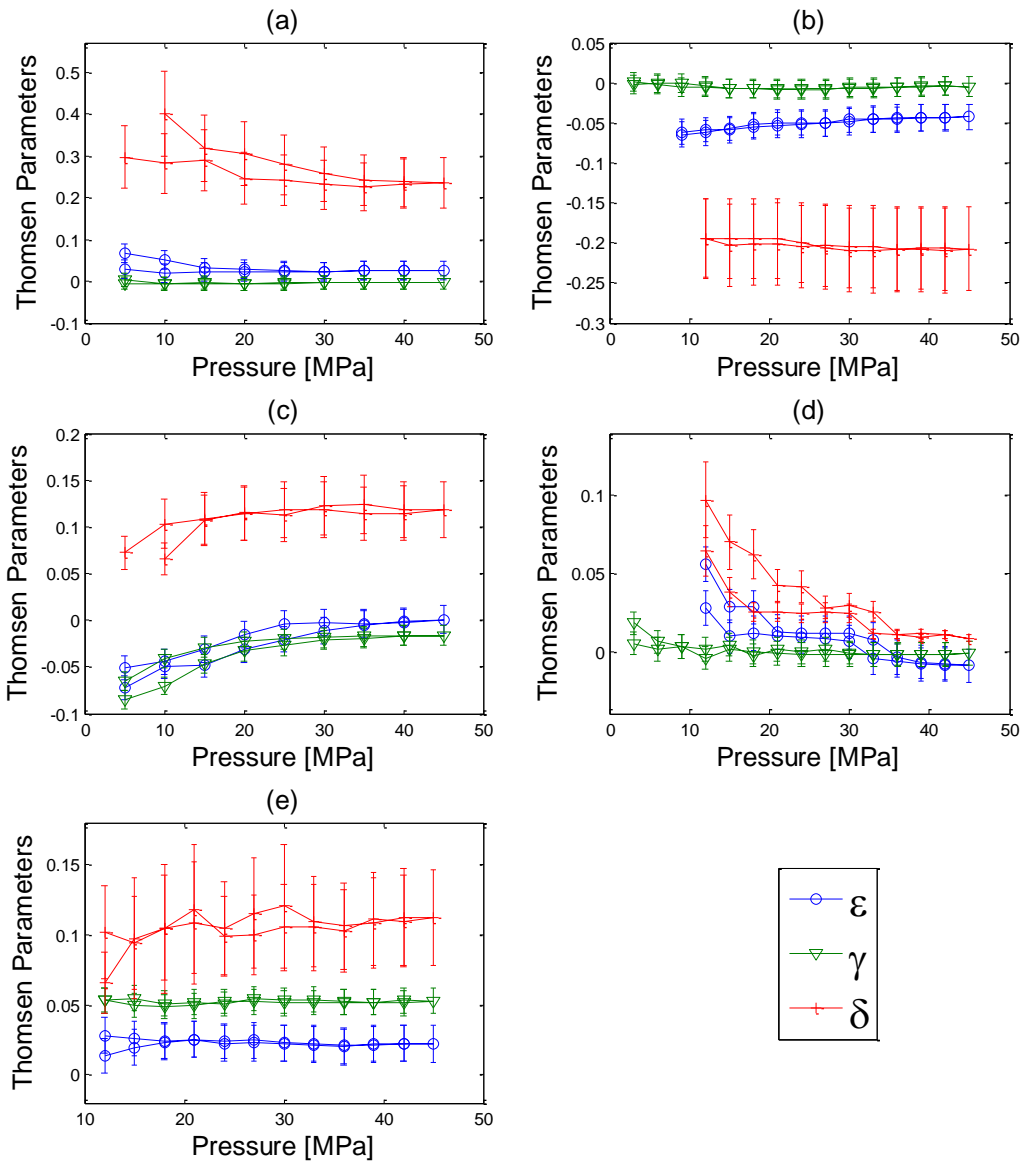
Figure 4.15 Thomsen parameters as function of confining pressure for all the samples along with the estimated error.

Bibliography

Adam, L., Batzle, M. & Brevik, L. 2006. Gassmann's fluid substitution and shear modulus variability in carbonates at laboratory seismic and ultrasonic frequencies, *Geophysics,* 71, F173-F183.

Baechle, G.T., Weger, R.J., Eberli, G.P., Massaferro, J.L. and Sun, Y.-F. 2005. Changes of shear moduli in carbonate rocks: Implications for Gassmann applicability, *Leading Edge,* 24, 507-510.

Bakhorji, A.M. 2010. Laboratory measurements of static and dynamic elastic properties in carbonate, *PhD Thesis*, University fo Alberta, Edmonton, Alberta, Canada.

Bellefleur, G., Adam, L., White, D., Mattocks, B. and Davis, T. 2003. Seismic imaging and anisotropy analysis of 9C 3D-VSP data at Weyburn Field, Saskatchewan, Canada, *SEG Technical Program Expanded Abstracts,* 22, 1326-1329.

Best, A.I., Sothcott, J. and McCann, C. 2007. A laboratory study of seismic velocity and attenuation anisotropy in near-surface sedimentary rocks, *Geophysical Prospecting,* 55, 609-625.

Brown, L.T. 2002. Integration of Rock Physics and Reservoir Simulation for the Interpretation of Time-lapse Seismic Data at Weyburn Field, Saskatchewan, *MSc Thesis*, Colorado School of Mines, Golden, Colorado, USA.

Bunge, R.J. 2000. Midale Reservoir Fracture Characterization Using Integrated Well and Seismic Data, Weyburn Field, Saskatchewan, *MSc Thesis*, Colorado School of Mines, Golden, Colorado, USA.

Cheadle, S.P., Brown, R.J. and Lawton, D.C. 1991. Orthorhombic anisotropy - a physical seismic modeling study, *Geophysics*, 56, 1603-1613.

Daley, P.F. and Hron, F. 1977. Reflection and transmission coefficients for transversely isotropic media, *Bulletin of the Seismological Society of America*, 67, 661-675.

Dey-Barsukov, S., Durrast, H., Rabbel, W., Siegesmund, S. and Wende, S. 2000. Aligned fractures in carbonate rocks: laboratory and in situ measurements of seismic anisotropy, *International Journal of Earth Sciences,* 88, 829-839.

Gardner, G.H.F., Wyllie, M.R.J. and Droschak, D.M. 1965. Hysteresis in the velocity-pressure characteristics of rocks, *Geophysics*, 30, 111-116.

He, T. 2006. P- and S-wave velocity measurement and pressure sensitivity analysis of AVA response, *MSc Thesis*, University fo Alberta, Edmonton, Alberta, Canada.

Hemsing, D.B. 2007. Laboratory determination of seismic anisotropy in sedimentary rock from the Western Canadian Sedimentary Basin, *MSc Thesis*, University fo Alberta, Edmonton, Alberta, Canada.

Hornby, B.E. 1998. Experimental laboratory determination of the dynamic elastic properties of wet, drained shales, *Journal of Geophysical Research-Solid Earth*, 103, 29945-29964.

Johnston, J.E. and Christensen, N.I. 1994. Elastic constants and velocity surfaces of indurated anisotropic shales, *Surveys in Geophysics*, 15, 481-494.

Kebaili, A. and Schmitt, D.R. 1997. Ultrasonic anisotropic phase velocity determination with the Radon transformation, *Journal of the Acoustical Society of America,* 101, 3278-3286.

Kuster, G.T. and Toksoz, M.N. 1974. Velocity and attenuation of seismic-waves in 2-phase medi: Part 1. Theoretical formulations, *Geophysics*, 39, 587-606.

Mah, M. and Schmitt, D.R. 2001. Experimental determination of the elastic coefficients of an orthorhombic material, *Geophysics*, 66, 1217-1225.

Meléndez, J. and Schmitt, D.R. 2011. Investigating anisotropy in rocks by using pulse transmission method, *Canadian Society of Exploration Geophysicists Recorder,* 36-10, 38-42.

Moberg, R., Stewert, D.B. and Stachniak, D. 2003. The IEA Weyburn CO_2 monitoring and storage project, *6th International Conference on Greenhouse Gas Control Technologies*, Kyoto, Japan, 219-224.

Rafavich, F., Kendall, C.H.S. and Todd, T.P. 1984. The relationship between acoustic properties and the ptrographic character of carbonate rocks, *Geophysics,* 49, 1622-1636.

Reinicke, A., Rybacki, E., Stanchits, S., Huenges, E. and Dresen, G. 2010. Hydraulic fracturing stimulation techniques and formation damage mechanisms-Implications from laboratory testing of tight sandstone-proppant systems, *Chemie Der Erde-Geochemistry,* 70, 107-117.

Schijns, H., Schmitt, D.R., Heikkinen, P.J. and Kukkonen, I.T. 2012. Seismic anisotropy in the crystalline upper crust: observations and modelling from the Outokumpu scientific borehole, Finland, *Geophysical Journal International,* 189, 541-553.

Schmitt, D.R. and Li, Y.Y. 1995. A high-pressure technique for determining the microcrack porosities of damaged brittle materials, *Canadian Journal of Physics*, 73, 330-337.

Scotellaro, C., Vanorio, T. and Mavko, G. 2007. The effect of mineral composition and pressure on carbonate rocks, *SEG Technical Program Expanded Abstracts,* 26, 1684-1689, San Antonio.

Thomsen, L. 1986. Weak elastic anisotropy, *Geophysics*, 51, 1954-1966.

Verdon, J.P. and Kendall, J.M. 2011. Detection of multiple fracture sets using observations of shear-wave splitting in microseismic data, *Geophysical Prospecting,* 59, 593-608.

Vernik, L. and Liu, X.Z. 1997. Velocity anisotropy in shales: A petrophysical study, *Geophysics*, 62, 521-532.

Verwer, K., Braaksma, H. and Kenter, J.A.M. 2008. Acoustic properties of carbonates: Effects of rock texture and implications for fluid substitution, *Geophysics,* 73, B51-B65.

Wang, Z.J. 2002. Seismic anisotropy in sedimentary rocks, part 1: A single-plug laboratory method, *Geophysics*, 67, 1415-1422.

Wang, Z.J. 2002. Seismic anisotropy in sedimentary rocks, part 2: Laboratory data, *Geophysics,* 67, 1423-1440.

Wong, R.C.K., Schmitt, D.R., Collis, D. and Gautam, R. 2008. Inherent transversely isotropic elastic parameters of over-consolidated shale measured by ultrasonic waves and their comparison with static and acoustic in situ log measurements, *Journal of Geophysics and Engineering*, 5, 103-117.

Zimmermann, G. and Reinicke, A. 2010. Hydraulic stimulation of a deep sandstone reservoir to develop an Enhanced Geothermal System: Laboratory and field experiments, *Geothermics,* 39, 70-77.

CHAPTER 5

Mudstones

5.1 Introduction

Mudstones, the most abundant sedimentary rocks (Jones and Wang 1981; Potter, Maynard and Depetris 2005), have become increasily important to study since they are present in many productive sectors such as oil and gas industry, waste disposal, ceramic industry and mining (Potter *et al*. 2005). In oil and gas reservoir for example, mudstones are a source rock, serves as a seal and drive the migration of hydrocarbons (Potter *et al*. 2005).

Clay and silt minerals with grain sizes < 62.5 μm are the main constituents of mud. After physical and chemical processes that occur during burial, mud grades into mudstone. The name shale refers to mudstone that presents fissility. Fissility is the tendency to break along parallel planes that are formed due to preferred alignment of clay minerals during deposition and subsequent burial (Aplin and Macquaker 2011). This plane is called bedding plane. Figure 5.1 shows an example of the bedding present on a shale sample. Other components of shales are carbonate minerals, feldspars and organic material as well as sulfides such as pyrite (Potter, Maynard and Depetris 2005).

Chemical and physical weathering of rocks are the main origins of detrital clay and silt minerals (Garrels and MacKenzi 1971; Potter *et al.* 2005), being chemical weathering the main factor involved in the formation of clays minerals (< 2 μm

in size) (Aplin and Macquaker 2011), while physical processes such as abrasion and fracture of rich quartz rocks during transportation are the main generators of silt minerals (2 - 62.5 μm in size) (Aplin and Macquaker 2011). Ash from volcanoes and glacial rock flour also contribute, although to a lesser extent, to the formation of such minerals (Potter, Maynard and Pryor 1980).

The main transport media are rivers and to a lesser extent wind and glaciers (Gorsline 1984; Potter *et al.* 2005). The depositional environment mainly includes sedimentary basins such as shallow seas, lagoons, deltas and bays (Potter *et al.* 2005).

Sedimentation occurs when the flow rate decreases below the point necessary to maintain the suspended material. However, flocculation is also an important mechanism for sediment deposition[2]. During flocculation, electrically charged clay minerals stick together forming a flake-like structure called a floc.

During sedimentation, organic material and mineralized remnants of microorganisms present in the water column above the sediments and in the interface water-sediments are added to the mixture of clay and silt minerals. This organic material (and its preservation) is vital in the subsequent generation of hydrocarbons.

The apparent homogeneity of shales suggests that mud sediments were deposited in 'low energy' depositional environment (Garrels and MacKenzi 1971; Potter *et al.* 1980; Chamley 1989; Arthur and Sageman 1994; Aplin, Fleet and Macquaker

---

[2] Nicholas B. Harris, personal comunication.

1999; Harris 2005; Potter *et al.* 2005); however, high magnification analysis on such rock show heterogeneity in their mineralogical content and texture, which suggests that mud is also frequently dispersed by a combination of forces among which are waves, tidal and storms (Aplin and Macquaker 2011).

Because physical properties of shales such as porosity, permeability, and seismic anisotropy are influenced by their mineral and organic material content, it is important to know the physical and chemical processes that drive the formation of shales.

The main purpose of this chapter is to review the provenance, the compositions, and the structures of 'shales' in support of the next chapter. In this chapter, a description of the origin and the mineral composition of shales is first given followed by the role of the oxygen in defining texture and economic importance of shales as well as the factors that involve the preservation of organic material as a source of hydrocarbons. Physical and chemical processes that occur during burial are also presented. The latter processes have a key role in the production of kerogen, which during maturation leads to the production of oil and gas. The texture of shales and its contribution to seismic anisotropy is also discussed.

5.2 Clay and silt minerals

Submarine and soil weathering of both felsic and mafic rocks such as granite and basalt as well as volcanic ejecta are the sources of clay minerals (e.g. kaolinite, illite, smectite) while most usually felsic rocks such as granite and gneiss are the source of the primary silt minerals (e.g. quartz, feldspar). Some of the primary

minerals comprising those rocks that produce clay minerals due to weathering are K-feldespar, muscovite (mica) and volcanic glass.

The general processes that involves the production of clay minerals in soils is described by Potter *et al.* (2005) as follows:

H^+ + primary mineral → intermediate clay mineral + solution → gibbsite + solutions
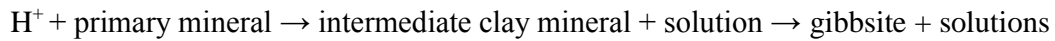
Using this equation, the production of clay minerals from K-feldespar, muscovite and volcanic glass can be expressed as (Potter *et al.* 2005):

$$H^+ + \text{K-feldspar} » \text{smectite} » \text{illite} » \text{kaolinite} » \text{gibbsite}$$

$$H^+ + \text{muscovite} » \text{smectite} » \text{illite} » \text{kaolinite} » \text{gibbsite}$$

$$H^+ + \text{glass} » \text{allophones} » \text{smectite} » \text{hallosyte} » \text{kaolinite} » \text{gibbsite.}$$
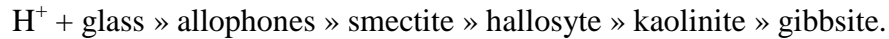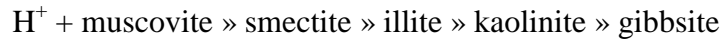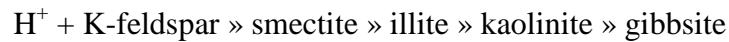
where H^+ is released through a chemical reaction between CO_2 and H_2O :

$$CO_2 + H_2O » H^+ + HCO_3^-$$
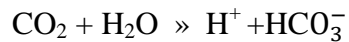
In soils, water is provided by rainfall, rivers, melting glaciers, etc., while dissolved CO_2 in water is supplied by bacterial respiration.

The predominat mineral in silt particles is quartz. These particles can have both terrigenous and biological origins. According to (Potter *et al.* 2005), production of silt can be expressed as

Silt = **abrasion** + **weathering** + **biologic production** + **metamorphism** + **recycling**

Abrasion produces fracture or chipping of rich quartz-feldspar rocks when they are transported by wind and currents of water. Weathering such as drastic changes in temperature expands and contracts the rock which eventually breaks it, allowing the release of feldspathic silt.

Biogenic silica is synthetized by algae in lakes and seas, and can represent over 5% of total silica present in soils (Clarke 2003). Meanwhile Schieber, Krinsley and Riciputi (2000) demonstrated the biologic origin of silica present in Devonian black shales by using imaging techniques such as backscatter electron and cathode luminescence as well as using a ion probe to measure oxygen isotopes. Before this discovery, it was long believed that silica was only derived from non-biogenic activity.

During burial, overgrowing of detrital quartz and production of authigenic quartz can occur as a consequence of increase of depth and temperature. According to Bjorlykke and Egeberg (1993), this happens at depths of 2000 m and temperatures that vary from 80 to 100° C, where slates and phyllites are the main rock sources of quartz (Blatt 1987).

Since clay minerals are of one the main components of mudstones are, they control many of physical and chemical properties of such rocks. Stiffness, cation exchange capacity and water absorption capacity for example, depend on their clay mineral content (Potter *et al.* 2005), so that the knowledge of the types of these minerals is fundamental in geotechnical problems such as borehole and slope stability (Durand *et al* 1995; Ghobadi 2000).

Clays form sheet-like structures and are classified depending on the number of sheets that form a basic structure (Bailey 1980; Moore and Reynolds 1997). The types of sheets that clay minerals form are tetrahedral and octahedral. The tetrahedral sheets consist of silica tetrahedron that shares three of its oxygen with other silica tetrahedra forming a hexagonal array. Octahedral sheets consist of connected octahedron units of around an aluminum, magnesium or iron ion surrounded by oxygen and hydroxide ions (Potter *et al.* 2005). Figure 5.2 shows the tetrahedron and octahedron units that form clay minerals.

Different types of clay minerals are obtained from tetrahedral and octahedral sheets that combine to form layers which are separated by interlayer space that can hold water and absorb cations. The proportion of tetrahedral sheets to octahedral sheets in a clay mineral is expressed as *a:b*, where *a* is the number of tetrahedral sheets and *b* is the number of octahedral sheets.

The main group of clay minerals present in mudstones along with their general chemical formulae and structure are as follows:

$$\text{Kaolinite} \rightarrow (Al_2, Mg_3)\, Si_2\, O_5\, (OH)_4 \rightarrow \textit{1:1}$$

$$\text{Illite (mica)} \rightarrow K(Al_3, Mg_3)\, Si_3\, O_{10}\, [OH]_2 \rightarrow \textit{2:1}$$

$$\text{Chlorite} \rightarrow (Mg_3, Fe_3, Al_2)\, (Si,Al)_4\, O_{10}\, Mg_3\, (OH)_6 \rightarrow \textit{2:1}$$

$$\text{Smectite} \rightarrow (Al_2, Mg_3)\, Si_4\, O_{10}\, [OH]_2\, n\, H_2O \rightarrow \textit{2:1}$$

$$\text{Vermiculite} \rightarrow (Al_2, Mg_3)\, Si_4\, O_{20}\, [OH]_2\, n\, H_2O \rightarrow \textit{2:1}$$
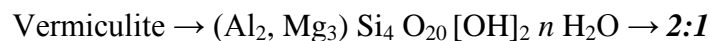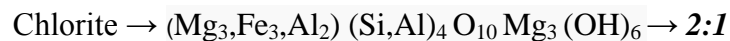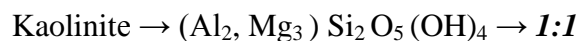
Figure 5.3 shows tetrahedral and octahedral sheets combined to form kaolinite. Depending on their capacity to increase their volume by absorbing water in the interlayer space, clay minerals can also be classified as expandable and non-expandable. Smectite and vermiculite are expandable clay minerals while kaolinite, illite and chlorite are non-expandable.

5.3 Preservation of organic material

Stratification and color of shales are indicators of their possible economic importance. Black shales for example, have rich organic content and can be source of petroleum and become important reservoirs of vanadium, uranium, zinc and copper. In recent years these rocks have to become the reservoir with hydraulic stimulation attempting to overcome their otherwise impermeable nature. Total Organic Carbon percent (TOC) in these rocks can be between 2 and 30% (Tyson 1995). However, organic-poor shales with TOC percent about 0.8 % (Tyson 1995) have several industrial uses such as material to make bricks, cements for roofing, etc (Potter *et al.* 2005).

In this sense, understanding preservation of organic material in mudstones is important since oil and gas derive from its maturation during burial. However, preservation of organic material is not common due to the high efficiency of the carbon cycle in returning the organic carbon to the biosphere and only 1% of the annual production of the organic material in the photic zone is preserved (Waples 1985).

The main factors that are involved in the preservation of organic material are the concentration of oxygen in the column of water overlying the sediments and the in the sediments themselves, as well as the rate of sedimentation that distances organic material from the water-sediments interface where they can be oxidized due the oxygen present in water (Waples 1985; Canfield 1989; Pedersen and Calvert 1990; Tyson 2001; Bohacs *et al* 2005; Potter *et al.* 2005; Aplin and Macquaker 2011) .

Oxygen levels directly controls organic content and stratification in shales. Low levels of oxygen results from high organic content since the supply of oxygen is insufficient for its demand. As a consequence, bioturbation (i.e., biodegradation of the rock due to organic activity) rate is low and lamination arises (Droser and Bottjer 1986). Figure 5.4 shows a Scanning Electron Microscopy, SEM, of a shale sample where thin laminae due to horizontal alignment of clay mineral flakes can be appreciated. In contrast, high levels of oxygen lead to high benthic life activity and the rates of bioturbation increases, resulting in a poor layered media and maroon and gray colors arise (Potter *et al.* 2005).

In this sense, from the physical point of view anoxia leads to seismic anisotropy due to lamination layering that is generated (Lo, Coyner and Toksoz 1986; Johnston and Christensen 1994; Kebaili and Schmitt 1997; Hornby 1998; Mah 2005). On the other hand, bioturbation results in a decrease in anisotropy (Yang and Aplin 1998).

Briefly, organic content increases as sediment rate increases due to a higher rate of organic content removal from the shallow layers that present high oxygen content and hence microbial activity (Muller and Suess 1979).

As mentioned earlier, rich organic content shales are also associated with the presence of metals such as vanadium, uranium, zinc and copper (Arthur and Sageman 1994; Potter *et al.* 2005; Dean 2007). The reason of this is because these metals can remain in the system of organisms as a consequence of their metabolic activity as pointed out by Aplin and Macquaker (2011), and therefore rich organic shales are important for the mining industry as well (Kamradt *et al* 2012).

5.4 Burial

Burial can occur due to either sinking of sedimentary basins or increase in the sea level, which allows sediments to gather on the upper layer of the pre-existing sediments. The additional weight and the increase of temperature leads to lithification of the muddy sediments that subsequently grade into mudstone and eventually into shale. During burial, organic material is converted into kerogen, which after a maturation process can be turn in to oil and gas (Waples 1985; Tissot and Welte 2012). Among the important mineralogical changes that are carried out are the conversion of smectite to illite , kaolinite to illite, illite to chlorite, silica to opal and glass to zeolites. Water that is ejected in the process has a significant role in the mobility of oil (Athy 1930a; Michael and Bachu 2001; Pang *et al* 2005) towards geological traps that can eventually become important reservoirs. Processes occurring during burial can be divided into physical and chemical processes, which are addressed in the following sections.

5.4.1 Physical Processes

At temperatures up to 70°C mechanical compaction is the leading process in siliciclastic sedimentary basins (Hedberg 1926; Hedberg 1936).Water expelled during burial causes porosity and permeability to decrease. In contrast, density and seismic velocity increase. These physical processes have been studied by several authors.

Athy (1930b) presented early laboratory work where empirical relationships of porosity, density and compaction as a function of burial´s depth for different sediments are obtained.

Aplin and Macquaker (2011) point out that initial porosity of muds when deposited and they remain essentially colloidal suspensions is about 80-90%; however, due to compaction large amounts of water are expelled and the porosity of the formation quickly decreases reaching 5% at 6 km of depth.

As a consequence of the increase depth with burial, the volume of the sediments decrease (compaction) and the density and the observed seismic velocities increase (Mackey and Bridge 1995). Additionally, an increase in the velocities has also been related not only with the burial´s depth but also with the geological age (Faust 1951).

Effects of effective stress on compaction of mudstones have been studied for several authors. For example, Skempton (1969) studies the effect of effective overburden stress on porosity in argillaceous mudstones finding an increase in strength with depth. Burland (1990) presents compression curves of reconstituted

clays that can be used as a basic reference to study compaction on natural clays due to burial.

It has also been pointed out (Aplin and Macquaker 2011) that the grain size of the sediments influence the rate at which they are compacted (compressibility), with fine grains less compressible than coarse grains (Burland 1990; Aplin, Yang and Hansen 1995). The latter has implications in the rate of compaction of shales during burial since mineralogy of such rocks present both fine grain mineral (e.g. smectite) and coarser grain minerals (e.g. kaolinite). In this sense, experimental works carried out by Chilingar and Knight (1960) and Mondol *et al* (2007) show that the rate of compaction of kaolinite aggregates are significantly greater than smectite aggregates.

As a result of decrease in porosity due compaction during burial, fluids are expelled from mudstones; however, overpressure arises if the rate of compaction is greater than the rate at which fluids are expelled (Smith 1971; Mann and Mackenzie 1990; Audet 1996; Osborne and Swarbrick 1997; Nordgård Bolås, Hermanrud and Teige 2004; Loseth, Wensaas and Gading 2011; Ramdhan and Goulty 2011), which have serious consequences when drilling for hydrocarbons (Obrien and Lerche 1994; Potter *et al.* 2005; Chatterjee, Mukhopadhyay and Paul 2011).

The sediment permeability is the main factor driving the rate of compressibility (Aplin and Macquaker 2011). Results from several permeability measurements on mudstones indicate that for a single porosity the permeability is affected by the

grain size and the mineralogy (Dewhurst *et al* 1998; Dewhurst, Aplin and Sarda 1999; Yang and Aplin 2007).

Since pore size is correlated to permeability (Aplin and Macquaker 2011), clay-rich mudstones form more efficient seal reservoir than silt-rich mudstones due to their smaller pore size (Dewhurst *et al.* 1998; Yang and Aplin 1998; Dewhurst *et al.* 1999).

4.4.2 Chemical processes

One of the most important chemical process during burial is the transformation of smectite into illite and chlorite (Potter *et al.* 2005) which is carried out at temperatures above 70° C as a consequence of increase in depth in the geothermal gradient (Aplin and Macquaker 2011). Illite is produced from transformation of dioctahedral smectite via a mixed layer called illite-smectite, *I/S (*Hower *et al 1976)*. Illitization requires a source of potassium (Hower *et al.* 1976; Berger, Velde and Aigouy 1999) which can come from detrital potassium feldspar and potassium ion solution. Chemical reactions from these sources can be described as (Potter *et al.* 2005):

$$Al_2 Si_4 O_{10} [OH]_2 \, n \, H_2O \text{ (smectite)} + KAlSi_3O_8 \text{ (K-feldspar)} =$$
$$KAl_3 Si_3 O_{10} [OH]_2 \text{ (illite)} + 4SiO_2 \text{ (quartz)} + n \, H_2O$$

and

$$2K^+ + 3Al_2 Si_4 O_{10} [OH]_2 \, n \, H_2O \text{ (smectite)} =$$
$$2KAl_3 Si_3 O_{10} [OH]_2 \text{ (illite)} + 6SiO_2 \text{ (quartz)} + 2H^+ + 3 \, n \, H_2O$$
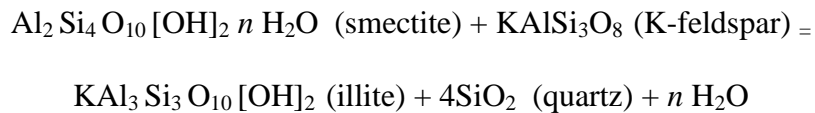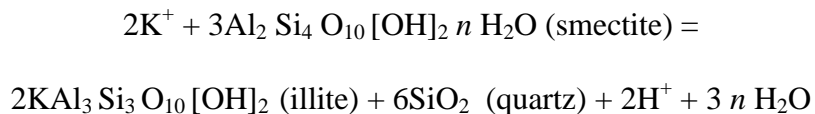
At this point, it should be mentioned that the release of H_2O is substantial in both cases above mentioned and this can drive some effective pressures that counteract consolidation.

Transformation of kaolinite into illite also requires potassium, however, this reaction requires temperatures above 130° C (Bjorlykke 1998). This chemical reaction can be described as follows (Potter *et al.* 2005):

$$2K^+ + 3Al_2\,Si_2\,O_5\,[OH]_4\,(kaolinite) =$$

$$2KAl_3\,Si_3\,O_{10}\,[OH]_2\,(illite) + 2H^+ + 3H_2O$$
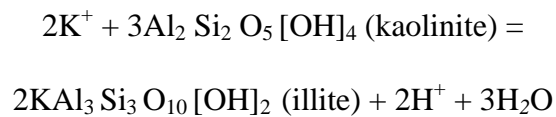
Meanwhile, production of chlorite from illite requieres a source of magnesium which can be provided by in some cases by serpentine minerals (Essene and Peacor 1995):

$$6KAl_3\,Si_3\,O_{10}\,[OH]_2\,(illite) + 5Mg_6Si_4\,O_{10}\,[OH]_8\,(serpentine) =$$

$$6Mg_5Al_2\,Si_3\,O_{10}\,[OH]_8\,(chlorite) + KAlSi_3O_8\,(K\text{-}feldspar)$$

$$+6SiO_2\,(quartz) + 2H_2O$$
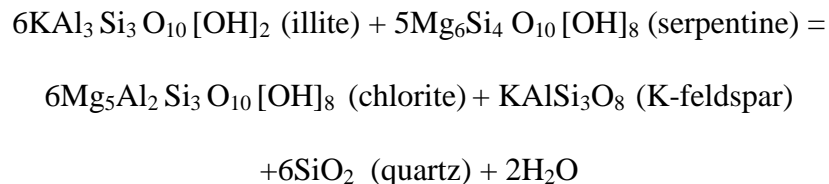
Since illite tends to align in layers perpendicular to the maximum effective stress (Ho, Peacor and van der Pluijm 1999; Day-Stirrat *et al* 2008), it contributes to the observed seismic anisotropy that characterizes shales and hence has an impact on defining their elastic and mechanical properties (Marion *et al* 1992; Hornby, Schwartz and Hudson 1994; Draege, Jakobsen and Johansen 2006).

Another important chemical process during burial is the transformation of silica. Biogenic silica grades from amorphous opal (opal-A) to cristobalite and tridymite opal (opal-CT) and finally into quartz due to increasing temperature and time (Potter *et al.* 2005). The range of temperature of these transitions is from 45 to 90° C.

Opal A rich sediments can have porosities up to 75% (Volpi *et al* 2003); however transformation of Opal A to Opal CT involves dissolution and re-precipitation reactions that reduce porosity by 40% (Keller and Isaacs 1985). As a consequence of these dramatic decrease in porosity (and hence increase density) strong seismic reflectors are produced (Davies and Cartwright 2002).

Zeolite group minerals are also present in mudstones as cement between clay minerals, particularly in those which provenance is volcanic glass. The key reactions that summarizes the conversion of volcanic glass into zeolites due to increase of temperature during burial is as follows (Potter *et al.* 2005):

Glass » alkali zeolites :

$Na + (Na,K,Ca)_{2-3}Al_3(Al,Si)_2Si_{13}O_{36} \cdot 12H_2O$ (K

clinoptilolite)$+(Ca, Na_2, K_2)Al_2Si_{10}O_{24} \cdot 7H_2O$ (mordenite)

» $NaAlSi_2O_6 \cdot H_2O$ (analcite)

» $NaAlSi_3O_8$ (albite) + $KAlSi_3O_8$ (K feldspar)
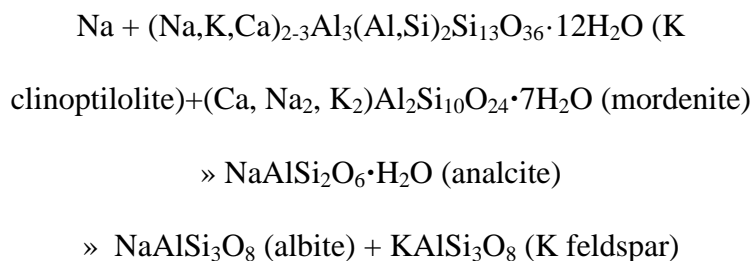
Feldspars such as detrital fine-grained plagioclase is also present in mudstones, although in much smaller quantities, which is converted into albite during burial

(Potter *et al.* 2005). Other changes experienced by detrital plagioclase is its destruction by organic acids that are released during maturation of organic material (Surdam, Crossey and Lahamn 1984; Pittman and Lewan 2012).

From the economical point of view, the most important change during depth burial is the maturation of organic material since this process leads to the formation of hydrocarbons, on which modern world base its development. Because of its importance, this topic will be treated separately in the next section.

5.5 Kerogen

Red and maroon shales, as well as some grey ones, have Total Organic Content (TOC) around 0.2 to 0.5%, while TOC contents for dark grey shales to black shales is 2 to 25% (Potter *et al.* 2005). This organic matter is transformed by diagenetic chemical and biochemical processes resulting in kerogen (Durand *et al.* 1995).

Kerogen is defined as the organic fraction contained in mudstones that is insoluble in organic solvents due to its high molecular weights (Selley 1998). As pressure and temperature increase during burial over long periods of time, kerogen becomes unstable, and rearrangement in its molecular structure occurs to maintain the thermodynamic equilibrium proceeding the generation of oil and gas (Waples 1985). This process is called maturation.

Organic matter that gives rise to kerogen have several origins: marine, lacustrine, and terrestrial (Waples 1985; Selley 1998; Potter *et al.* 2005; Tissot and Welte

2012). Additionally, it can also be recycled from pre-existing kerogen (Hunt 1984; Tissot and Welte 2012).

Kerogen that has been generated from marine and lacustrine source rocks mainly produces oil, meanwhile coal and gas have their origin in kerogen that was generated from terrestrial organic matter (primarily wood and peat). Recycled kerogen is chemically inert and is not considered as a source of oil and gas (Waples 1985).

Chemical elements such as carbon (C), hydrogen (H), oxygen (O), nitrogen (N) and sulfur (S) comprise kerogen; however, during burial it degrades and loses H faster than C (Potter *et al.* 2005), which affects its capacity to produce hydrocarbons. Therefore the quality of kerogen can be estimated based on its hydrogen content and is expressed as the ratio H/C (Waples 1985; Selley 1998; Potter *et al.* 2005; Tissot and Welte 2012).

Oil prone source rocks, i.e., marine and lacustrine rich kerogen rocks, have H/C ratios of 1.20 to 1.50 (Saxby 1980; Baskin 1997) while terrestrial kerogen have H/C ratios below 1.0 (Powell *et al* 1991).

Taking into account its origin and its capacity to produce hydrocarbons, kerogen can be classified as follows (Waples 1985; Selley 1998; Potter *et al.* 2005; Tissot and Welte 2012):

Type I: Originates from fresh water algae and is very rare. This type of kerogen is considered to have a high capacity to generate liquid hydrocarbons and have H/C ratios > 1.25.

Examples of rich Type I kerogen shales are the Mahogany oil shale from the Eocene Green River Formation in the U.S. (Lewan and Roy 2011) and the Goynuk oil shale in Turkey (Ballice 2003; Sert *et al* 2009).

Type II: It has several origins such as fresh water algae, pollen, spores and fatty and waxy constituents. This type of kerogen is also considered to have a high capacity to generate liquid hydrocarbons. Its H/C ratios are between 1.0 and 1.25. Examples of shales that are rich in Type II kerogen are the Toarcian shales of the Hills Syncline in northern Germany (Vandenbroucke *et al* 1993), the Oligocene Menilite Shales of the Polish Carpathians (Lewan *et al* 2006), and the Devonian black shales from the Illinois and Western Canada Sedimentary Basins (Lis *et al* 2005).

Type III: It is mainly generated by cellulose and lignin. This type of kerogen is considered to have a lower capacity to generate liquid hydrocarbons than Types I and II, and generates mainly gas. Their H/C ratios are between 1.0 and 1.25 as keroken type II but have higher sulfur content. The Tyrolean shale from Hahntennjoch, Austria (Bajc *et al* 2008) is an example of shale that are rich in type III kerogen.

Type IV: The origin of the type of kerogen is high oxygen content environments and has no potential to produce hydrocarbons. Its H/C ratios are < 0.5. The

Jurassic Oxford Clay unit form Southern England contains both Type II and Type IV kerogen (Ebukanson and Kinghorn 1985).

5.5.1 Kerogen maturation

Formation of oil and gas from kerogen maturation during burial depends on three factors: pressure, temperature and time (Waples 1985; Selley 1998; Potter *et al.* 2005; Tissot and Welte 2012). The thermal reactions involved in the degradation of kerogen are catagenesis and metagenesis (Waples 1985), in that order.

During catageneis, the hydrogen content of kerogen decreases as a result of generation of oil and gas (Waples 1985; Potter *et al.* 2005). The range of temperatures in which oil is produced is between 50 and 170° C and is called the "oil window" (Waples 1985; Potter *et al.* 2005).

This window oil can be very different for different kind of shales. For example, the oil window for the Monterey shale in the Santa Maria Basin, USA ranges 50 to 100° C (Orr 1986; Potter *et al.* 2005). In contrast, Miocene shales in the Gulf of Mexico have an oil window that goes between 130 and 170° C (Potter *et al.* 2005). However, a typical value is between 110 and 150° C as with Kimmeridge shale of the North Sea (Potter *et al.* 2005).

The reason for such big differences in the oil windows for different kind of shales lies in their sulfur content. High sulfur content, as in Monterey shale for example, is translated into fast oil production since sulfur acts as a catalyst by reducing the energy needed to disrupt the Carbon links that conform the organic matter (Orr 1986; Potter *et al.* 2005).

As depth increases with burial, temperature and pressure also increases, and between 120 and 225° C the main hydrocarbon that is released is gas (Selley 1998; Tissot and Welte 2012) as a consequence of irreversible aromatization of kerogen.

At higher pressures and at temperatures between 200 and 250 ºC, catagenesis is followed by metagenesis, being this phase the last stage of kerogen degradation. This phase is characterized by the decline of the H/C ratio since most of the hydrogen has been already consumed in the production of oil and gas in the catagenesis phase so that only methane is released (Waples 1985; Selley 1998; Lorant and Behar 2002; Mahlstedt and Horsfield 2012; Tissot and Welte 2012). Kerogen becomes inert at temperatures above 225° C and the only carbon content that recalls its organic origin remains as graphite (Selley 1998).

In the late phases of metagenesis all types of kerogen (I, II and III) become chemically similar and all of them have already lost their capacity to generate hydrocarbons (Durand 1980; Waples 1985; Verweij 1993).

As a result of polymerization and aromatization reactions during catagenesis and metagenesis, the color and internal structure of kerogen gradually changes (Waples 1985). The change in color follows the path yellow - golden – orange – light brown – dark brown – black (Waples 1985; Bjorlykke 2011), i.e., the more mature the kerogen is the darker it becomes (Peters, Ishiwatari and Kaplan 1977). Hence color of kerogen can be used as a maturity index.

The internal structure of kerogen becomes more ordered as kerogen matures (Waples 1985). This has a direct effect in the optical properties of kerogen since

ordered molecules have a better capacity to reflect light than randomly ordered particles. In this sense, reflectance of kerogen gives information about its maturity (Hunt 1984; Mukhopadhyay 1994).

Knowledge of maturity in shales and in mudstones in general is important since physical properties such as elastic impedance, textural heterogeneity as well as density and hence velocity increase as the maturity of the kerogen component of the mudstone increases (Prasad *et al* 2011).

5.6 Sources of anisotropy

The main sources of anisotropy in shales are layering or bedding of materials, preferred alignment of minerals and preferred orientation of cracks and pores.

As pointed out in Chapter 4, horizontal orientation of the above mentioned causes of anisotropy leads to a VTI medium.

In a fine layered media, Backus (1962) theoretically showed that VTI anisotropy arises if the wavelength of the elastic waves travelling through such media is long compared to the thickness of the layer even if the layer is isotropic itself. This long-wavelength approximation has been experimentally tested using synthetic materials. Melia and Carlson (1984) for example, use a medium composed of epoxy and glass with varying layer thicknesses to measure P waves finding that the proposed layered media was transversally isotropic, TI. Meanwhile, numerical experiments (Carcione, Kosloff and Behle 1991; Hovem 1995; Liu and Schmitt 2006) have shown that the long-wavelength approximation is valid if the ratio of the seismic wavelength (λ) to the layer thickness (*a*) is at least 5-10. Regarding to geological material, there have been experimental works on shales where the

observed anisotropy has been attributed to the presence of fine layering (Lo *et al.* 1986; Johnston and Christensen 1994; Hornby 1998; Mah 2005).

As noted earlier, preferred mineralogical alignment (texture) is also a source of anisotropy. Compaction of shales during burial causes rotation of clay minerals and their alignment in the direction perpendicular to maximum compressive stress. As a result clay minerals are oriented horizontally along bedding (Maltman 1994). This preferred mineralogical orientation results in VTI medium which leads to anisotropy (Kaarsberg 1959; Rai and Hanson 1988; Johnston and Christensen 1995; Sayers 2005; Cholach and Schmitt 2006).

Among the different techniques that have been used to relate preferred orientation of clay minerals with the observed seismic anisotropy in shales are X-ray diffraction (Kaarsberg 1959; Johnston and Christensen 1995) and Scanning Electron Microscopy (SEM) (Jones and Wang 1981). However, these techniques reduce to qualitatively determine the orientation of minerals. In this sense, a new technique has been developed using X-ray diffraction synchrotron (Lonardelli *et al* 2005; Lonardelli, Wenk and Ren 2007; Wenk *et al* 2007) to quantitatively find the orientation of clay minerals.

Preferred orientation of cracks and pores also contributes to the observed anisotropy. This particularly observed in experimental works where geological samples are under confining pressure. In particular, a high gradient velocity increase at low pressures followed by a slow velocity increase at higher pressures characterizes a velocity increase due to microcracks (He 2006). Vernik and Nur (1992) and (Johnston and Christensen 1995) observe a decrease in anisotropy up

to 50 and 29 % respectively on shale samples as a function of confining pressure as a consequence of closure of microcracks and pores.

5.7 Conclusions

Influence of mineral and organic material content of mudstones on their physical properties such as porosity, permeability, and seismic anisotropy has been reviewed in this chapter. Thus, for example, due to their characteristic low permeability values, such rocks can trap large volumes of hydrocarbons and water. Presence of high organic content as an indicator of potential source rock since oil and gas derive from its maturation during burial was discussed as well as the role of anoxic enviroment in the preservation of organic content.

On the other hand, the tendency of flake-like minerals to be aligned along a preferential direction arises in seismic anisotropy which must be taken into account during seismic processing in oil and gas exploration. However this laminae can be affected, and therefore reduce anisotroy, if high oxygen levels are present due to degradation of the rock as a result of organic activity (bioturbation).

Kerogen (organic matter) maturation during burial is also addressed, and depending on its origin, kerogen can produce oil (marine and lacustrine origin) or coal and gas (terrestial origin). Kerogen maturity is also important to study since impacts physical properties such as density and velocity of mudstones.

Thus, chemical and physical properties of mudstones are important to know since they can assist identificacition of natural resources as well as to carry out their proper exploitation.

Figures
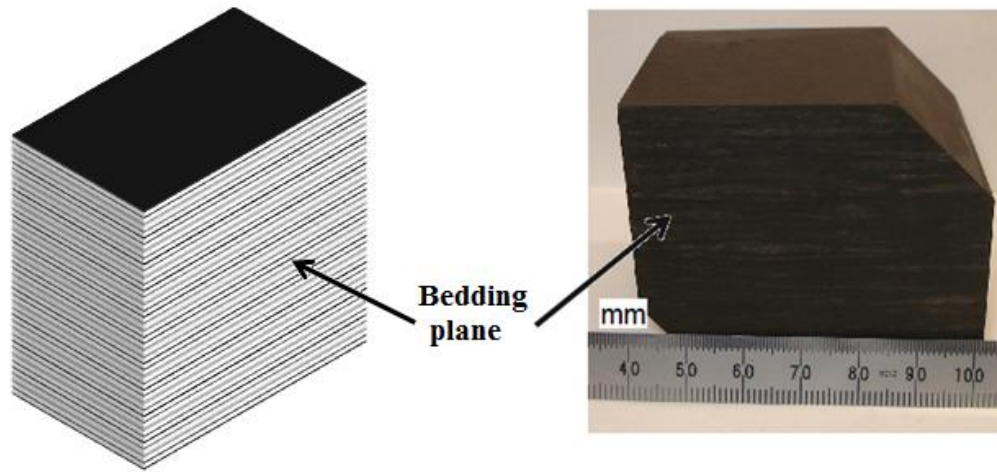
Figure 5.1 Shales tend to break in thin laminae along bedding.

Tetrahedron   **Octahedron**

O^{-2} Si^{+4} Al^{+3}, Fe$^{+2,3}$ or Mg^{+2} H^{+}
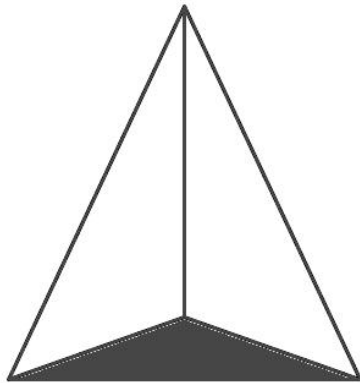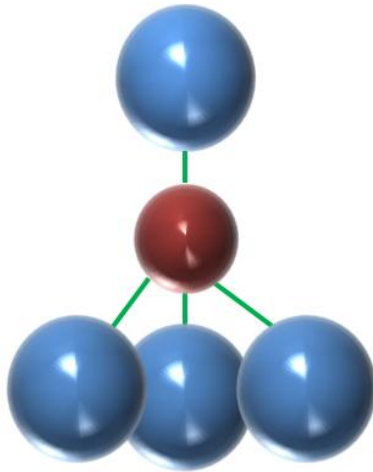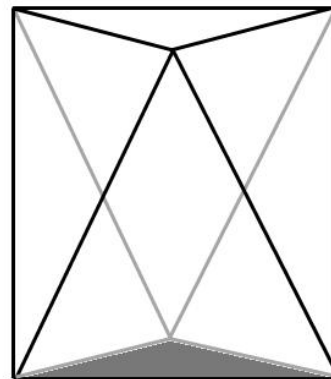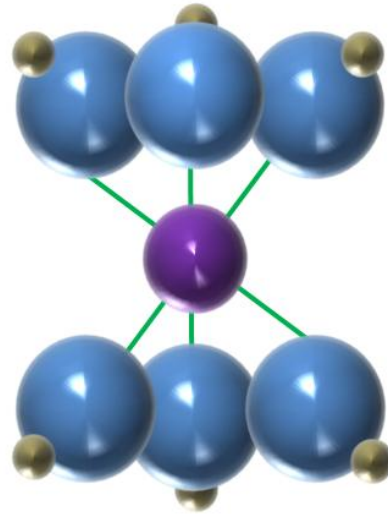
Figure 5.2 Tetrahedron and octahedron basic units that comprise clay minerals. *Modified from Grim 1968 and http://www.swac.umn.edu/classes/soil2125/doc/s11ch1.htm.*
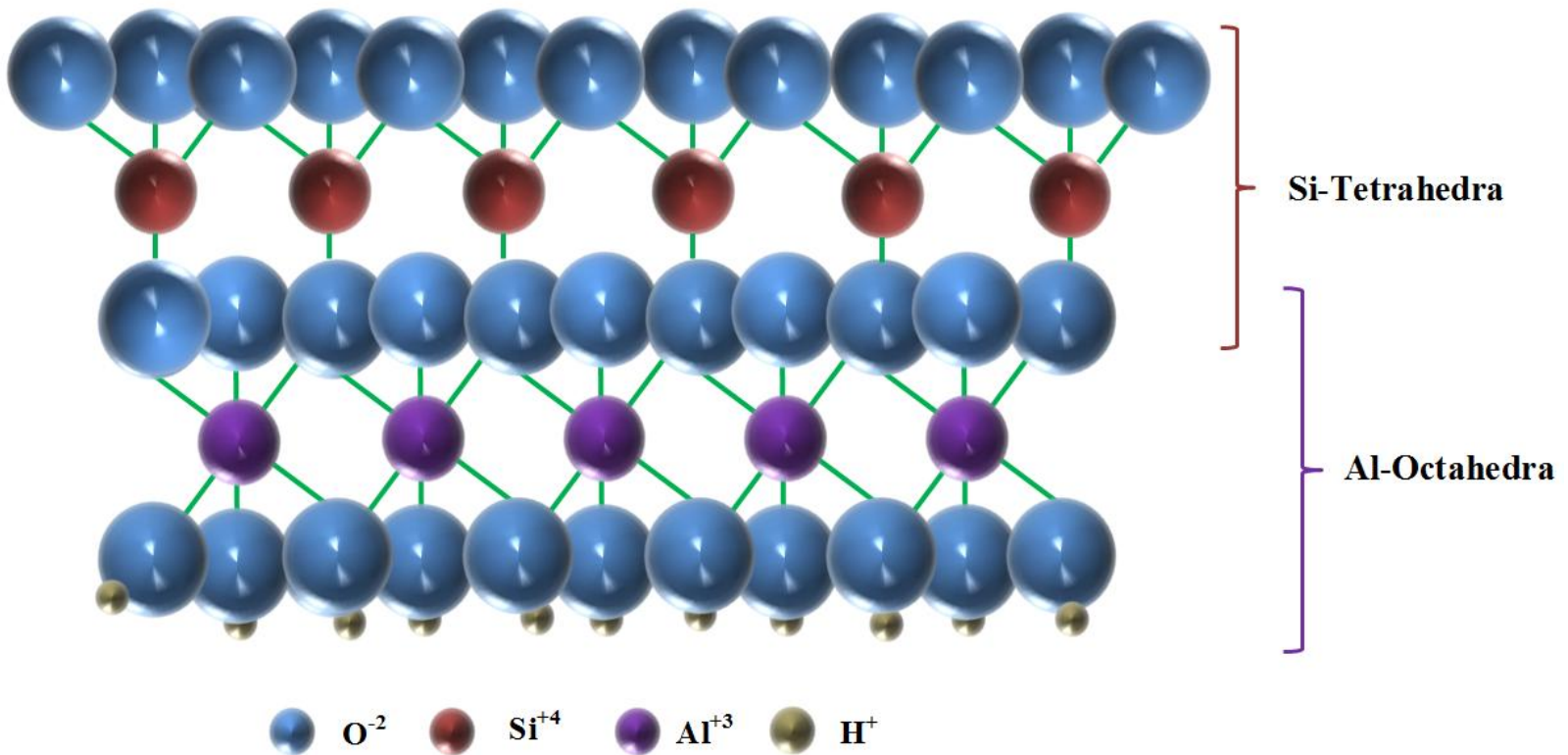
Figure 5.3 Kaolinite mineral formed with a combination of layers of Si-Tetrahedra and Al-Octahedra. *Modified from Grim 1968 and http://www.swac.umn.edu/classes/soil2125/doc/s11ch1.htm.*
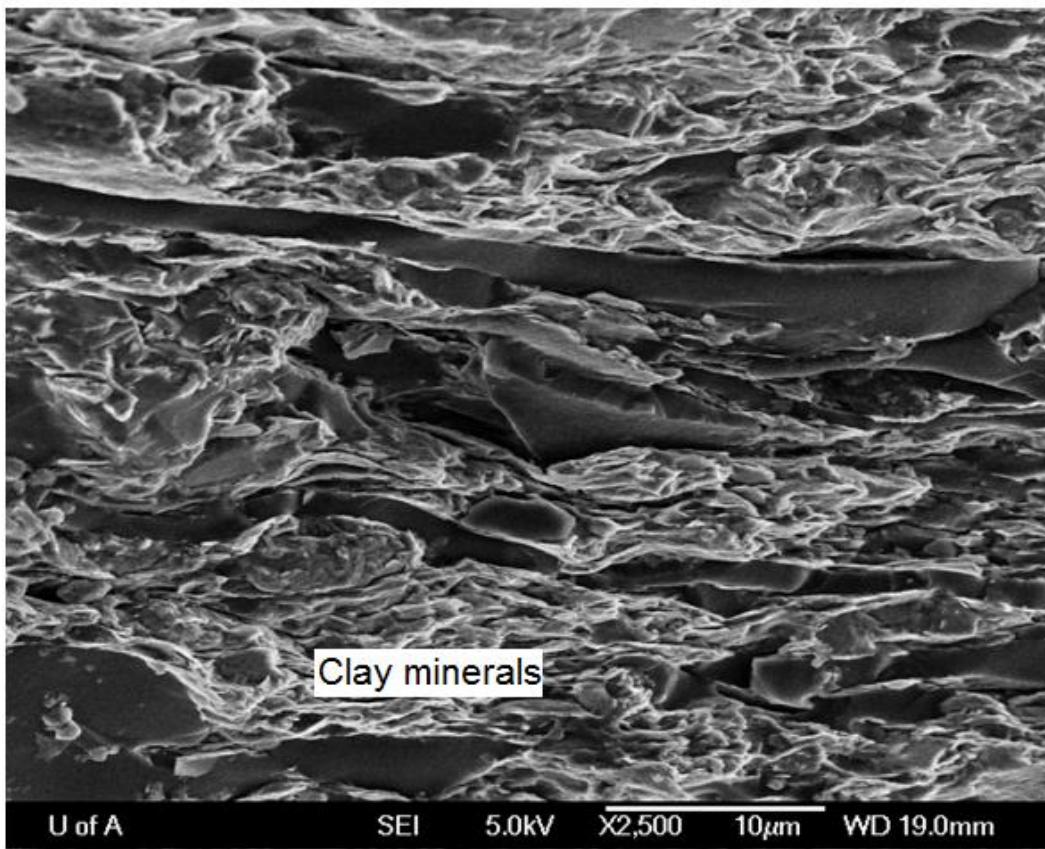
Figure 5.4 SEM image of shale sample shown in Figure 5.1.

Bibliography

Aplin, A.C., Fleet, A.J. and Macquaker, J.H.S. 1999. *Muds and Mudstones: Physical and Fluid-Flow Properties.* Geological Society Publishing House.

Aplin, A.C. and Macquaker, J.H.S. 2011. Mudstone diversity: Origin and implications for source, seal, and reservoir properties in petroleum systems, *American Association of Petroleum Geologists Bulletin,* 95, 2031-2059.

Aplin, A.C., Yang, Y.L. and Hansen, S. 1995. Assessment of beta, the compression coefficient of mudstones and its relationship with detailed lithology, *Marine and Petroleum Geology,* 12, 955-963.

Arthur, M.A. and Sageman, B.B. 1994. Marine black shales: depositional mechanisms and environments of ancient-deposits, *Annual Review of Earth and Planetary Sciences,* 22, 499-551.

Athy, L.F. 1930a. Compaction and oil migration, *American Association of Petroleum Geologists Bulletin,* 14, 25-35.

Athy, L.F. 1930b. Density, porosity, and compaction of sedimentary rocks, *American Association of Petroleum Geologists Bulletin,* 14, 1-24.

Audet, D.M. 1996. Compaction and overpressuring in Pleistocene sediments on the Louisiana Shelf, Gulf of Mexico, *Marine and Petroleum Geology,* 13, 467-474.

Backus, G.E. 1962. Long-wave elastic anisotropy produced by horizontal layering, *Journal of Geophysical Research,* 67, 4427–4440.

Bailey, S.W. 1980. Summary of recommendations of AIPEA nomenclature committee on clay-minerals, *American Mineralogist,* 65, 1-7.

Bajc, S., Cvetkovic, O., Ambles, A. and Vitorovic, D. 2008. Characterization of type III kerogen from Tyrolean shale (Hahntennjoch, Austria) based on its oxidation products, *Journal of the Serbian Chemical Society,* 73, 463-478.

Ballice, L. 2003. Solvent swelling studies of Goynuk (Kerogen Type-I) and Beypazari oil shales (Kerogen Type-II), *Fuel,* 82, 1317-1321.

Baskin, D.K. 1997. Atomic H/C ratio of kerogen as an estimate of thermal maturity and organic matter conversion, *American Association of Petroleum Geologists Bulletin,* 81, 1437-1450.

Berger, G., Velde, B. and Aigouy, T. 1999. Potassium sources and illitization in Texas Gulf Coast shale diagenesis, *Journal of Sedimentary Research,* 69, 151-157.

Bjorlykke, K. 1998. Clay mineral diagenesis in sedimentary basins - a key to the prediction of rock properties. Examples from the North Sea Basin, *Clay Minerals,* 33, 15-34.

Bjorlykke, K. 2011. *Petroleum Geoscience: From Sedimentary Environments to Rock Physics.* Springer.

Bjorlykke, K. and Egeberg, P.K. 1993. Quartz cementation in sedimentary basins, *Aapg Bulletin,* 77, 1538-1548.

Blatt, H. 1987. Perspectives; Oxygen isotopes and the origin of quartz, *Journal of Sedimentary Research,* 57, 373-377.

Bohacs, K.M., Grabowski, G.J., Carroll, A.R., Mankiewicz, P.J., Miskell-Gerhardt, K.J., Schwalbach, J.R., Wegner, M.B. and Simo, J.A. 2005. Production, destruction, and dilution-the many paths to source-rock development. In: *Deposition of Organic-Carbon-Rich Sediments: Models, Mechanisms, and Consequences,*Vol. 82 (ed. N.B. Harris), pp. 61-101

Burland, J.B. 1990. On the compressibility and shear-strength of natural clays, *Geotechnique,* 40, 329-378.

Canfield, D.E. 1989. Sulfate reduction and oxic respiration in marine sediments: implications for organic carbon preservation in euxinic environments, *Deep-Sea Research Part a-Oceanographic Research Papers,* 36, 121-138.

Carcione, J.M., Kosloff, D. and Behle, A. 1991. Long-wave anisotropy in stratified media: a numerical test, *Geophysics,* 56, 245-254.

Clarke, J. 2003. The occurrence and significance of biogenic opal in the regolith, *Earth-Science Reviews,* 60, 175-194.

Chamley, H. 1989. *Clay sedimentology.* Springer-Verlag.

Chatterjee, R., Mukhopadhyay, M. and Paul, S. 2011. Overpressure zone under the Krishna-Godavari offshore basin: geophysical implications for natural hazard in deeper-water drilling, *Natural Hazards,* 57, 121-132.

Chilingar, G.V. and Knight, L. 1960. Relationship between pressure and moisture content of kaolinite, illite, and montmorillonite clays, *American Association of Petroleum Geologists Bulletin,* 44, 101-106.

Cholach, P.Y. and Schmitt, D.R. 2006. Intrinsic elasticity of a textured transversely isotropic muscovite aggregate: Comparisons to the seismic anisotropy of schists and shales, Journal of Geophysical Research-Solid Earth, 111.

Davies, R.J. and Cartwright, J. 2002. A fossilized Opal A to Opal C/T transformation on the northeast Atlantic margin: support for a significantly elevated Palaeogeothermal gradient during the Neogene?, *Basin Research,* 14, 467-486.

Day-Stirrat, R.J., Aplin, A.C., Srodon, J. and van der Pluijm, B.A. 2008. Diagenetic reorientation of phyllosilicate minerals in Paleogene mudstones of the Podhale Basin, southern Poland, *Clays and Clay Minerals,* 56, 100-111.

Dean, W.E. 2007. Sediment geochemical records of productivity and oxygen depletion along the margin of western North America during the past 60,000 years: teleconnections with Greenland Ice and the Cariaco Basin, *Quaternary Science Reviews,* 26, 98-114.

Dewhurst, D.N., Aplin, A.C. and Sarda, J.P. 1999. Influence of clay fraction on pore-scale properties and hydraulic conductivity of experimentally compacted mudstones, *Journal of Geophysical Research-Solid Earth,* 104, 29261-29274.

Dewhurst, D.N., Aplin, A.C., Sarda, J.P. and Yang, Y.L. 1998. Compaction-driven evolution of porosity and permeability in natural mudstones: An

experimental study, *Journal of Geophysical Research-Solid Earth,* 103, 651-661.

Draege, A., Jakobsen, M. and Johansen, T.A. 2006. Rock physics modelling of shale diagenesis, *Petroleum Geoscience,* 12, 49-57.

Droser, M.L. and Bottjer, D.J. 1986. A semiquantitative field classification of ichnofabric, *Journal of Sedimentary Petrology,* 56, 558-559.

Durand, B. 1980. *Kerogen: Insoluble Organic Matter from Sedimentary Rocks.* Editions Technip.

Durand, C., Forsans, T., Ruffet, C., Onaisi, A. and Audibert, A. 1995. Influence of clays on borehole stability: a literature survey, Part 2. Occurrence of drilling problems physicochemical description of clays and of their interaction with fluids, *Revue De L Institut Francais Du Petrole,* 50, 187-218.

Ebukanson, E.J. and Kinghorn, R.R.F. 1985. Kerogen facies in the major Jurassic mudrock formations of Southern England and the implication on the depositional environments of their precursors, *Journal of Petroleum Geology,* 8, 435-462.

Faust, L.Y. 1951. Seismic velocity as a function of depth and geologic time, *Geophysics,* 16, 192-206.

Garrels, R.M. and MacKenzi, F.T. 1971. Gregor´s denudation of continents, *Nature,* 231, 382-383.

Ghobadi, M.H. 2000. *Petrology, weathering and long-term stability slopes.*

Gorsline, D.S. 1984. Origins, transport, and deposition of fine-grained sediments, *Geo-Marine Letters,* 4, 131-131.

Grim, R.E. 1968. *Clay mineralogy.* McGraw-Hill

Harris, N.B. 2005. The deposition of organic-carbon-rich sediments: models, mechanisms, and consequences-introduction. In: *Deposition of Organic-*

Carbon-Rich Sediments: Models, Mechanisms, and Consequences,Vol. 82 (ed. N.B. Harris), pp. 1-5. Society for Sedimentary Geology Special Publication.

He, T. 2006. P- and S-wave velocity measurement and pressure sensitivity analysis of AVA response*, MSc Thesis*, University of Alberta, Edmonton, Alberta, Canada.

Hedberg, H.D. 1926. The effect of gravitational compaction on the structure of sedimentary rocks, *American Association of Petroleum Geologists Bulletin,* 10, 1035-1072.

Hedberg, H.D. 1936. Gravitational compaction of clays and shales, *American Journal of Science,* 31, 241-287.

Ho, N.C., Peacor, D.R. and van der Pluijm, B.A. 1999. Preferred orientation of phyllosilicates in Gulf Coast mudstones and relation to the smectite-illite transition, *Clays and Clay Minerals,* 47, 495-504.

Hornby, B.E. 1998. Experimental laboratory determination of the dynamic elastic properties of wet, drained shales, *Journal of Geophysical Research-Solid Earth,* 103, 29945-29964.

Hornby, B.E., Schwartz, L.M. and Hudson, J.A. 1994. Anisotropic effective-medium modeling of the elastic properties of shales, *Geophysics,* 59, 1570-1583.

Hovem, J.M. 1995. Acoustic waves in finely layered media, *Geophysics,* 60, 1217-1221.

Hower, J., Eslinger, E.V., Hower, M.E. and Perry, E.A. 1976. Mechanism of burial metamorphism of argillaceous sediment: 1. Mineralogical and chemical evidence, *Geological Society of America Bulletin,* 87, 725-737.

Hunt, J.M. 1984. Generation and migration of light hydrocarbons, *Science,* 226, 1265-1270.

Ibach, L.E.J. 1982. Relationship between sedimentation rate and total organic carbon content in ancient marine sediments, *American Association of Petroleum Geologists Bulletin,* 66, 170-188.

Johnston, J.E. and Christensen, N.I. 1994. Elastic constants and velocity surfaces of indurated anisotropic shales, *Surveys in Geophysics,* 15, 481-494.

Johnston, J.E. and Christensen, N.I. 1995. Seismic anisotropy of shales, *Journal of Geophysical Research-Solid Earth,* 100, 5991-6003.

Jones, L.E.A. and Wang, H.F. 1981. Ultrasonic velocities in Cretaceous shales from the Williston Basin, *Geophysics,* 46, 288-297.

Kaarsberg, E.A. 1959. Introductory studies of natural and artificial argillaceous aggregates by sound-propagation and x-ray diffraction methods, *Journal of Geology,* 67, 447-472.

Kamradt, A., Borg, G., Schaefer, J., Kruse, S., Fiedler, M., Romm, P., Schippers, A., Gorny, R., du Bois, M., Bieligk, C., Liebetrau, N., Nell, S., Friedrich, B., Morgenroth, H., Wotruba, H. and Merkel, C. 2012. An Integrated Process for Innovative Extraction of Metals from Kupferschiefer Mine Dumps, Germany, *Chemie Ingenieur Technik,* 84, 1694-1703.

Kebaili, A. and Schmitt, D.R. 1997. Ultrasonic anisotropic phase velocity determination with the Radon transformation, *Journal of the Acoustical Society of America,* 101, 3278-3286.

Keller, M.A. and Isaacs, C.M. 1985. An evaluation of temperature scales for silica diagenesis in diatomaceous sequences including a new approach based on the Miocene Monterey Formation, California, *Geo-Marine Letters,* 5, 31-35.

Lewan, M.D., Kotarba, M.J., Curtis, J.B., Wieclaw, D. and Kosakowski, P. 2006. Oil-generation kinetics for organic facies with Type-II and -IIS kerogen in the Menilite Shales of the Polish Carpathians, *Geochimica Et Cosmochimica Acta,* 70, 3351-3368.

Lewan, M.D. and Roy, S. 2011. Role of water in hydrocarbon generation from Type-I kerogen in Mahogany oil shale of the Green River Formation, *Organic Geochemistry,* 42, 31-41.

146

Lis, G.P., Mastalerz, M., Schimmelmann, A., Lewan, M.D. and Stankiewicz, B.A. 2005. FTIR absorption indices for thermal maturity in comparison with vitrinite reflectance R-0 in type-II kerogens from Devonian black shales, *Organic Geochemistry,* 36, 1533-1552.

Liu, Y.B. and Schmitt, D.R. 2006. The transition between the scale domains of ray and effective medium theory and anisotropy: Numerical models, *Pure and Applied Geophysics,* 163, 1327-1349.

Lo, T.W., Coyner, K.B. and Toksoz, M.N. 1986. Experimental determination of elastic-anisotropy of Berea sandstone, Chicopee shale, and Chelmsford granite, *Geophysics,* 51, 164-171.

Lonardelli, I., Wenk, H.R., Lutterotti, L. and Goodwin, M. 2005. Texture analysis from synchrotron diffraction images with the Rietveld method: dinosaur tendon and salmon scale, *Journal of Synchrotron Radiation,* 12, 354-360.

Lonardelli, I., Wenk, H.R. and Ren, Y. 2007. Preferred orientation and elastic anisotropy in shales, *Geophysics,* 72, D33-D40.

Lorant, F. and Behar, F. 2002. Late generation of methane from mature kerogens, *Energy & Fuels,* 16, 412-427.

Loseth, H., Wensaas, L. and Gading, M. 2011. Deformation structures in organic-rich shales, *American Association of Petroleum Geologists Bulletin,* 95, 729-747.

Mackey, S.D. and Bridge, J.S. 1995. Three-dimensional model of alluvial stratigraphy: theory and application, *Journal of Sedimentary Research Section B-Stratigraphy and Global Studies,* 65, 7-31.

Mah, M. 2005. Determination of the elastic constants of orthorhombic and transversely isotropic materials: experimental application to a kerogen rich rock*, PhD Thesis*, University of Alberta, Edmonton, Alberta, Canada.

Mahlstedt, N. and Horsfield, B. 2012. Metagenetic methane generation in gas shales I. Screening protocols using immature samples, *Marine and Petroleum Geology,* 31, 27-42.

Maltman, A. 1994. *The geological deformation of sediments.* Chapman & Hall.

Mann, D.M. and Mackenzie, A.S. 1990. Prediction of pore fluid pressures in sedimentary basins, *Marine and Petroleum Geology,* 7, 55-65.

Marion, D., Nur, A., Yin, H. and Han, D. 1992. Compressional velocity and porosity in sand-clay mixtures, *Geophysics,* 57, 554-563.

Melia, P.J. and Carlson, R.L. 1984. An experimental test of p-wave anisotropy in stratified media, *Geophysics,* 49, 374-378.

Michael, K. and Bachu, S. 2001. Fluids and pressure distributions in the foreland-basin succession in the west-central part of the Alberta basin, Canada: Evidence for permeability barriers and hydrocarbon generation and migration, *American Association of Petroleum Geologists Bulletin,* 85, 1231-1252.

Mondol, N.H., Bjørlykke, K., Jahren, J. and Høeg, K. 2007. Experimental mechanical compaction of clay mineral aggregates—Changes in physical properties of mudstones during burial, *Marine and Petroleum Geology,* 24, 289-311.

Moore, D.M. and Reynolds, R.C. 1997. *X-Ray Diffraction and the Identification and Analysis of Clay Minerals.* Oxford University Press.

Mukhopadhyay, P.K. 1994. Vitrinite reflectance as maturity parameter: petrographic and molecular characterisation and its applications in basin modelling. In: *Vitrinite reflectance as a maturity parameter: Applications and Limitations,*Vol. 57 (eds. P.K. Mukhopadhyay and W.G. Dow), pp. 1-24. American Chemical Society, Symposium Series.

Muller, P.J. and Suess, E. 1979. Productivity, sedimentation rate, and sedimentary organic matter in the oceans: 1. Organic carbon preservation, *Deep-Sea Research Part A.Oceanographic Research Papers,* 26, 1347-1362.

Nordgård Bolås, H.M., Hermanrud, C. and Teige, G.M.G. 2004. Origin of overpressures in shales: Constraints from basin modeling, *American Association of Petroleum Geologists Bulletin,* 88, 193-211.

Obrien, J. and Lerche, I. 1994. Understanding subsalt overpressure may reduce drilling risks, *Oil & Gas Journal,* 92, 28-34.

Orr, W.L. 1986. Kerogen/asphaltene/sulfur relationships in sulfur-rich Monterey oils, *Organic Geochemistry,* 10, 499-516.

Osborne, M.J. and Swarbrick, R.E. 1997. Mechanisms for generating overpressure in sedimentary basins; a reevaluation, *American Association of Petroleum Geologists Bulletin,* 81, 1023-1041.

Pang, X.Q., Jiang, Z.X., Zuo, S.J. and Lerche, I. 2005. Dynamics of hydrocarbon expulsion from shale source rocks, *Energy Exploration & Exploitation,* 23, 333-355.

Pedersen, T.F. and Calvert, S.E. 1990. Anoxia vs productivity; what controls the formation of organic carbon rich sediments and sedimentary rocks?, *American Association of Petroleum Geologists Bulletin,* 74, 454-466.

Peters, K.E., Ishiwatari, R. and Kaplan, I.R. 1977. Color of kerogen as index of organic maturity, *American Association of Petroleum Geologists Bulletin,* 61, 504-510.

Pittman, E.D. and Lewan, M.D. 2012. *Organic Acids in Geological Processes.* Springer.

Potter, P.E., Maynard, J.B. and Depetris, P.J. 2005. *Mud and Mudstones: Introduction and Overview.* Springer.

Potter, P.E., Maynard, J.B. and Pryor, W.A. 1980. *Sedimentology of shale: study guide and reference source.* Springer-Verlag.

Powell, T.G., Boreham, C.J., Smyth, M., Russell, N. and Cook, A.C. 1991. Petroleum source rock assessment in nonmarine sequences: pyrolysis and petrographic analysis of Australian coals and carbonaceous shales, *Organic Geochemistry,* 17, 375-394.

Prasad, M., Mba, K.C., McEvoy, T.E. and Batzle, M.L. 2011. Maturity and Impedance Analysis of Organic-Rich Shales, *Spe Reservoir Evaluation & Engineering,* 14, 533-543.

Rai, C.S. and Hanson, K.E. 1988. Shear-wave velocity anisotropy in sedimentary rocks: A laboratory study, *Geophysics,* 53, 800-806.

Ramdhan, A.M. and Goulty, N.R. 2011. Overpressure and mud rock compaction in the Lower Kutai Basin, Indonesia: A radical reappraisal, *American Association of Petroleum Geologists Bulletin,* 95, 1725-1744.

Saxby, J.D. 1980. Atomic H-C ratios and the generation of oil from coals and kerogens, *Fuel,* 59, 305-307.

Sayers, C.M. 2005. Seismic anisotropy of shales, *Geophysical Prospecting,* 53, 667-676.

Schieber, J., Krinsley, D. and Riciputi, L. 2000. Diagenetic origin of quartz silt in mudstones and implications for silica cycling, *Nature,* 406, 981-985.

Selley, R.C.A. 1998. *Elements of Petroleum Geology.* Academic Press.

Sert, M., Ballice, L., Yuksel, M., Saglam, M., Reimert, R. and Erdem, S. 2009. Effect of solvent swelling on pyrolysis of kerogen (type-I) isolated from Goynuk oil shale (Turkey), *Journal of Analytical and Applied Pyrolysis,* 84, 31-38.

Skempton, A.W. 1969. The consolidation of clays by gravitational compaction, *Quarterly Journal of the Geological Society,* 125, 373-411.

Smith, J.E. 1971. The dynamics of shale compaction and evolution of pore-fluid pressures, *Mathematical Geology,* 3, 239-263.

Surdam, R.C., Crossey, L.J. and Lahamn, R. 1984. Mineral oxidants and porosity enhancement, *American Association of Petroleum Geologists Bulletin,* 68, 532-532.

Tissot, B. and Welte, D. 2012. *Petroleum Formation and Occurrence: A New Approach to Oil and Gas Exploration.* Springer.

Tyson, R.V. 1995. *Sedimentary organic matter: organic facies and palynofacies.* Chapman & Hall.

Tyson, R.V. 2001. Sedimentation rate, dilution, preservation and total organic carbon: some results of a modelling study, *Organic Geochemistry,* 32, 333-339.

Vandenbroucke, M., Behar, F., Santorcuato, A. and Rullkotter, J. 1993. Kerogen maturation in a reference kerogen type-II series: the toarcian shales of the hils syncline, NW Germany, *Organic Geochemistry,* 20, 961-972.

Vernik, L. and Nur, A. 1992. Ultrasonic velocity and anisotropy of hydrocarbon source rocks, *Geophysics,* 57, 727-735.

Verweij, J.M. 1993. *Hydrocarbon Migration Systems Analysis.* Elsevier Science Limited.

Volpi, V., Camerlenghi, A., Hillenbrand, C.D., Rebesco, M. and Ivaldi, R. 2003. Effects of biogenic silica on sediment compaction and slope stability on the Pacific margin of the Antarctic Peninsula, *Basin Research,* 15, 339-363.

Waples, D. 1985. *Geochemistry in petroleum exploration.* International Human Resources Development Corporation.

Wenk, H.R., Lonardelli, I., Franz, H., Nihei, K. and Nakagawa, S. 2007. Preferred orientation and elastic anisotropy of illite-rich shale, *Geophysics,* 72, E69-E75.

Yang, Y.L. and Aplin, A.C. 1998. Influence of lithology and compaction on the pore size distribution and modelled permeability of some mudstones from the Norwegian margin, *Marine and Petroleum Geology,* 15, 163-175.

Yang, Y.L. and Aplin, A.C. 2007. Permeability and petrophysical properties of 30 natural mudstones, *Journal of Geophysical Research-Solid Earth,* 112.

CHAPTER 6

Anisotropic dynamic and static elastic moduli of four shale

samples and one argillaceous sample from Southern Alberta,

Canada

6.1 Introduction

Mudstones such as shales and argillites comprise about 75% of all the sedimentary rocks (Jones and Wang 1981; Potter, Maynard and Depetris 2005). Shales in particular have significant economic importance because of their low permeability form seals that trap large volumes of gas, oil and water (Potter *et al.* 2005; Aplin and Macquaker 2011). Organic rich 'shales' are considered as a petroleum source rock and, in recent times, shales have also been considered as a reservoir of exploitable gas and hydrocarbon liquids due to modern hydraulic fracturing techniques (Curtis 2002; Douglas *et al* 2011). On the other hand, because of high mechanical strength and low permeability of argillaceous rocks (Yang, Billiotte and Su 2010) they have been recently considered as container rock disposal for nuclear waste (Yang *et al* 2013). In this sense, the aforesaid motivates our work in laboratory measurements of elastic properties of mudstones, which are known to be anisotropic (Podio, Gregory and Gray 1968; Jones and Wang 1981; Hornby, Schwartz and Hudson 1994; Johnston and Christensen 1994; Vernik and Liu 1997; Hornby 1998; Hemsing 2007; Wong *et al* 2008; Yang *et al.* 2010; Yang *et al.* 2013). The observed anisotropy in

mudstones is intrinsic to the rock itself and is associated with their microstructure which comprises layering (bedding), preferred mineralogical alignment or a preferred orientation of cracks and pores as a result of depositional and diagenetic processes that, when presenting horizontal orientation, leads to a VTI medium. Further, this anisotropy can also be influenced by local and regional field stresses. Thus contribution of intrinsic anisotropy of shales, for example, on anisotropy observed at seismic scales must be considered when assisting image and depth estimation (Banik 1984) and Amplitude Versus Offset (AVO) analysis (Wright 1987).

The vastly increased use of hydraulic fracture stimulations in low permeability formations, too, has motivated a better understanding of such materials. Engineers have devised methods that require knowledge of the material Young's modulus and Poisson's ratios in order to be able to make estimates of the state of stress in the earth on the basis of well log observations under the assumption of the elastic uniaxial strain model. This model essentially assumes that horizontal stresses, σ_H, are a byproduct of the attempt by the rock to horizontally expand due to the Poisson´s ratio, μ, effect upon vertical loading, σ_V, by the overburden (Thiercelin and Plumb 1994). That is

$$\sigma_H = \frac{\mu}{1-\mu}\sigma_V \qquad\qquad 6.1$$

Most of the work has assumed that the rock is elastically isotropic (Warpinski *et al* 1998; Barree, Gilbert and Conway 2009). However, the effects of transverse isotropy while not having gone unnoticed (Theircelin and Plumb 1994) have not been applied in practical situations probably due to the lack of appropriate data.

The need for appropriate knowledge of the rock mechanical anisotropy becomes increasingly important for deviated boreholes where the borehole axis differs from the symmetry axis of the transversely isotropic rock.

The term dynamic moduli is used to name the moduli that are obtained from elastic wave-velocity measurements. On the other hand, static moduli are derived from the direct stress-strain relations observed in quasi-static deformational experiments as might be carried out on mechanical testing machines. The static and dynamic moduli often differ significantly for rocks with the dynamic moduli greater than the 'static' moduli.

Tutuncu *et al* (1998), for example, report differences of up to 6 times between dynamic and static moduli for pressures < 20 MPa on dry and fully saturated sandstones, pointing out that such dissimilarities can be due to differences in frequency and strain amplitude during measurements. Simmons and Brace (1965) found that dynamic moduli on granite samples were 2 times higher than static moduli at atmospheric pressure, decreasing to unit at 300 MPa. Cheng and Johnston (1981) and King (1983) obtained similar results on sandstone, limestone oil shale and biotite schist samples. In a more recent work, Wong *et al.* (2008) observed that anisotropic dynamic moduli was close to 4 times higher than anisotropic static moduli on drained shale samples at 6 MPa.

As above mentioned, dynamic moduli (obtained from seismic velocities) can assist seismic studies. On the other hand, proxy information on static moduli is necessary, for example, for development of borehole stability and mechanical modeling in order to avoid drilling related failures (Carvajal-Jiménez *et al* 2007),

particularly in areas that show strong anisotropy due presence of weak bedding and fractures (Zhang 2013). Static stress-dependent moduli are also used in hydraulic fracturing modeling to generate a high fracture conductivity path to enhance hydrocarbon production (Meyer and Jacot 2001).

In order to fully determine the dynamic elastic moduli of an ideal VTI medium, velocities with different particle polarization must be made in a minimum of three different directions: perpendicular, parallel and oblique to the material´s layering. Multiple cylindrical cores taken at different angles from a single specimen are often used to characterize layered rocks (Lo, Coyner and Toksoz 1986; Johnston and Christensen 1994; Vernik and Liu 1997; Hornby 1998; Hemsing 2007; Meléndez and Schmitt 2013). Other geometries use specially machined single samples to obtain the appropriate information (Arts, Rasolofosaon and Zinszner 1991; Cheadle, Brown and Lawton 1991; Schmitt and Li 1995; Wang 2002; Wong *et al.* 2008).

In this work we use the pulse transmission method along with strain gauges to simultaneously measure compressional (P)- and shear (S)-wave velocities and deformation on single samples obtained from a variety of well cores and from one outcrop from Southern Alberta, Canada. To take the velocity measurements, a prism-like shaped sample is trimmed in different orientations from a main core as in shown in Figure 6.1: perpendicular to bedding (i.e, within plane $X_1 - X_2$, $\theta = 90$), parallel to bedding (within plane $X_1 - X_2$, $\theta = 90^o$) and oblique to bedding, i.e., between symmetry axis X_3 and bedding plane $X_1 - X_2$ (usually at $\theta = 45^o$). Although the oblique direction is often taken at $\theta = 45^o$, this is not limited to that

angle, hence in our experiment, for example, oblique direction in argillaceous sample is taken at $\theta = 53^{\circ}$. On the other hand, estimation of static elastic properties involves deformation measurements both along symmetry axis X_3 and the direction of the bedding plane $X_1 - X_2$.

In this work, a theoretical background involving elastic dynamic moduli is first given, followed by sample description, experimental procedure, and analysis of results.

6.2 Theoretical Background

The use of wide piezoelectric ceramic transducers in pulse transmission method to generate and record P- and S- wave velocities ensures generation of plane waves (Auld 1973), which are fundamental to determine dynamic elastic properties from phase velocities (i.e., plane waves). Figure 6.2 shows both the direction of propagation and particle polarization for each pair pulser-receiver transducer mode with respect to the symmetry axis X_3 used in this work when oblique direction is $\theta = 45^{\circ}$.

6.2.1 Elastic stiffnesses and dynamic moduli

In the current experiments we make measurements using both strain gauges for static values and piezoelectric ceramic transducers for dynamic values. The samples are subject to hydrostatic states of stress and under these conditions the strain gauges provide a measure of strain (and hence a modulus) in that direction only. In contrast, the ultrasonic velocity measurements yield values of the anisotropic moduli directly according to the formulas developed in Chapter 2. As

we need some way to make proper comparisons between the static and dynamic measurements, we develop here a set of comparative linear moduli that can be determined either from the observed strains or calculated from the dynamic elastic moduli.

Under hydrostatic pressure we have that (Musgrave 1970) $\sigma_1 = \sigma_2 = \sigma_3 = -p$ and $\sigma_4 = \sigma_5 = \sigma_6 = 0$. Therefore, combining equations 2.3 and 2.11 it holds that

$$\varepsilon_1 = -(S_{11} + S_{12} + S_{13})\, p \qquad\qquad 6.2$$

$$\varepsilon_2 = -(S_{12} + S_{11} + S_{13})\, p \qquad\qquad 6.3$$

$$\varepsilon_3 = -(S_{13} + S_{13} + S_{33})\, p \qquad\qquad 6.4$$

with $\varepsilon_1 = \varepsilon_2 \neq \varepsilon_3$ for a TI medium.

Correspondingly, equations 6.2 through 6.4 can be expressed in terms of the elastic constants as

$$-p = C_{11}\varepsilon_1 + C_{12}\varepsilon_2 + C_{13}\varepsilon_3 \qquad\qquad 6.5$$

$$-p = C_{12}\varepsilon_1 + C_{11}\varepsilon_2 + C_{13}\varepsilon_3 \qquad\qquad 6.6$$

$$-p = C_{13}(\varepsilon_1 + \varepsilon_2) + C_{33}\varepsilon_3 \qquad\qquad 6.7$$

which leads to

$$\frac{\varepsilon_1}{p} = \frac{\varepsilon_2}{p} = -\frac{(C_{33} - C_{13})}{(C_{11} + C_{12})C_{33} - 2C_{13}^2} = -\frac{1}{Kl_1} = -\frac{1}{Kl_2} = -\beta l_1$$
$$= -\beta l_2 \qquad\qquad 6.8$$

$$\frac{\varepsilon_3}{p} = -\frac{(C_{11} + C_{12} - 2C_{13}^2)}{(C_{11} + C_{12})C_{33} - 2C_{13}^2} = -\frac{1}{Kl_3} = -\beta l_3. \qquad\qquad 6.9$$

157

Where βl_i and $K l_i$, i=1,2,3, are the linear stiffnesses and linear compliances in the i direction of the Cartesian system. We derive these as this is what the appropriately placed strain gages will measure.

Volumetric compressibility β is the inverse of the bulk modulus K and, in a VTI medium, is defined as

$$\beta = \frac{1}{K} = 2\beta l_1 + \beta l_3. \qquad\qquad 6.10$$

Hence, the bulk modulus is given by

$$K = \frac{(C_{11} + C_{12})C_{33} - 2C_{13}^2}{2C_{33} + C_{11} + C_{12} - 4C_{13}}. \qquad\qquad 6.11$$

At this point, it should be noted that dynamic moduli given so far corresponds to the dynamic moduli of a anisotropic single crystal under hydrostatic pressure, however when dealing with composite materials such as rocks what is more often provided is the Voigt-Reuss-Hill (VRH) value with which elastic moduli of an anisotropic single crystal can be converted into elastic moduli of an isotropic polycrystalline material (Chung and Buessem 1967). Thus, the VRH value is defined as the arithmetic mean of the upper (Voigt 1928) and lower Reuss (1929) bounds (Hill 1952) of an isotropic polycrystalline composite assuming isostrain and isostress conditions respectively. Hill (1952) provide the expressions for the Voigt bulk K_V and shear μ_V moduli for any crystal class as follows:

$$K_V = \frac{1}{9}[(C_{11} + C_{22} + C_{33}) + 2(C_{12} + C_{23} + C_{13})] \qquad\qquad 6.12$$

$$\mu_V = \frac{1}{15}[(C_{11} + C_{22} + C_{33}) - (C_{12} + C_{23} + C_{13}) \\ + 3(C_{44} + C_{55} + C_{66})]. \qquad\qquad 6.13$$

For a VTI medium we have that

$$K_V = \frac{1}{9}[(2C_{11} + C_{33}) + 2(C_{12} + 2C_{13})]$$ 6.14

$$\mu_V = \frac{1}{15}[(2C_{11} + C_{33}) - (C_{12} + 2C_{13}) + 3(2C_{44} + C_{66})].$$ 6.15

The corresponding Reuss bulk and shear moduli are given by:

$$K_R = \frac{1}{[(S_{11} + S_{22} + S_{33}) + 2(S_{12} + S_{13} + S_{23})]}$$ 6.16

$$\mu_R = \frac{15}{[4(S_{11} + S_{22} + S_{33}) - 4(S_{12} + S_{13} + S_{23}) + 3(S_{44} + S_{55} + S_{66})]}.$$ 6.17

For a VTI medium it holds that

$$K_R = \frac{1}{[(2S_{11} + S_{33}) + 2(S_{12} + 2S_{13})]}$$ 6.18

$$\mu_R = \frac{15}{[4(2S_{11} + S_{33}) - 4(S_{12} + 2S_{13}) + 3(2S_{44} + S_{66})]}.$$ 6.19

VRH values for Young modulus and Poisson´s ratio can be then estimated as follows using standard elastic relations between the isotropic moduli (Landau *et al* 1986) :

$$E_{VRH} = \frac{9K_{VRH}\,\mu_{VRH}}{3K_{VRH} + \mu_{VRH}}$$ 6.20

$$v_{VRH} = \frac{3K_{VRH} - 2\mu_{VRH}}{2(3K_{VRH} + \mu_{VRH})}.$$ 6.21

Where K_{VRH} and μ_{VRH} are the VRH bulk and shear moduli respectively.

6.3 Sample description

The Precambrian argillaceous sample of the Purcell-Belt Supergroup was obtained from a trailside outcrop in SW Alberta. Cretaceous shale samples, labeled SSA-24, SSA-27, SSA-41, and SSA-42, were obtained from a series of core materials. Table 6.1 shows the depth and location of each sample in Alberta Township System (ATS) coordinates. Figure 6.3 portrays the location of the four shale samples in ATS coordinates projected on a latitude-longitude grid as well as the geological formation.

The core material is quite limited in dimension, and the trimmed prism-like shaped samples are about 4.12-5.38 cm in height and 5.04-5.99 cm in maximum width. Photographs of the resulting sample geometry are shown in Figure 6.4.

Bulk and grain volumes of all samples were obtained using different techniques. A Helium pycnometer (Micromeritics MVP-6DC) and a Geopyc (Micrometrics 1360) were used to determine grain and bulk densities, respectively while a mercury porosimeter (Micrometrics Autopore IV) was used to determine both bulk and grain volumes and to indicate the distributions of the pore throat dimensions. Figure 6.5 shows some examples of the differential mercury intrusion against pore-size diameter for samples SSA-24, SSA-27 and SSA-42. Curves for samples SSA-24 and SSA-27 show mono-modal distribution with sharp peaks at pore throat sizes of 6 nm and 110 nm respectively, which suggest that porosity of such samples are mainly contained in a unique range of pore size. In contrast, curve for sample SSA-42 shows a tri-modal distribution with sharp peaks at pore

throat sizes 12 nm, 6 nm, and 4 nm. The measured physical properties for all samples are summarized in Table 6.2. Samples present low porosities (<5%). This study is not concerned with transport properties of the materials and permeabilities have not been measured. Even though mudstones show a wide range of porosities (Potter *et al.* 2005), low permeability values are characteristic of such rocks because flake-like clay minerals lie over one another generating unconnected porosity and sinuous path that makes difficult for fluids to flow.

X-Ray Fluorescence (XRF) analysis was performed on all samples to determine the content of oxides in terms of weight percent. Loss on ignition (LOI) is used to estimate carbonate and organic content in those sediments (Dean 1974; Heiri, Lotter and Lemcke 2001) in terms of weight percent. X-Ray Diffraction (XRD) analysis was used to identify their mineralogical content. Results are presented in Tables 6.3 and 6.4.

Alumina (Al_2O_3) and potassium oxide (K_2O) are associated with presence of clay minerals (Boggs 2009) as can be noted in Table 6.4 where clay minerals identified in such samples include chlorite, and kaolinite, as well as smectite and illite. According to Boggs (2009), the weight percent of silica (SiO_2), alumina and potassium oxide in a typical mudstone ranges 57-68 %, 16-19 %, and 2.5-5 % respectively; however, such percentages may considerably vary subjected to the mineralogy of the rock, thus for example, silica and alumina content in Table 6.3 ranges 35.77-66.50 % and 7.32-17.57 % for each oxide. The high content of magnesium oxide (MgO) and calcium oxide (CaO) indicate presence of

carbonates such as dolomite in the argillite and samples SSA-27, SSA-41 and SSA-42. Meanwhile, sodium and potassium oxides (Na_2O and K_2O) identify existence of feldspars among which can be found albite (SSA-41 and SSA-42) and microcline (Argillite). Pyrite (iron sulfide) in samples SSA-27, SSA 41, and SSA-42 indicate that those shales developed in an anoxic environment (Potter *et al.* 2005). Mica minerals found are muscovite (Argillite and sample SSA-42) and alurgite (sample SSA-27). Other oxides identified in the samples studied in this work include titanium dioxide (TiO_2), phosphorous pentoxide (P_2O_5), Chromium oxide (Cr_2O_3), and vanadium oxide (V_2O_5).

Although LOI is not a direct measure of Total Organic Carbon (TOC), different works found high degree of correlation between LOI results and TOC in a variety of organic sedimentary samples (Dean 1974; De Vos *et al* 2005; Wright, Wang and Reddy 2008). In this sense, LOI percentages in Table 6.3 would indicate that the samples studied have a rich organic content, i.e., their TOC percent ranges 2-30% (Tyson 1995).

Figures 6.6 and 6.7 show photographs of thin sections, Scanning Electron Microscopy (SEM) images and 15.6 μm resolution X-ray Microtomography (μ-CT) images for samples SSA-24, SSA-27 and SSA-42 in the direction perpendicular to bedding ($X_3 - X_1$ plane). Thin sections for samples SSA-24 and SSA-27 (Figures 6.6a and 6.6d) show interbedded clay-silt minerals (white portions) with abundant organic material (black portions). The proportion of organic material significantly decreases in sample SSA-42 with respect to samples SSA-24 and SSA-27 as can be observed in Figure 6.7a where there is a higher

prevalence of clay-silt minerals than organic material leading to poor layering. LOI results (see Table 6.3) also confirm that sample SSA-42 has the lowest proportion of organic material among the samples studied. Flake-like shaped clay minerals lying horizontally can be observed in Figures 6.6b, 6.6e and 6.7b, the presence of which has long been known to produce anisotropy (Kaarsberg 1959; Jones and Wang 1981; Lo *et al.* 1986; Johnston and Christensen 1995). μ-CT images show that internal structure of samples SSA-24 and SSA-27 comprises microcracks lying parallel (Figure 6.6c) and quasi-parallel to bedding plane (Figure 6.6f). Meanwhile horizontal quartz minerals laminae are observed in μ-CT images of sample SSA-42 (Figure 6.7c).

6.4 Experimental procedure

Dynamic and static moduli and their dependence on confining pressure on prism-like shape samples trimmed from an outcrop and a variety of well cores from Southern Alberta, Canada are studied. Measurements were taken by using a pressure vessel in two different cycles: compressing and decompressing.

6.4.1 Velocity measurements

As explained in section 3.4.4, velocities were determined using pulse transmission method by simply dividing the sample´s length on the measured direction over the travel time; however, another dynamic effect that is taken into account when estimating ultrasonic velocities is the pulser transducer excitation delay, a topic that is addressed in Appendix A1. This correction is automatically accounted for when end caps are used (as in Chapter 4). Here, however, the piezoelectric

ceramics are mounted directly onto the sample and the finite rise-time of the ceramic once it has been activated must be accounted for to provide the proper transit time through the sample.

6.4.2 Strain measurements

The foil strain gauge technique is used in this work to measure strain on studied samples. This technique is based on the piezo-resistive effect which is characteristic of some materials and consists of the property of changing their resistance when subjected to stress. The foil SG technique has been extensively employed by several authors (Schock and Heard 1974; Batzle and Simmons 1976; Schmitt and Zoback 1989; Schmitt and Li 1995; Adam *et al* 2009; Bakhorji 2010). The relationship between the change in resistance and strain is expressed by (Bakhorji 2010):

$$\frac{\Delta R}{R} = G_f \varepsilon \qquad\qquad 6.22$$

where R is the resistance of the undeformed SG and G_f is the sensitivity strain or gauge factor provided by the manufacturer. When measuring strain, the changes in resistance are small compared to that of the resistance of the strain gauges (3 to 6 orders of magnitude). Such small values are difficult to measure since most ohm- meters lack of required resolution; in this sense, what is most often used to measure changes in resistance is the Wheatstone bridge circuit. Thus, the strain gauge takes the place of one of the four resistances that comprises the Wheatstone bridge circuit and then the strain can be estimated as (Bakhorji 2010):

164

$$\varepsilon = \frac{-4V_r}{G_f(1 + 2V_r)} \qquad\qquad 6.23$$

V_r is defined as follows

$$V_r = \frac{V_{out}(strained) - V_{out}(unstrained)}{V_{in}} \qquad\qquad 6.24$$

where $V_{in}$is the input voltage of the circuit, $V_{out}(unstrained)$is the output voltage under unstrained conditions and $V_{out}(strained)$ is the output voltage when applying stress; however, several authors (Brace 1964; Milligan 1967; Kular 1972) have shown that strain measurements are affected by pressure effects, i.e., theoretical strain differs from measured strain. Such pressure effects are subject to the employed strain gauges and are independent on the sample´s elastic properties (Brace 1964). Appendix A2 addresses strain gauges calibration due to pressure effects.

6.4.3 Sample preparation

Samples were trimmed from the main core by using a rotating saw to obtain the three different orientations. In order to reduce noise and improve coupling between transducers and the sample, the trimmed surfaces were smoothed and ground to be parallel to one another (within ± 0.1 mm) employing both a spinning polisher and a fine grain sand paper.

Samples were dried under a vacuum at 70°C for 72 hours to avoid presence of free water and then kept in a desiccator jar.

To mount the transducers, a thin strip of copper acting as a ground (negative pole) is attached to the sample using quick epoxy. Once the quick epoxy is solidified the transducer is bonded to the strip cooper with a layer of conductive silver

epoxy and on top on the transducer another strip of copper (positive pole) is attached to the transducer with conductive silver epoxy. At this point, proper alignment of the highly laterally polarized transmitter and receiver S-wave transducers with each other across the sample is essential. After the conductive epoxy is solidified two wires are soldered on each piece of copper. Transducers arrangement is as follows: $V_P(0^o), V_P(90^o)$, and $V_P(45^o)$ as well as $V_S(0^o)$ and $V_{SH}(90^o)$ are measured on all samples as needed to determine the required elastic constants. For comparative purposes, $V_{SH}(45^o, 53^o)$ are estimated on SSA-24 and argillaceous samples respectively; however, $V_{SV}(45^o)$ are estimated on samples SSA-27, SSA-41, and SSA-42 in order to reduce uncertainty in the estimation of elastic constant C_{13} (Hemsing 2007).

For strain measurements, two strain gauges (CEA-06-250UT-350) from Vishay Micro-Measurements with gauge factor G_f =2.11 and nominal resistances of 350 ohms were glued directly on the sample in directions perpendicular and parallel to bedding.

Each strain gauge was independently connected in a Wheatstone bridge with three high-quality fixed resistors each of 350 ohms to create the unbalanced Wheatstone bridge.

Figure 6.8(a) shows a picture of the transducer and strain gauge set up on sample SSA-27. The sample is then sealed with urethane putty to avoid leakage of the confining pressure fluid into the sample as shown in Figure 6.8(b). Once the

sample has been sealed, it and the fused quartz standard are placed into a pressure vessel.

6.4.4 Experimental Configuration

The experiment consists basically of a pulse- generator/receiver system, a digital oscilloscope and a pressure vessel that can apply a confining pressure of up to 60 MPa. The transmitter is activated by applying a fast rising (5 ns) 200 V square wave to the piezoelectric ceramic which produces a mechanical disturbance. The generated elastic wave is then recorded by the digital oscilloscope after travelling through the sample. Pressure was increased from 0 to 48 MPa in the compressing cycle and from 48 to 0 MPa in the decompressing cycle for argillaceous sample and 0 to 60 MPa in the compressing cycle and from 60 to 0 MPa in the decompressing cycle for samples SSA-24, SSA-27, SSA-41 and SSA-42.

A full set of 6 waveforms at the different orientations and polarizations were recorded at increments of approximately every 3 MPa. The ultrasonic signals were digitized with a sampling period of 10 ns.

For the strain measurements, the setup consists in a Wheatstone bridge circuit activated by V_{in} = 2.5 V provided from a constant voltage supply with V_{out}. recorded with a digital voltmeter to measure V_{out}. This setup was controlled by an in-house designed Labview® program. Figure 6.9 shows a schematic of the experimental configuration.

6.5 Results

6.5.1 Velocity results

One P-wave and one S-wave velocity were measured on the directions perpendicular, parallel and oblique to bedding for each specimen. Figure 6.10 shows some examples of the recorded waveforms. The error sources considered when estimating velocities, besides the piezo-electric ceramic delay, are the sample´s parallelism uncertainty (0.1 mm) and the sum of the picking travel time (sampling rate) of both sample and standards recorded waveforms (0.02 μs). In this sense, the estimated error is a maximum of 0.3 and 0.2 % for P-waves and S-waves respectively.

Comparison of the various wave speeds for the samples (see Figure 6.11) displays strong anisotropy. There are a few points to highlight:

- All of the observations are consistent with the assumed transverse isotropy for the samples with,

  i. $V_P(0^o) < V_P(53^o, 45^o) < V_P(90^o)$

  ii. $V_S(0^o) < V_{SH}(53^o, 45^o) < V_{SH}(90^o)$ for argillaceous and SSA-24 samples, and $V_S(0^o) < V_{SV}(45^o) < V_{SH}(90^o)$ for samples SSA-27, SSA-41 and SSA-42.

  iii. Table 6.5 show the differences in percentage between horizontal $(\theta = 90^o)$ and vertical $(\theta = 0^o)$ P- and S- waves at low and peak pressures for all samples in the compressive cycle where a decrease in anisotropy as a function of confining pressure can be observed as a

consequence of closure of microcracks and pores. Sample SSA-24 exhibits the highest anisotropy and, in contrast, anisotropy in sample SSA-42 is significantly lower than anisotropy observed in the rest of the studied samples, which can be as a result of the poor layering shown by this sample as shown in Figure 6.7a.

- Observations show that velocities increase as a function confining pressure, i.e., samples become stiffer as a consequence of closure of microcracks and pores.

- Hysteresis effects are observed in all samples, i.e., pressurization velocities are slightly lower than depressurization velocities as a result of differences in the closing/opening rate of microcracks and pores during the the compression/decompression cycles respectively (Gardner *et al* 1965).

- The high gradient velocity increase at low pressures (< 25 MPa) followed by a slow velocity increase at higher pressures observed for $V_P(0^o)$ in sample SSA-41 suggests that velocities in such sample are controlled by microcraks (He 2006) aligned parallel to bedding unlike measured velocities in samples SSA-24, SSA27, SSA-42 and argillaceous samples which show a quasi-linear behaviour characteristic of the closure of more equant-dimensioned pores (Kuster and Toksöz 1974).

6.5.2 Phase and group velocities

In ultrasonic experiments, dynamic elastic properties of geologic materials are estimated from recorded P- and S- waveforms under the assumption that phase velocities rather than group velocities are measured. In a VTI medium this is

particularly true when P- and S-wave velocities are measured in the directions parallel and perpendicular to symmetry axes since both phase and group velocities propagate with the same angle on such orientations. However, at off-axis symmetry directions, both phase and group velocities propagate both with different angles. Thus, it is important to know whether phase or group traveltimes are detected by the piezoelectric transducer before we attempt to estimate the critical parameter C_{13}. In ultrasonic experiments, group velocity represents the wave energy, or ray, propagation whereas the phase velocity denotes plane wave propagation. Figure 6.12 shows an example of an arbitrary wavefront at a given time t_n that propagates through a VTI medium at an oblique orientation with respect to bedding. If the plane portion of the wavefront (in black) reaches the receiver transducer (of length-diameter l) then what is measured is the phase velocity represented by the vector $\vec{V}$ and instead, if the curved part of the wavefront (in red) contacts the receiver transducer then the group velocity $\vec{g}$ is recorded. The angle between the group and phase velocity is denoted by $\Delta = \emptyset - \theta$. Thus, in order to determine whether receiver transducer detected phase or group traveltimes is necessary to estimate the lateral energy displacement of the wavefront. Dellinger and Vernik (1994) provided the expression to estimate the total lateral energy displacement, D, at 45° from the separation distanced between the piezo-electric ceramics H, and the estimated velocities:

$$D_x$$

$$= H \frac{\left(V_P^2(90^o) - V_P^2(0^o)\right)}{2V_x^2(45^o)}$$

$$\cdot \frac{\left(V_{SV}^2(90^o) + V_{SV}^2(0^o)\right) - 2V_x^2(45^o)}{\left(V_P^2(90^o) + V_P^2(0^o)\right) + \left(V_{SV}^2(90^o) + V_{SV}^2(0^o)\right) - 4V_x^2(45^o)} \qquad 6.25$$

where x represents either P or SH. The expression for SH is given by

$$D_{SV} = H \frac{\left(V_{SH}^2(90^o) - V_{SH}^2(0^o)\right)}{2V_{SH}^2(45^o)}. \qquad 6.26$$

In this sense, if $D < l$ we will claim that phase traveltimes were recorded. In addition, Δ can be estimated in terms of D and H as follows: $\Delta = arctan(D/H)$. Even though equations 6.25 and 6.26 are suited for samples SSA-24, SSA-27, and SSA-41 as well as SSA-42 where oblique orientation was cut at 45°, waveform displacement and Δ for argillaceous sample (oblique orientation at 53°) were also estimated. Table 6.6 summarizes the results for the studied samples at low and peak pressures in the compressive cycle considering a diameter of 20.00 mm for the circular P-wave transducers and a width of 10.00 mm for the square S-wave transducers. Results suggest that receiver transducer is detecting phase traveltimes since $D_P < l_P = 20\ mm$ and $D_{SV} < D_{SH} < l_S = 10\ mm$ for all samples at both low and peak pressures besides the displacement decreases as confining pressure increases, i.e., samples become less anisotropic as shown in Table 6.5. Even if Dellinger´s equations are underestimating results for argillaceous sample, the fact that P- and S- wave deflection values for sample SSA-24 (the one that shows the most anisotropy) lays within size´s transducers

would guarantee that P- and S-receiver transducers in argillaceous sample are detecting phase velocities due to the correlation between level of anisotropy and wavefront deflection, i.e., the more anisotropic the sample the more the deflection as shown in Tables 6.5 and 6.6. Consequently, the velocities measured in the experiments may properly be used to calculate the material's elastic moduli.

6.5.3 Elastic stiffness and Thomsen parameters

Elastic constants now can be estimated from measured velocities since Dellinger´s equations suggests that both P- and S-wave receiver transducers recorded ultrasonic phase velocities. Elastic constants C_{11}, C_{33}, and C_{44} as well as C_{66} are calculated using equations 2.39 through 2.43 for all samples. However, an alternative expression to equation 2.43 was proposed by Hemsing (2007) to estimate C_{13} by using a combination of $V_P(45^o)$ and $V_{SV}(45^o)$ in order to reduce the degree of uncertainty in C_{13}:

$$C_{13}$$

$$= -C_{44} + \left[\frac{4\rho^2[V_P^2(45^o) - V_{SV}^2(45^o)]^2 - [C_{11} - C_{33}]^2}{4} \right]^{\frac{1}{2}}. \qquad 6.27$$

Thus, elastic constant C_{13} for sample SSA-24 was estimated via equation 6.27 while for samples SSA-27, SSA-41 and SSA-42 equation 2.43 was employed. In the case of the argillaceous sample, C_{13} was estimated after manipulating equation 2.35 assuming $\theta = 53^o$. Figure 6.13 shows the calculated elastic constants as a function of confining pressure for studied samples. Plots show that $C_{33} < C_{11}$ and $C_{44} < C_{66}$ as expected for a VTI symmetry in sedimentary rocks. Table 6.7 gives the corresponding calculated elastic constants along with estimated error for all

172

samples at low and peak pressures in the compressive cycle. As can be noted, samples become stiffer as confining pressure increases. The error in C_{13} is about one order of magnitude higher than the rest of the elastic constants due to the more complex expressions involving C_{13} estimation.

In order to quantify anisotropy, Thomsen parameters (Thomsen 1986) are estimated from elastic constants by using equations 4.1 to 4.3 and are plotted in Figure 6.14. Table 6.8 shows the Thomsen parameters at low and peak confining pressures in the compressive cycle. Results show that samples become less anisotropic as function of confining pressure as a consequence of closure of microcracks and pores. P- and S-wave anisotropy values (ε and γ parameters) for samples SSA-24, SSA-27, and SSA 42 practically overlap within error in a wide range of pressures, not so for argillaceous and SSA-41 samples were ε > γ. A particular case of elliptical anisotropy is observed in sample SSA-41 where ε = δ within error as well (Daley and Hron 1977).The error in C_{13} and the more complex expression to estimate δ leads to error in δ to be one order of magnitude higher than ε and γ.

6.5.4 Dynamic and static moduli

In this section, results of dynamic and static moduli as function of confining pressure obtained respectively from velocities and strain measurements are presented.

Dynamic shear and Young´s moduli as well as Poisson´s ratios assuming both a single anisotropic crystal and an isotropic polycrystalline composite are shown in

Figures 6.15 and 6.16. It can be observed from Figure 6.15 that $E_3 < E_{VRH} < E_1$ and that $\mu_V < \mu_R < G$ for all samples in all range of pressures, where $G = G_{23}$. Thus, E_{VRH} is bounded by the anisotropic vertical and horizontal Young's moduli, being $E_3 < E_1$ typically expected for laminated mudstones (Sayers 2013). In the case of Poisson's ratio, Sayers (2013) points out that ν_{31} may be less than, equal to or greater than ν_{12} for mudstones as well; where the effect of preferred alignment of clay minerals causes that $\nu_{31}/\nu_{12} > 1$, being this the case of argillaceous, SSA-27, and SSA-41 samples in all range of pressures; while the effect of the preferred alignment of organic content and microcracks causes $\nu_{31}/\nu_{12} < 1$. At low pressures, < 10 MPa, the dominant trend is $\nu_{31}/\nu_{12} < 1$ for samples SSA-24 and SSA-42; however, as confining pressure increases the trend changes to $\nu_{31}/\nu_{12} > 1$, which suggests that at low pressure the preferred orientation of organic material and microcraks have more influence in the anisotropy observed on such samples and that, at high pressures, the preferred orientation of clay minerals contributes the most to the anisotropy observed as well. On the other hand, the great variability of ν_{VRH} with respect of the vertical and horizontal Poisson's ratio does not allow a clear relation between both approximations to be obtained.

In order to estimate the static moduli, deformation as a function of confining pressure must be measured on the direction parallel and perpendicular to bedding. Stress-strain relations for all samples obtained from strain gauges measurements are shown in Figure 6.17 (top row), where it can be observed that samples deform more along axis of symmetry than along bedding plane.

Deformation along bedding is labeled as $\varepsilon_1(sta)$ and, along symmetry axis labeled as $\varepsilon_3(sta)$. Thus, by taking the slope (tangent) of the strain-stress curves (bottom row) the horizontal and vertical static linear moduli $Kl_1(sta)$ and $Kl_3(sta)$ respectively are determined. The observations show that samples are stiffer in the horizontal direction than in the vertical direction. For comparative purposes, the dynamic linear moduli are estimated by using equations 6.8 and 6.9 and are presented in Figure 6.18, confirming that samples are stiffer along bedding than within symmetry axes. Static bulk modulus for each sample is estimated by taking the slope of the volumetric deformation, $\varepsilon_V(sta)$, which for a VTI medium is defined as $\varepsilon_V(sta) = 2\varepsilon_1(sta) + \varepsilon_3(sta)$. Static bulk moduli $K(sta)$ for studied samples are presented in Figure 6.19 along with the estimated dynamic bulk moduli assuming an anisotropic single crystal K as well as the upper, K_V, and lower, K_R, bulk moduli bounds for an isotropic composite material. Plots show that $K < K_R < K_V$ for the studied samples in all range of pressures. On the other hand, for pressures > 40 MPa, static bulk modulus $K(sta)$ is greater than K for samples SSA-24 and SSA-41. In the case of sample SSA-42, $K(sta) > K$ for pressures >55 MPa. Since dynamic modulus is expected to be higher than static modulus at the same pressure, the fact that $K(sta) > K$ for three of the studied samples at high pressures suggests that the assumption of an isotropic composite material may be better suited than the approximation of the anisotropic single crystal due to $K(sta) < K_R < K_V$ for all studied samples at all pressure range. Thus, in order to quantitatively compare static bulk modulus with the dynamic bulk modulus obtained from Voigt-Reuss bounds, the VRH bulk

modulus is calculated, i.e., $K_{VRH} = (K_V + K_R)/2$. In the compressive cycle, at low pressure (3MPa), $K_{VRH}/K(sta)$ ranges from 1.64 (SSA-24) to 2.31 (SSA-27) and at peak pressure (60 MPa) from 1.11 (SSA-41) to 1.79 (SSA-27). As can be noted, the difference between static and dynamic moduli decreases as a function of confining pressure. Such difference decreases in the decompresive cycle at 60 MPa ranging from close to the unit for samples SSA-24, SSA.41, and SSA-42 to 1.36 for sample SSA-27; however, at the same decompressive cycle such ratio ranges from 1.68 (SSA-24) to 3.31 (Argillite).

6.5.5 Adiabatic and isothermal bulk moduli

The above comparisons show the relatively large differences between the dynamic and the static elastic moduli. One possible reason for this is that to begin with a ultrasonic wave propagation experiment will provide the adiabatic bulk modulus, K_{ad}, as pointed out in section 3.4.4. In contrast, static deformation measurements are made at constant temperature and the isothermal bulk, K_{iso}, is obtained. As such one possible reason for the difference between the ultrasonic and the strain gage measurements is that strictly they are measuring different elastic moduli. The adiabatic and isothermal bulk moduli can differ significantly for fluids. Indeed, Newton made this error when he first attempted to estimate the speed of sound in air when he assumed that isothermal bulk modulus applied; this resulted in his estimate of the sound speed being too low by about 20%. The differences between the two moduli are, generally, much less for most solids but it is important to test to see to what degree this may apply in our samples. We are not aware of other such tests in the literature.

K_{iso} is estimated by using equation 3.5;

$$\frac{1}{K_{iso}} = \frac{1}{K_{ad}} + \frac{T\alpha^2}{C_p}$$ where, in this case, C_p is assumed to be as that as silty clay, i.e., 1087.84 J/Kg °K (Bowers and Hanks 1962), $\alpha = 4.15\times10^{-5}$ °K^{-1} for shales (Gilliam and Morgan 1987), and T= 298.15 K. In this work, K_{ad} is taken as that obtained from the VRH average for a composite material under hydrostatic pressure, i.e., $K_{ad} = K_{VRH}$.

Table 6.9 shows a comparison between K_{ad} and K_{iso} at low and peak pressure for studied samples, where $\Delta K = K_{ad} - K_{iso}$. The result shows that temperature effect tends to overestimate the value of the bulk modulus and that this effect increases as function of confining pressure. However, differences between adiabatic and isothermal bulk modulus are marginal, of only 0.000001 %, indeed this is in reality much below any reasonable application of uncertainty with the unrealistic number of significant digits shown for purposes of illustration only. As such, we do not believe the effects of the choice of the bulk modulus employed is important here but we do not rule out potentially larger effects in kerogen rich samples.

6.6 Conclusions

We found that samples exhibit VTI symmetry, where differences in percentage between vertical and horizontal velocities can be up to 24% for P-wave velocities and 19% for S-wave velocities in sample SSA-24 for example.

Poisson's ratios obtained from estimated elastic constants as well as thin sections and SEM and µ-CT images suggest that layering and preferred orientation of microcracks and clay minerals cause the observed anisotropy. Dynamic and static measurements also show that samples are stiffer on the direction perpendicular to assumed axis of symmetry (i.e., within the $X_1 - X_2$ plane) than perpendicular to it. Results for dynamic bulk modulus show that, statistically speaking, the assumption of an isotropic polycrystalline material is better suited than considering an anisotropic single crystal to represent the dynamic bulk modulus of specimens studied in this work. In this sense, K_{VRH} can be up to 3.31 times higher than $K(sta)$ at low pressures (3 MPa), and close to the unit for peak pressures (60 MPa).

On the other hand, estimation of isothermal bulk modulus from adiabatic bulk modulus shown that temperature has a marginal effect on elastic properties of studied samples.

Apendix A1. Calibration of traveltimes

In order to calibrate ultrasonic traveltimes due to the excitation delay of the transducers, waveforms of ultrasonic P- and S- waves travelling through four calibration standards at room pressure were recorded. Such standards consists of Aluminum 6061-T6 cylinders of 5.080 cm of diameter and lengths of 0.029, 0.040, 0.050 and 0.060 cm respectively (Figure 6-A1). To take the measurements, one P- and one S- wave transducers with proper alignment and polarization were mounted on each standard´s flat side. Thus, ultrasonic P- and S- wave travel times were picked from the first extremum of the recorded waveforms and then

plotted against their corresponding length as shown in Figure 6-A2, where the intercepts of the fitted linear equations correspond to the transducer excitation delays for each mode of propagation, i.e., $\Delta t_P = 0.49\ \mu s$ for P-wave mode and $\Delta t_S = 1.13\ \mu s$ for S-wave mode, while slopes represent the P- and S-wave slowness of the medium, i.e., $V_P = 1/162$ m/μs = 6098 m/s and $V_S = 1/319$ m/μs = 3135 m/s .

For comparative purposes, P- and S-wave velocities of Aluminum 6061-T6 at atmospheric pressure are 6299 m/s and 3178 m/s respectively (http://ndtsystems.com/Reference/Velocity_Table/velocity_table.html), being correspondingly 3.64 and 1.37 % higher than the estimated velocities.

Velocities of both P- and S-waves travelling through different orientations of the sample are then estimated using the travel times picked from the first extremum of the recorded signals and then subtracting their corresponding mode transducer delay.

Apendix A2. Calibration of strain gauges

To correct strain gauge measurements for pressure effects, a fused quartz calibration standard, which pressure dependent properties are well known, was used. Thus, strain measurements on both sample and fused quartz standard were simultaneously measured as a function of confining pressure. The measured strain values for the standard fused quartz were then corrected by using the calculated strain values obtained from its known bulk modulus which changes as a function of confining pressure were calculated by using the following relation:

$$K_s(P) = K_{so} + (\partial K/\partial P)\Delta P + (\partial K/\partial T)\Delta P \qquad \text{6-A1}$$

where, at ambient conditions, the bulk modulus of the fused quartz is $K_{so}= 36.24$ GPa (Ohno *et al* 2000), P is the confining pressure and T the temperature in Kelvins. Values for $\partial K/\partial P$ and $\partial K/\partial T$ used in this work are -6 and 16 MPaK^{-1} respectively (Ohno *et al.* 2000). Hence, the correction strain values for fused quartz strain measurements can then be calculated from the following equation:

$$K_s(P) = \frac{\Delta P}{\Theta} = \frac{\Delta P}{3\varepsilon} \qquad \text{6-A2}$$

where Θ is the volumetric strain.

Thus, the corrected standard fused quartz values (pressure effects) were then used to correct the observed strain sample data.

Tables

Sample	Sample depth (m)	Alberta Township System (ATS) location	Formation
SSA-24	4236.0	16-05-06-01 **W5**	Nord
SSA-27	1041.3	10-34-42-22 **W4**	Second White Speckled Shale
SSA-41	627.28	11-12-06-16 **W4**	Base Fish Scales Marker
SSA-42	1647.4	04-08-13-27 **W5**	Colorado

Table 6.1 Depth, location, and geological formation of shale samples studied.

Sample	Bulk density (Geopyc) g/cm^3	Grain density (Helium pycnometer) g/cm^3	Porosity %	Bulk density* g/cm^3	Grain density* g/cm^3	Porosity * %	Pore size diameter* (μm)
Argillite	2.6848	2.6856	< 1.0	2.6980	2.7134	< 1.0	32.932
SSA-24	2.2710	2.3058	1.5	2.3386	2.4101	3.0	0.006
SSA-27	2.4822	2.4902	< 1.0	2.3942	2.5054	4.4	0.011
SSA-41	2.3890	2.4621	3.0	2.4139	2.5216	4.3	0.005, 0.004
SSA-42	2.6546	2.6976	1.6	2.6005	2.6454	1.7	0.012, 0.006,004

Table 6.2 Physical properties of the samples. * Values obtained from mercury porosimeter.

Sample	SiO$_2$ %	Al$_2$O$_3$ %	Fe$_2$O$_3$ %	MnO %	MgO %	CaO %	Na$_2$O %	K$_2$O %	TiO$_2$ %	P$_2$O$_5$ %	Cr$_2$O$_3$ %	V$_2$O$_5$ %	LOI %	Total %
Argillite	35.77	7.32	1.22	0.03	12.06	14.55	0.42	4.46	0.23	0.09	< 0.01	0.01	23.38	99.53
SSA-24	57.64	17.57	0.80	0.01	0.39	0.16	0.12	1.38	0.90	0.06	0.01	0.04	20.12	99.19
SSA-27	63.32	9.84	3.05	0.013	1.95	5.07	0.55	2.08	0.56	0.2	0.02	0.035	11.85	98.53
SSA-41	66.27	9.30	4.06	0.02	2.00	2.35	0.67	2.00	0.44	0.34	0.02	0.03	11.31	98.80
SSA-42	66.50	10.90	3.64	< 0.01	2.38	2.93	0.53	2.24	0.55	0.15	0.01	0.01	7.18	97.00

Table 6.3 Whole rock analysis. XRF and LOI results are presented as weight percent.

Sample	Minerals
Argillite	Dolomite, Clinochlore, Muscovite, Microcline, Quartz.
SSA-24	Quartz, Kaolinite.
SSA-27	Alurgite, Calcite, Quartz, Pyrite, Dolomite, Kaolinite.
SSA-41	Quartz, Dolomite, Pyrite, Beidellite, Illite, Clinochlore, Albite.
SSA-42	Quartz, Dolomite, Pyrite, Muscovite, Chlorite, Albite.

Table 6.4 Minerals identify from XRD analysis.

Sample	Pressure [MPa]	VP(%)	VS(%)
Argillite	3	22	14
	48	18	12
SSA-24	3	24	19
	60	15	15
SSA-27	0	19	17
	60	14	15
SSA-41	0	18	13
	60	12	11
SSA-42	0	10	9
	60	6	6

Table 6.5 Differences in percentage between horizontal and vertical P- and S-wave velocities in the compressive cycle.

Sample	Pressure [MPa]	D_P (mm)	D_S (mm)	Δ_P (Degrees)	Δ_S (Degrees)
Argillite	3	15.46	6.87	19.82	9.09
	48	12.57	6.10	16.33	8.10
SSA-24	6	17.24	12.03	16.85	11.94
	60	10.90	9.74	10.84	9.71
SSA-27	3	8.64	2.64	9.22	2.85
	60	6.49	1.20	6.95	1.29
SSA-41	3	7.25	1.19	10.39	1.72
	60	4.81	0.51	6.94	0.74
SSA-42	3	4.92	0.21	6.28	0.27
	60	2.86	0.20	3.66	0.25

Table 6.6 Total lateral displacement and angle between group and phase velocities. D_S and δ_S correspond to SH-waveforms for Argillite and sample SSA-24 and, on the other hand, they are referred to SV-waveforms for samples SSA-27, SSA-41 and SSA-42.

Sample	Pressure [MPa]	C_{11} [GPa]	C_{33} [GPa]	C_{44} [GPa]	C_{66} [GPa]	C_{13} [GPa]
Argillite	3	39.41 +/- 0.17	23.72 +/-0.13	14.03+/-0.07	19.03+/-0.07	10.54+/-0.72
	48	42.41 +/-0.19	28.69 +/-0.17	15.29 +/- 0.08	19.96+/- 0.08	9.10+/-1.03
SSA-24	3	22.74 +/-0.09	13.95 +/-0.06	7.42 +/-0.03	11.23 +/- 0.04	-0.10 +/-0.19
	60	24.09+/-0.10	17.60 +/- 0.08	8.24 +/- 0.03	11.50+/- 0.05	1.25+/-0.20
SSA-27	3	37.98+/-0.12	25.13 +/-0.11	11.83 +/-0.05	17.19 +/-0.07	9.24 +/-0.17
	60	42.25+/-0.13	31.01 +/-0.13	13.31 +/-0.06	18.30 +/-0.08	11.82+/-0.19
SSA-41	3	33.45 +/- 0.18	22.41+/- 0.15	11.02 +/- 0.08	14.55 +/- 0.08	5.08+/-0.22
	60	35.55 +/-0.19	27.36+/-0.19	12.25 +/-0.08	15.48 +/-0.08	6.47 +/-0.24
SSA-42	3	55.84 +/-0.26	45.64 +/- 0.29	16.93 +/- 0.11	20.35 +/- 0.09	13.60+/-0.34
	60	59.38 +/- 0.28	52.38 +/-0.33	19.26 +/-0.12	21.85+/-0.10	16.37+/- 0.38

Table 6.7 Elastic constants for all samples at low and peak pressures.

Sample	Pressure [MPa]	ε	γ	δ
Argillite	3	0.331+/-0.006	0.178+/-0.005	0.517+/-0.040
	48	0.239+/-0.005	0.153+/-0.004	0.430+/-0.043
SSA-24	3	0.369+/-0.005	0.275+/-0.004	0.130+/ -0.021
	60	0.184+/-0.004	0.198+/-0.004	0.007+/ -0.013
SSA-27	3	0.255+/-0.004	0.234+/-0.005	0.399+/-0.016
	60	0.181+/-0.004	0.187+/-0.004	0.290+/-0.013
SSA-41	3	0.246+/-0.007	0.159+/-0.006	0.254+/-0.021
	60	0.150+/-0.006	0.132+/-0.006	0.148+/-0.016
SSA-42	3	0.112+/-0.005	0.104+/-0.005	0.041+/-0.012
	60	0.067+/-0.004	0.067+/-0.005	0.050+/-0.012

Table 6.8 Thomsen parameters for all the samples at low and peak pressures.

Sample	Pressure [MPa]	$K_{ad}(VRH)$ [Pa]	K_{iso} [Pa]	ΔK [Pa]
Argillite	3	13138500904	13138500823	82
	48	16012991597	16012991476	121
SSA-24	3	6352087753	6352087734	19
	60	8025385085	8025385054	30
SSA-27	3	16032609384	16032609263	122
	60	19302734581	19302734405	176
SSA-41	3	12958559054	12958558975	79
	60	14770165353	14770165249	103
SSA-42	3	26745807483	26745807144	338
	60	29738199878	29738199460	418

Table 6.9 Comparative between adiabatic bulk modulus and isothermal bulk modulus.

Figures
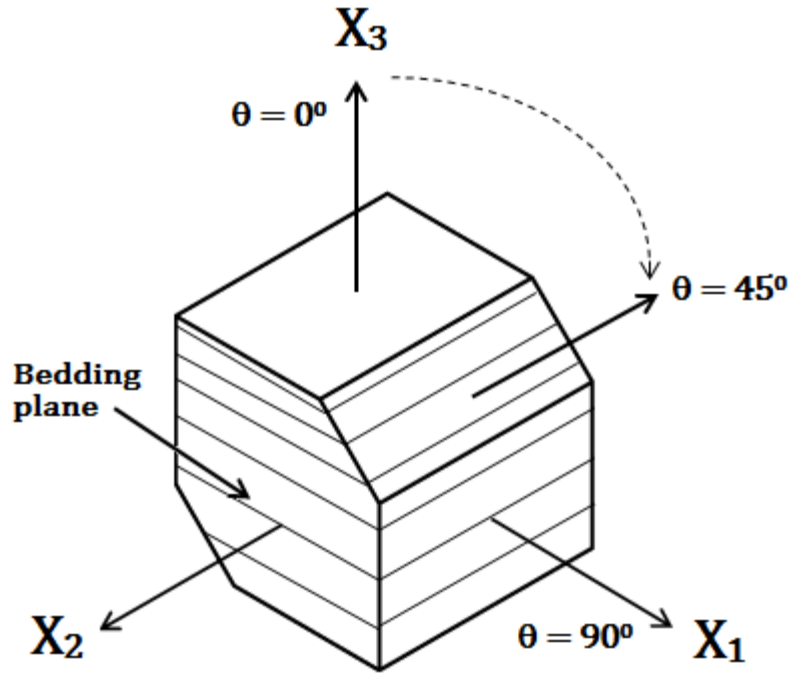
Figure 6.1 Schematic of the geometry used in the experiment to characterize a VTI medium (in this case, the oblique orientation is taken at $\theta = 45^\circ$).
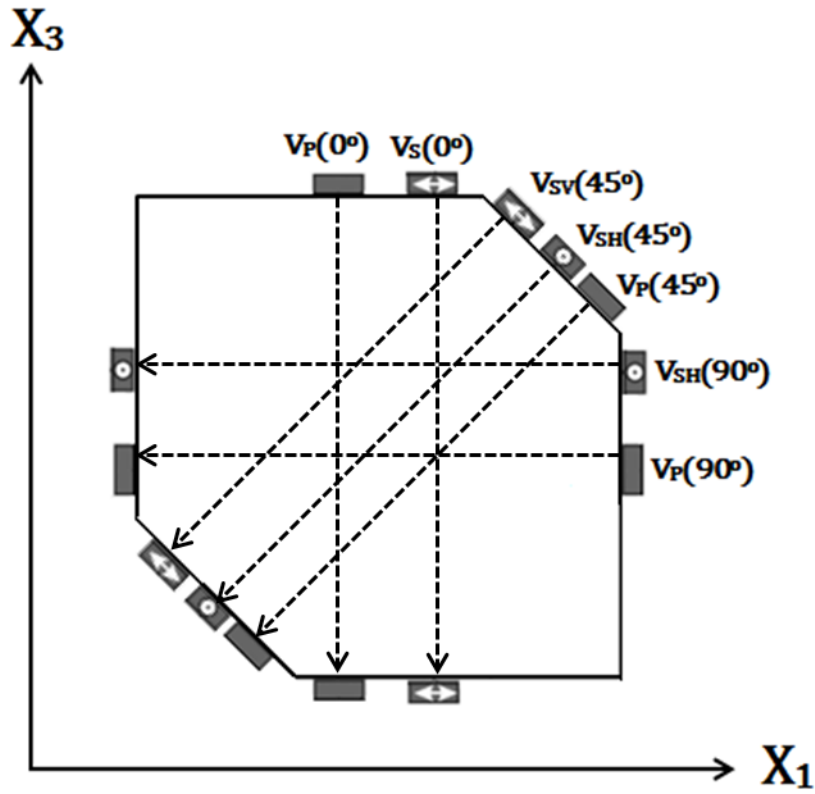
Figure 6.2 Profile in the $X_1 - X_3$ plane of the geometry portrayed in Figure 1 showing layout of pulser-receiver transducers and particle polarization with respect to symmetry axisX_3. *Modified from Wong et al 2008.*
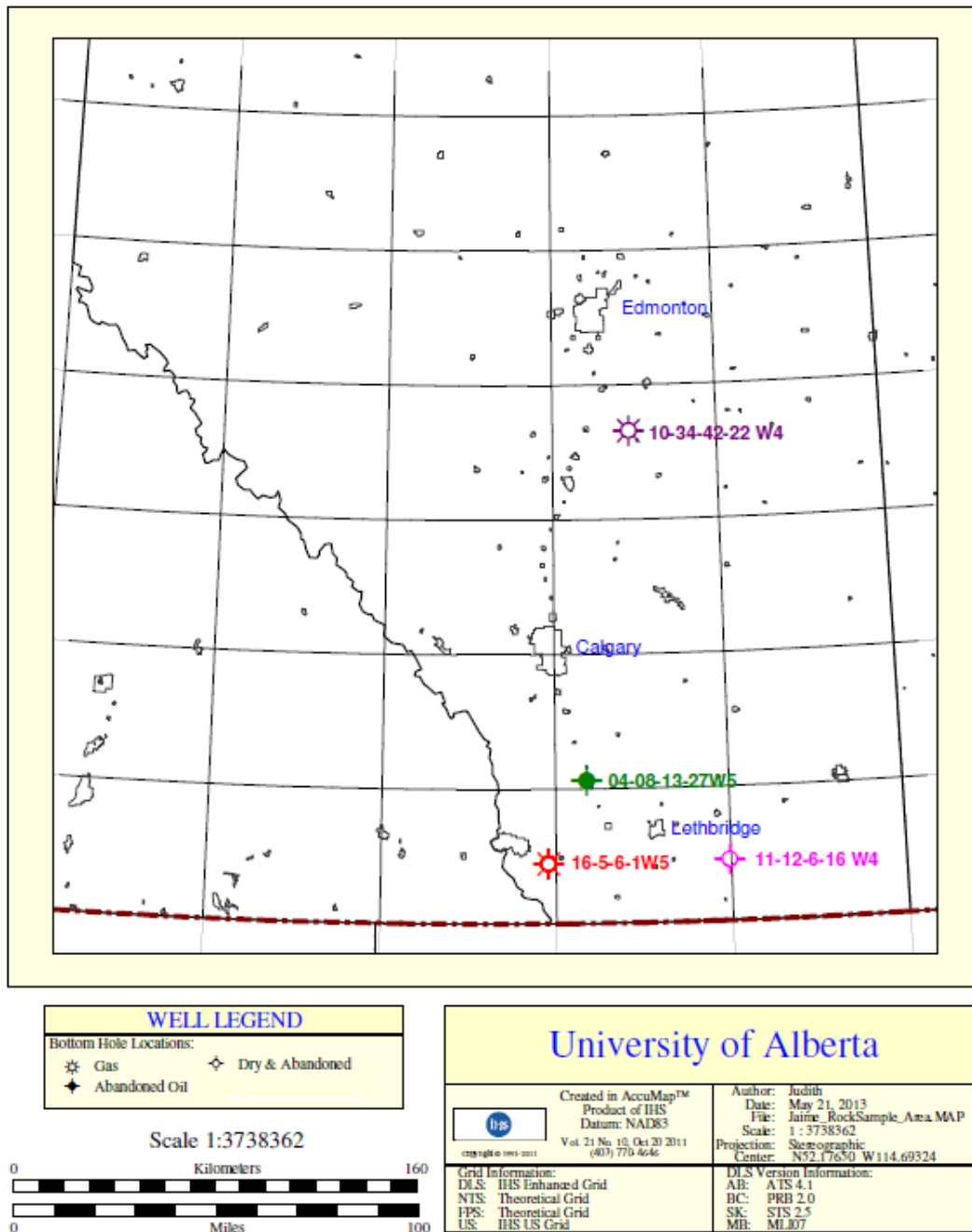
Figure 6.3 Location of shale sample in ATB coordinates projected on a latitude-longitude grid.
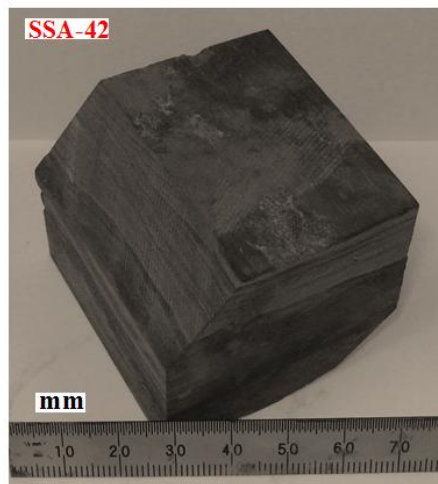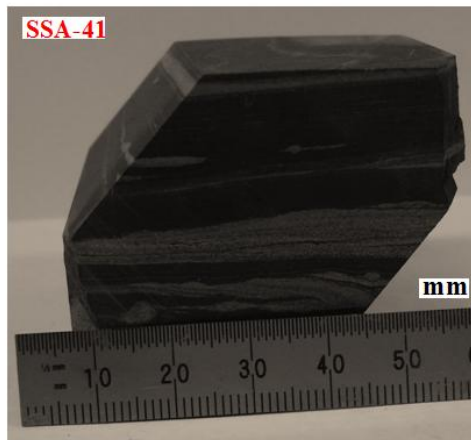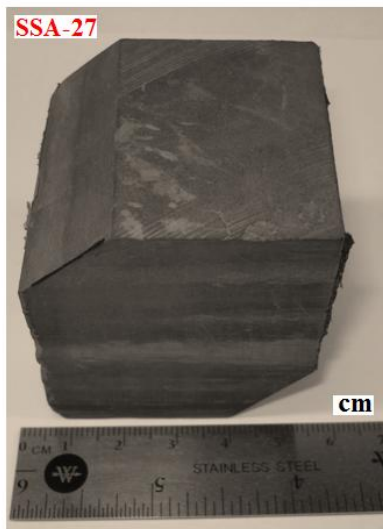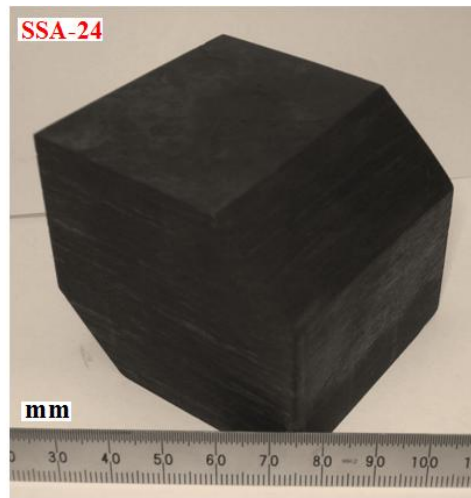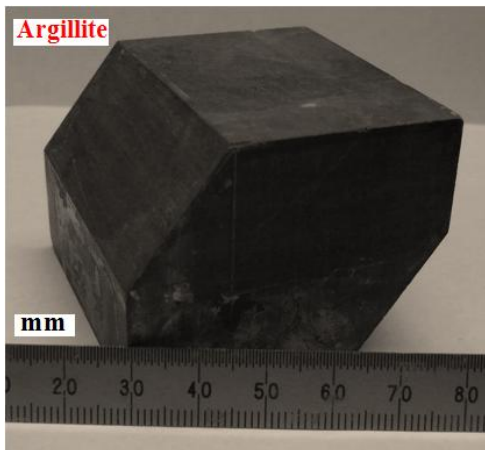
Figure 6.4 Photographs showing the samples trimmed in a prism-like shape needed to characterize a VTI medium.
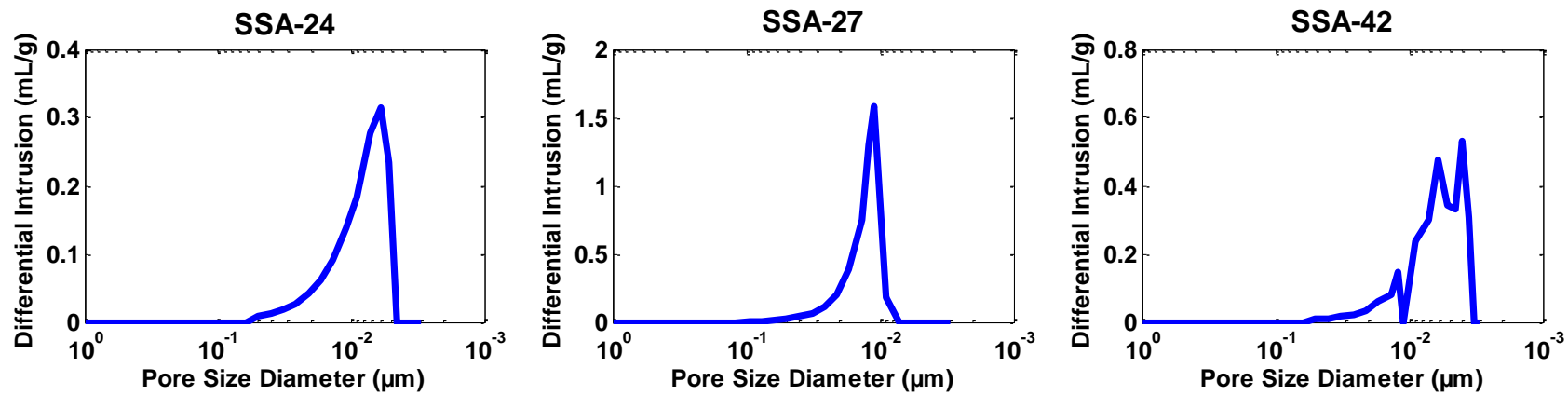
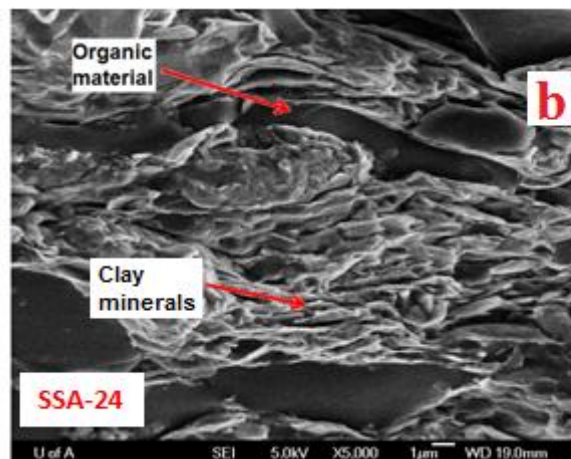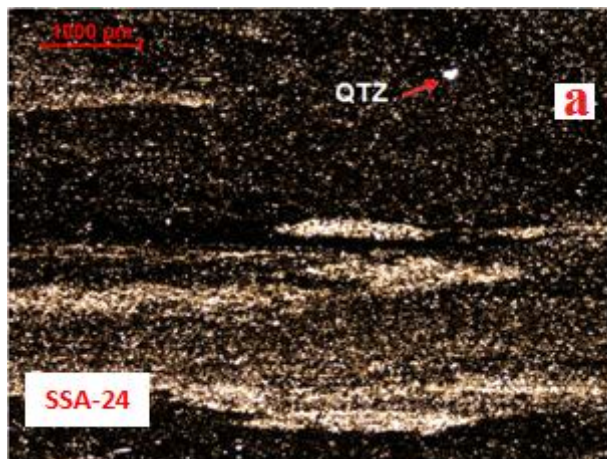Figure 6.5 Differential intrusion against pore-size diameter.
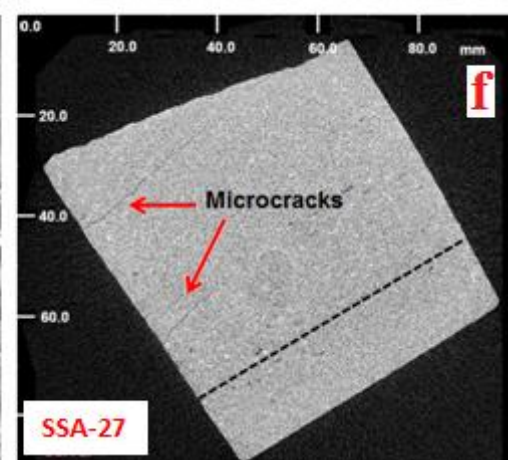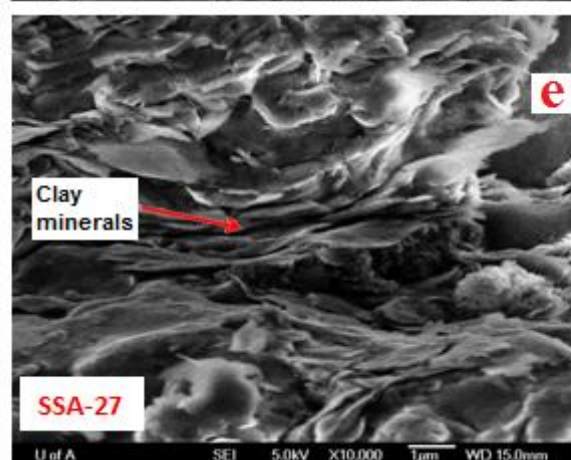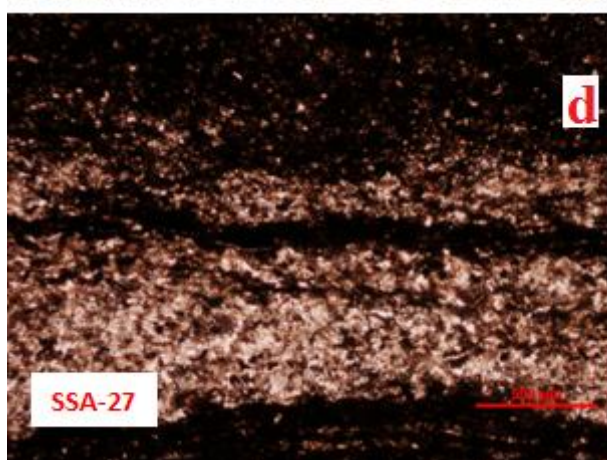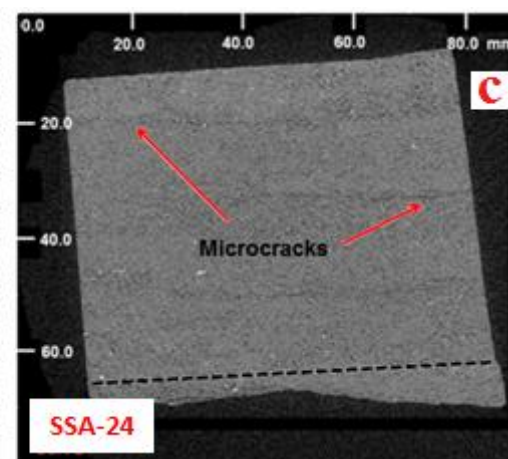
Figure 6.6 a) Thin section for sample SSA-24.Interbbed clay-silt minerals (white portions) with organic material (black portions) comprises this sample. A dispersed quartz clast is also identitified. b) SEM image for sample SSA-24. Flake-like minerals (Kaolinite) along with organic material lying horizontally can be observed. c) μ - CT image of sample SSA-24. Dotted black line (as in Figures 6f and 7c) represent the bedding plane. Internal structure shows microcracks along bedding direction. d) Thin section for sample SSA-27 showing interbedded clay-silt minerals with organic content. e) SEM image for sample SSA-2 shows kaolinite minerals aligned parallel to bedding as in sample SSA-24 f) μ - CT image for sample SSA-27 reveals quasi-parallel to bedding microcraks.
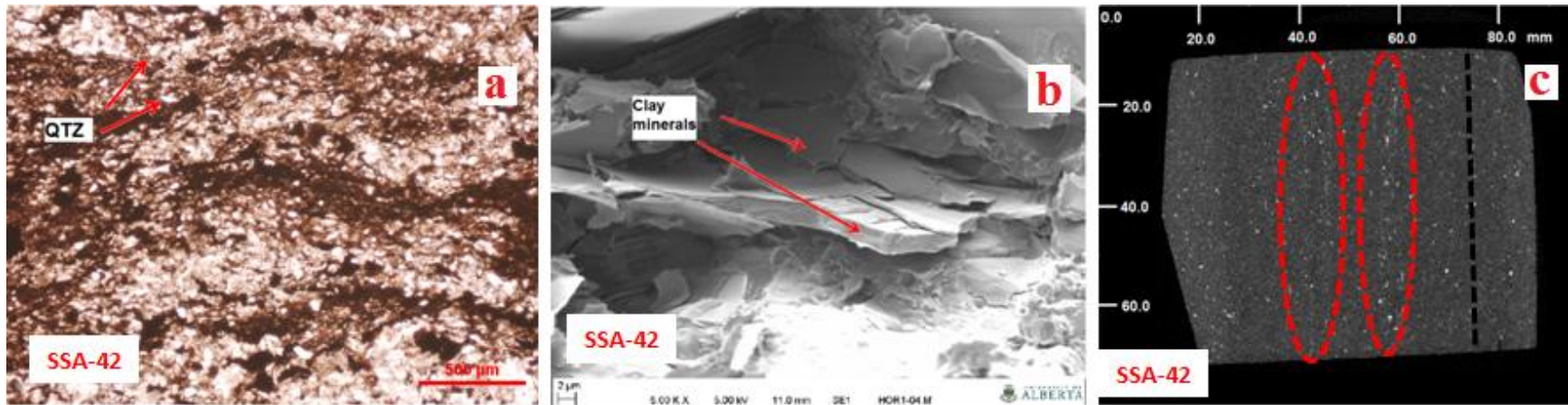
Figure 6.7 a) Thin section for sample SSA-42 reveals a considerable decrease in organic material content with respect to samples SSA-24 and SSA-27. Poor layering is observed. b) SEM image for sample SSA-42 shows, clay minerals aligned parallel to bedding. c) μ - CT image of sample SSA-42 shows horizontal quartz minerals laminae (red dotted circles) aligned along bedding.
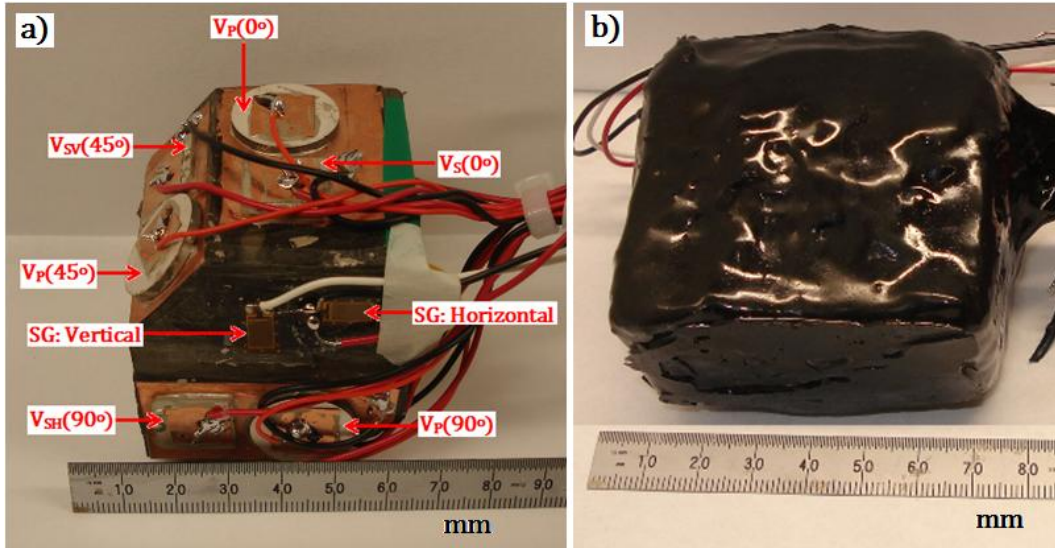
Figure 6.8 a) Photographs showing the piezoelectric transducers and the strain gauges (SG) mounted on sample SSA-27, b) and sample sealed with urethane putty.
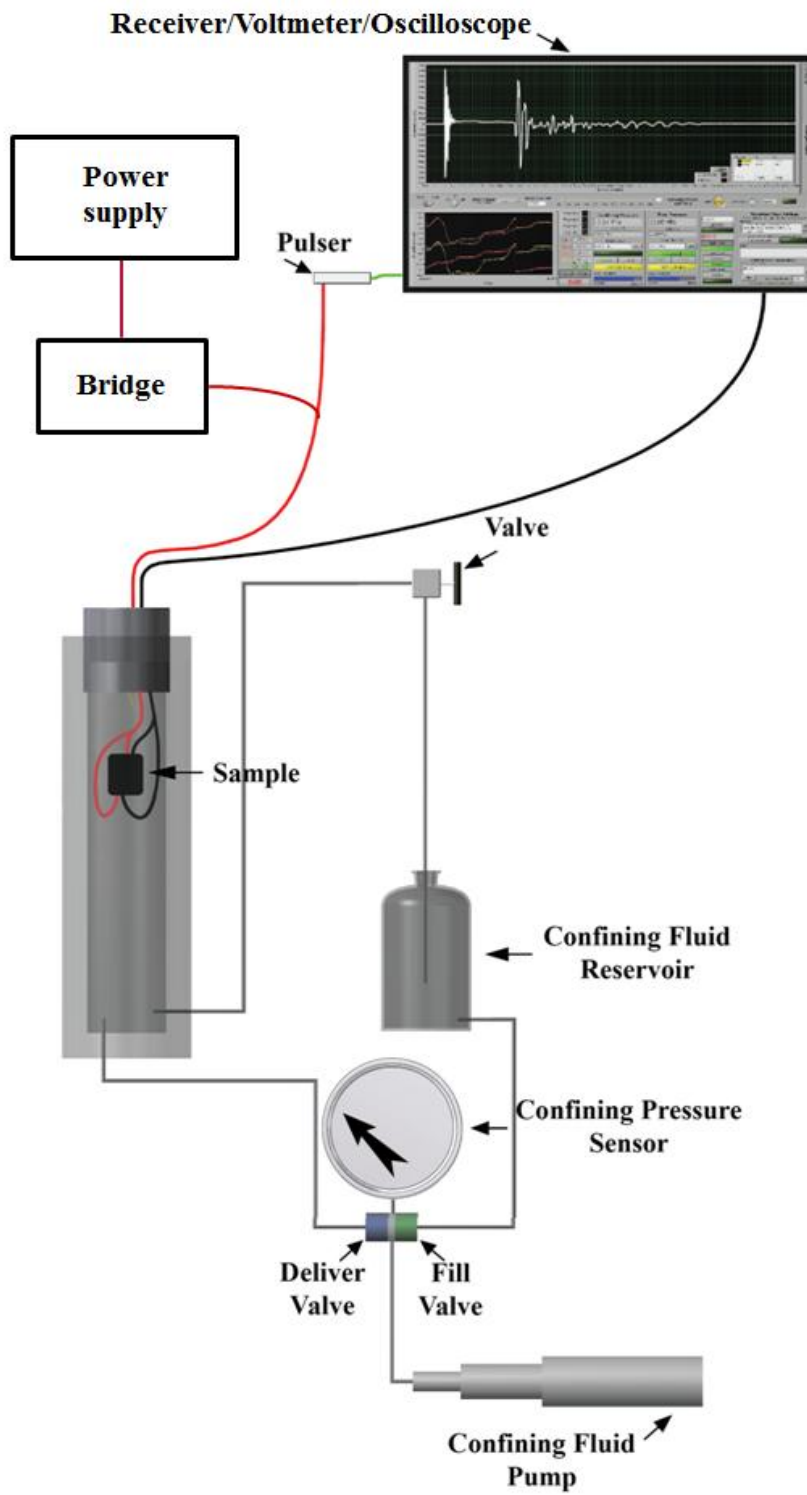
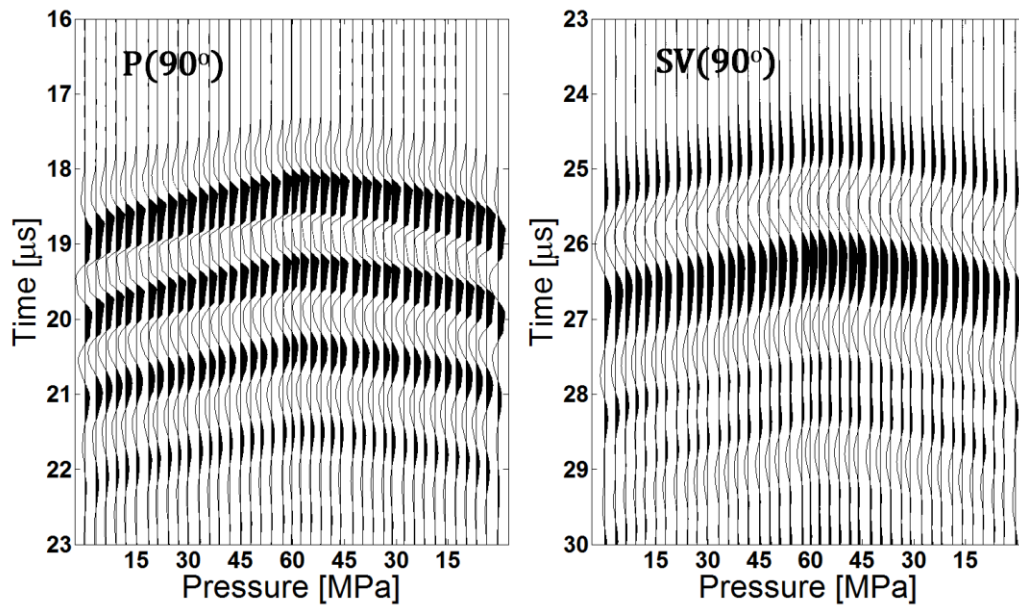Figure 6.9 Experimental configuration.

Figure 6.10 Set of waveforms for sample SSA-27. A dependence on traveltime as a function of confining pressure is observed.
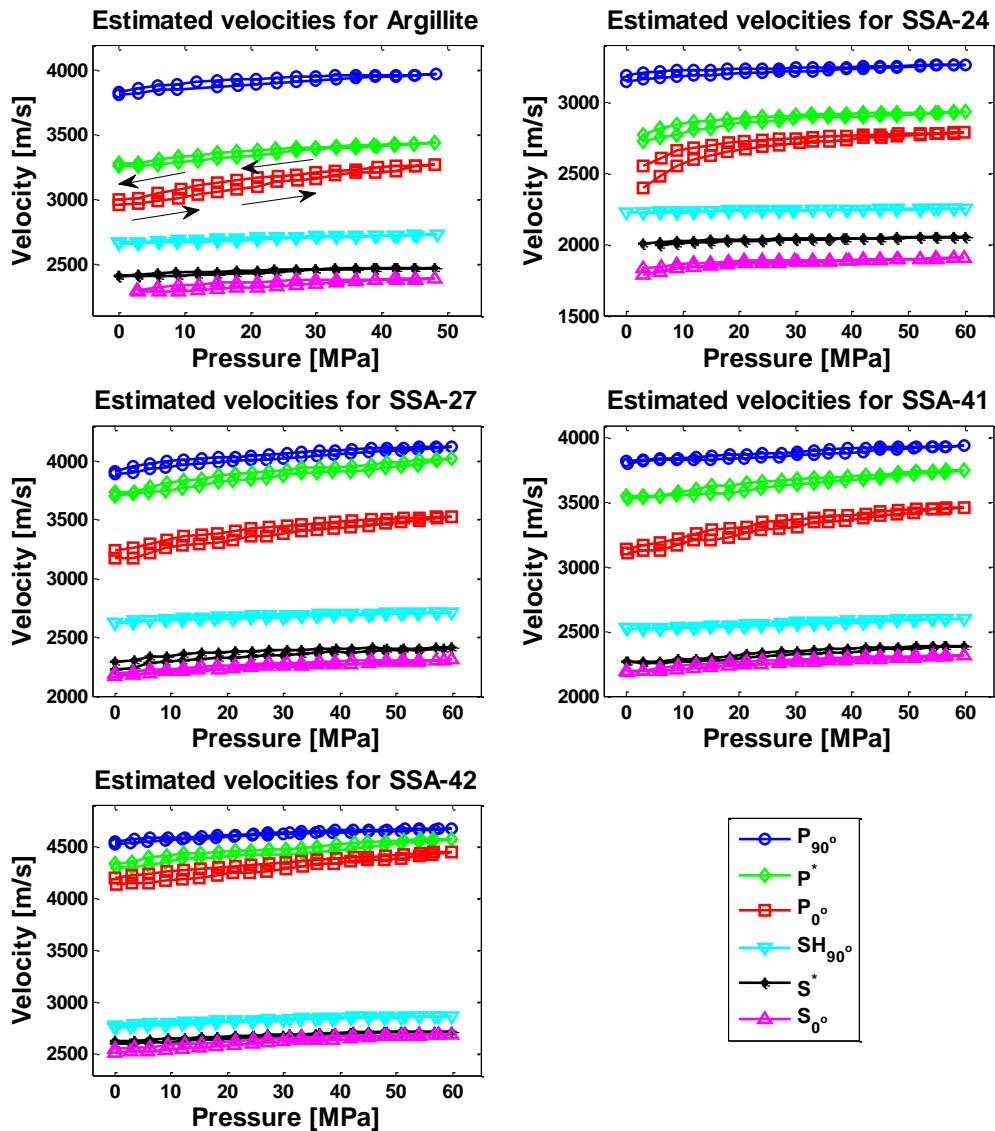
Figure 6.11 Estimated P- and S-wave velocities for studied samples. S^* represents SH_{53^o} for Argillite, SH_{45^o} for sample SSA24, and SV_{45^o} for samples SSA-27, SSA-41, and SSA-42. Arrows show the evolution of measurements and follow the sample trend for all samples. Effect of hysteresis can be observed in the pressurization and depressurization cycles.

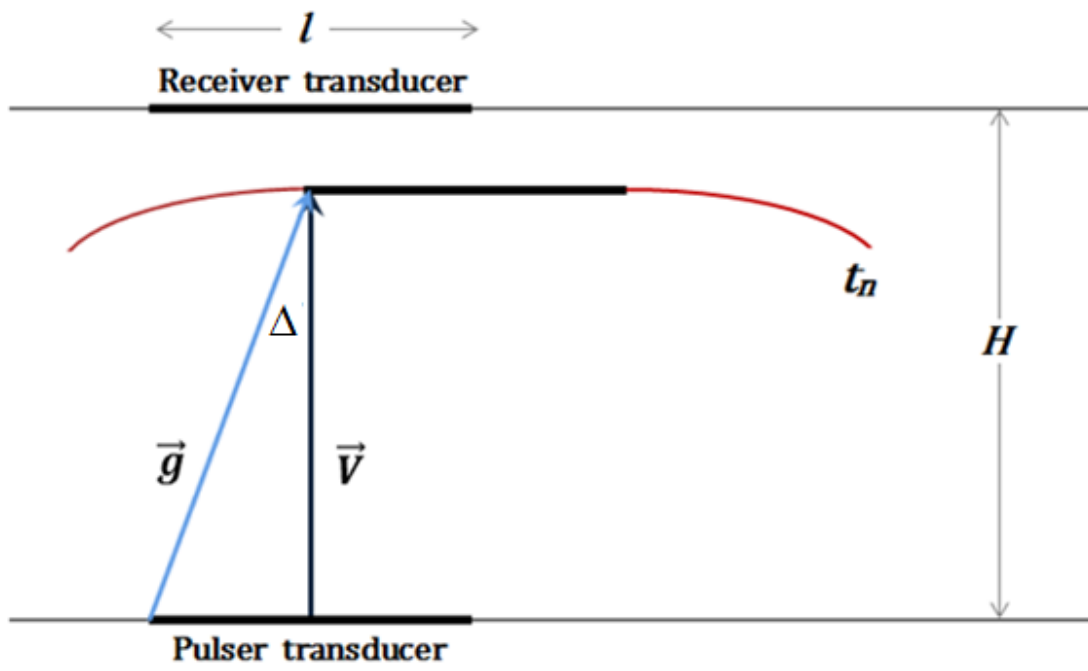Figure 6.12 Geometrical description of the ultrasonic experiment at oblique direction.
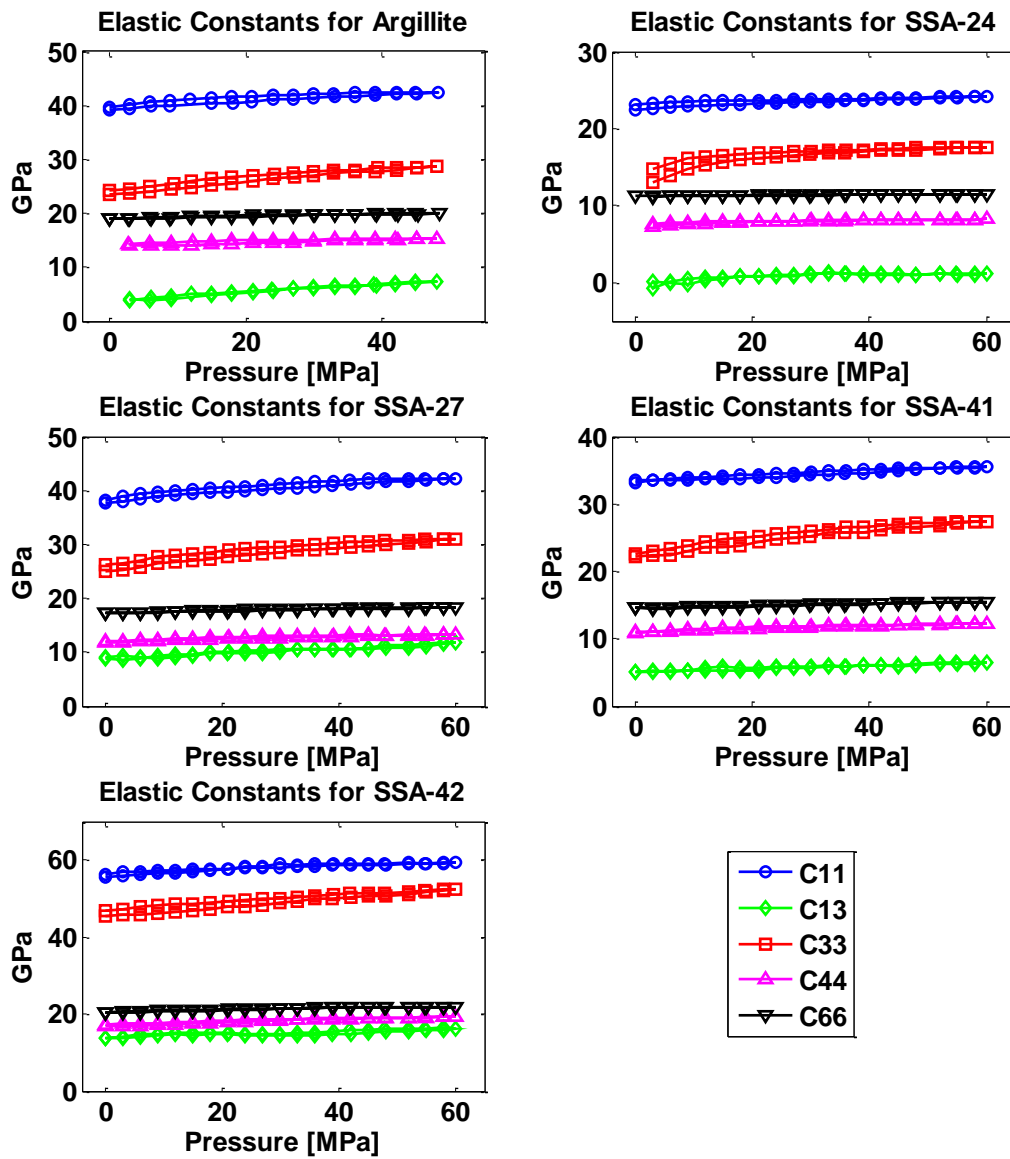
Figure 6.13 Elastic constants for studied samples as a function of confining pressure.
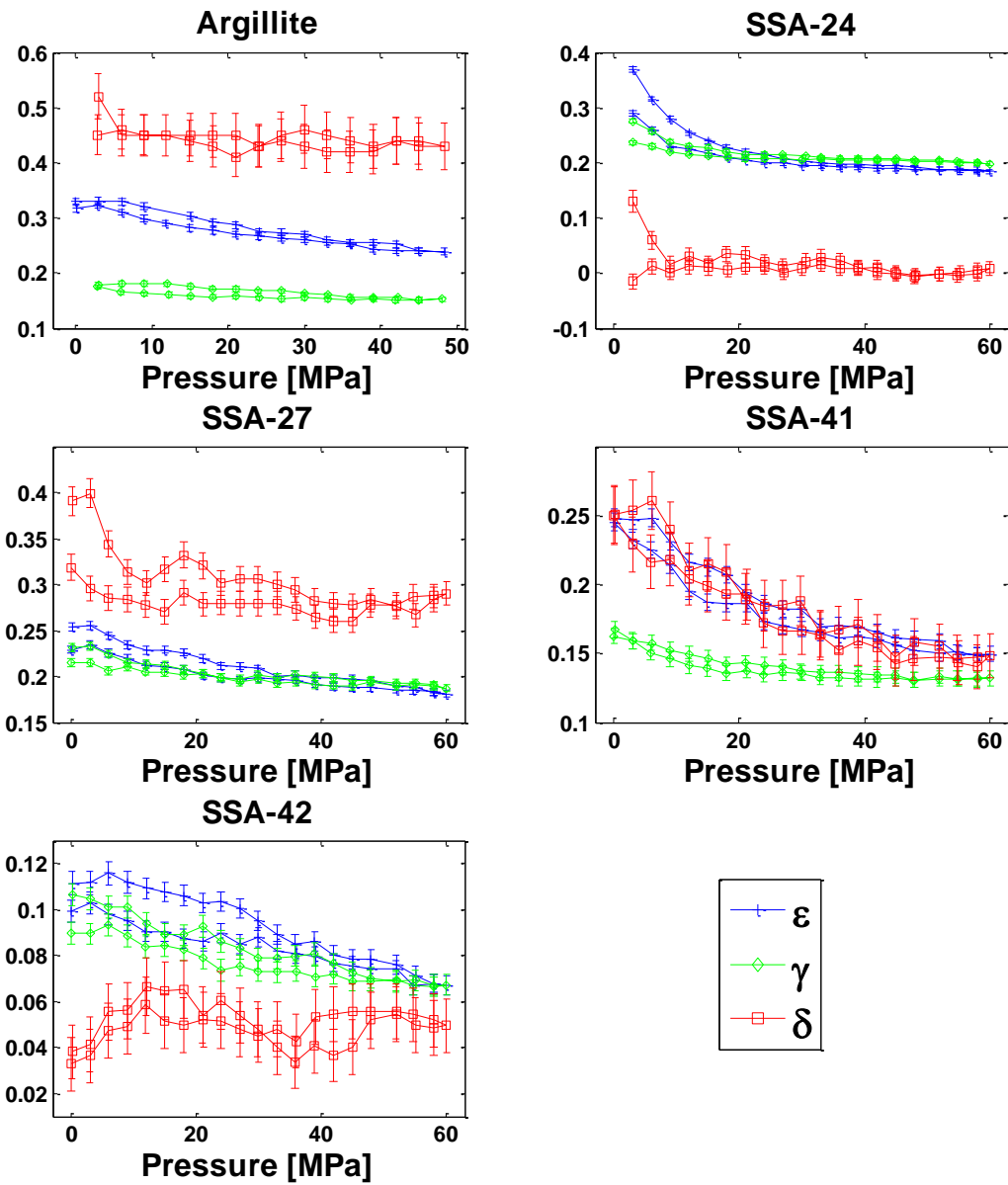
Figure 6.14 Thomsen parameters for all samples as a function of confining pressure along with the estimated error.
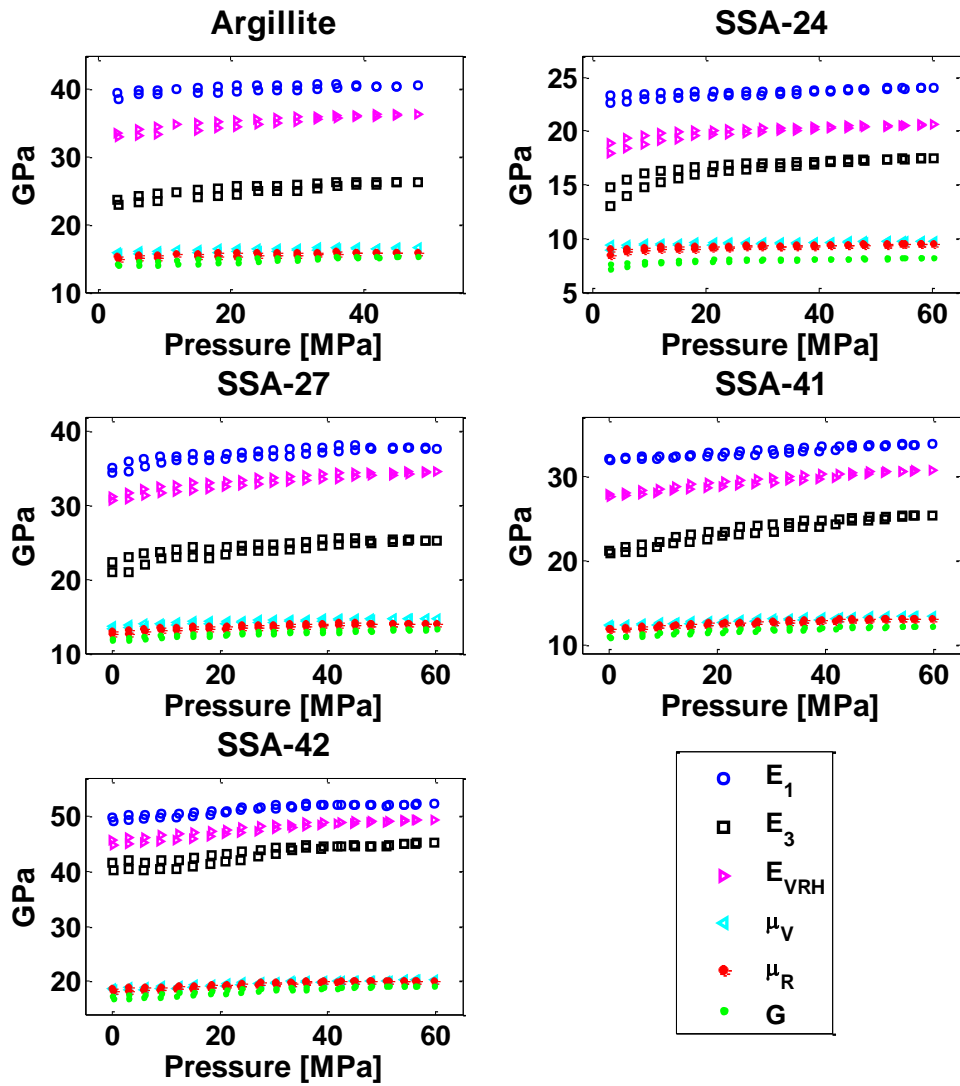
Figure 6.15 Dynamic moduli estimated from elastic constants assuming both an anisotropic single crystal and an isotropic composite.
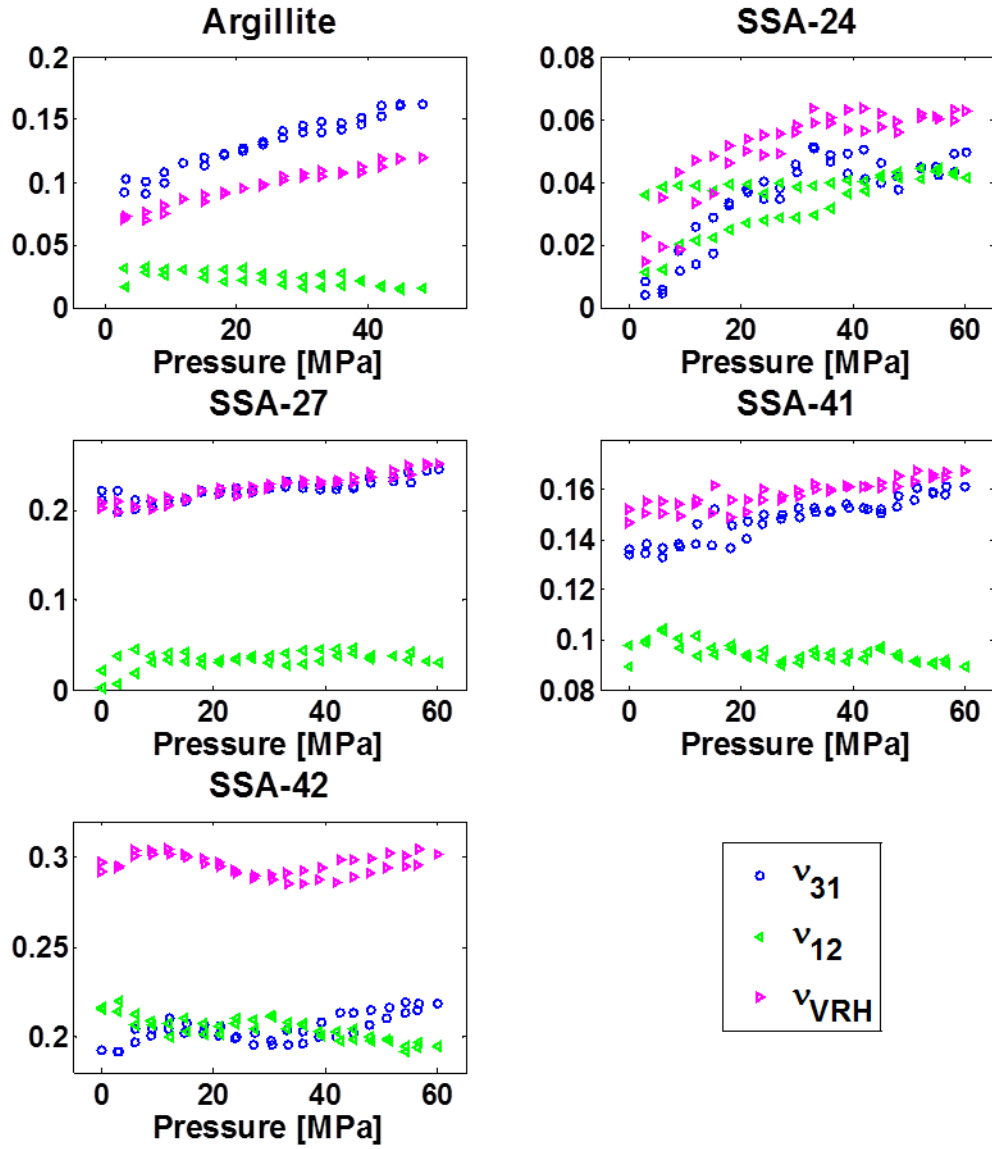
Figure 6.16 Poisson´s ratios estimated from elastic constants assuming both an anisotropic single crystal and an isotropic composite.
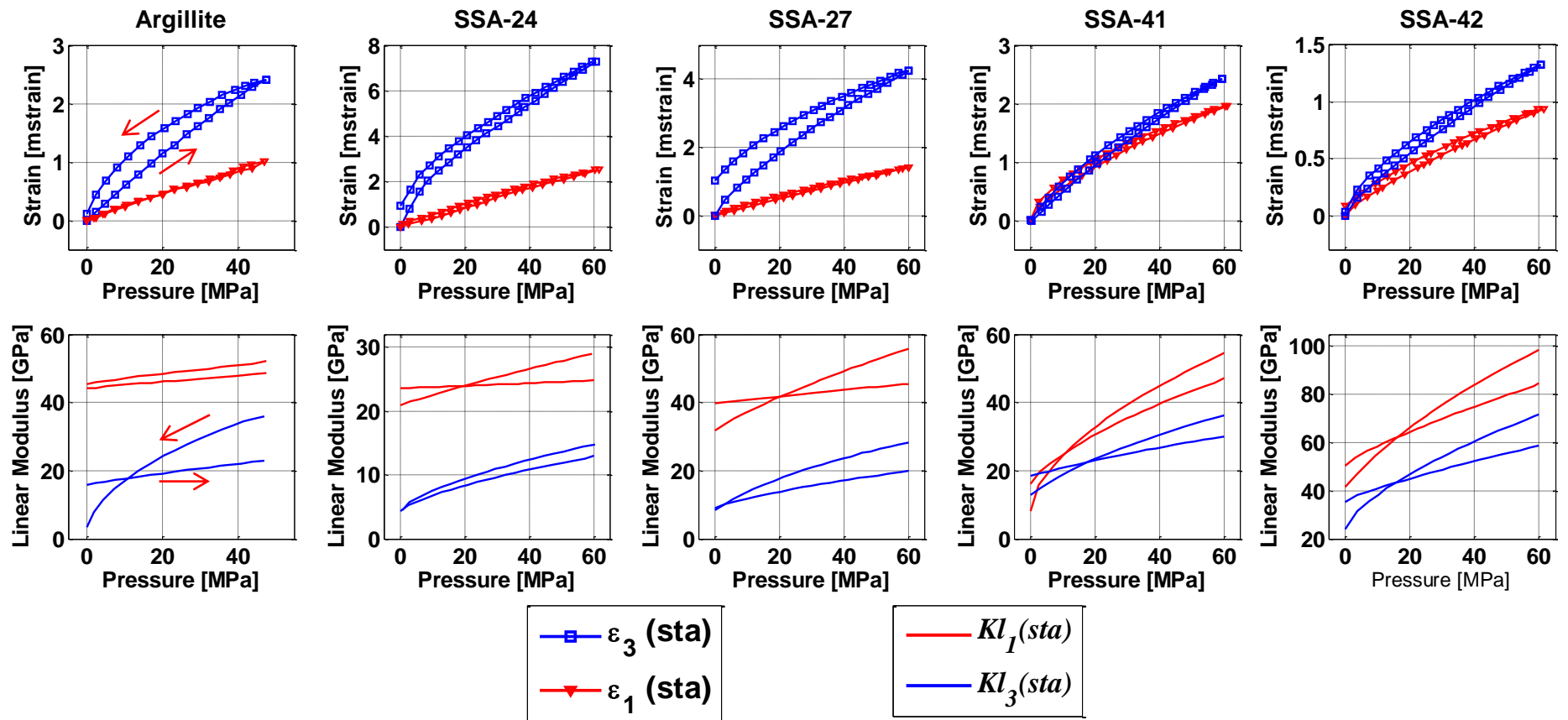
Figure 6.17 Top row: stress-strain relations for all samples as a function of confining pressure. Samples deform more along symmetry axes than along bedding. Bottom row: slope of the stress-strain relations confirms that samples are stiffer in the direction parallel to bedding than perpendicular to bedding. Red arrow show the evolution of measurements.
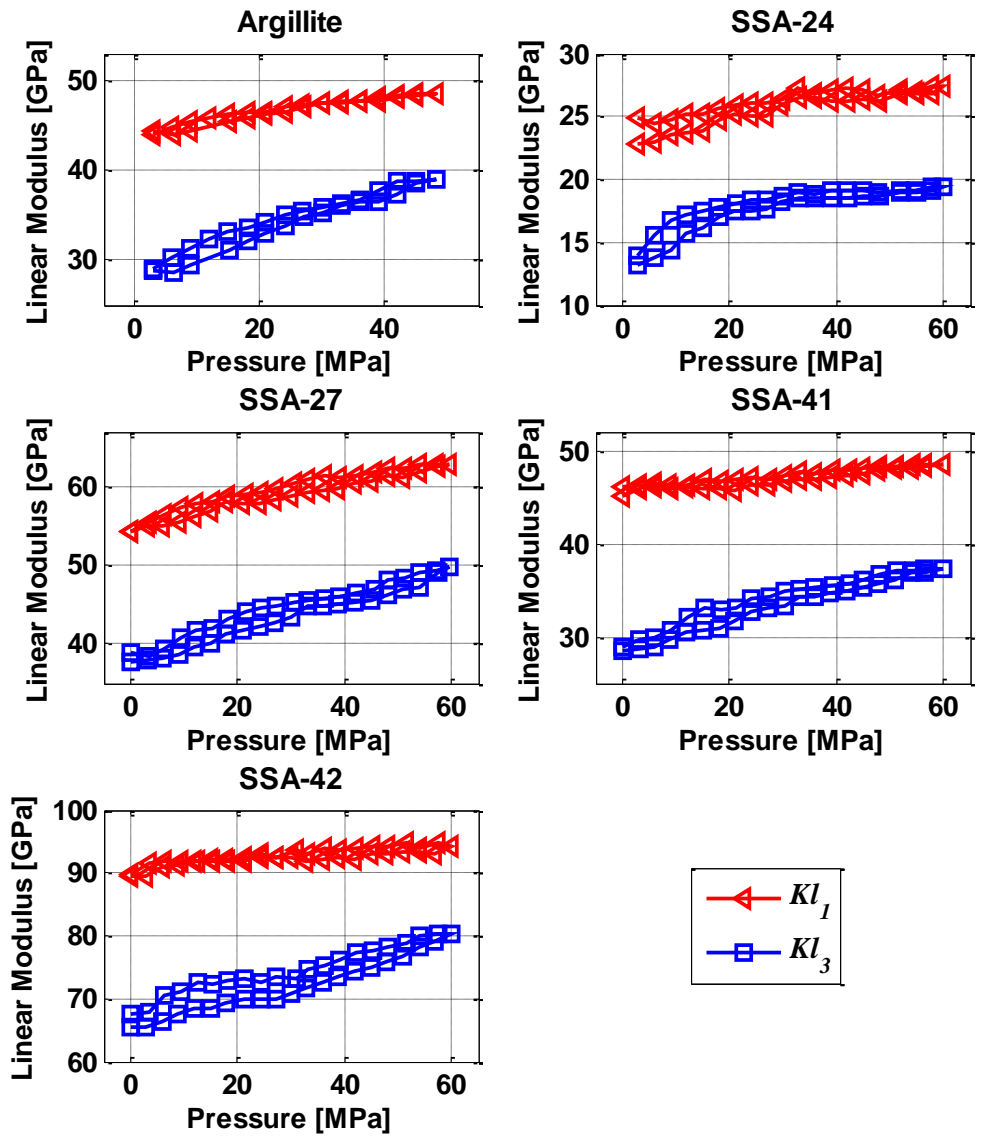
Figure 6.18 Estimated dynamic linear moduli for all samples. Results agree with static linear moduli in Figure 21 in the sense that both show that samples are stiffer along symmetry axes than parallel to bedding plane.
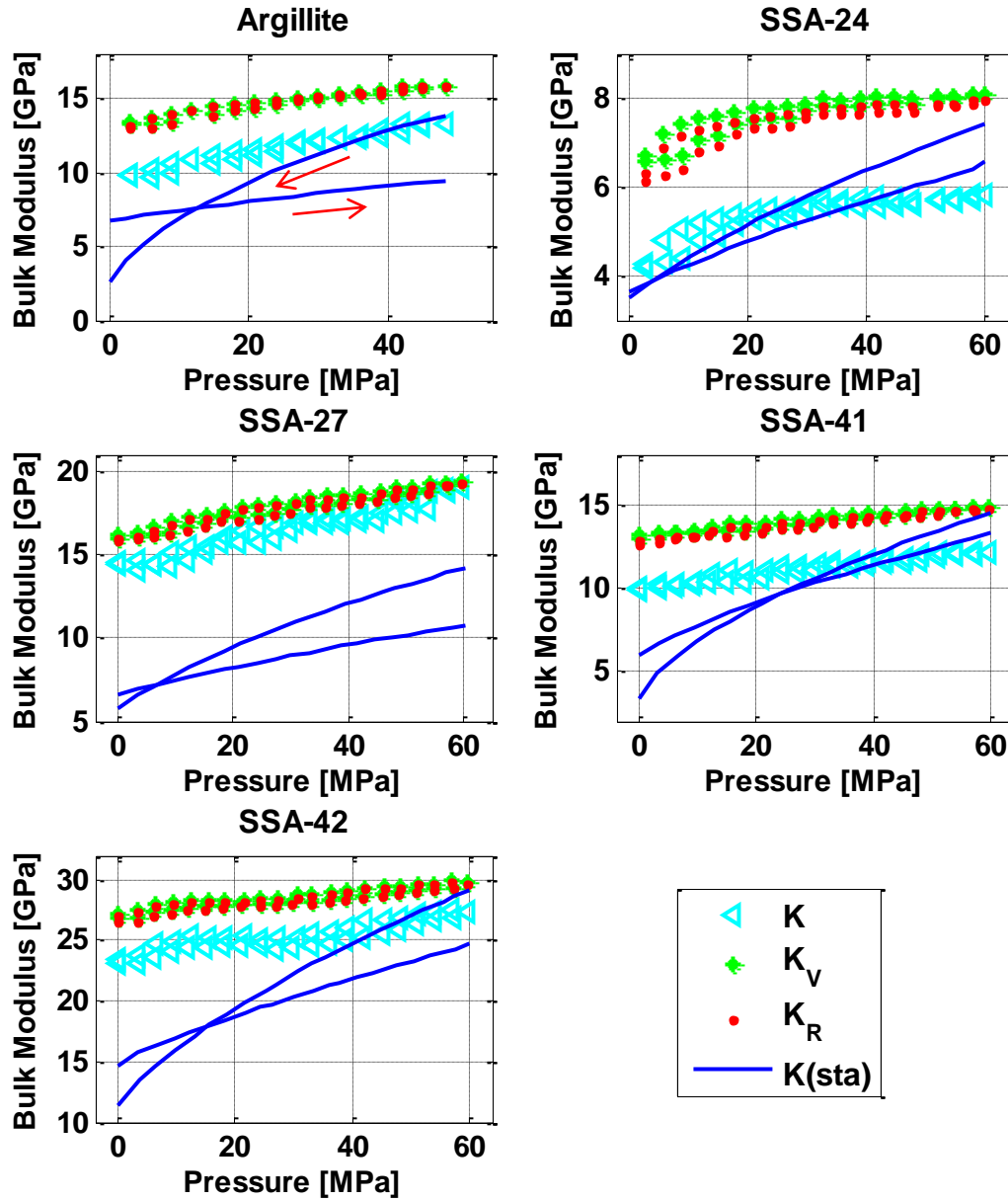
Figure 6.19 Comparative between dynamic and static bulk moduli. Red arrows show evolution of measurements.

Figure 6-A1 Set of Aluminum 6061-T6 used to calibrate P- and S- travel times shown at increasing length.
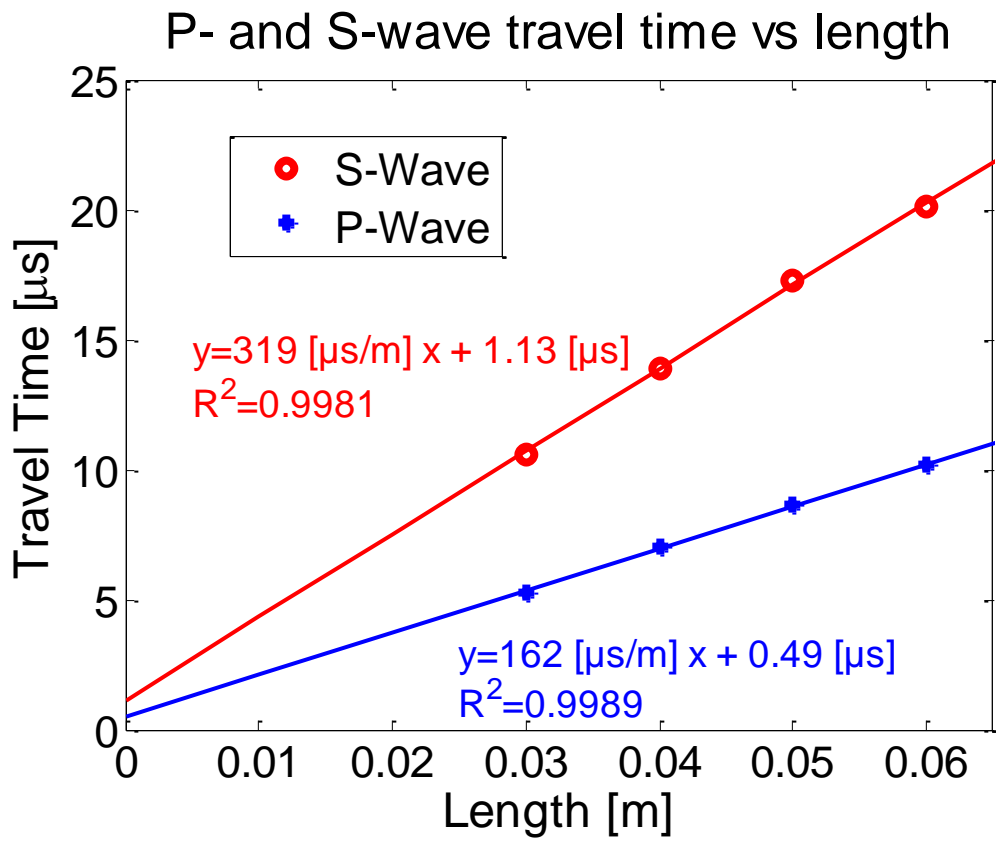
Figure 6-A2 P- and S-wave travel times against length for aluminum.

Bibliography

Adam, L., Batzle, M., Lewallen, K.T. and van Wijk, K. 2009. Seismic wave attenuation in carbonates, *Journal of Geophysical Research-Solid Earth,* 114, B06208.

Aplin, A.C. and Macquaker, J.H.S. 2011. Mudstone diversity: Origin and implications for source, seal, and reservoir properties in petroleum systems, *American Association of Petroleum Geologists Bulletin,* 95, 2031-2059.

Arts, R.J., Rasolofosaon, P.N.J. and Zinszner, B.E. Year. Complete inversion of the anisotropic elastic tensor in rocks: Experiment versus theory. 61st Annual Meeting Society of Exploration Geophysicists Expanded Abstracts,, 1538-1541.

Auld, B.A. 1973. *Acoustic fields and waves in solids.* 1 Wiley-Interscience Publication.

Bakhorji, A.M. 2010. Laboratory measurements of static and dynamic elastic properties in carbonate*, PhD Thesis*, University fo Alberta, Edmonton, Alberta, Canada.

Banik, N.C. 1984. Velocity anisotropy of shales and depth estimation in the North-Sea basin, *Geophysics,* 49, 1411-1419.

Barree, R.D., Gilbert, J.V. and Conway, M. 2009. Stress and Rock Property Profiling for Unconventional Reservoir Stimulation. In: *SPE Hydraulic Fracturing Technology Conference*. Society of Petroleum Engineers.

Batzle, M.L. and Simmons, G. 1976. Microfractures in rocks from two geothermal areas, *Earth and Planetary Science Letters,* 30, 71-93.

Boggs, S. 2009. *Petrology of Sedimentary Rocks.* Cambridge University Press.

Bowers, S.A. and Hanks, R.J. 1962. Specific heat capacity of soils and minerals as determined with a radiation calorimeter, *Soil Science,* 94, 392-396.

Brace, W. 1964. Effect of pressure on electric-resistance strain gages, *Experimental Mechanics,* 4, 212-216.

Carvajal-Jiménez, J.M., Valera-Lara, L.C., Rueda, A. and Saavedra.Trujillo, N. 2007. Geomechanical wellbore stability modeling of exploratory wells - study case at middle Magdalena basin, *CT&F Ciencia, Tecnología y Futuro,* 3, 85-102.

Cheadle, S.P., Brown, R.J. and Lawton, D.C. 1991. Orthorhombic anisotropy: a physical seismic modeling study, *Geophysics,* 56, 1603-1613.

Cheng, C.H. and Johnston, D.H. 1981. Dynamic and static moduli, *Geophysical Research Letters,* 8, 39-42.

Chung, D.H. and Buessem, W.R. 1967. The Voigt-Reuss-Hill Approximation and elastic moduli of polycrystalline MgO, CaF_2, β-ZnS, ZnSe, and CdTe, *Journal of Applied Physics,* 38, 2535-2540.

Curtis, J.B. 2002. Fractured shale-gas systems, *American Association of Petroleum Geologists Bulletin,* 86, 1921-1938.

Daley, P.F. and Hron, F. 1977. Reflection and transmission coefficients for transversely isotropic media, *Bulletin of the Seismological Society of America,* 67, 661-675.

De Vos, B., Vandecasteele, B., Deckers, J. and Muys, B. 2005. Capability of Loss-on-Ignition as a Predictor of Total Organic Carbon in Non-Calcareous Forest Soils, *Communications in Soil Science and Plant Analysis,* 36, 2899-2921.

Dean, W.E. 1974. Determination of carbonate and organic matter in calcareous sediments and sedimentary rocks by loss on ignition; comparison with other methods, *Journal of Sedimentary Research,* 44, 242-248.

Dellinger, J. and Vernik, L. 1994. Do travel-times in pulse-transmission experiments yield anisotropic group or phase velocities?, *Geophysics,* 59, 1774-1779.

Douglas, C.C., Qin, G., Collier, N. and Gong, B. 2011. Intelligent fracture creation for shale gas development. In: *Proceedings of the International Conference on Computational Science,*Vol. 4 (eds. M. Sato, S. Matsuoka, P.M.A. Sloot, G.D. Van Albada and J. Dongarra), pp. 1745-1750

Gardner, G.H.F., Wyllie, M.R.J. and Droschak, D.M. 1965. Hysteresis in the velocity-pressure characteristics of rocks, *Geophysics,* 30, 111-116.

Gilliam, T.M. and Morgan, I.L. 1987. Shale: Measurement of thermal properties. Oak Ridge National Laboratory ORNLTM-10499.

He, T. 2006. P- and S-wave velocity measurement and pressure sensitivity analysis of AVA response, MSc Thesis, University fo Alberta, Edmonton, Alberta, Canada.

Heiri, O., Lotter, A.F. and Lemcke, G. 2001. Loss on ignition as a method for estimating organic and carbonate content in sediments: reproducibility and comparability of results, *Journal of Paleolimnology,* 25, 101-110.

Hemsing, D.B. 2007. Laboratory determination of seismic anisotropy in sedimentary rock from the Western Canadian Sedimentary Basin*, MSc Thesis*, University of Alberta, Edmonton, Alberta, Canada.

Hill, R. 1952. The elastic behaviour of a crystalline aggregate, *Proceedings of the Physical Society of London Section A,* 65, 349-355.

Hornby, B.E. 1998. Experimental laboratory determination of the dynamic elastic properties of wet, drained shales, *Journal of Geophysical Research-Solid Earth,* 103, 29945-29964.

Hornby, B.E., Schwartz, L.M. and Hudson, J.A. 1994. Anisotropic effective-medium modeling of the elastic properties of shales, *Geophysics,* 59, 1570-1583.

Johnston, J.E. and Christensen, N.I. 1994. Elastic constants and velocity surfaces of indurated anisotropic shales, *Surveys in Geophysics,* 15, 481-494.

Johnston, J.E. and Christensen, N.I. 1995. Seismic anisotropy of shales, *Journal of Geophysical Research-Solid Earth,* 100, 5991-6003.

Jones, L.E.A. and Wang, H.F. 1981. Ultrasonic velocities in Cretaceous shales from the Williston Basin, *Geophysics,* 46, 288-297.

Kaarsberg, E.A. 1959. Introductory studies of natural and artificial argillaceous aggregates by sound-propagation and x-ray diffraction methods, *Journal of Geology,* 67, 447-472.

King, M.S. 1983. Static and dynamic elastic properties of rocks from the Canadian Shield, *International Journal of Rock Mechanics and Mining Sciences,* 20, 237-241.

Kular, G. 1972. Use of foil strain gage at high hydrostatic pressure, *Experimental Mechanics,* 12, 311-316.

Kuster, G.T. and Toksoz, M.N. 1974. Velocity and attenuation of seismic-waves in 2-phase medi: Part 1. Theoretical formulations, Geophysics, 39, 587-606.

Landau, L.L.D., Lifshits, E.M., Kosevič, A.M. and Pitaevskiĭ, L.P. 1986. *Theory of Elasticity 7.* Elsevier.

Lo, T.W., Coyner, K.B. and Toksoz, M.N. 1986. Experimental determination of elastic-anisotropy of Berea sandstone, Chicopee shale, and Chelmsford granite, *Geophysics,* 51, 164-171.

Marion, D., Mukerji, T. and Mavko, G. 1994. Scale effects on velocity dispersion - from ray to effective-medium theories in stratified media, *Geophysics,* 59, 1613-1619.

Mavko, G., Mukerji, T. and Dvorkin, J. 2009. *The Rock Physics Handbook: Tools for Seismic Analysis of Porous Media.* Cambridge University Press.

Meléndez, J. and Schmitt, D.R. 2013. Anisotropic elastic moduli of carbonates and evaporites from the Weyburn-Midale reservoir and seal rocks, *Geophysical Prospecting,* 61, 363-379.

Meyer, B.R. and Jacot, R.H. 2001. Impact of stress-dependent Young's moduli on hydraulic fracture modeling. In: *Rock Mechanics in the National Interest,*

Vols 1 and 2 (eds. D. Elsworth, J.P. Tinucci and K.A. Heasley), 297-306, ISBN 90-2651-827-7.

Milligan, R.V. 1967. The gross hydrostatic-pressure effect as related to foil and wire strain gages, *Experimental Mechanics,* 7, 67-74.

Musgrave, M.J.P. 1970. *Crystal acoustics: introduction to the study of elastic waves and vibrations in crystals.* Holden-day.

Ohno, I., Abe, M., Kimura, M., Hanayama, Y., Oda, H. and Suzuki, I. 2000. Elasticity measurement of silica glass under gas pressure, *American Mineralogist,* 85, 288-291.

Podio, A.L., Gregory, A.R. and Gray, K.E. 1968. Dynamic properties of dry and water-saturated Green River shale under stress, *Society of Petroleum Engineers Journal,* 8, 389-&.

Potter, P.E., Maynard, J.B. and Depetris, P.J. 2005. *Mud and Mudstones: Introduction and Overview.* Springer.

Reuss, A. 1929. Account of the liquid limit of mixed crystals on the basis of the plasticity condition for single crystal, *Zeitschrift Fur Angewandte Mathematik Und Mechanik,* 9, 49-58.

Sayers, C.M. 2013. The effect of anisotropy on the Young's moduli and Poisson's ratios of shales, *Geophysical Prospecting,* 61, 416-426.

Schmitt, D.R. and Li, Y.Y. 1995. A high-pressure technique for determining the microcrack porosities of damaged brittle materials, *Canadian Journal of Physics,* 73, 330-337.

Schmitt, D.R. and Zoback, M.D. 1989. Poroelastic effects in the determination of the maximum horizontal principal stress in hydraulic fracturing tests - a proposed breakdown equation employing a modified effective stress relation for tensile failure, *International Journal of Rock Mechanics and Mining Sciences & Geomechanics Abstracts,* 26, 499-506.

Schock, R.N. and Heard, H.C. 1974. Static mechanical properties and shock loading response of granite, *Journal of Geophysical Research,* 79, 1662-1666.

Simmons, G. and Brace, W.F. 1965. Comparison of static and dynamic measurements of compressibility of rocks, *Journal of Geophysical Research,* 70, 5649-&.

Thiercelin, M.J. and Plumb, R.A. 1994. Core-based prediction of lithologic stress contrasts in East Texas formations, *SPE Formation Evaluation*, 9, 251-258.

Thomsen, L. 1986. Weak elastic anisotropy, *Geophysics,* 51, 1954-1966.

Tutuncu, A.N., Podio, A.L., Gregory, A.R. and Sharma, M.M. 1998. Nonlinear viscoelastic behavior of sedimentary rocks, Part I: Effect of frequency and strain amplitude, *Geophysics,* 63, 184-194.

Tyson, R.V. 1995. *Sedimentary organic matter: organic facies and palynofacies.* Chapman & Hall.

Vernik, L. and Liu, X.Z. 1997. Velocity anisotropy in shales: A petrophysical study, *Geophysics,* 62, 521-532.

Voigt, W. 1928. *Lehrbuch der kristallphysik (mit ausschluss der kristalloptik).* B. G. Teubner.

Wang, Z.J. 2002a. Seismic anisotropy in sedimentary rocks, part 1: A single-plug laboratory method, *Geophysics,* 67, 1415-1422.

Warpinski, N.R., R.E., P., Branagan, P.T., Engler, B.P. and Wolhart, S.L. 1998. In situ stress and moduli: Comparison of values derived from multiple techniques. In: *SPE Annual Technical Conference and Exhibition*. Society of Petroleum Engineers.

Wong, R.C.K., Schmitt, D.R., Collis, D. and Gautam, R. 2008. Inherent transversely isotropic elastic parameters of over-consolidated shale measured by ultrasonic waves and their comparison with static and

acoustic in situ log measurements, *Journal of Geophysics and Engineering,* 5, 103-117.

Wright, A., Wang, Y. and Reddy, K.R. 2008. Loss-on-Ignition Method to Assess Soil Organic Carbon in Calcareous Everglades Wetlands, *Communications in Soil Science and Plant Analysis,* 39, 3074-3083.

Wright, J. 1987. The effects of transverse isotropy on reflection amplitude versus offset, *Geophysics,* 52, 564-567.

Yang, D.S., Billiotte, J. and Su, K. 2010. Characterization of the hydromechanical behavior of argillaceous rocks with effective gas permeability under deviatoric stress, *Engineering Geology,* 114, 116-122.

Yang, D.S., Chanchole, S., Valli, P. and Chen, L.F. 2013. Study of the Anisotropic Properties of Argillite Under Moisture and Mechanical Loads, *Rock Mechanics and Rock Engineering,* 46, 247-257.

Zhang, J.C. 2013. Borehole stability analysis accounting for anisotropies in drilling to weak bedding planes, *International Journal of Rock Mechanics and Mining Sciences,* 60, 160-170.

CHAPTER 7

General discussion and conclusions

7.1 Summary

An extensive laboratory study of the elastic and physical properties of a variety of sedimentary rocks has been presented in this thesis. The materials studied include glacial sediments, mudstones, carbonates and evaporites. Ultrasonic P- and S-waves were measured under dry conditions at pressures ranging from 0 to 60 MPa. In addition, static strain measurements were performed on mudstones. Closure of microcracks and pores leads to the increase of P-and S-wave velocities as a function of confining pressure, the variations are more dramatic in high porosity samples than in low porosity samples.

Comparison between laboratory densities of glacial sediments to those obtained from whole-core (*on site*) and wireline logging (*in situ*) data shows that laboratory densities follow the general trend of that of the *in situ/on site* densities, however a better agreement among them is obtained when water saturated samples is assumed. However, application of Gassmann´s substitution of fluids relation on ultrasonic compressional velocities has a negligible impact on velocities assuming water saturated samples, which suggests that state of saturation it is no so important in defining such velocities and instead they are mainly frame-controlled. Ultrasonic compressional velocities also follow the general trend of that of the *in situ/on site* measurements, being MSCL P-wave velocities of 8%

higher in average than ultrasonic velocities and these in turn are 13% higher than sonic velocities. Exact agreement between velocities is not expected since laboratory samples are affected by rebound effect, besides the fact the measured volumes differ significantly. On the other hand, anisotropy measurements on carbonate and evaporite samples suggests that intrinsic anisotropy of such rocks has negligible impact on the anisotropy observed at seismic scale which is due to the preferred alignment of fractures. The elastic constants obtained from the observed velocities and densities showed that the samples become stiffer as confining pressure increases.

Ultrasonic velocities and static strain measurements on shale and argillite samples demonstrated that they are highly anisotropic and that the dynamic moduli is higher than the static moduli. The samples become stiffer as a function of confining pressure as is well known. However because we are measuring the anisotropy, we see that samples are stiffer in the direction parallel to bedding than perpendicular to bedding. Preferred alignment of clay minerals and microcracks play a fundamental role in defining the above mentioned behavior. This means that the material anisotropy changes with confining pressure.

7.2 Contributions

This work highlights both dynamic and static measurements on a completely new data set of sedimentary rocks under confining pressure and hopes to assist in the understanding the elastic properties of mudstones, carbonates and evaporites. Although elastic properties of decimeter scale samples cannot represent entirely the seismic response of the entire formation or at the reservoir scale, they do

provide initial physical baselines from which more complex models at larger scales could be constructed.

Thus, the measured geophysical properties of glacial sediments can be used for engineering design and geophysical evaluations when investigating prospects of exploitable ground water resources and waste disposal.

On the other hand, results showed that the influence of the intrinsic anisotropy of the carbonates and evaporites from Weyburn-Midale oild field can be safely ignored when modelling stress-strain concentrations on potential boreholes located on such field, for example.

However, the main contribution of this work is the development of a methodology to simultaneously measure the dynamic and static moduli on single anisotropic fissile 'shale' samples. This is particularly important to achieve because conventional multicore methods used, for example in Chapter 4, to obtain the required information can introduce heterogeneity issues so that the estimated elastic moduli would be biased. In this sense, the prism-like shaped geometry presented in this thesis overcomes that problem and hence reduces the uncertainty in the elastic moduli determinations. The latter has several implications in both seismological and geomechanical problems such as image and depth estimation, migration, and amplitude vs offset (AVO) analysis as well as stress concentration and fracture propagation where accurate information in needed.

7.3 Future directions

This thesis has focused primarily on the task of making the complex anisotropic measurements, but a great deal remains to be accomplished in attempting to

interpret these results in light of the material structure and composition. Future work would include the study of effects of porosity on both compressional and shear measured ultrasonic velocities through derivation of empirical relationships. In the case of the shaly Antarctic samples and mudstones, quantitative determination of clay fraction is also important to establish those relationships. In this sense, estimation of the exact amount of clay minerals would be an interesting research topic as well.

On the other hand, determining mathematical relationships between dynamic and static moduli of analyzed shales and argillaceous samples can assist stress-strain prediction studies about how those geologic materials would behave at formations scale. Since orientation of clay minerals plays a fundamental role in defining anisotropy in studied samples, additional work would be the quantification of preferred orientation of such minerals which can be useful to model rock physical properties at a macroscopic level.

Investigating elastic anisotropic dynamic and static moduli on kerogen rich samples would be an interesting research topic since kerogen might have potential significant effects in the estimated moduli. A first step in this direction will be to carry our more sophisticated estimates of the total organic content in the material as currently we only used estimates of this from the loss on ignition during whole rock analsyis.

The dependence of rock stiffness on frequency and strain amplitude also needs to be investigated. This is important to know since by establishing equivalence relationships between elastic and dynamic properties would allow assisting

geomechanical studies from dynamic properties when stress-strain experiments are not available.

It would also be interesting to develop a methodology to study attenuation and controlled pore pressure on saturated shale samples. This topic is particularly challenging because of the low permeability characteristic of those rocks. However, rock physics community is interested in new sets of data since importance of unconventional reservoirs has been recently increasing as a source of oil and gas. As these rocks are still only poorly understood it is important to continue research in order to assist in unlocking these resources both more efficiently and with less impact to the environment.